Milad Ghasemi, M.Sc.

Mechanical Assessment of the Risk of Atherosclerotic Plaque Rupture in Carotid Arteries with a Focus on Damage Accumulation

---

Trinity College Dublin, 2019

A thesis submitted to the University of Dublin in partial fulfilment of the requirements for the degree of

Doctor in Philosophy

Supervisor: Prof. Caitríona Lally

Internal Examiner: Prof. Daniel J.Kelly

External Examiner: Prof. Estefanía Peña

Declaration

I declare that this thesis has not been submitted as an exercise for a degree at this or any other university and it is entirely my own work.

I agree to deposit this thesis in the University's open access institutional repository or allow the library to do so on my behalf, subject to Irish Copyright Legislation and Trinity College Library conditions of use and acknowledgement.

Milad Ghasemi

_____

Summary

Carotid atherosclerotic plaque rupture is one of the leading causes of death. Growth and development of atherosclerotic plaque alters the geometry and mechanical environment of the healthy arterial tissue. Supra-physiological stress values can occur in regions around the plaque shoulders in atherosclerotic plaques. Surgical interventions such as stenting or endarterectomy can also induce large loads on the arterial wall. To assess the risk of atherosclerotic plaque rupture in carotid arteries, in this thesis, a constituent specific study was first performed to investigate the role of collagenous and non-collagenous tissue in the response of arterial walls to supra-physiological loads. A structural constitutive model was also developed to capture the mechanical behaviour of non-collagenous and collagenous tissue under physiological and supra-physiological loading conditions.

Observing the important role of collagen fibres in damage relevant phenomena, the orientation of collagen fibres in healthy and diseased carotid bifurcations was studied in the next step. Collagen fibres can re-orient in biological tissues to maximize the load bearing capacity of their underlying structure. In this thesis, an optimum distribution of collagen fibres was predicted in both healthy and diseased carotid bifurcations. A novel remodelling metric was also introduced to characterize the lack of remodelling in terms of re-orientation in the atherosclerotic plaques which weakens the arterial tissue and may increase the risk of plaque rupture.

To accurately capture the mechanical behaviour of the arterial tissue, constitutive laws require accurate material properties. Different forms of mechanical tests can be conducted to calibrate these material models. However, using constitutive models to accurately assess the risk of atherosclerotic plaque rupture requires patient specific material parameters. To address this limitation, a geometrical metric was introduced and systematically assessed in the final study of this thesis. The high-risk areas predicted using this remodelling metric were compared with regions at highest stress values and areas where the maximum damage was accumulated in the collagen fibres within the arterial wall. Such geometrical metrics can be used independently, or in parallel with other indicators of risk of atherosclerotic plaque rupture to more efficiently and accurately assess the vulnerability of plaques in carotid arteries.

Acknowledgement

First of all I would like to acknowledge the assistance and support of my supervisor Professor Caitríona Lally. This work could not be accomplished without her guidance and all the very inspiring discussions we had through the last three years and three months of my life. Her enthusiasm for research and insightful ideas always kept me motivated and on the track.

I would also like to thank the European Research Council, Science Foundation Ireland and the Irish Research Council for funding this research. Without their support none of this work could have been carried out.

I would also like to acknowledge the assistance of Peter O'Reilly, the Senior experimental Officer of the Department of Mechanical and Manufacturing Engineering at Trinity College Dublin.

I have met and worked with many wonderful researchers during the course of my PhD. I have made some great friends in Trinity College Dublin. I would like to thank Robbie for all his help during different stages of my PhD and all the joyful moments we spent together. I would also like to thank Rob for all the great discussions and consultations we had over the past years. I would like to mention other great researchers of our lab whose company and friendship were invaluable through this journey; Céline, Pattie, Alix, David, Salman, Gaurav, Emma, Orla, Siobhan, Alan and Brooke. I would also like to express my gratitude to my friends outside our lab; Tracey, Liviu, Maria, Farhad, Sajad ,Emad, Saman, Reza and Shruty.

I would also like to express my sincere gratitude to my family and particularly my mother, Marzieh, for all the support and advice through a very long distance over the last years. Without their company, this work would have not been achieved.

List of Publications, Conference Proceedings and Prizes

First-author journal publications

Ghasemi, M., Nolan, D.R. and Lally, C., 2018. An investigation into the role of different constituents in damage accumulation in arterial tissue and constitutive model development. *Biomechanics and Modeling in Mechanobiology*, *17*(6), pp.1757-1769.

Ghasemi, M., Nolan, D.R. and Lally, C., 2018. Assessment of mechanical indicators of atherosclerotic plaque vulnerability; Geometrical curvature metric, plaque stresses and damage in tissue fibres. *Journal of the Mechanical Behaviour of Biomedical Materials*. [Submitted].

Ghasemi, M., Johnston R.D, Nolan, D.R. and Lally, C., 2018. Re-orientation of collagen fibres in healthy and patient specific carotid arteries; Towards a clinically relevant indicator of plaque vulnerability. [In preparation].

Conference Proceedings

Ghasemi, M., Nolan, D.R., Lally, C, 2018, A constituent specific study of damage accumulation in arterial tissue, *8th World Congress of Biomechanics*. July, 8-12, Dublin, Ireland.

Johnston, R., Ghasemi, M., Nolan, D.R., Lally, C, 2018, Optimized patient specific finite element models at the carotid bifurcation, *8th World Congress of Biomechanics*. July, 8-12, Dublin, Ireland.

Ghasemi, M., Nolan, D.R., Lally, C, 2018, Exploring the influence of damage accumulation on collagen fibre remodellingin arteries under supra-physiological loads, *16th European Mechanics of Materials Conference*. March, 26-28, Nantes, France.

Johnston, R., Ghasemi, M., Nolan, D.R., Lally, C, 2018, Optimiztion of Magnetic Resonance Imaging (MRI) based patient specific models with mechanical property estimation with inverse finite element analysis, *16th European Mechanics of Materials Conference*. March, 26-28, Nantes, France.

Ghasemi, M., Nolan, D.R., Lally, C, 2018, Damage accumulation in arterial tissue; Experimental observations on the role of matrix and fibres and constitutive model development, *Proceedings of the 24th Annual Conference of the Section of*

Bioengineering of the Royal Academy of Medicine in Ireland. January, 25-26, Meath, Ireland.

Johnston, R., Ghasemi, M., Nolan, D.R., Lally, C, 2018, An in-vivo study on the impact of axial resolution on peak stresses at carotid bifurcation, *Proceedings of the 24th Annual Conference of the Section of Bioengineering of the Royal Academy of Medicine in Ireland*. January, 25-26, Meath, Ireland.

Ghasemi, M., Nolan, D.R., Lally, C, 2017, Toward the development of a constitutive model to capture arterial collagen fibre remodelling and damage. 23rd *Congress of the European Society of Biomechanics*, July 2-5 2017, Seville, Spain.

Ghasemi, M., Nolan, D.R., Lally, C, 2017, Mechanical assessment of risk of rupture in arteries, *20th Sir Bernard Crossland Symposium*. April 27-28, Dublin, Ireland.

Ghasemi, M., Nolan, D.R., Lally, C, 2017 Collagen fibre remodelling in arterial soft tissue, *Proceedings of the 23rd Annual Conference of the Section of Bioengineering of the Royal Academy of Medicine in Ireland*. January, 20-21, Belfast, UK.

Nolan, D.R., Ghasemi, M,Lally, C, 2017, Assessment of clinically relevant measure for identifying vulnerable carotid plaque, *Proceedings of the 23rd Annual Conference of the Section of Bioengineering of the Royal Academy of Medicine in Ireland*. January, 20-21, Belfast, UK.

Ghasemi, M., Nolan, D.R., Lally, C, 2016, A review of arterial tissue remodelling, *Proceedings of the 22nd Annual Conference of the Section of Bioengineering of the Royal Academy of Medicine in Ireland*. January, 20-21, Galway, Ireland.

Prizes

Winner of the best Biomechanics talk at 24th Annual Conference of the Section of Bioengineering of the Royal Academy of Medicine in Ireland.

Contents

List of Figures

List of Tables

Chapter 1 Introduction

1.1 Introduction

Mechanical properties of soft biological tissues have been the focus of many studies in recent years. This is particularly the case for arterial tissue. One important motivation of such studies is the belief that changes in the mechanical properties of arteries can trigger some major cardiovascular diseases (CVDs) (Holzapfel and Ogden 2010). CVD is one of the leading causes of death worldwide (Benjamin et al. 2017). An estimated 17.5 million people died from CVDs in 2012 (Roger et al. 2011). However, the harm of CVDs is not limited only to an individual's health. CVD acts as a large financial burden as well. The combined direct and indirect costs of CVD in the United States was estimated to be $444 billion in 2010 (Amponsah et al. 2015).

Atherosclerosis and aneurysm are among the most common CVDs (Auerbach and Garfinkel 1980). These diseases mainly affect arteries and can lead to myocardial and cerebral infarctions. Development of these diseases alter both geometry and mechanical properties of the healthy arterial walls. Therefore, gaining a good understanding of the structure of healthy and diseased arteries is an essential primary step toward the prevention and treatment of these diseases. Such valuable information can also enhance the process of development of biomedical devices.

To-date, many techniques have been employed to explore the structure of arterial tissue. Collagen fibres are the main load bearing constituent of the arteries and, as such, they have been the focus of many studies. Quality and distribution of collagen fibres are known to play a major role in the mechanical response of the vessel walls (Driessen et al. 2003a; Holzapfel 2000). Various techniques have been employed to investigate the orientation of fibres *ex vivo* such as polarised light microscopy (PLM) (Schriefl et al. 2012a), confocal microscopy (Krasny et al. 2017), electron microscopy (Hilbert et al. 1996)and small angle light scattering (SALS) (Gaul et al. 2017). However, many limitations can be attributed to these techniques including the inherent destructive nature of these imaging modalities and also the time required to perform these observations. Developments in emerging imaging modalities such as diffusion tensor imaging (DTI) have recently shown great promise in being able to determine fibre directions (Shahid et al. 2017), although further progress is still required.

Although several experimental methods are employed to explore the orientation of fibres in soft biological tissues, relatively few types of experiments have been performed to investigate the influence of the quality of collagen fibres on the overall mechanical behaviour of arteries. Mechanical tests are among the most commonly used experiments for exploring the influence of quality of fibres. Monotonic and cyclic uniaxial tests, along with pressure inflation experiments, are widely employed to explore the mechanical behaviour of arteries under supra-physiological loads and to study damage accumulation in the non-collagenous and collagenous tissue (Calvo et al. 2007; Schriefl et al. 2015a; Sommer et al. 2010; Weisbecker et al. 2013).

Since destructive tests on arteries cannot be conducted on living human tissue, a key challenge is to find ways to make the required observations in a non-destructive way without affecting the biological tissue in any unintentional ways. In recent years, interest has been growing in computational models. One reason behind such motivation is the non-destructive nature of these simulations. Computational models enable us to predict the response of the tissue under various loading scenarios without the need to harvest samples from arteries or to make new experimental devices to explore the mechanical behaviour of the tissue under certain loading conditions.

In general, the main aim of a computational model is to replicate the behaviour of the system it parallels using mathematics, physics and computer science (Brodland 2015). In the case of arteries, computational methods have been widely applied to improve our understanding of the mechanical behaviour of the healthy and diseased tissue in a variety of ways such as:

1. Developing constitutive laws for predicting the passive and active mechanical response of fibrous arterial tissue under physiological (Fung et al. 1979; Gasser et al. 2006; Holzapfel et al. 2000; Holzapfel and Ogden 2010; Weiss et al. 1996) and supra-physiological loading conditions (Balzani et al. 2012; Balzani and Schmidt 2015; García et al. 2013; Pena 2014).
2. Investigating the influence of collagen fibre distribution and reorientation in overall mechanical behaviour of arteries (Driessen et al. 2003a; Fausten et al. 2016; Hariton et al. 2007; Humphrey 1999b).
3. Understanding the remodelling process in arteries and how arteries adapt to the changes in their mechanical environment (Driessen et al. 2003b; Gyoneva et al. 2016; Humphrey 1999b; Humphrey and Rajagopal 2002; Taber and Humphrey 2001).
4. Using geometrical determinants for assessment of atherosclerotic plaque vulnerability (Creane et al. 2010a; Li et al. 2008; Teng et al. 2010b)

5. Investigating the mechanical implications of vascular angioplasty and stenting (LaDisa et al. 2005; Lally et al. 2005; Timmins et al. 2007)
6. Assessment of effects of mural and induced stresses on pathogenesis of atherosclerosis (Davies 2009; Malek et al. 1999; Steinman et al. 2003)
7. Development of risk measures for aneurysm rupture (Brown and Powell 1999; Sicard et al. 2006; Steinman et al. 2003)

Although computational methods have great potential for predicting the response of the healthy arterial wall and atherosclerotic plaques under different loading conditions, most of these techniques are still dependent on inputs from experiments. One good example of such inputs can be material parameters. Most of the constitutive models proposed in the literature require accurate material properties to predict the mechanical behaviour of the tissue such as stress or damage accumulation in the arterial wall. Performing mechanical tests on the arterial tissue is a very common method for obtaining such material constants. However, recently, studies such as Liu et al. (2017) and Wittek et al. (2016) have suggested methods for *in-vivo* determination of these material properties by capturing the deformation of the arteries in the body and estimating the material properties using the inverse Finite Element Method (FEM). Advancements in imaging techniques such as Magnetic Resonance Imaging (MRI) can also facilitate the development of computational methods by providing information about the underlying structure of the healthy and diseased arteries in the body such as stiffness of the arterial wall or distribution of fibres in the arteries non-invasively (Liu et al. 2017; Shahid et al. 2017). Such information can be used as an input for computational methods to predict the mechanical behaviour of healthy and diseased arterial tissue under different loading conditions. In the case of carotid atherosclerotic plaques, this information can provide further insights into the risk assessment of plaque rupture in symptomatic and asymptomatic patients.

Geometrical metrics, such as curvature, are also among the other important computational methods that can reveal insightful information about the areas exposed to the highest stresses independent of material properties. Geometrical assessment of arterial tissue can decrease the computational costs of large models as they can identify the areas at the highest risk. Assessment of the orientation or quality of collagen fibres in those areas using constitutive laws or imaging technique can then be performed more efficiently.

1.2 Objectives

The overall aim of this thesis is to improve the risk assessment of atherosclerotic plaques in carotid arteries by gaining a better insight into the biomechanical properties and structure of healthy arteries and atherosclerotic plaques. To achieve this aim both experimental and computational approaches were employed. The following outlines the main objectives of this thesis.

1. To explore the mechanical behaviour of the collagenous and non-collagenous arterial tissue under high supra-physiological loads. Four damage relevant phenomena were investigated to achieve this aim, namely (i) softening, (ii) hysteresis (iii) permanent set and (iv) matrix failure and collagen fibre rupture.
2. To develop a constitutive model to successfully capture the aforementioned damage relevant phenomena in the collagenous and con-collagenous arterial tissues.
3. To determine the optimum structure of collagen fibres which maximize the load bearing capacity of healthy and diseased arterial tissue at carotid bifurcations.
4. To explain how re-orientation of collagen fibres toward their optimum configuration decreases the risk of atherosclerotic plaque rupture.
5. To introduce a remodelling metric that characterises the lack of remodelling in the atherosclerotic plaques in terms of lack of re-orientation from the optimum collagen fibre distribution in the diseased arterial tissue.
6. To introduce a novel geometrical metric for assessing the vulnerability of atherosclerotic plaques in carotid arteries.
7. To compare the areas at high risk of atherosclerotic plaque rupture predicted by the new geometrical metric with areas of highest stress values and highest damage accumulation in the collagen fibres.

1.3 Thesis Structure

This thesis consists of six chapters. Three main studies have been performed to achieve the previously mentioned goals. The structure of this thesis can be briefly explained as follows;

Chapter 1: Outlines the need for gaining further insights into the development of CVDs in the body. Different methods that can be used to investigate the structure of the healthy and diseased arteries are mentioned in this chapter. It is also emphasised that computational models show great promise in non-invasively assessing the vulnerability of atherosclerotic plaques and risk of rupture in carotid arteries. The overall objectives of this thesis are described, and an overview of this thesis is provided.

Chapter 2: Begins with a general review of the circulatory system and classification of arteries in the body. In the following sections, mechanical properties of healthy arteries under physiological and supra-physiological load levels are discussed. This chapter continues by explaining the process of development of atherosclerotic plaque in the arteries, the structure of atherosclerotic plaques and different risk assessment methods. The last part of this chapter reviews the constitutive models proposed to-date to capture the mechanical behaviour of healthy and diseased arterial tissue.

Chapter 3: Explores the role of non-collagenous and collagenous arterial tissue under cyclic supra-physiological loads. This chapter continues by developing a constitutive model to capture damage relevant phenomena in both collagenous and non-collagenous tissue under high cyclic loads. In the last part of this chapter the functionality of this constitutive model is verified for both collagenous and non-collagenous tissue.

Chapter 4: Starts with explaining how re-orientation of collagen fibres increases the load bearing capacity of arterial tissue, then subsequently demonstrates a method to predict the optimum distribution of fibres in real carotid bifurcations obtained from healthy volunteers. In the next step, the optimum configuration of the fibres is established for the geometries obtained from symptomatic patients who were undergoing endarterectomy surgery. In the last part of this study, a novel remodelling metric is introduced which correlates with the lack of orientation of fibres with their optimum configuration and relates to the level of softening in the tissue using the concept of continuum damage mechanics, as explained in Chapter 3.

Chapter 5: Outlines the need for a quick and simple patient specific metric to assess the risk of atherosclerotic plaque rupture. This chapter continues by introducing a new geometrical metric for assessing the vulnerability of carotid atherosclerotic plaques. This geometrical metric is systematically examined using idealized 2D and 3D models. The functionality of this metric is compared with stress values obtained from isotropic and anisotropic material models and damage parameters outlined in Chapter 3.

Chapter 6: Outlines the key findings and achievements of this thesis. This chapter also highlights the key contributions of this work in the field of arterial biomechanics. Finally, future perspectives emanating from this work are outline

Chapter 2 Literature Review

2.1 Cardiovascular system

The cardiovascular system consists of the heart, blood vessels and blood. This system contributes in many important body functions by transporting oxygen, nutrients and hormones to cells and carrying away waste from them by distributing the blood throughout the arteries and veins. The cardiovascular system can be divided up into two circuits known as the pulmonary circuit and the systemic circuit with the heart located at the centre of each, see Figure 2.1. The pulmonary loop carries oxygen-poor blood to the lungs and back to the heart while the systemic loop carries oxygenated blood from the heart to the rest of the body.

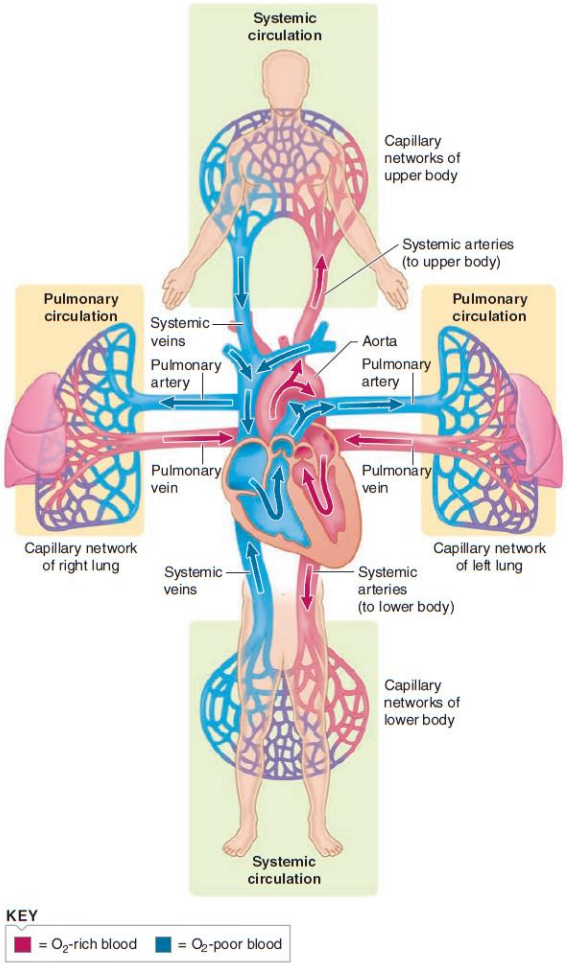

Figure 2.1. *A schematic presenting the pulmonary and systemic circulations in relation to the heart (Sherwood 2011)*

The heart is a muscular organ which is divided into the right and left valves. Two chambers are associated with each section. The upper chambers are called atria. These chambers receive blood returning to the heart and transfer it to the ventricles, the lower chambers, which pump blood from the heart. The vessels that return the blood from the tissues to the atria are veins and those that carry blood away from the heart to the tissues are arteries, see Figure 2.2.

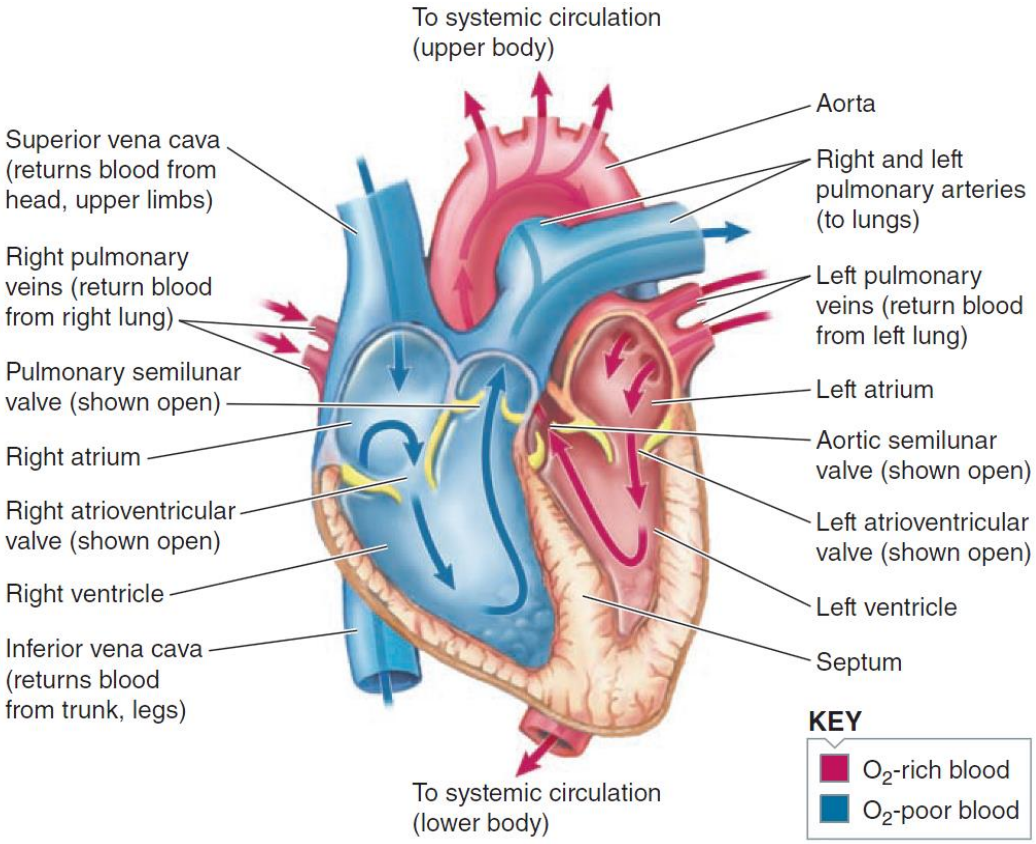

Figure 2.2. *Schematic of the heart showing its major components (Sherwood 2011)*

2.2 The Carotid Arteries

Carotid arteries are large blood vessels located in the neck and supply blood to the face, neck and brain. There are two carotid arteries. The main branch of the carotid artery is called the common carotid artery. Common carotid arteries bifurcate into the internal and external branches. The internal carotid artery provides the brain with rich-oxygenated blood while the external carotid artery supplies the face and neck (Gray 2001). Figure 2.3 presents a schematic of carotid arteries in the neck.

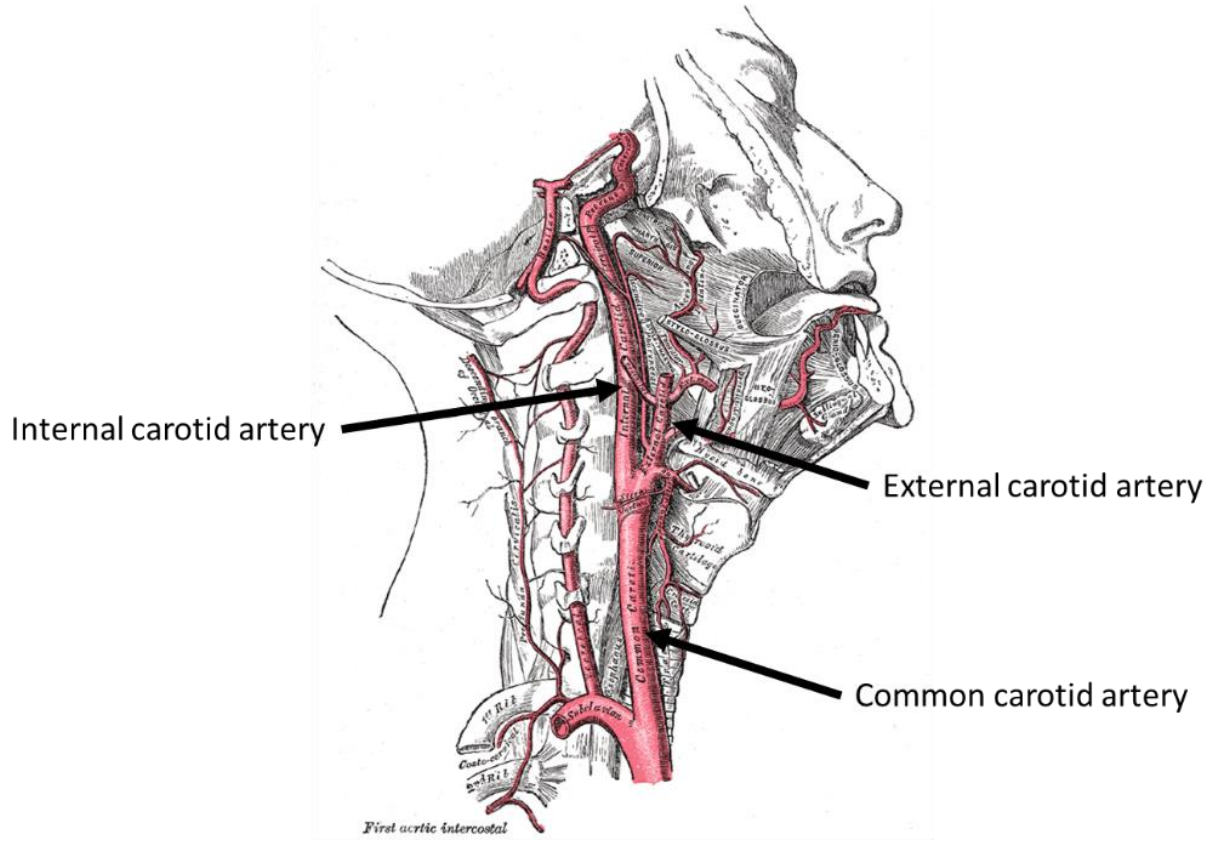

Figure 2.3. *Location of a right common carotid artery in the neck along with internal and external branches modified from (Gray 2001).*

2.3 Arterial Structure and Function

As mentioned in the previous sections, arteries are the blood vessels which carry oxygen-rich blood along with nutrients from the heart to various parts of the body. As arteries move from the heart, their diameter decreases. Arterioles are the smallest type of the arteries in the body with an average radius of 0.15 mm. (Burton 1962). Arterioles distribute the blood to the capillary network where oxygen and nutrients are exchanged with the tissue.

2.3.1 Arterial layers

Healthy arterial walls are composed of three distinct layers, the tunica intima, the tunica media and the tunica adventitia, see Figure 2.4. The inner-most layer of the arterial wall is the tunica intima. This layer consists of a single layer of endothelial cells, a thin basal membrane and a subendothelial layer. The subendothelial layer is comprised mainly of smooth muscle cells and bundles of collagen fibrils. The embedded collagen fibres within the subendothelial layer result in this layer playing a more significant role in bearing the loads in comparison with the endothelial layer (Gasser et al. 2006; Rhodin 1980). The medial layer is composed of a three-dimensional network of smooth muscle cells, elastin and collagen fibres. This layer is separated from the intima and adventitia by internal and external elastic

laminas (Gasser et al. 2006; Holzapfel et al. 2000). The outermost layer is the tunica adventitia. The adventitia layer consists of fibroblasts, fibrocytes, histological ground matrix and thick bundles of collagen fibres arranged in helical structures (Holzapfel et al. 2000; Rhodin 1980).

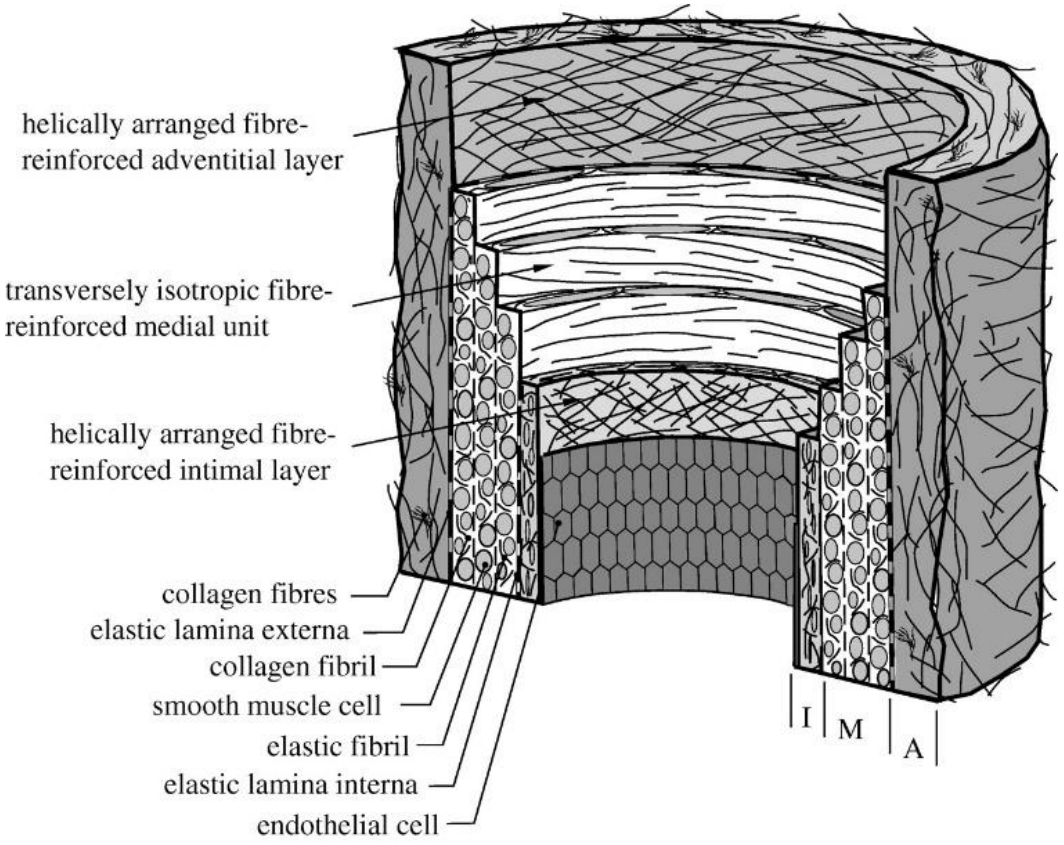

Figure 2.4. *A schematic presenting the three distinct layers of a healthy arterial wall, the tunica intima (I), the tunica media (M) and the tunica adventitia (A), along with the structure and constituents of each layer (Gasser et al. 2006).*

2.3.2 Artery types

Arteries can be classified into two main categories, elastic and muscular (Gasser et al. 2006; Rhodin 1980). Elastic arteries are conducting arteries which are located near the heart such as the aorta or carotid arteries. Elastic arteries have larger diameters compared to muscular arteries as they transport a larger volume of blood and they should have the lowest resistance to the blood flow. In terms of structure, in the elastic arteries ,the tunica media contains more elastic laminae compared to smooth muscle cells, whereas, the media layer of muscular arteries is less elastic and smooth muscle cells prevail (Rhodin 1980).

2.4 Mechanical properties of arterial tissue

2.4.1 Mechanical properties of arteries under physiological load levels

2.4.1.1 Non-linearity in the response of arteries to loads

As mentioned in the previous sections, healthy arterial walls are composed of various constituents such as smooth muscle cells, elastin fibres and collagen fibres. The distribution of each component differs through the arterial wall thickness. Figure 2.5 presents the orientation of smooth muscle cells and elastic laminae in elastic arteries (Rhodin 1980).

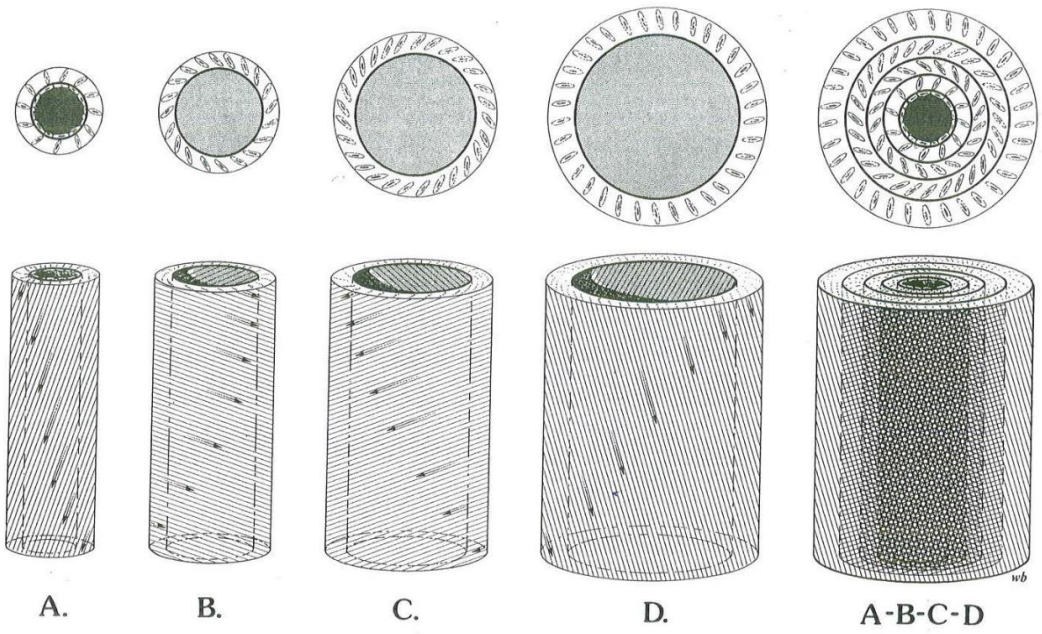

Figure 2.5. *A schematic drawing presenting different layers of elastic laminae (A-D) and orientation of smooth muscle cells through the arterial wall thickness (Rhodin 1980).*

Although all the constituents within the arterial wall contribute in bearing the loads, collagen fibres are believed to play the most significant role to withstand the physiological and supra-physiological loads (Driessen et al. 2004; Hariton et al. 2006; Holzapfel 2008) .

The non-linearity that arises in the response of the arterial tissue has been associated with the presence of the collagen fibres. The study conducted by Roach et al. (1957) is one of the first studies that investigated the non-linear response of the arterial tissue under loads. In that study, samples obtained from human iliac arteries, were subjected to differential digestion of collagen fibres, using formic acid, and elastin fibres, using trypsin. Performing pressure inflation tests, they showed that non-linearity which arises in the response of the arterial tissue, particularly at higher levels of loads, is due to the presence of collagen fibres. They also concluded that at physiological loads the response of the tissue is primarily dominated by elastin fibres, see Figure 2.6, (Roach et al. 1957).

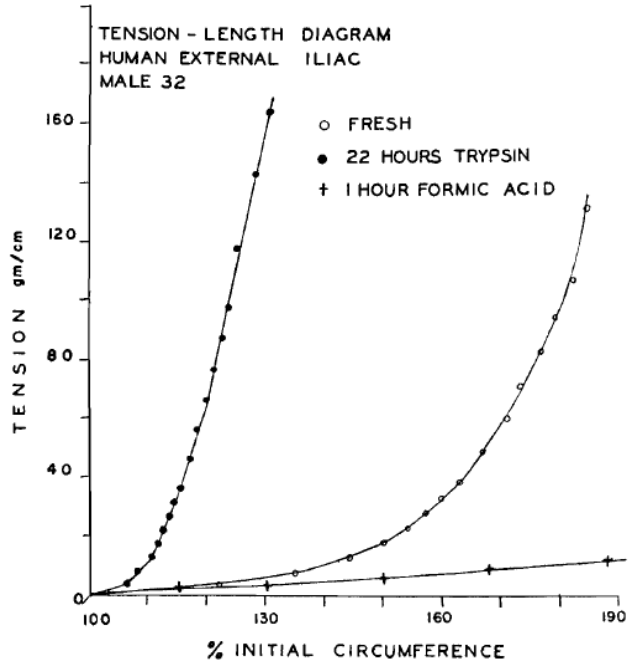

Figure 2.6. *Mechanical response of a fresh human iliac artery compared with digested tissue by trypsin and formic acid (Roach et al. 1957).*

These observations were confirmed later in many studies (Fung et al. 1979; Gasser et al. 2006; Holzapfel 2000) -just to name a few. Studies such as (Humphrey 1999b) and (Holzapfel et al. 2000) then associated the inability of collagen fibres to contribute in bearing the low loads with their waviness at such stages. Response of a healthy arterial wall under physiological blood pressure is schematically explained in Figure 2.7 (Singh et al. 2015). Figure 2.7 (A) presents a J-shaped curve obtained by increasing the pressure and measuring the increase in the diameter of an artery. The mechanical response of the vessel wall can be subdivided into three regions; elastin dominated, upturning region and collagen dominated. In the elastin dominated region, Figure 2.7 (B), non-collagenous tissue plays a more significant role in bearing the load of pressure as collagen fibres are undulated at this stage. At the upturning region, Figure 2.7 (C), elastin fibres are fully stretched. In this part of the curve the waviness of collagen fibres also decreases. The response of the arterial wall at this stage is the superposition of the response of elastin fibres and increasing numbers of stretched collagen fibres. Also, this is the stage where the non-linearity arises in the tissue response. By increasing the pressure from this stage, all of the collagen fibres become stretched and the stiffness of the arterial tissue increases, Figure 2.7 (D). These observations are confirmed in studies such as (Gasser et al. 2006; Holzapfel et al. 2000; Humphrey 1994; Zulliger et al. 2004).

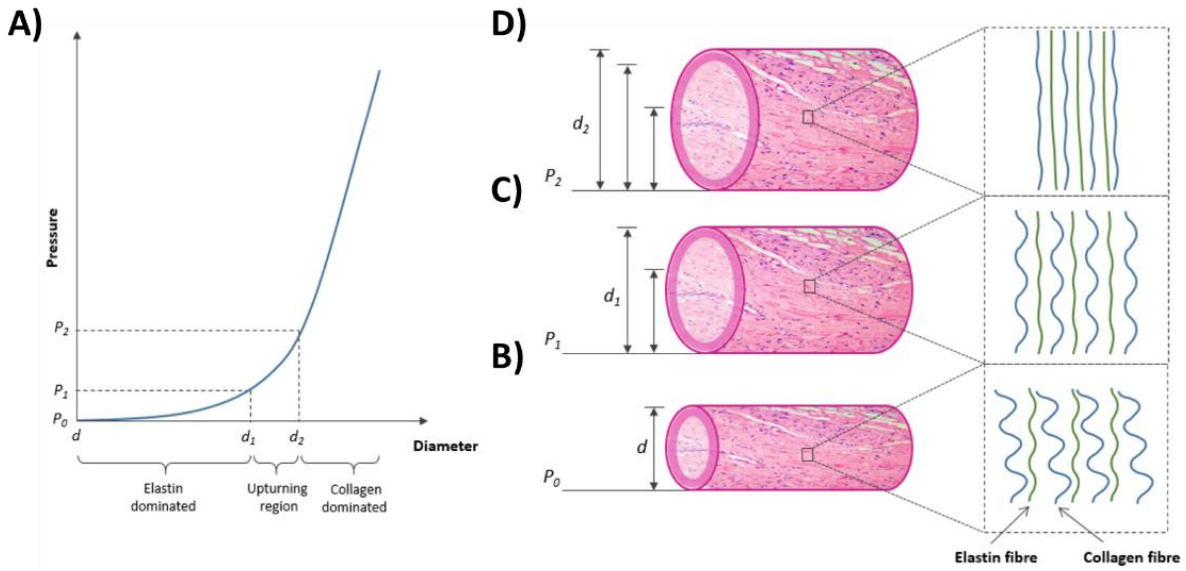

Figure 2.7. *A schematic presenting the response of a cylindrical artery to different levels of pressure (Singh et al. 2015).*

2.4.1.2 Anisotropic response of the arteries to loads

Anisotropy is the other important mechanical property of the arterial tissue. Studies such as (Patel et al. 1969; Weizsacker and Pinto 1988) are among the first studies that reported different levels of stiffness in the circumferential and axial directions of arterial walls. The anisotropic mechanical response of the arterial tissue is associated with the distribution of fibres in the vessel wall and is explored in studies such as (Gasser et al. 2006; Holzapfel et al. 2000). Figure 2.8 presents the mean response of different layers of 13 human left anterior descending coronary specimens in the circumferential and axial directions (Holzapfel et al. 2005). Figure 2.8 indicates large differences in the mechanical response of various layers of arterial wall in the circumferential and axial directions. One important reason behind such large differences is the various distributions of collagen fibres in different layers of the vessel wall.

Optical techniques such as Polarised Light Microscopy (PLM) (Schriefl et al. 2012a) , see Figure 2.9, Second Harmonic Generation (SHG) (Ghazanfari et al. 2012) and multiphoton microscopy (Krasny et al. 2017) have also confirmed the difference in the distribution of collagen fibres in different layers of arterial tissue. Gaul et al. (2017) also explained the various architecture of collagen fibres within the different layers of arterial tissue using the Small Angle Light Scattering (SALS) technique.

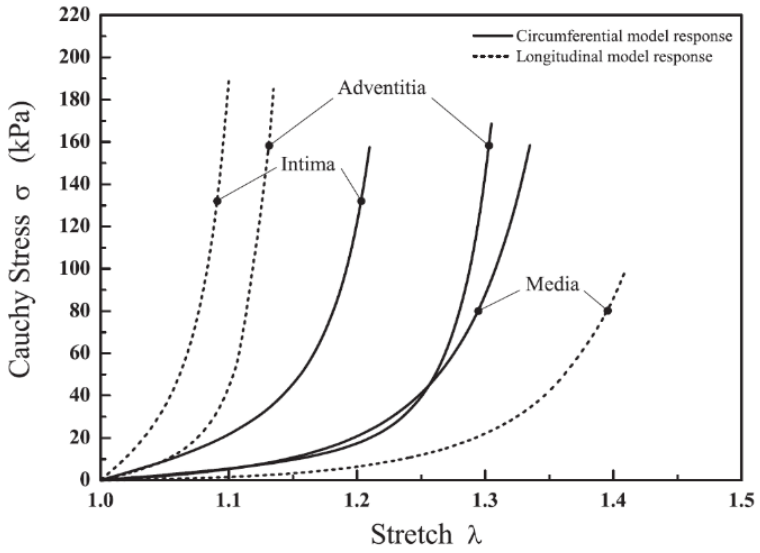

Figure 2.8. *Mean Cauchy stress-stretch curves of different layers of 13 human left anterior descending coronary specimens in the circumferential and axial directions (Holzapfel et al. 2005).*

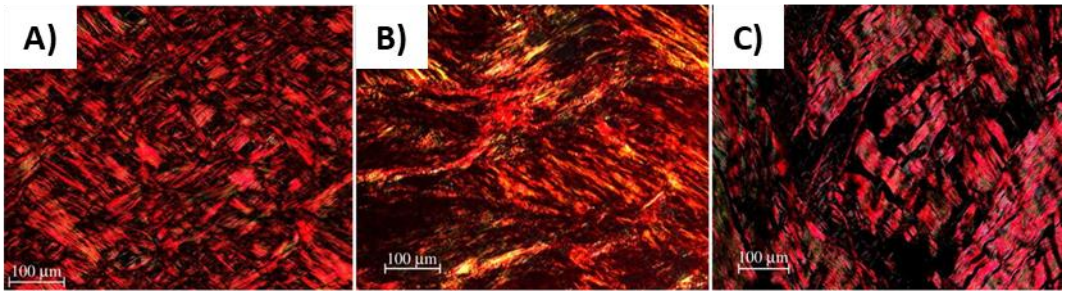

Figure 2.9. *Images obtained from A) the tunica intima B) the tunica media and C) tunica adventitia of a human thoracic aorta using PLM indicating different distribution of collagen fibres in different layers of arterial tissue (Schriefl et al. 2012a).*

To-date, many studies have confirmed the anisotropic response of arteries and shown that the mechanical response of the arteries varies through the arterial wall thickness, as mentioned above. Studies such as (Hariton 2006; Kuhl et al. 2005) suggested that growth of collagen fibres through the process of aging is the main reason behind the anisotropic response of the arterial tissue in adolescence and adulthood, while the mechanical response of the arteries is isotropic at the embryonic stages.

Alignment of collagen fibres through the healthy arterial wall can also be explained according to the mechanical environment of the arterial tissue. Maximum values of stresses and strains occur in the innermost layer of the arterial wall where collagen fibres are highly aligned. However, collagen fibres are shown to be less aligned in the adventitial layer where both stress and strain have their minimum values through the wall thickness. This arrangement of

collagen fibres through the arterial wall thickness results in helical paths of collagen fibres through the arterial wall, see Figure 2.10 (Hariton et al. 2006).

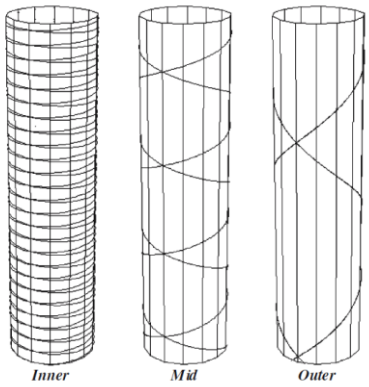

Figure 2.10. *A schematic presenting the distribution of fibres in three different layers of arterial wall (Hariton et al. 2006).*

2.4.1.3 Residual stress in the arteries

The importance of residual stress in the mechanical response of the arterial tissue is emphasised in many studies in the literature such as (Alastrue et al. 2008; Delfino et al. 1997; Holzapfel et al. 2007; Schroder and Brinkhues 2014)-just to name a few. The research conducted by Vaishnav and Vossoughi (1983) is among the first studies that investigated the residual stress in arterial walls. In that study, Vaishnav and Vossoughi (1987) made circular samples of bovine and porcine abdominal aortas. They observed that by cutting the samples in the radial direction, the specimens opened up into a horseshoe shape indicating the residual stress in the arterial wall at an unloaded stage, see Figure 2.11 (Vaishnav and Vossoughi 1987).

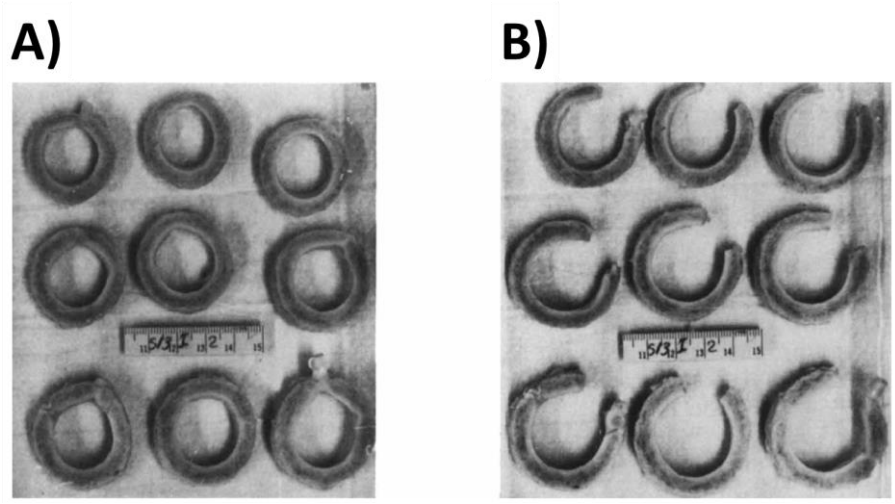

Figure 2.11. *A) Ring samples obtained from aortic sections. B) The open configuration of ring samples shown in section A obtained by cutting the samples in the radial direction (Vaishnav and Vossoughi 1987).*

Greenwald et al. (1997) explored the distribution of residual strains in the arteries by selectively eliminating the elastin and collagen fibres and measuring the obtained opening angles. In that study, they showed that digesting the collagen fibres does not have a significant influence on the measured opening angles in different samples. This observation suggested that collagen fibres do not play a major role in the presence of residual stress in the arterial tissue (Schroder and Brinkhues 2014). These observations are also confirmed in studies such as (Cardamone et al. 2009; Yu et al. 2018).

Many studies explored the origin of residual stress in the arterial tissue within the literature such as (Cardamone et al. 2009; Fung 1991). Fung (1991) associated the residual stress with non-uniform growth and remodelling within the healthy arterial tissue. This suggestion was in agreement with other observations when residual stress was increased in the arterial wall as a result of ageing or hypertrophy in adults (Schroder and Brinkhues 2014).

Fung et al. (1992) demonstrated that the presence of the residual stress in the arterial tissue smooths the gradient of the stress distribution in the vessel wall which was also subsequently confirmed in many studies such as (Holzapfel et al. 2007; Rachev and Greenwald 2003).

2.4.1.4 Viscoelasticity in the arteries

Arterial tissues behave viscoelastically indicating that they possess both elastic behaviour and viscous damping during the deformation. Exhibiting hysteresis under cyclic loading, Figure 2.12 (A), stress relaxation under a constant stretch, Figure 2.12 (B) and creep under a constant load, Humphrey (2013) showed the viscoelastic response of the arterial tissue.

The study conducted by Gow and Taylor (1968) is among the first studies that explored the viscoelasticity in arterial tissue by measuring dynamic elastic moduli and viscous moduli of the arterial wall obtained from living dogs and performing pressure inflation tests. Pena et al. (2010) explained the viscoelasticity in the arterial tissue by attributing this behaviour to fluid transport within the solid matrix and the friction between the solid and fluid constituents of the arterial tissue.

The viscoelastic behaviour of the arterial tissue diminishes after preconditioning which is a necessary step in performing mechanical tests on arteries (Macrae et al. 2016). The behaviour of arterial tissue is considered repeatable once they are preconditioned (Humphrey 2013; Pena et al. 2010).

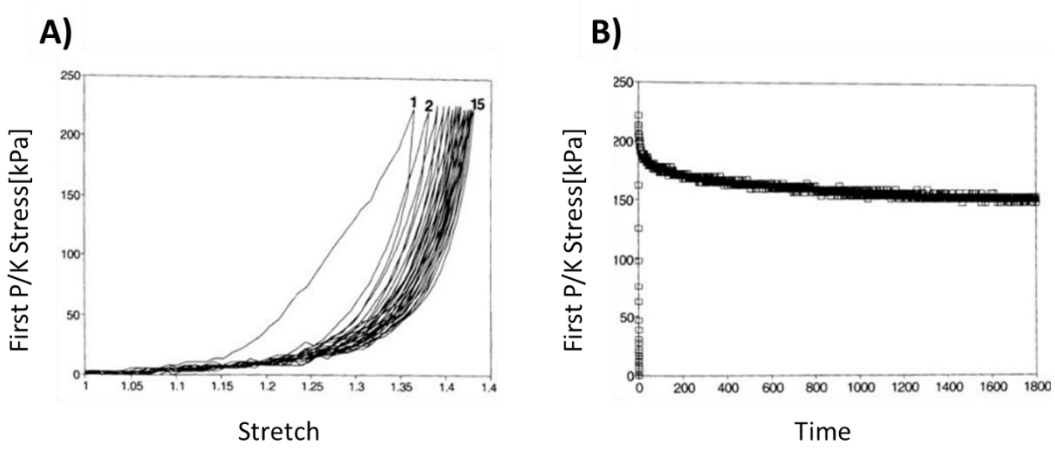

Figure 2.12. *A) 15 cycles of preconditioning during a uniaxial mechanical test on samples from bovine coronary artery. B) Uniaxial stress relaxation in the same specimen (Humphrey 2013).*

2.4.2 Mechanical properties of arteries under supra-physiological load levels

In cases of pathology or acute trauma arterial tissues may be subjected to supra-physiological loadings and large deformations. Experimental techniques have revealed softening and damage accumulation within biological soft tissues can be associated with five phenomena.

The first one describes the microscopic softening mechanism known as Mullins effect. The Mullins effect was captured for the first time by the experiments conducted by Mullins (1948) and further investigated by studies such as (Harwood et al. 1965; Mullins 1948; Mullins 1969; Mullins and Tobin 1957; Mullins and Tobin 1965). According to the Mullins effect, when a tissue is under cyclic loading from its virgin state, the required stress in the reloading path to capture the previous maximum stretch is less than the primary path, see Figure 2.13.

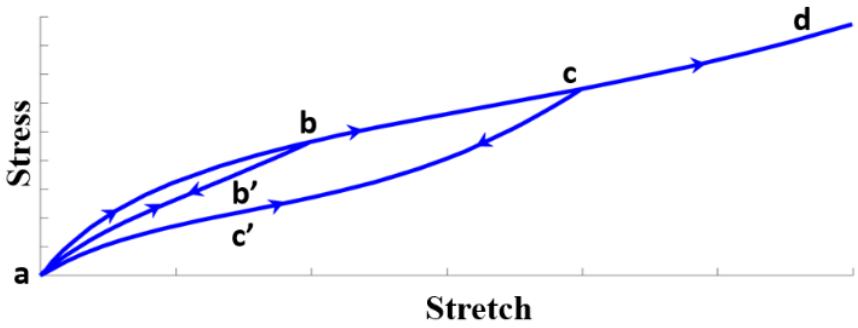

Figure 2.13. *Schematic representation of idealized Mullin's effect. Material is at virgin state in point* a *when cyclic loading of the specimen starts. Loading of specimen is terminated at point* b*. Stress strain curve then follows the unloading path* bb'a*. In the second cycle of loading the required stress in order to capture the stress at point* b *is less than the experienced in first cycle, this phenomenon is known as Mullin's effect. As it can be seen from the figure, the stress strain curve follows the primary loading path (*abcd*) when the same scenario repeated in the unloading path* cc'a*.*

The second phenomenon describes the permanent deformation of arterial tissues under high loads. These large loads can result in residual strains in the arterial wall, see Figure 2.14, similar to the well-known permanent set phenomenon in the rubber industry (Holzapfel 2000; Pena 2014)

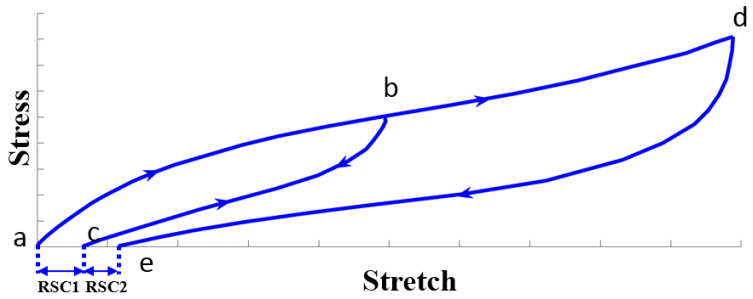

Figure 2.14. *Schematic presentation of Mullins effect and residual strains (RSC1& RSC2) in two cycles of loading* abc *and* cbde*. When the loading is terminated in point b and unloading starts, in contrast to idealized Mullin effect, Figure 2.13, residual strains accumulated in the material (RSC1). The permanent set continuous to accumulate in the specimen in the next cycles.*

Continuous softening or hysteresis is the third phenomenon that explains the behaviour of tissues under cyclic loadings at the same load level until reaching a saturation state (Humphrey 2003; Pena 2014; Pena et al. 2009), see Figure 2.15. This phenomenon has been studied in the research conducted by, for example, Chaboche (1981), Kaliske et al. (2001), Laraba-Abbes et al. (2003) ,Dorfmann and Ogden (2004), Diani et al. (2006).

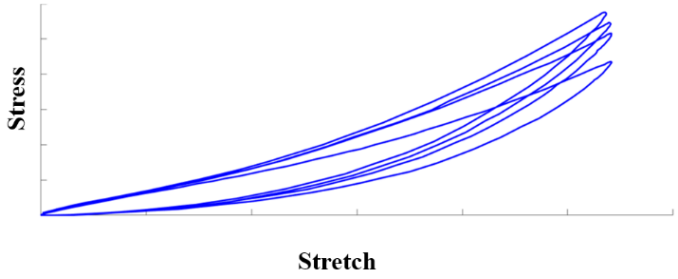

Figure 2.15. *Schematic presentation of hysteresis phenomeon.*

Softening of smooth muscle cells can also play a major role in the load bearing capacity of arteries *in-vivo* (Famaey et al. 2010). Supra-physiological loading of an artery may result in rupture of actin-myosin bindings. Progress in modelling the influence of smooth muscle cells in the response of the arterial tissue to large loads has been made on the basis of a research conducted by Huxley and Simmons (1971) that elucidate the kinetics of movement of cross bridges by recording and analysis of the response of a muscle to a sudden step wise length change.

Rupture of collagen fibres is the fifth phenomenon which is associated with the response of the soft biological tissues to supra-physiological loads and damage accumulation in the arteries. This phenomenon is investigated in studies such as (Calvo et al. 2009; Gasser et al. 2006; Pena et al. 2011), see Figure 2.16.

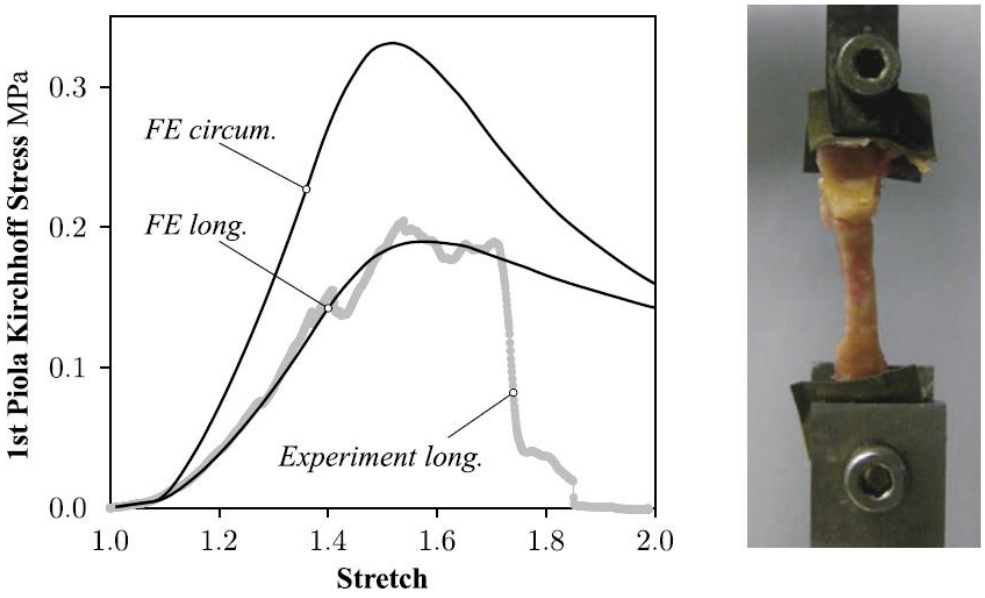

Figure 2.16. *1st Piola-Kirchhoff stress-stretch curve obtained from a monotonic tensile test on an abdominal aortic aneurysms and Finite Element (FE) prediction of rupture in the axial and circumferential samples (Gasser 2011).*

2.5 Atherosclerosis

Atherosclerosis is defined as focal fatty (plaque) thickening in the inner layer of arterial wall. This illness starts early in the life often with no symptoms, and slowly progresses to obstruct the lumen (Cham and Chase 2013).

Growth of the plaque in the healthy arterial wall is associated with accumulation of lipids in the intimal layers of the arteries. When low density lipoproteins (LDLs) are retained in the basement membrane of an artery, they become oxidized and they can be taken by macrophages. Normally macrophages live in the basement membrane. When too many particles are present in the basement membrane, macrophages will be converted to foam cells. The accumulation of foam cells can be seen by the formation of fatty streaks in the arterial wall. Smooth muscle cells proliferate and matrix synthesis promotes extracellular matrix accumulation in the growing atherosclerotic plaque. In later stages, a thin fibrous cap may also form over a large lipid pool. This is the typical formation of lesion growth associated with rupture, see Figure 2.17. Lesions with high risk of rupture are termed vulnerable. This process can continue by arterial remodelling, fibrous cap rupture and thrombosis (Bentzon et al. 2014; Zohdi et al. 2004).

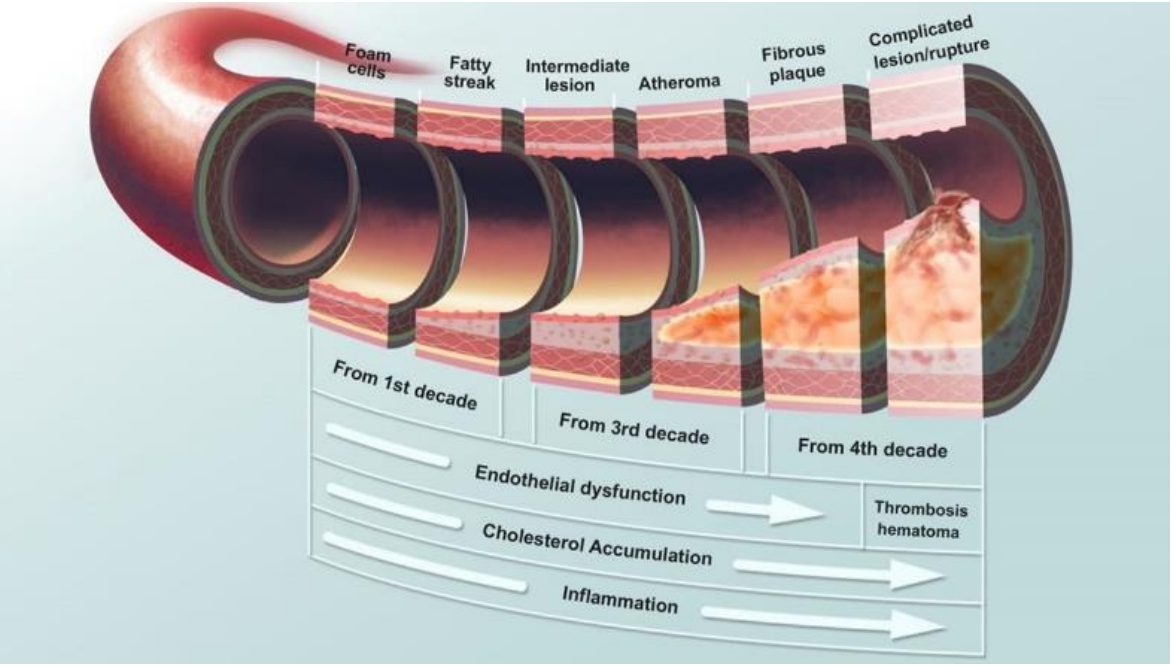

Figure 2.17. *A schematic presenting different stages of plaque build-up in the artery (Cham and Chase 2013).*

2.5.1 Vulnerability of atherosclerotic plaques

As mentioned in the preceding section, the term vulnerable plaque is attributed to an atherosclerotic plaque at a higher risk of rupture. These plaques most commonly consist of large lipid pools and thin fibrous caps. Many of these plaques also contain intraluminal thrombosis and intraplaque haemorrhage (De Luca and Tomai 2015). A broader definition of a vulnerable plaque includes not only rupture-prone plaques but also erosion-prone and thrombosis-prone plaques. Figure 2.18 shows different forms of vulnerable atherosclerotic plaques.

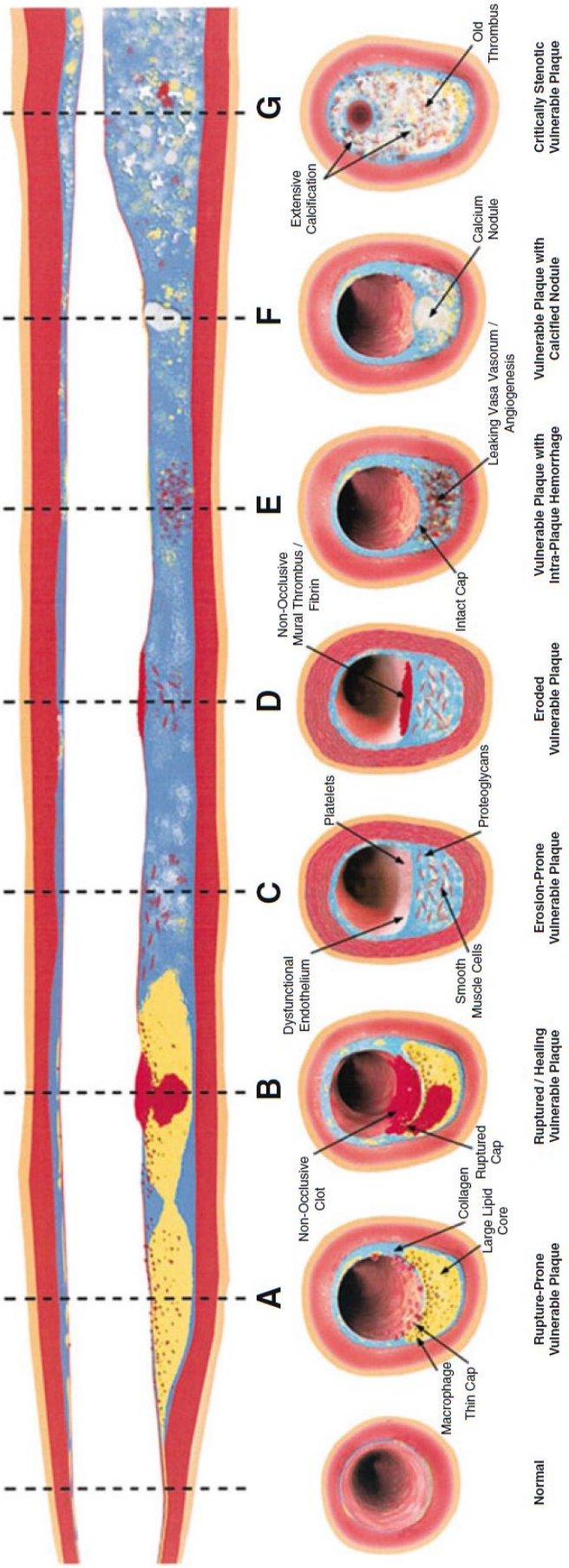

Figure 2.18. *A schematic presentation of different forms of atherosclerotic plaques. A) High-risk rupture-prone plaque with a large lipid pool and a thin fibrous cap. B) Presents a plaque when rupture of the thin fibrous cap allows the blood to enter the plaque which commonly promotes to the thrombosis in the lumen of the arterial wall. C) An erosion-prone plaque which can from due to the erosion of luminal endothelial cells from smooth muscle and proteoglycan-rich fibrous cap. D) An eroded plaque with a thrombosis. E) A vulnerable plaque with intraplaque haemorrhage. F) A vulnerable plaque with calcification. G) A stenotic vulnerable plaque (De Luca and Tomai 2015) .*

2.5.2 Remodelling of arterial wall as a result of plaque development

During atherosclerotic vascular disease, arterial walls remodel in parallel with the formation of atherosclerotic plaque. Within this process the area of lumen is preserved until the accumulation of the plaque exceeds the compensatory response of the artery (Bentzon et al. 2014; Nishioka et al. 1996). Remodelling of an arterial wall in response to the growth of plaque could be by either outward expansion of the vessel wall, positive remodelling, or vessel shrinkage, negative remodelling (Varnava et al. 2002), see Figure 2.19.

Positive remodelling is more commonly seen with fibroatheromas. The extent of enlargement of the arterial wall in this case is attributed to plaque inflammation, medial atrophy and the size of the necrotic core (Varnava et al. 2002). Evidence suggests that outward remodelling may be advantageous in terms of luminal stenosis but also harmful since remodelling may make the plaque more vulnerable to disruption (Varnava et al. 2002). On the other hand, constrictively remodelled segments often contain lesions rich in fibrous tissue (Bentzon et al. 2014). Negative remodelled vessels can lead to high grade stenosis but may appear more stable (Varnava et al. 2002). The form of arterial remodelling is as important as plaque size in determining the areas at risk of rupture (Varnava et al. 2002).

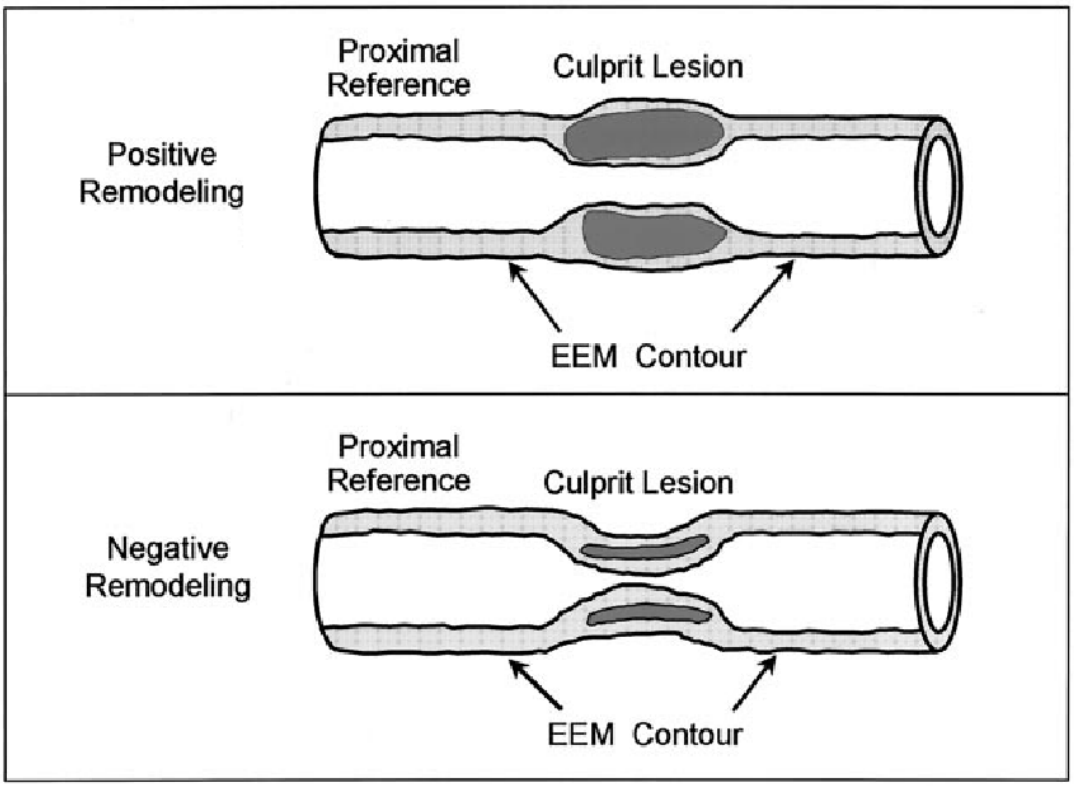

Figure 2.19. *Positive and negative arterial remodelling describes the compensating mechanism of the arterial wall is response to plaque growth (Varnava et al. 2002).*

2.6 Structure of collagen fibres in the atherosclerotic plaque

Collagen is also a prominent constituent of atherosclerotic plaques (Rekhter et al. 1993). Chai et al. (2015) measured the local anisotropic mechanical response of different components of atherosclerotic plaque. By performing indentation tests at large strain levels Chai et al. (2015) concluded that different components of atherosclerotic plaque show different levels of anisotropic behaviour. In that study, they associated the level of characterised anisotropy in the mechanical response of the tissue with the stiffness and distribution of collagen fibres in the plaque.

Pagiatakis et al. (2015) compared the orientation of fibres in fibrous caps which were obtained from human specimens of coronary atherosclerotic plaques with the direction of the maximum principal stresses calculated using fluid-structure interaction computational models. Making this comparison between samples with different stenosis severities, they observed that the principal stresses were oriented circumferentially in the healthy portion of the tissue and axially in the fibrous cap. They found their measurements of the directions of maximum principal stresses in agreement with the orientation of fibres measured experimentally using histopathological techniques. The important role of orientation of fibres in the plaque atheroma was also emphasised in the study conducted by Akyildiz et al. (2017) where Diffusion Tensor Imaging (DTI) was applied to characterise the 3-D orientation of fibres in carotid atherosclerotic plaques. In that study they showed that distribution of collagen fibres varies in different parts of atherosclerotic plaque where 52% percent of the fibres in the plaque atheroma were reported to be in the circumferential direction, 34 % were in the axial direction and 14 % were reported to be in the radial directions. They also showed that fibres at the luminal side were mainly orientated in the longitudinal direction of the vessel wall while fibres were mainly in the circumferential direction at abluminal regions, see Figure 2.20.

Douglas et al. (2017) also compared the distribution of fibres at different locations of plaque atheroma in coronary atherosclerotic plaques. In that study they associated the extracted data from histological images with material parameters for angle and dispersion of collagen fibres in the constitutive model proposed in (Gasser et al. 2006). They also investigated the values of stress measured using these material properties as a clinical measure for assessing the risk of rupture.

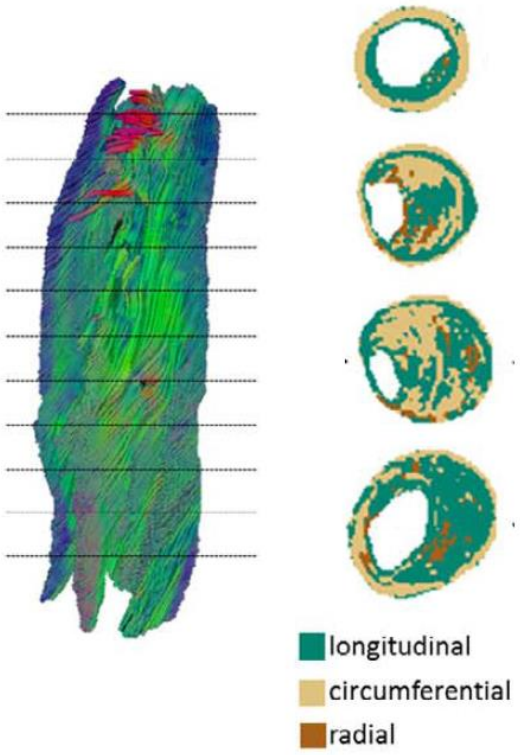

Figure 2.20. Characterised orientation of the collagen fibres in a human carotid artery using DTI (Akyildiz et al. 2017).

2.7 Risk Assessment of Atherosclerotic Plaque

Atherosclerotic plaque disruption is more commonly an asymptomatic process and can cause myocardial infarctions and ischemic strokes, as mentioned in the previous sections. A detailed study of the location of vulnerable plaques and mechanical conditions therein can lead to a better understanding of atherosclerotic plaque rupture.

Development of atherosclerotic plaque changes both geometry and mechanical properties of the vessel wall, as mentioned in the previous sections. Development of atherosclerotic plaque in the arterial tissue can also result in the stiffening of the vessel wall and damage accumulation in the artery (Duprez and Cohn 2007; Laurent et al. 2006; Palombo and Kozakova 2016). While carotid plaque rupture is one of the main reasons behind a stroke, finding a clinical measure to quantitatively assess the risk of rupture in asymptomatic and symptomatic patients still remains a challenge.

Clinical assessment for a surgical intervention, such as a carotid stent or carotid endarterectomy, is currently still based on percentage of lumen area stenosed (Khedr et al. 2016; Moore et al. 2016; Yadav et al. 2004) even though stenosis has not been found to correlate with the likelihood of plaque rupture (Golledge et al. 2000). In fact, positive, outward

remodelling has been identified to result in more unstable plaques than negative, stenotic remodelling which causes a high degree of stenosis (Fukuda et al. 2014; Miura et al. 2011).

Angiography is one the most commonly used methods for identifying the atheromatous lesions that encroach significantly into the lumen (Teng et al. 2010b). However, as discussed in the preceding sections, arterial wall remodelling can be either positive or negative. The type of arterial remodelling will influence the location of plaque vulnerability (Bentzon et al. 2014). Therefore, imaging of the lumen of an artery by itself does not provide sufficient information to diagnose the presence of an atherosclerotic plaque at risk of vulnerable plaque rupture.

Measurement of the thickness of the tunica intima and tunica media layers of the artery wall via ultrasound imaging is another proposed measure for atherosclerosis onset. This method was first introduced by Pignoli (1984) as a direct measure from ultrasound. Grobbee and Bots (1994) demonstrated the use of this parameter to measure the risk of generalized atherosclerosis. Though the threshold of intima and media thickness that will lead to plaque formation is not clear and may vary from a patient to another, there is evidence in the research conducted by Bots et al. (1997) that plaques have a higher risk of rupture when the thickness of intima and media exceeds 0.90 mm, see Figure 2.21.

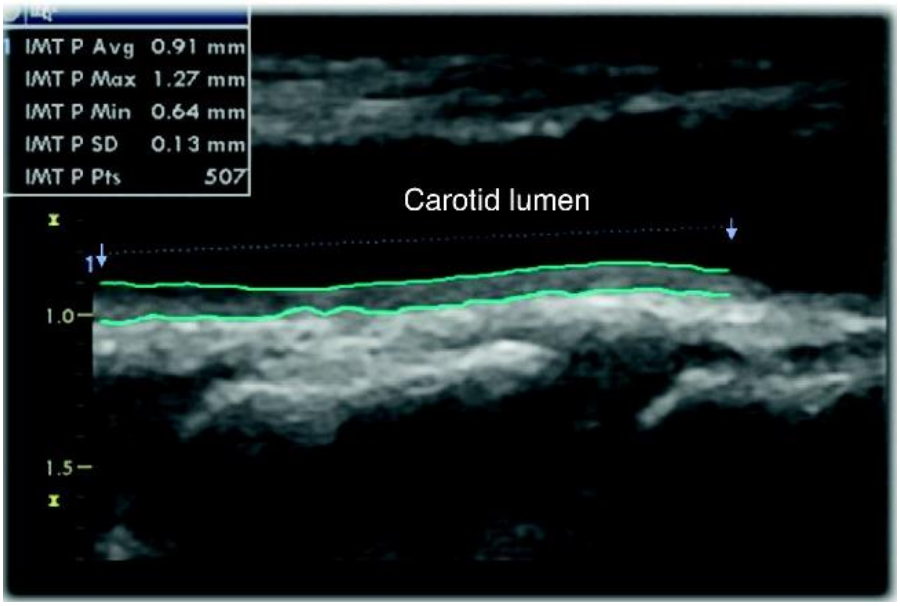

Figure 2.21. *Carotid ultrasound showing a pathological increase in the mean (0.91 mm) and the maximum (1.27 mm) carotid intima-media thickness by means of automated border detection. IMT, intima-media thickness (Mateo et al. 2011).*

Due to the pulsatile nature of blood flow, there are axial, circumferential and shear stresses in blood vessels. In healthy arterial walls the stress distribution is homogeneous (Thondapu et al. 2016). However, in the case of atherosclerotic vessels, due to the changes in the mechanical properties of the vessel wall and arterial wall remodelling, the stress distribution

is heterogeneous (Thondapu et al. 2016). The regions with highest values of stress are shown to be plaque shoulder regions which indicate the sites of higher risk of plaque rupture (Li et al. 2006), see Figure 2.22. Creane et al. (2010a) also showed that the regions with the highest von-Mises stresses in realistic 3-D models of stenosed carotid bifurcations are the plaque shoulder regions.

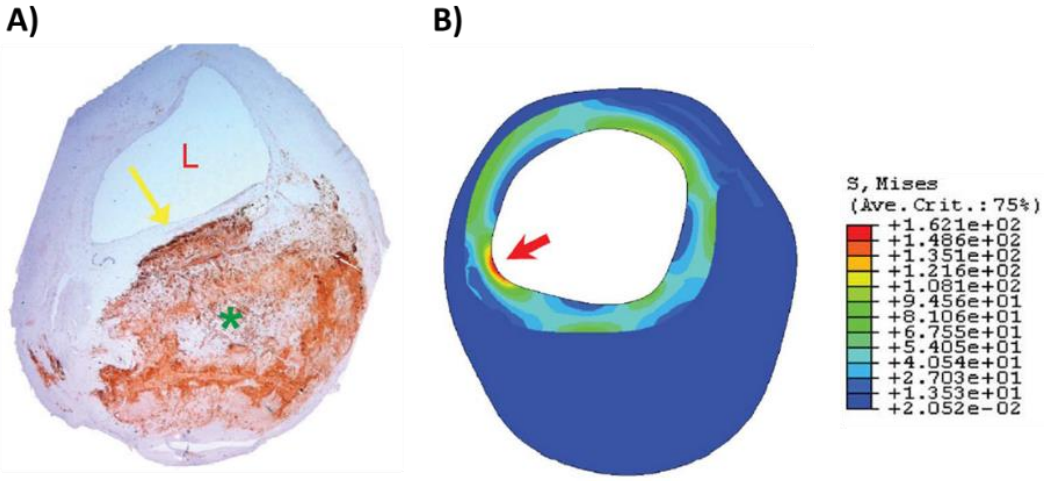

Figure 2.22. *A) A cross section of an atherosclerotic carotid artery. Yellow arrow presents the area of the fibrous cap. Von-Mises stress counter plots indicating the highest stress present at plaque shoulders (Li et al. 2006).*

Whilst stress analysis is accurate and widely used, this method has its own drawbacks such that it cannot be readily used in a clinical setting. To perform an accurate stress analysis, the specific mechanical properties of a vessel need to be determined. This is not practically feasible as vessels cannot be harvested every time analysis has to be conducted. Moreover, calculation of stress metrics and generation of computational models also requires (i) significant expertise, (ii) specialized hardware and software, and (iii) considerable time for the models to run, which are among the main limitations for a stress metric to become a standard preclinical or clinical support.

Fibrous cap thickness and lipid core size are also used to assess the plaque vulnerability in arteries. The fibrous cap is a layer of smooth muscle cells and collagen between the lumen surface and the lipid core. This layer prevents the interaction of lipid core with the blood. Thus, when the fibrous cap thickness is small, and the lipid core size is large, it indicates that the risk of plaque rupture is high. It has been shown that MRI can quantify fibrous cap and lipid core components (Trivedi et al. 2004). Li et al. (2008) observed that the maximum stress occurs at locations of minimum fibrous cap thickness, see Figure 2.23.

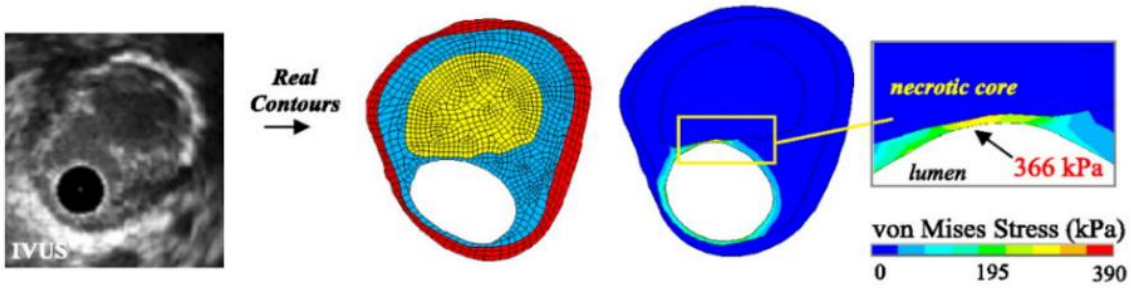

Figure 2.23. *von-Mises stress distribution in an unstable vulnerable coronary plaque attributing the regions of highest stress with the location of larger necrotic lipid core and smaller fibrous cap adapted from (Ohayon et al. 2008).*

Curvature analysis of the lumen and vessel wall of arteries have also been used to identify the areas at higher risk of rupture (Creane et al. 2010a; Guo and Sluys 2008; Teng et al. 2010b). Lumen and plaque curvature change with progression of atherosclerosis. Creane et al. (2010a) analysed real atherosclerotic arteries by measuring the difference between the inner and outer plaque boundaries curvature. Their analysis showed high curvature values at circumferential plaque shoulder regions which correlated with high-stress regions, see Figure 2.24. Curvature analysis has been performed mainly on two dimensional cross-sections of atherosclerotic arteries (Li et al. 2006; Li et al. 2008; Teng et al. 2010b). Although these studies have shown the potential of geometrical metrics in assessing the vulnerability of the atherosclerotic plaques in the vessel wall, to-date, no study has been conducted to systematically explore the capability of a geometrical metric to identify the areas at risk of rupture and compare it with other commonly used metrics such as damage or von-Mises or maximum principal stress.

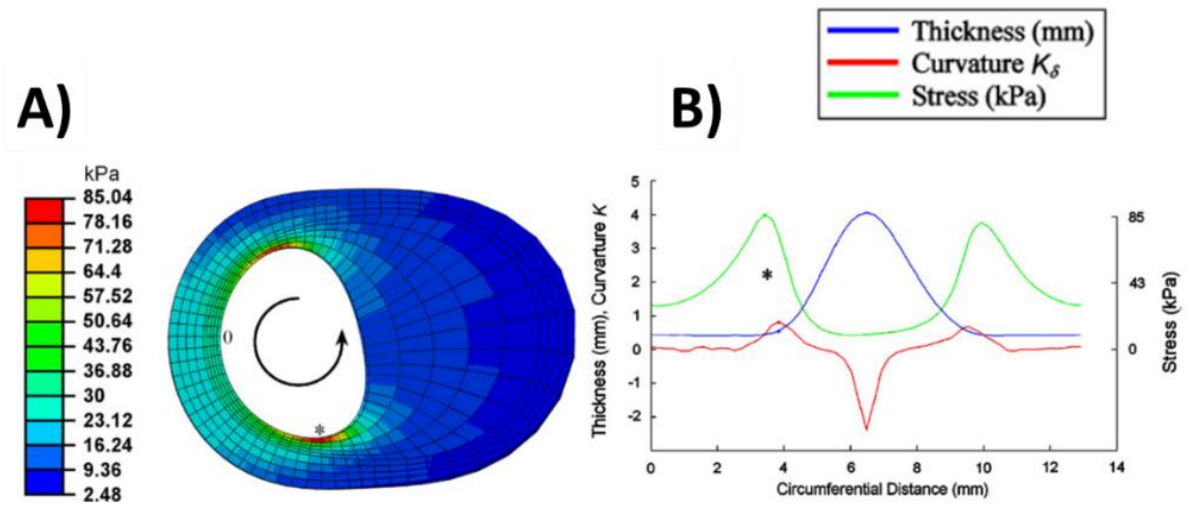

Figure 2.24. A) *Von Mises stress distribution on a cross section with a large plaque burden of a human carotid artery. B). graph of difference between the inner and outer plaque boundary curvature(κ_δ), von Mises stress distribution and plaque thickness. It can be seen that both stress analysis and curvature analysis predict the same areas at highest risk of atherosclerotic plaque rupture (Creane et al. 2010a).*

2.8 Constitutive models

2.8.1 Models to capture the response of arterial tissue to physiological loads

To-date many studies have quantified the nonlinear behaviour of biological soft tissues in the form of constitutive equations. In the research conducted by Fung et al. (1979) the behaviour of arteries were firstly defined as pseudoelastic where different elastic laws were applied to capture the mechanical behaviour of the tissue in the loading and reloading paths. Although a pseudoelastic material model was useful to explore the physiology of arteries, it was difficult to capture the viscoelastic response of arterial walls using this type of material model (Gasser et al. 2006; Holzapfel and Gasser 2001).

The mechanical behaviour of arteries is most commonly described using hyperelastic anisotropic material models where the existence of a Strain Energy Function (SEF) is postulated to describe the behaviour of the arterial wall (Holzapfel 2000). Gasser et al. (2006) classified the constitutive models for arterial walls into two main groups. The first group defines the behaviour of the arterial walls using a purely phenomenological approaches such as (Demiray 1972; Takamizawa and Hayashi 1987a). The second group uses the structural information of underlying histology of arterial tissues to capture the overall behaviour of the vessel wall (Holzapfel et al. 2000; Humphrey and Rajagopal 2002; Zulliger et al. 2004).

Humphrey (1999c) compared three phenomenological constitutive models proposed by von Maltzahn et al. (1984), Takamizawa and Hayashi (1987b) and Chuong and Fung (1986). All these three constitutive models were non-linear, anisotropic, incompressible and pseudo-elastic. Table 2.1 shows the corresponding SEF of each constitutive law. In this table the value of each SEF is presented by W. $E_{RR}, E_{\theta\theta}, E_{zz}$ are the values of Green strains, C_1, C_2, C_3, C_4, C_5 and C_6 are material properties. Humphrey (1999a) used these three constitutive models to capture the response of common carotid arteries, see Figure 2.25. The model proposed by von Maltzahn et al. (1984) captured the anisotropic behaviour of the arterial tissue. However, it showed a stiffer response in the longitudinal direction of the vessel wall in an equi-biaxial mechanical test. The constitutive model suggested by Takamizawa and Hayashi (1987b) captured an almost isotropic response for the arterial wall. The model proposed by Chuong and Fung (1986) was the only model that successfully captured the anisotropic behaviour of carotid arteries where samples where stiffer in the circumferential direction.

Table 2-1. *The SEFs proposed by von Maltzahn et al. (1984), Takamizawa and Hayashi (1987b) and (Chuong and Fung 1986).*

$W = \frac{1}{2}C[e^Q - 1]$ $Q = C_1E_{\theta\theta}^2 + C_2E_{zz}^2 + 2C_3E_{\theta\theta}E_{zz}$	(von Maltzahn et al. 1984)
$W = -C\ln(1-Q)$ $Q = \frac{1}{2}C_1E_{\theta\theta}^2 + \frac{1}{2}C_2E_{zz}^2 + C_3E_{\theta\theta}E_{zz}$	(Takamizawa and Hayashi 1987b)
$W = \frac{1}{2}C[e^Q - 1]$ $Q = C_1E_{RR}^2 + C_2E_{\theta\theta}^2 + C_3E_{zz}^2 + 2C_4E_{\theta\theta}E_{RR} + 2C_5E_{\theta\theta}E_{zz} + +2C_6E_{\theta\theta}E_{RR}$	(Chuong and Fung 1986)

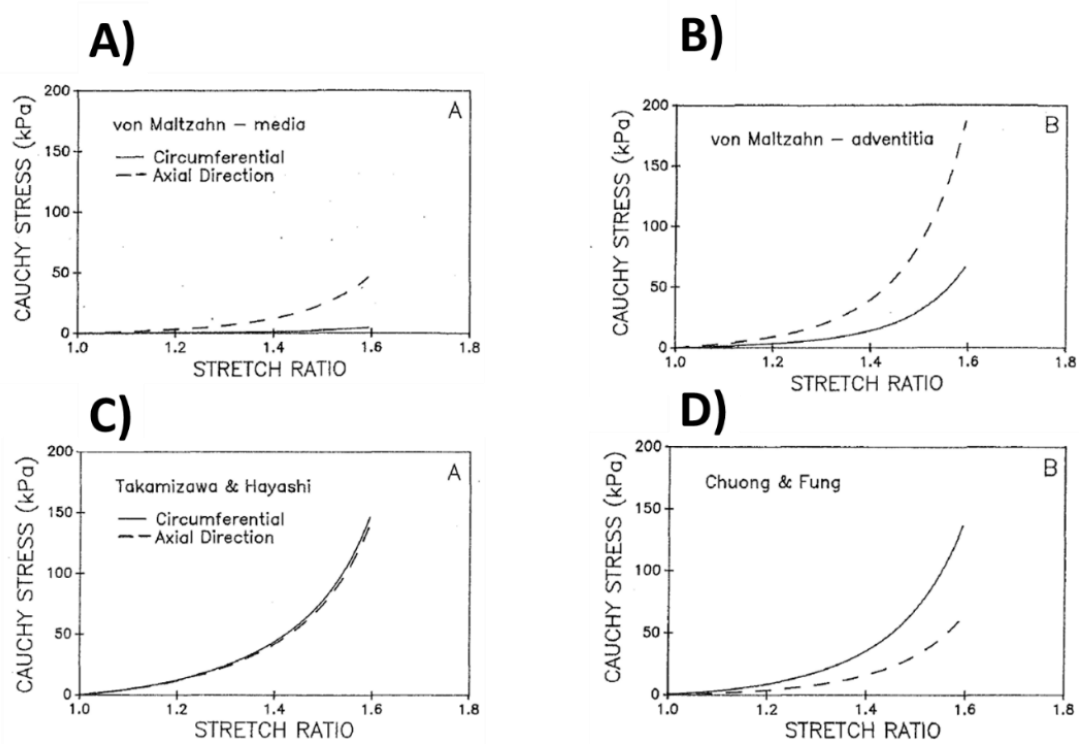

Figure 2.25. *The response of the model proposed by von Maltzahn et al. (1984) for the media and adventitia layers of rabbit carotid arteries (A) and (B), respectively. The response of the models for the intact arterial wall suggested by Takamizawa and Hayashi (1987b) and Chuong and Fung (1986) are shown in sections (C) and (D), respectively,(Humphrey 1999c).*

The structural constitutive model proposed by Holzapfel, Gasser and Ogden-referred to as the HGO model is one of the most commonly used material models in the literature to describe the nonlinear, anisotropic behaviour of soft biological tissues (Holzapfel et al. 2000). In this model, two families of collagen fibres are assumed to be embedded in an isotropic ground matrix. A common assumption of this structural formulation is the characterization of the

embedded collagen fibres by means of parallel aligned fibres in each family of collagen fibres, see Table 2.2.

Following Holzapfel et al. (2000), Zulliger et al. (2004) emphasised the need for structural Strain Energy Functions (SEF) to more accurately capture the mechanical behaviour of arterial walls in the axial and circumferential directions. Such constitutive models, would allow identification of parameters such as elastic moduli of the tissue and distribution of fibres. Zulliger et al. (2004) used separate SEFs to capture the behaviour of non-collagenous tissue and collagen fibres in the arterial wall. In that study, a log-logistic probability distribution function was used to incorporate the distribution of fibres in the arterial tissue to capture the anisotropic response of the tissue, see Table 2.2.

Although the constitutive model proposed by Holzapfel et al. (2000) fitted very well for experimental data obtained from the medial layer of arterial tissue, it cannot predict the mechanical behaviour of the tunica intima or tunica adventitia as accurately as the tunica media. This material model along with other material models, proposed by for example (Wuyts et al. 1995; Zulliger et al. 2004) , share a similar limitation which is neglecting the effect of fibre dispersion in each family of collagen fibres. To take the dispersion of collagen fibres into the account, Holzapfel et al. (2005), proposed a new form of SEF which had a scaler parameter incorporating the influence of dispersion of fibres in each family of the collagen fibres in the arterial wall. The influence of dispersion of fibres was also explored in the study conducted by (Gasser et al. 2006). Gasser et al. (2006) used generalized structure tensors to incorporate the influence of the distribution of fibres into the constitutive model proposed by (Holzapfel 2000). This work was then further developed by the research conducted by (Holzapfel et al. 2015) where a non-symmetric dispersion in the tangential plane of the tissue is incorporated to construct a new form of structure tensors.

Table 2.2 provides a summary of some the most frequently used SEFs to characterise the anisotropic mechanical behaviour of the arterial tissue. In this table, the value of each SEF is presented by ψ. C_{10} is a stress like material property defining the stiffness of the non-collagenous tissue using a neo-Hookean material model. k_1 and k_2 are stress like and dimension less material properties defining the stiffness of the collagenous tissue. C_{elast} is a stress like material property defining the behaviour of the non-collagenous tissue in (Zulliger et al. 2004) f_{elast} and f_{coll} are the area fraction of the load bearing elastin and collagen fibres, respectively. ρ_{fibre} is the collagen fibre engagement strain distribution and ε is the collagen fibre engagement strain. $\boldsymbol{C_{coll}}$ is the Young's modulus of the collagen fibres. I_1 is the first invariant of the right Cauchy-Green deformation tensor. I_4 and I_6 represent the square of stretch in the tissue in the direction of collagen fibres . ρ and κ are scalar dimensionless material properties indicating

the dispersion of the collagen fibres in each family of the fibres. κ_{in} and k_{op} indicate the in-plane and out of plane dispersion of the fibres in each family of the collagen fibres, respectively.

Table 2-2. *A brief summary of some of the most frequently used structural constitutive models in the literature.*

$\psi = C_{10}(I_1 - 3) + \frac{k_1}{2k_2}\sum_{i=4,6}\{e^{[k_2(I_i-1)^2]} - 1\}$	(Holzapfel et al. 2000)
$\psi = C_{elast}f_{elast}(I_1 - 3)^{\frac{3}{2}} + \sum_{i=4,6}\{f_{col}(\frac{1}{2}\left(\int_{-\infty}^{\infty}(C_{coll}(\varepsilon - \log(\varepsilon + 1)))\rho_{fibre}d\varepsilon\right)(\sqrt{I_i} - 1)\}$	(Zulliger et al. 2004)
$\psi = C_{10}(I_1 - 3) + \frac{k_1}{2k_2}\sum_{i=4,6}\{e^{k_2[(1-\rho)(I_i-3)^2+\rho(I_i-1)^2]} - 1\}$	(Holzapfel et al. 2005)
$\psi = C_{10}(I_1 - 3) + \frac{k_1}{2k_2}\sum_{i=4,6}\{e^{k_2[(\kappa I_1+(1-3\kappa)I_i-1)^2]} - 1\}$	(Gasser et al. 2006)
$\psi = C_{10}(I_1 - 3) + \frac{k_1}{2k_2}\sum_{i=4,6}\{e^{k_2[\left(2\kappa_{op}\kappa_{ip}I_1+2\kappa_{op}(1-2\kappa_{ip})I_i+\left(1-32\kappa_{op}\kappa_{ip}-2\kappa_{op}(1-2\kappa_{ip})\right)\lambda_3^2-1\right)^2]} - 1\}$	(Holzapfel et al. 2015)

Decoupled forms of strain energy functions have been widely used to capture the passive mechanical properties of arteries where different forms of SEFs have been used for the non-collagenous matrix and collagen fibres (Alastrué et al. 2010; Balzani et al. 2012; Gasser et al. 2002; Humphrey 2003; Nolan et al. 2014; Sommer and Holzapfel 2012; Sommer et al. 2010) - just to name a few. However, there are only a few studies that have investigated the mechanical response of the cells.

Smooth muscle cells are the other load bearing components of arterial walls. The research conducted by Hill (1938) is one of the first studies that proposed a mathematical model to capture the response of the smooth muscle cells in the overall mechanical behaviour of the tissue. Hill (1938) demonstrated the viscoelasticity of skeletal muscle to be governed by a three mechanical components arranged in series, see Figure 2.26 (Fung 1970), (i) a contractile element which could extend freely at rest, this component is capable of shortening when activated. It should be mentioned that the main function of the contractile element is to change the length. (ii) An elastic element arranged in series with the contractile element. (iii) A parallel elastic element is also added to the model to capture the elastic behaviour of the muscle at rest. It is also worth mentioning that as the main responsibility of the contractile element was to change the length, determination of the tension was according to the response of the series and parallel elements.

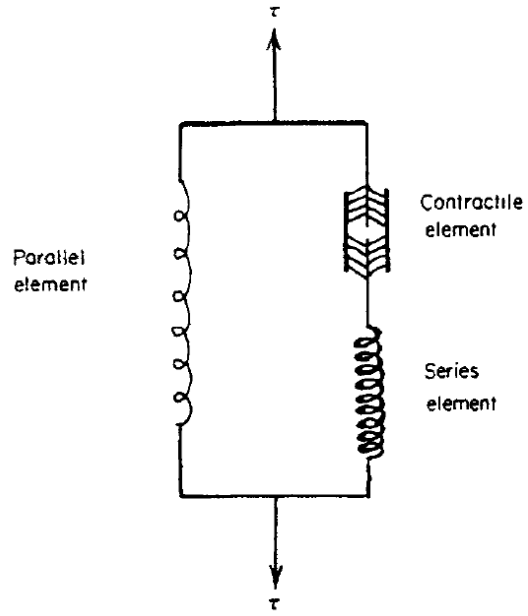

Figure 2.26. *A schematic presenting Hill's model (Fung 1970).*

Hill's model is also known as the three-element model or the sliding element theory. On the basis of the theory of sliding elements, Fung (1970) proposed a mathematical formulation of the mechanical properties of the heart muscle to represent the tensile stress the in-parallel and in-series element. The three sliding element method then further developed in research conducted by, for example, (Gestrelius and Borgstrom 1986; Yang et al. 2003).

SEFs are also used to investigate the effect of smooth muscle cells on the mechanical behaviour of the tissue. Stålhand et al. (2008) used a free energy potential function to demonstrate the behaviour of smooth muscle cells. This approach let the behaviour of smooth muscle cells to be analysed in more complex environments and in combination with hyperelastic material models (Murtada et al. 2010). 2.8.2 Models to capture the response of arterial tissue to supra-physiological loads.

2.8.2 Models to capture the response of arterial tissue to supra-physiological loads.

In order to add the softening of biological tissues to existing constitutive models two common approaches are used in the literature namely: the continuum damage mechanics (CDM) method and pseudo-elastic damage method. Either of these two approaches primarily are used to demonstrate the softening phenomena in rubber like materials where existence of a Helmholtz free-energy function, also referred to as a strain-energy function, is postulated in most of the material models. In both approaches the hyperelastic strain-energy function is multiplied by a reduction factor that controls the softening of the material.

The theory of pseudo elasticity was used by Ogden and Roxburgh (1999) to capture the main features of Mullins effect in the rubber-like materials. The formulation of this method is based on the concept of pseudo-elasticity used by Fung et al. (1979). This method is amended by the incorporation of a single continuous parameter, interpreted as a damage parameter, for simulation of the behaviour of the material under cyclic loading conditions. This theory, describes the material behaviour as one elastic material in the loading path and another elastic material in the unloading path.

Not many studies in the literature have used pseudo-elastic damage models to study the effect of supra-physiological loading on biological soft tissues. Franceschini et al. (2006) used a pseudo-elastic damage model to capture the Mullins effect and permanent set in brain tissues using a series of uniaxial mechanical tests following the model proposed by Dorfmann and Ogden (2004). Weisbecker et al. (2011) implemented a pseudo elastic damage model by defining different damage variables for arterial matrix and fibres. In that study, a neo-Hookean material model was used to describe the behaviour of the non-collagenous tissue and the anisotropic SEF proposed by Holzapfel et al. (2000) was used to define the mechanical properties of collagen fibres. Pena and Doblare (2009) also implemented a pseudo-elastic damage model to capture the discontinuous softening in soft biological tissues. García et al. (2013) also used a pseudo-elastic damage model to reproduce the softening and residual stretches obtained from swine carotid arteries. Results of that study showed that mechanical behaviour of porcine carotid arteries can also be affected by the location from which samples were harvested.

CDM models have been extensively employed to describe the progressive degradation of material before the initiation of micro cracks (Simo and Ju 1987). This theory has been used to model damage in fatigue (Chaboche 1974; Lemaitre 1972), creep (Hult 1974; Rabotnov 1963) and creep fatigue interaction (Lemaitre and Chaboche 1975) in the literature. The theory of CDM is based on the thermodynamics of irreversible processes (Clausius-Duhem inequality for the internal dissipation) and internal state variables (Miehe 1995; Simo and Ju 1987). According to this theory, the effect of the initiation or growth of micro-cracks in a material can be captured using internal damage variables, which can be defined as scalar variables for capturing isotropic damage or tensorial form for anisotropic damage where the evolution of damage depends on the orientation of the material constituents (Simo and Ju 1987).

Decoupled forms of CDM models have been extensively applied to simulate damage accumulation phenomena in soft biological tissues. Balzani et al. (2006) demonstrated a constitutive model to capture damage phenomena in circumferentially overstretched atherosclerotic arteries, whereby, different internal variables were assigned to the isotropic

ground matrix and fibrous anisotropic strain energy functions. The model proposed by Balzani et al. (2006) for discontinuous damage has since been further developed by Famaey et al. (2013), who explored damage accumulation in smooth muscle cells at supra-physiological load levels. Using a CDM approach, Pena (2011a) presented a structural constitutive model to capture discontinuous damage and inelastic deformation simultaneously within a soft tissue. However, relatively few studies have investigated the influence of stress softening and permanent set simultaneously in cyclic loading conditions (Alastrue et al. 2008; Munoz et al. 2008). The CDM approach was also used by Maher et al. (2012) to capture the discontinuous damage along with permanent set phenomenon in biological fibrous tissues. Balzani et al. (2012) used a decoupled form of CDM to propose a constitutive model that captures discontinuous and continuous softening along with the permanent set phenomenon; the main limitation of that study was that no damage was considered to accumulate in the non-collagenous tissue. Pena (2014) employed CDM to capture Mullins effect simultaneously with continuous damage, permanent set and tissue rupture in arterial tissue. The number of material parameters required to define the model, however, was mentioned as a limitation of that study. For further information on existing damage models and their classifications the reader is referred to, for example, Li (2016).

2.8.3 Models to capture the mechanical response of the atherosclerotic plaque

As mentioned in the previous sections many different forms of constitutive models have been used to predict the mechanical behaviour of arterial walls under physiological and supra-physiological loads. These constitutive models can also be used to determine the mechanical behaviour of the atherosclerotic plaque.

Isotropic material models are the most commonly used constitutive models to capture the mechanical behaviour of different plaque components, see Figure 2.27.

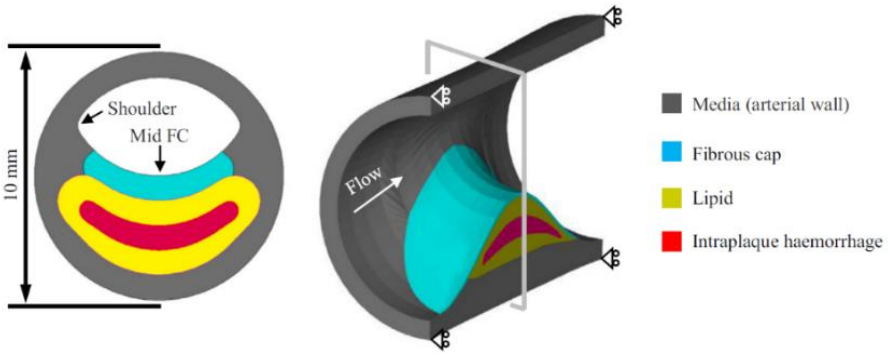

Figure 2.27. *A schematic presenting the different components of the plaque in an idealized geometry (Teng et al. 2015).*

Teng et al. (2015) investigated the influence of selecting different isotropic material models to capture the mechanical behaviour of different components of the atherosclerotic plaques including intra-plaque hemorrhage or thrombus (IPH/T), lipid, media and fibrous cap as shown in Figure 2.27. In that study, the accuracy of the numerical fit obtained for each component using different SEFs was used as an indicator of the suitability of the model to capture the response of the atherosclerotic plaques. Figure 2.28 shows the quality of fits obtained using different SEFs for the components of human carotid arteries. The SEFs along with the material parameters for each constitutive law are shown in Table 2.3.

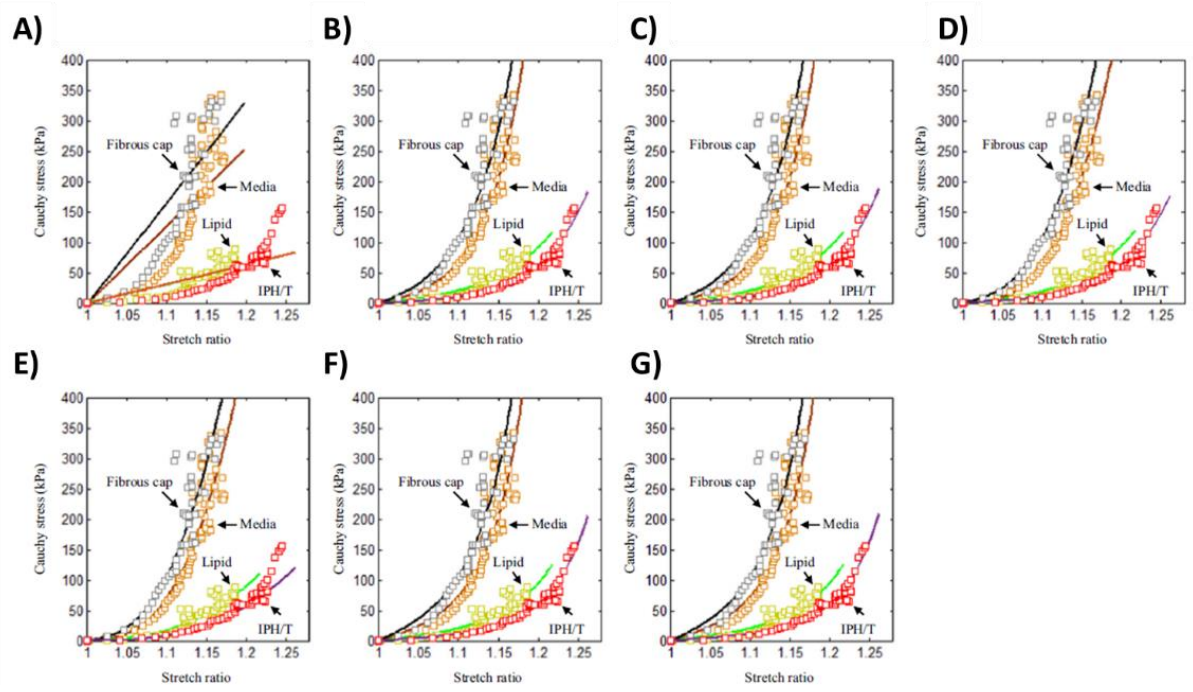

Figure 2.28. *Mechanical response of different components of human atherosclerotic components captured using different constitutive laws. A)neo-Hookean, B)One-term Ogden, C)Two-term Ogden, D)Yeoh, E) 5-parameter Mooney-Rivlin. The constitutive laws are shown in Table 2.3(Teng et al. 2015).*

In Table 2.3, W presents the values of different SEFs where J is the determinant of the deformation gradient tensor, λ_1, λ_2 and λ_3 are the values of principal stretches in the tissue. I_1 is the first invariant of the right Cauchy-Green deformation tensor and $\bar{I}_1$, $\bar{I}_2$ and $\bar{I}_3$ represent the isochoric invariants of the isochoric counterpart of the right Cauchy-Green deformation tensor. Performing such a study, Teng et al. (2015) demonstrated that non-linear isotropic material models capture the mechanical behaviour of different components of the atherosclerotic tissue more accurately.

As mentioned in the section 2.6 of this thesis, it is well documented that the orientation of collagen fibres varies in different components of the plaque. To take the effect of distribution

of collagen fibres on the mechanical behaviour of atherosclerotic plaques into account, anisotropic constitutive laws have been used. Table 2.4 presents studies that investigated the mechanical response of the atherosclerotic plaque along with details about the type of material models used and the imaging techniques applied to obtain the geometry of these plaques (Holzapfel et al. 2014).

Table 2-3. *Different isotropic material models used to capture the mechanical response of atherosclerotic plaque (Teng et al. 2015). The response of each model is shown in Figure 2.28.*

Material model	Tissue type	Constants				
neo-Hookean		C_1 (kPa)				
$W = C_1(I_1 - 3) + \kappa(J-1)$	FC	274.432				
	Media	210.986				
	Lipid	50.537				
	IPH/T	51.675				
one-term Ogden		μ_1 (kPa)	α_1			
$W = \frac{\mu_1}{\alpha_1}(\lambda_1^{\alpha_1} + \lambda_2^{\alpha_1} + \lambda_3^{\alpha_1} - 3) + \kappa(J-1)$	FC	13.922	21.817			
	Media	6.826	24.496			
	Lipid	4.748	16.335			
	IPH/T	1.427	20.851			
two-term Ogden		μ_1 (kPa)	α_1	μ_2	α_2	
$W = \sum_{p=1}^{2} \frac{\mu_p}{\alpha_p}(\lambda_1^{\alpha_p} + \lambda_2^{\alpha_p} + \lambda_3^{\alpha_p} - 3) + \kappa(J-1)$	FC	0.150	22.874	13.773	21.804	
	Media	1.272	25.794	5.583	24.127	
	Lipid	2.030	1.843	4.514	16.548	
	IPH/T	0.549	23.971	1.324	14.877	
Yeoh		C_1 (kPa)	C_2 (kPa)	C_3 (kPa)		
$W = \sum_{i=1}^{3} C_i(I_1 - 3)^i + \kappa(J-1)$	FC	53.724	2201.011	42.551		
	Media	5.636	1816.773	162.037		
	Lipid	18.548	207.371	422.652		
	IPH/T	11.225	69.214	781.546		
5-parameter Mooney–Rivlin		C_{10} (kPa)	C_{01} (kPa)	C_{11} (kPa)	C_{20} (kPa)	C_{02} (kPa)
$W = C_{10}(\bar{I}_1 - 3) + C_{01}(\bar{I}_2 - 3) + C_{11}(\bar{I}_1 - 3)(\bar{I}_2 - 3) + C_{20}(\bar{I}_1 - 3)^2 + C_{02}(\bar{I}_2 - 3)^2 + \kappa(J-1)$	FC	28.499	8.634	56.755	150.483	2721.008
	Media	9.267	3.508	1183.007	305.463	504.507
	Lipid	5.162	4.317	5.886	6.390	402.562
	IPH/T	0.662	0.091	21.177	228.249	2.512
Demiray		D_1 (kPa)	D_2			
$W = D_1[e^{D_2(I_1-3)} - 1] + \kappa(J-1)$	FC	6.217	17.444			
	Media	3.841	18.789			
	Lipid	2.466	10.466			
	IPH/T	0.976	13.007			
modified Mooney–Rivlin		C_1 (kPa)	D_1 (kPa)	D_2		
$W = C_1(I_1 - 3) + D_1[e^{D_2(I_1-3)} - 1] + \kappa(J-1)$	FC	0.130	6.208	17.452		
	Media	0.138	3.832	18.803		
	Lipid	0.049	2.460	10.477		
	IPH/T	2.779	0.787	13.861		

Table 2-4. *A review of different computational studies conducted on the atherosclerotic plaques along with the imaging modalities used to obtain the geometries and the material model used (Holzapfel et al. 2014).*

FE study	Imaging modality[c]	Vessel type	Material model[d]
Cheng et al. (1993)	Histology	Coronary	Linear elastic, transversely isotropic
Huang et al. (2001)	Histology	Coronary	Mooney–Rivlin
Holzapfel et al. (2002)	hr-MRI	Iliac	Nonlinear anisotropic Holzapfel et al. (2000), Gasser and Holzapfel (2002)
Kaazempur-Mofrad et al. (2003)	Histology, MRI	Carotid bifurcation	Demiray (1972)
Patel et al. (2003)	Histology	Carotid	Mooney-Rivlin
Williamson et al. (2003)	Histology	Coronary	Linear elastic, orthotropic+ Demiray (1972)
Chau et al. (2004)	Histology, OCT	Coronary	Mooney Rivlin
Kaazempur-Mofrad et al. (2004)	IVUS, MRI	Carotid bifurcation	Artery: rigid; Blood: INF
Holzapfel et al. (2005b)	Histology, hr-MRI	External iliac	Nonlinear anisotropic: Holzapfel et al. (2005a)
Imoto et al. (2005)	Idealized model, IVUS	Coronary	Linear elastic, orthotropic
Ohayon et al. (2005)	IVUS	Coronary	Linear elastic, orthotropic
Tang et al. (2005)	MRI	Coronary	Artery: Mooney–Rivlin+ Demiray (1972); Blood: INF
Li et al. (2006)	Histology, hr-MRI	Carotid	Ogden (1972); two terms
Gasser and Holzapfel (2007b)	Histology, hr-MRI	External iliac	Nonlinear anisotropic: Gasser et al. (2006)
Ohayon et al. (2007)	Histology	Coronary	Neo-Hookean
Kock et al. (2008)	MRI	Carotid bifurcation	Artery: neo-Hookean; Blood: INF
Li et al. (2008)	hr-MRI	Carotid	Ogden (1972); two terms
Ohayon et al. (2008)	IVUS	Coronary	Linear elastic, orthotropic
Gao et al. (2009)	hr-MRI	Carotid bifurcation	Artery: 5-parameter Mooney–Rivlin Blood: INF
Kiousis et al. (2009)	hr-MRI	Carotid bifurcation	Nonlinear anisotropic: Holzapfel et al. (2005a)
Le Floc'h et al., (2009)	Idealized model, IVUS	Coronary	Hooke's law
Mortier et al. (2010)	Rotational angiography	Coronary bifurcation	Nonlinear anisotropic Holzapfel et al. (2005a)
Sadat et al. (2010)	hr-MRI	Carotid	Ogden (1972); two terms
Auricchio et al. (2011)	CTA	Carotid bifurcation	5-parameter Mooney–Rivlin
Speelman et al. (2011)	Histology	Coronary	Neo-Hookean
Kelly-Arnold et al. (2013)	hr-μCT	Coronary	Hooke's law

2.8.4 Models to capture collagen fibres architecture and adaptation

Re-orientation of collagen fibres in the healthy arterial wall has been the focus of many studies (Creane et al. 2011a; Driessen et al. 2008; Fausten et al. 2016; Hariton et al. 2007). Collagen fibres re-orient in the healthy arterial wall to maximize the load bearing capacity of the tissue (Baaijens et al. 2010). Different forms of mechanical stimulus have been employed to calculate the optimum distribution of collagen fibres which gives the maximum strength to the tissue. Hariton et al. (2006) assumed that collagen fibre distribution evolves toward the optimum

distribution of fibres which was measured from the ratio of the maximum and intermediate principal stresses. Similar assumptions were made in studies conducted by (Fausten et al. 2016; Pagiatakis et al. 2015). Hariton et al. (2007) applied the re-orientation algorithm presented by (Hariton et al. 2006) to capture the distribution of fibres in an idealized human carotid bifurcation. The ratio of the two largest principal stretches and strains were used in studies such as (Creane et al. 2011a; Driessen et al. 2005a; Driessen et al. 2008; Grytz and Meschke 2010) to calculate the optimum configuration of the fibres. Waffenschmidt and Menzel (2014) assumed that direction of collagen fibres evolves to minimize total potential energy of the arterial tissue. This approach was compared with methods implemented by Hariton et al. (2006) and Hariton et al. (2007) in the research conducted by Qi et al. (2015). For further information on different re-orientation algorithms implemented to capture the orientation of fibres in the arteries, the reader is referred to, for example, Baaijens et al. (2010) or Qi et al. (2015).

However different forms of re-orientation algorithms are suggested in the literature, only a few of them have been used to investigate the distribution of fibres in real healthy and patient specific geometries. Creane et al. (2011a) compared the distribution of collagen fibres in a healthy arterial wall with the distribution of fibres obtained from symptomatic and asymptomatic patients undergoing endarterectomy, see Figure 2.29. In that study, they showed that a strain driven re-orientation algorithm can predict the helical distribution of collagen fibres in the non-branching regions of bifurcations.

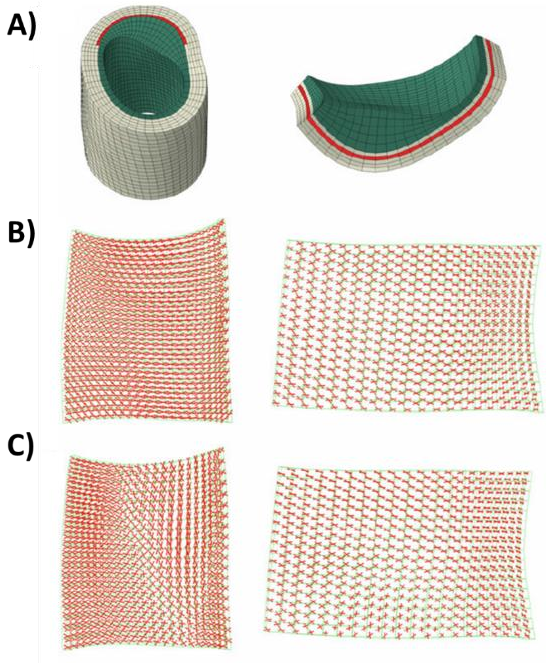

Figure 2.29. *A) Two stenotic regions in human common carotid arteries. B) Structure of fibres in the healthy arteries. C) Structure of arteries in the diseased arteries (Creane et al. 2011a).*

However, a more complex distribution of fibres was obtained at the apex of the bifurcations where fibres were predicted to be highly aligned and at regions of large plaque burden. These complex distributions of collagen fibres can alter the mechanical properties of the arterial wall and change the values of the stress in the arterial wall at those regions. In that study, Creane et al. (2011a) also mentioned that their prediction of distribution of fibres in the healthy arterial wall is in agreement with experimental observations by Finlay et al. (1995b). Fausten et al. (2016) used a stress driven re-orientation algorithm to investigate the distribution of fibres in a geometry of a human common carotid.

2.9 Experimental studies exploring damage accumulation in the arteries

Although several constitutive models have been proposed to predict the behaviour of arterial tissues under physiological and supra-physiological loading conditions, relatively few types of experiments have been performed to investigate the accuracy of such models. Mullins (1948) performed a series of cyclic uniaxial experiments to determine the differences in the properties of rubber like material in each cycle. Cyclic uniaxial and biaxial experiments then have been used extensively to validate/verify the proposed constitutive models to capture the mechanical response of arterial tissue under large loads (Balzani et al. 2006; Calvo et al. 2007; Calvo et al. 2009; Dorfmann and Ogden 2004; Holzapfel et al. 1999; Maher et al. 2012; Martins et al. 2010; Pena 2011a; Pena 2011b; Pena 2014; Peña et al. 2008; Pena and Doblare 2009; Pena et al. 2009; Rodriguez et al. 2006; Weisbecker et al. 2011; Weisbecker et al. 2012; Weisbecker et al. 2013).

Weisbecker et al. (2013) performed cyclic uniaxial mechanical tests on elastase and collagenase treated tissue along with untreated specimens from the media of human thoracic aortas to explore the role of each constituent of the arterial wall in the cyclic loading at supra-physiological level. Figure 2.30 presents the structure of the intact, elastase treated and collagenase treated samples using electron microscopy.

The stress-strain curves obtained by performing cyclic mechanical tests on intact samples, partially collagen fibre digested samples and fully collagen fibre digested samples are shown in Figure 2.31. It can be seen from this figure that untreated sample show the highest level of softening because of cyclic loading at large loads. This observation is an indicator that the softening phenomenon in the arterial tissue is mainly due to the presence of collagen fibres. Doing these mechanical tests, they also concluded that the collagen fibre digested samples ruptured at much lower strain levels.

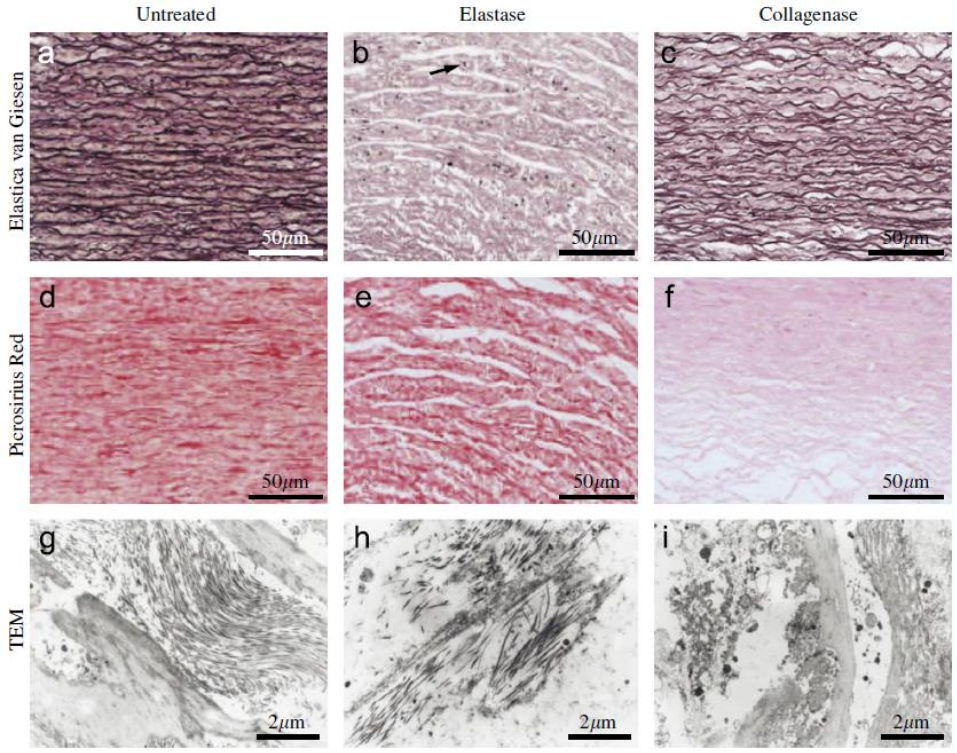

Figure 2.30. *Representative comparison of untreated specimens (left), elastase treated (middle) and collagenase treated (right) of the medial layer of the human thoracic aorta using transmission electron microscopy (TEM):(a)–(c) Elastica van giesen stain visualizing elastic fibres and smooth muscle cell nuclei (arrow)in black;(d)–(f) Picro sirius red stain visualizing collagen fibres in dark red; (g)–(i) TEM of the ultrastructure of collagen and elastin (Weisbecker et al. 2013).*

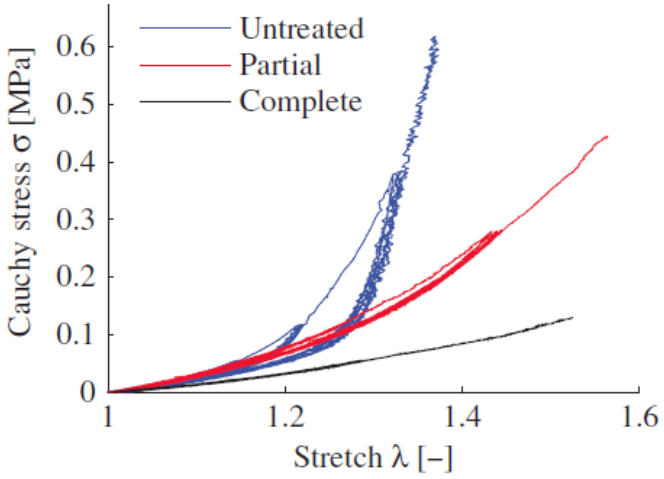

Figure 2.31. *Uniaxial cyclic loading of untreated, partial collagenase treated and complete collagenase treated tissue (Weisbecker et al. 2013).*

Weisbecker et al. (2013) also concluded that elastase treated specimen exhibit continuous softening under cyclic loading at the same load level. This conclusion was confirmed in a subsequent study conducted by Schriefl et al. (2015a). By performing cyclic mechanical tests on elastase and collagenase treated samples obtained from human abdominal aortic tissue, Schriefl et al. (2015c) related the integrity of the tissue to the presence of elastin fibres. This observation can be due to this fact that after removing the elastin fibres, collagen fibres are no longer adequately connected to the non-collagenous matrix, and fibres can then slide against one another. Although these observations can provide valuable information about the discontinuous softening in the collagenous and non-collagenous tissue, they do not provide enough insight into the role of different constituents of the arterial tissue in other damage relevant phenomenon such as tissue rupture, hysteresis or permanent set.

To investigate the response of the smooth muscle cells under supra-physiological loads, Famaey et al. (2010) developed a custom made functional myograph, see Figure 2.32. This device consists of a water-jacketed organ chamber in which an excised cylindrical section of an artery can be mounted. Two rods slide into the lumen of the sample, where one rod is connected to the base of the setup, and the other to a load cell suspended above the set-up, so that isometric tension can be recorded.

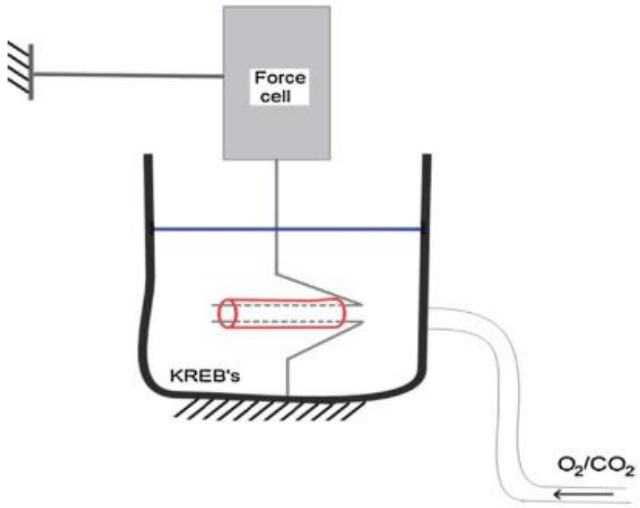

Figure 2.32. *A schematic presenting the myograph (Famaey et al. 2010).*

To perform the experiment, they immersed intact samples and arteries damaged during clamping in Krebs buffer at body temperature and continuously gassed with a mixture of 95% oxygen and 5% carbon dioxide. After stabilisation, a contraction stimulus was generated by adding Phenylephrine (PE) at 10-6 M to the solution while Sodium nitroprusside (SNP) (10-6 M) was used to induce an endothelium- independent relaxation. The contraction force of intact

and damaged samples were then compared, see Figure 2.33. It can be seen from this figure that the damaged samples could induce lower contracting forces in the rods.

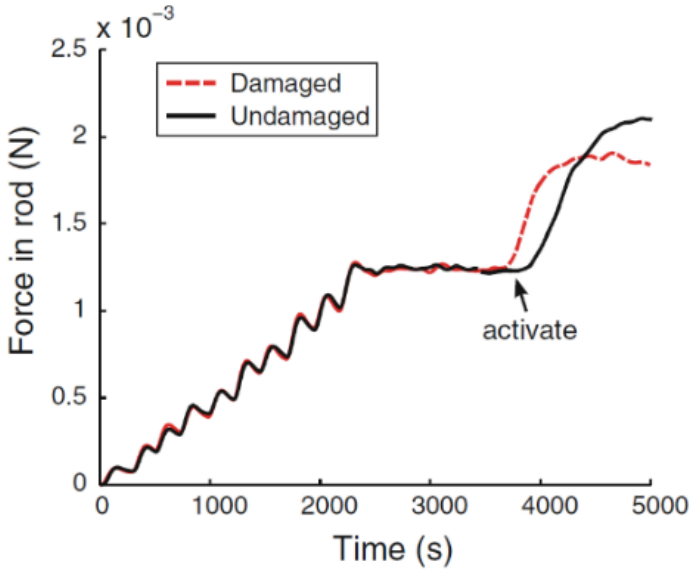

Figure 2.33. *The curve shows the force measured in the rod of myograph as a function of time. The response of undamaged artery is shown by black curve and the response of the clamped artery is shown by dashed red curve (Famaey et al. 2013).*

2.10 Summary

Cardiovascular disease is a major cause of death worldwide. Growth and disruption of atherosclerosis plaque is associated with myocardial and cerebral infarctions. A detailed analysis of areas at risk of rupture and mechanical conditions therein can help us to gain a better insight into how arterial tissue functions and also to differentiate between healthy and diseased arteries.

Many different forms of phenomenological and structural constitutive models are proposed in the literature to capture the mechanical response of the healthy arterial walls and atherosclerotic plaques under physiological and supra-physiological loads. These constitutive models enable us to predict the behaviour of arterial tissue under different loading conditions. This information the can be used to assess the vulnerability of atherosclerotic plaque and to distinguish the areas at higher risk of plaque rupture. These constitutive models can also be used to improve the design of biomedical devices.

Although the overall functionality of many of the constitutive models are validated and/or verified using mechanical experiments particularly under physiological loads, there has been a lack of information on the role of each constituent of the arterial tissue under different loading scenarios and particularly damage-relevant phenomena. Such constitutive specific

information can reveal valuable information which helps the development of structural constitutive models.

It is well documented that distribution of collagen fibres plays a major role in the mechanical behaviour of the healthy arterial tissue and atherosclerotic plaques. Re-orientation of collagen fibres is an important part of the remodelling process in the arteries. During this process collagen fibres re-orientate to maximize the load bearing capacity of the tissue. However, to the best of the author's knowledge, no study has investigated the optimum distribution of fibres specifically in atherosclerotic plaques. Knowing the optimum configuration of collagen fibres, and comparing that with the real distribution of fibres in the atherosclerotic plaque, can help identify lack of remodelling in diseased tissue. Such information reveals important information which could help to assess the risk of plaque rupture in carotid arteries.

Although it is shown that constitutive models can successfully predict the mechanical behaviour of healthy and diseased tissue, certain limitations can be associated with such techniques. Firstly, obtaining accurate patient specific material properties needs information which is commonly obtained by harvesting the tissue and performing mechanical tests on the samples. Although advancement in the imaging techniques such as MRI may minimize the need for harvesting the tissue and conducting mechanical tests in the future, currently, there is no other standard method to replace these mechanical tests. Secondly, using constitutive models for analysing the patient specific geometries can be computationally very expensive and result in delays in assessing and screening the risk of plaque rupture. These are the main limitations which can be associated with a stress metric to become a standard preclinical or clinical metric for assessing the vulnerability of the plaques.

Other clinical techniques for assessing the risk of rupture including angiography and ultrasound are based on percentage of lumen stenosed. However, studies show that there is not a direct correlation between the percentage stenosis and the likelihood of plaque rupture. Therefore, there is a need for a technique that can rapidly assess patient specific geometries and indicate the areas at higher risk of plaque rupture. Such techniques can then be used in combination with constitutive models to reveal more information about the underlying structure of the arterial tissue.

Chapter 3 An investigation into the role of different constituents in damage accumulation in arterial tissue and constitutive model development

3.1 Introduction

Carotid atherosclerotic plaque rupture and stroke are among the leading causes of death worldwide (Benjamin et al. 2017). Angioplasty, stenting and endarterectomy are the most common endovascular treatments to re-open atherosclerotic and narrowed arteries (Henry and Henry 2017; Moresoli et al. 2017). These treatments can apply supra-physiological loads on the vessel wall during the deployment of the intravascular device itself, or through external tissue clamping during surgery.

Experimental studies have revealed that passive damage accumulation in biological soft tissues is associated with four phenomena, (i) Mullins effect, (ii) hysteresis. (iii) permanent set and (iv) rupture, as discussed in section 2.4.2 of this thesis.

Although several constitutive models have been developed to model the damage relevant phenomena in arterial tissue, there has been a lack of experimental data to distinguish the role of each constituent of arteries in damage accumulation phenomena. Whilst Weisbecker et al. (2013) performed a series of uniaxial experiments on intact, elastase treated and collagenase treated media of human thoracic aorta to explore the role of elastin and collagen fibres in the discontinuous and continuous softening of the tissue, they did not elucidate the role of each constituent of the arterial wall on damage relevant phenomena such as permanent set or tissue failure, as discussed previously in section 2.7.

The main aim of this study is to gain further insights into the contribution of matrix and fibres to damage accumulation in arteries under supra-physiological loading conditions. To achieve this aim, mechanical tests at high strain levels on intact and collagenase treated media of porcine common carotid arteries in axial and circumferential directions were performed. Using the obtained experimental data, a new computational framework has been developed to capture all passive damage relevant phenomena in matrix and collagen fibres within arterial tissue.

3.2 Materials and Methods

3.2.1 Sample preparation

Fresh porcine common carotid arteries were harvested from 9 large white pigs aged 6 months and weighing approximately 80 kg. Carotid arteries were transported on ice and preparation began within 2 hours of slaughter. The harvested arteries were washed with phosphate-buffered saline (PBS) to remove residual blood, and excess connective tissue was removed. The samples were stored in tissue freezing medium (RPMI-60 Media, 1.8M DMSO; and 0.1M Sucrose), placed in a Mr. Frosty supplier cryosystem (containing isopropyl alcohol; VWR) and cryopreserved at -80℃. On the day of the experiments, samples were defrosted in PBS at ambient temperature. Arteries were cut into dog-bone shaped specimens with a 2mm width in the gauge region such that the gauge length $l_0 \geq 5.56 \times \sqrt{A}$, where A denotes the cross section area of the specimens (Davis 2004). The thickness of each sample was then calculated by taking the average of three measurements using a Mitutoyo FS70Z microscope after carefully removing the adventitial layer using tweezers.

3.2.2 Enzyme treatment

Collagenase solution was prepared (500 U ml^{-1}, chromatographically purified collagenase, Worthington Biochemical, NJ, USA) in buffer solution containing Dulbecco's PBS with $MgCl_2$ and $CaCl_2$. The arterial samples were incubated in the collagenase solution at 37℃ for 42 hours. Histological images were obtained to verify the digestion of collagen fibres at 0, 16 and 42 hours using Picrosirius red staining, see Figure 3.1.

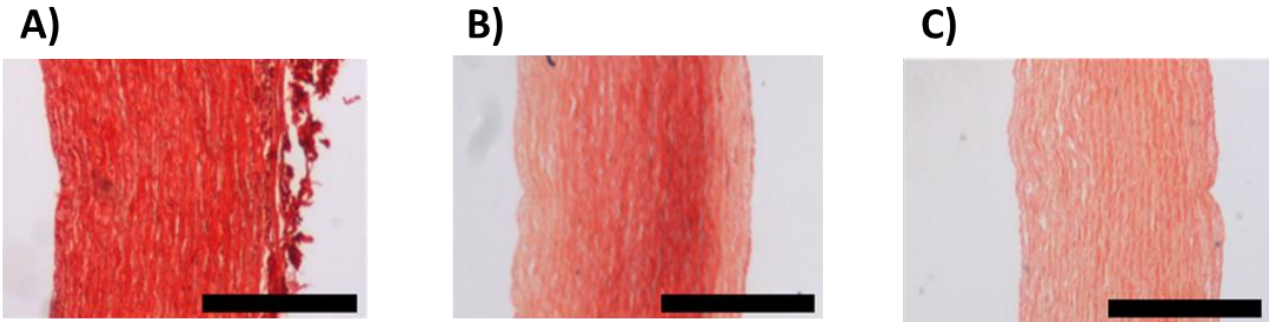

Figure 3.1. *Histology images obtained at different stages of collagen fibre digestion in samples of the porcine carotid arteries. (A) control sample (0 hour of collagenase treatment) (B) 16 hours of collagenase treatment (C) 42 hours of collagenase treatment. Scale bar: 500 μm.*

3.2.3 Tensile test

The mechanical tests were conducted on intact and digested specimens using a uniaxial test machine (Zwick ZO05, Zwick GmbH & Co. Ulm, Germany) equipped with a 20 N load cell. All the experiments were performed in a tissue bath of PBS at room temperature, see Figure 3.2. A custom designed video extensometer recorded the stretch in the gauge region of the

specimen by tracking six black dots on the dog-bone strips in the direction of the applied force. The measured displacement between dots was then used only to calculate the stretch in the direction of loading of the specimen. A sequence of cyclic loading was imposed on the tissue at a constant displacement rate of 10 $mm.min^{-1}$ with stress limits for each load step. The mechanical tests started with five cycles of preconditioning. Each cycle of preconditioning was set to the maximum nominal strain level of 15%. To the best of author's knowledge, to-date, no standard maximum stress or stretch levels are defined for preconditioning of arterial tissue, see also Macrae et al. (2016) . After preconditioning cycles, samples were subjected to three cycles for each load step to monitor the discontinuous and continuous softening in the specimens. The first load step was set to an engineering stress level of 80 kPa which was followed by 100 kPa increase for each subsequent load step. The cyclic mechanical tests continued in each sample until failure of the tissue. Only samples in which rupture occurred in the gauge length have been considered. The results obtained from our cyclic tensile tests on the intact and digested samples have been used to explore damage relevant phenomena in the media layer of porcine common carotid arteries. A summary of the samples which have been used in different parts of this study is outlined in Table 3.1.

Table 3-1. *A summary of samples which have been used in different parts of this study.*

Samples which have been used to investigate the permanent set phenomenon in the intact and collagen fibre digested samples.	
Total number of arteries	3
Samples per artery	4
Total number of circumferential samples	6
Total number of axial samples	6
Total number of digested samples in the circumferential direction	3
Total number of digested samples in the axial direction	3
Samples which have been used to investigate the response of the intact arteries to supra-physiological loads.	
Total number of the arteries	6
Total number of circumferential samples	6
Total number of axial samples	6
Arteries in which both axial and circumferential samples ruptured in the gauge length	3
Arteries used for material calibration.	2

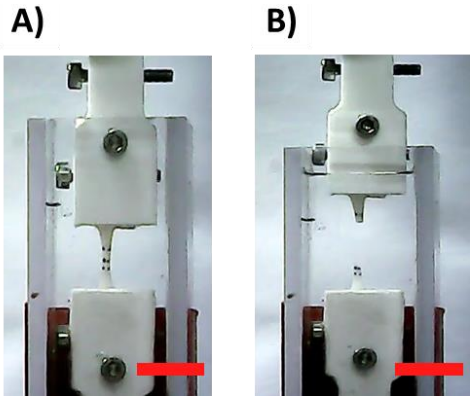

Figure 3.2. *Representative images of the experimental set-up which was used for the uniaxial mechanical tests. The sample (A) before and (B) after rupture, scale bar: 10mm.*

3.2.4 Constitutive modelling

3.2.4.1 Kinematics

Arterial tissue is commonly considered an almost incompressible material and therefore a multiplicative decomposition of the deformation gradient tensor $\mathbf{F}$ into volumetric $J^{\frac{1}{3}}\mathbf{I}$ and isochoric parts $\bar{\mathbf{F}}$ is usually performed to characterise the deformation processes. Following Flory (1961) multiplicative decomposition of the deformation gradient tensor can be written as;

$$\mathbf{F} = (J^{\frac{1}{3}}\mathbf{I})\bar{\mathbf{F}} \tag{3.1}$$

Where $\mathbf{I}$ is the identity tensor. The right Cauchy-Green tensor, denoted by $\mathbf{C}$, and its isochoric counterpart, denoted by $\bar{\mathbf{C}}$, are then defined as follows;

$$\mathbf{C} = \mathbf{F}^T\mathbf{F} = J^{\frac{2}{3}}\,\bar{\mathbf{C}}, \bar{\mathbf{C}} = \bar{\mathbf{F}}^T\bar{\mathbf{F}} \tag{3.2}$$

The deviatoric principal invariants of the right Cauchy-Green tensor takes the following representation.

$$\begin{aligned} \bar{I}_1 &= tr(\bar{\mathbf{C}}), \\ \bar{I}_2 &= \frac{1}{2}[tr^2(\bar{\mathbf{C}}) - tr(\bar{\mathbf{C}}^2)], \\ \bar{I}_3 &= \det(\bar{\mathbf{C}}) \end{aligned} \tag{3.3}$$

The unit vector M can be used to define the direction of fibres with respect to the circumferential direction of the arterial wall in the undeformed state. The isochoric configuration of the vector M in the spatial coordinate system can then be written as follows;

$$\bar{\mathbf{M}} = \bar{\mathbf{F}}\mathbf{M} \tag{3.4}$$

The deviatoric invariants associated with a unit vector $\mathbf{M}$ are represented as follows;

$$\bar{I}_M = tr(\bar{\mathbf{C}}\bar{\mathbf{M}}\otimes\bar{\mathbf{M}}) = \bar{\mathbf{M}}.(\bar{\mathbf{C}}\bar{\mathbf{M}}) \tag{3.5}$$

Generalized structure tensors have been used to represent the level of anisotropy of the fibres in the arterial tissue. Gasser et al. (2006) defined a structure tensor $\mathbf{H_M}$ that accounts for the effect of angular distribution of the fibres in the direction of M.

$$\mathbf{H_M} = \kappa\bar{\boldsymbol{I}} + (1 - 3\kappa)(\bar{\mathbf{M}}\otimes\bar{\mathbf{M}}) \tag{3.6}$$

where κ is a scalar value that represents the dispersion of fibres in the array of collagen fibres in the arterial tissue. The pseudo invariants $\bar{I}_M^*$ of $\mathbf{H_M}$ can then be defined as follows (Gasser et al. 2006) ;

$$\bar{I}_M^* = \bar{\mathbf{C}}:\mathbf{H}_\mathrm{M} = \kappa\bar{I}_\mathbf{1} + (1 - 3\kappa)\bar{I}_M \tag{3.7}$$

3.2.4.2 Response of arteries to physiological loading levels

The mechanical behaviour of arteries is commonly modelled using a hyperelastic anisotropic material model, whereby the existence of a Helmholtz free-energy function is postulated per unit reference volume for the tissue. Following Holzapfel et al. (2000), the total strain energy function of arterial tissues can be additively decomposed into: volumetric ψ_{vol} , isochoric isotropic $\bar{\psi}_{iso}$ and isochoric anisotropic parts (ψ_{ef} and ψ_{cf} for elastin and collagen fibres, respectively);

$$\psi = \psi_{vol} + \bar{\psi}_{iso} + \bar{\psi}_{ef} + \bar{\psi}_{cf} \tag{3.8}$$

The volumetric free energy ψ_{vol} can be expressed as follows;

$$\psi_{vol}(J) = \frac{1}{2}\kappa_0(J - 1)^2 \tag{3.9}$$

where κ_0 serves as a penalty parameter that controls the compressibility of biological soft tissue (Gasser and Holzapfel 2002).

Isotropic material models have been widely used to represent the mechanical behaviour of the ground matrix. In this research, a neo-Hookean material model along with two families of elastin fibres at 45 degrees with respect to the circumferential direction of the vessel wall has been employed to describe the mechanical behaviour of the ground matrix and elastin fibres which constitute the elastin sheets, similar to Holzapfel et al. (2000).

$$\bar{\psi}_{iso}(\bar{\mathbf{C}}) = \frac{1}{2}\mu(\bar{I}_1 - 3) \tag{3.10}$$

$$\bar{\psi}_{ef}(\bar{\mathbf{C}}) = \sum_{M_{ef}=M_{4ef,6ef}} \frac{k_{1ef}}{2k_{2ef}} (\exp(k_{2ef}\left(\bar{I}_{M_{ef}} - 1\right)^2) - 1) \tag{3.11}$$

Where μ is the shear modulus of the ground matrix and k_{1ef} and k_{2ef} are stress like and dimensionless material parameters respectively. $\bar{I}_{M_{4ef}}$ and $\bar{I}_{M_{6ef}}$ are the deviatoric invariants that indicate the square of stretch in elastin fibres and correspond to two unit vectors $\mathbf{M_{4ef}} = \{\cos(\alpha_{ef}), \sin(\alpha_{ef}), 0\}$ and $\mathbf{M_{6ef}} = \{\cos(\alpha_{ef}), -\sin(\alpha_{ef}), 0\}$ respectively, where α_{ef} is the angle of elastin fibres which has been chosen to be equal to 45° with respect to the circumferential direction of the vessel wall.

Following (Gasser et al. 2006), we have assumed that two symmetric families of collagen fibres contribute in bearing load in the arterial tissue. The contribution of these two families of collagen fibres in the overall mechanical behaviour of the tissue has been described using the strain energy function proposed in (Gasser et al. 2006) as follows;

$$\bar{\psi}_{cf}(\bar{\mathbf{C}}) = \sum_{M_{cf}=M_{4cf,6cf}} \frac{k_{1cf}}{2k_{2cf}} (\exp(k_{2cf}\left(\kappa\bar{I}_1 + (1-3\kappa)\bar{I}_{M_{cf}} - 1\right)^2) - 1) \tag{3.12}$$

where k_{1cf} and k_{2cf} are material parameters and $\bar{I}_{M_{4cf}}$ and $\bar{I}_{M_{6cf}}$ are the square of the stretch in the collagen fibres and correspond to two unit vectors $\mathbf{M}_{4\text{cf}} = \{\cos(\alpha_{cf}), \sin(\alpha_{cf}), 0\}$ and $\mathbf{M}_{6\text{cf}} = \{\cos(\alpha_{cf}), -\sin(\alpha_{cf}), 0\}$ respectively, where α_{cf} is the angle of collagen fibres with respect to circumferential direction.

3.2.4.3 Response of arteries to supra-physiological loading levels

To describe the response of arteries to supra-physiological loading conditions a CDM based approach was employed. As is common in CDM, to capture the energy dissipation in the vessel wall a reduction factor $(1 - D)$ can be incorporated in the overall strain energy function of the tissue to simulate the energy dissipation, where D is a scalar damage function which may take any value between 0 and 1, and evolve according to the loading history of the vessel wall. The incorporation of the reduction factor in the total undamaged strain energy function $\psi^0(\bar{\mathbf{C}})$ may be expressed as follows (Holzapfel 2000);

$$\psi(\bar{\mathbf{C}}, D) = (1 - D)\psi^0(\bar{\mathbf{C}}) \tag{3.13}$$

Although prefixing the reduction factor to the intact strain energy function can describe discontinuous softening in soft tissue, this technique cannot provide an accurate insight into other damage relevant phenomenon such as hysteresis or permanent set. In order to model all of the damage relevant phenomena in the arterial tissue, we have incorporated the reduction factor in the exponential part of the strain energy functions for both elastin and

collagen fibres given in Equations (11) and (12), similar approaches have been employed in (Balzani et al. 2012; Balzani and Schmidt 2015; Govindjee and Simo 1991).

$$\bar{\psi}_{ef}\left(\bar{\mathbf{C}}, D_{ef}\right) = \sum_{M_{ef}=M_{4ef},M_{6ef}} \frac{k_{1ef}}{2k_{2ef}} \left(\exp[k_{2ef}(1-D_{ef})\left(\bar{I}_{M_{ef}}-1\right)^2]-1\right) \tag{3.14}$$

$$\bar{\psi}_{cf}\left(\bar{\mathbf{C}}, D_{cf}\right) = \sum_{M_{cf}=M_{4cf},M_{6cf}} \frac{k_{1cf}}{2k_{2cf}} \left(\exp(k_{2cf}(1-D_{cf})\left(\kappa\bar{I}_1+(1-3\kappa)\bar{I}_{M_{cf}}-1\right)^2)-1\right) \tag{3.15}$$

Where D_{ef} and D_{cf} are the damage functions for elastin fibres and collagen fibres respectively. These damage functions evolve according to structural pseudo-invariant functions over the loading history using two internal variables, $\beta_{ef,cf}$ and $\gamma_{ef,cf}$, to capture continuous and discontinuous softening, respectively. $\beta_{ef,cf}$ is defined as follows;

$$\beta_{ef,cf} = \langle \tilde{\beta}_{ef,cf} - \tilde{\beta}^{ini}_{ef,cf} \rangle \tag{3.16}$$

where $\tilde{\beta}^{ini}$ is an internal variable at an initial damage state to ensure that the damage evolution starts when entering the supra-physiological domain and Macaulay brackets, $\langle(\bullet)\rangle = \frac{1}{2}[(\bullet)+|(\bullet)|]$, have been used to allow only positive values. $\tilde{\beta}_{ef,cf}$ is defined according to changes in the pseudo invariant $\bar{I}^*_{M_{ef,cf}}$ over the total loading history, as follows;

$$\tilde{\beta}_{ef,cf} = \int_0^t \langle \bar{I}^*_{Mef,Mcf} \rangle ds \tag{3.17}$$

It is worth mentioning here that although the internal variable $\tilde{\beta}_{ef,cf}$ is used to capture the response of the elastin and collagen fibres under cyclic loads at the same level, the evolution of this variable is not continuous over the loading history. The values of this internal variable only influence the damage accumulation in the arterial wall in the loading paths when tissue has been subjected to the supra-physiological loads. The value of this internal variable also does not change during the unloading paths.

The internal variable $\gamma_{ef,cf}$ is defined according to the maximum value $\bar{I}^*_{ef,cf}$ experienced over the loading history up to the current loading state of the arterial tissue and defined as follows;

$$\gamma_{ef,cf} = \max_{S\in[0,S]} \langle \bar{I}^*_{Mef,Mcf} - \bar{I}^{*ini}_{Mef,Mcf} \rangle \tag{3.18}$$

The damage functions D_{ef} and D_{cf} can then be written as follows for both elastin and collagen fibres, similar to procedures shown in (Balzani et al. 2012; Balzani and Schmidt 2015; Miehe 1995).

$$D_{ef,cf} = D_{\infty ef,cf}[1 - \exp(-\frac{\gamma_{ef,cf}}{\gamma_{\infty ef,cf}})]\left[1 - \exp\left(-\frac{\beta_{ef,cf}}{\beta_{s ef,cf}}\right)\right], D_{ef,cf} \in [0,1) \tag{3.19}$$

Where $D_{\infty ef,cf}$ denotes a predefined limit for the overall damage values for elastin and collagen fibres which we have selected to be 0.99. $\beta_{s ef,cf}$ and $\gamma_{\infty ef,cf}$ are the only material parameters which have been used to capture continuous and discontinuous softening in the arterial tissue, respectively.

3.2.5 Finite element implementation

To implement this material model into a commercial Finite Element (FE) software, such as Abaqus (Dassault Systèmes Simulia corporations, Vèlizy-Villacoublay, France), the Cauchy stress tensor σ and the elasticity tensor $\mathbb{C}$ (also referred to as the tangent modulus or the material Jacobian) should be defined. The Cauchy stress tensor is derived from the strain energy functions introduced in the preceding section, (Equation (8)), as follows, see appendix A;

$$\boldsymbol{\sigma} = \frac{2}{J}\mathbf{F}\frac{\partial \psi}{\partial \mathbf{C}}\mathbf{F}^T \tag{3.20}$$

The corresponding Kirchhoff stress is defined as follows;

$$\boldsymbol{\tau} = J\boldsymbol{\sigma} \tag{3.21}$$

In this research, following the procedure demonstrated by Sun et al. (2008), the material Jacobian has been derived by incrementally perturbing the deformation gradient tensor and performing a forward difference of the associated Kirchhoff stresses;

$$\mathbb{C}^{(ij)} \approx \frac{1}{J\varepsilon}(\boldsymbol{\tau}(\hat{\mathrm{F}}^{ij}) - \boldsymbol{\tau}(\hat{\mathrm{F}})) \tag{3.22}$$

where ε (10^{-8}) is a small perturbation parameter and the $\boldsymbol{\tau}$ denotes the Kirchhoff stress tensor. The tensor $\hat{\mathbf{F}}^{ij}$ describes the perturbed deformation gradient tensor which is;

$$\hat{\mathrm{F}}^{ij} = \mathbf{F} + \Delta \mathrm{F}^{\mathrm{ij}} \tag{3.23}$$

Following (Miehe 1996; Sun et al. 2008) $\Delta\mathbf{F}^{ij}$ can be defined as follows;

$$\Delta \mathrm{F}^{ij} = \frac{\varepsilon}{2}(\mathrm{e_i} \otimes \mathrm{e_j}\mathbf{F} + \mathrm{e_j} \otimes \mathrm{e_i}\mathbf{F}) \tag{3.24}$$

where $\{\mathrm{e_i}\}_{i=1,2,3}$ denotes the unit vectors in the spatial configuration over which the perturbation has been performed, $ij = \{11,22,33,12,23,31\}$. A similar approach has also been employed by (Creane et al. 2010a). The algorithmic FE implementation of the demonstrated damage model along with required quantities is shown in Table 3.2.

Table 3-2. The summary of the quantities required for finite element implementation of the presented constitutive model.

Material parameters for ground matrix μ

(1) Material parameters for elastin fibres $k_{1ef}, k_{2ef}, \alpha_{ef}, \gamma_{\infty_{ef}}, \beta_{s_{ef}}$

Material parameters for collagen fibres $k_{1cf}, k_{2cf}, \alpha_{cf}, \kappa, \gamma_{\infty_{cf}}, \beta_{s_{cf}}$

(2) Deformation gradient $\mathbf{F}$

(3) Deformation measures $\bar{\mathbf{F}} = J^{-\frac{1}{3}}\mathbf{F}$, $J = \det(\mathbf{F})$, $\bar{\mathbf{C}} = \bar{\mathbf{F}}^T\bar{\mathbf{F}}$, $\bar{I}_1$

(4) Pseudo invariant measures $\bar{I}^*_{M_{ef},M_{cf}} = \boldsymbol{\kappa}\bar{I}_{\mathbf{1}} + (\mathbf{1} - \mathbf{3}\boldsymbol{\kappa})\bar{I}_{M_{ef},M_{cf}}$

(5) Check the initial damage threshold $\bar{I}^{*ini}_{M_{ef},M_{cf}}$ for elastin and collagen fibres

If $\bar{I}^*_{M_{ef},M_{cf}} < \bar{I}^{*ini}_{M_{ef},M_{cf}}$ then go to (6) otherwise go to (10)

(6) $\psi = \psi_{vol} + \bar{\psi}_{iso} + \bar{\psi}_{ef} + \bar{\psi}_{cf}$

(7) $\sigma = \frac{2}{J}\mathbf{F}\frac{\partial \psi}{\partial \mathbf{C}}\mathbf{F}^T$

(8) $\mathbb{C} = \mathbb{C}_{vol} + \mathbb{C}_{iso} + \mathbb{C}_{ef} + \mathbb{C}_{cf}$

(9) Return to step number (2)

(10) $\beta_{ef,cf} = \langle \tilde{\beta}_{ef,cf} - \tilde{\beta}^{ini}_{ef,cf} \rangle$

(11) $\gamma_{ef,cf} = \max_{S\in[0,S]} \langle \bar{I}^*_{M_{ef,cf}} - \bar{I}^{*ini}_{M_{ef,cf}} \rangle$

(12) $D_{ef,cf} = D_{\infty_{ef,cf}}[1 - \exp(-\frac{\gamma_{ef,cf}}{\gamma_{\infty ef,cf}})]\,[1 - \exp(-\frac{\beta_{ef,cf}}{\beta_{s_{ef,cf}}})], D_\infty \in [0,1[$

(13) $\psi = \psi_{vol} + \psi_{iso} + \bar{\psi}_{ef}(\bar{\mathbf{C}}, D_{ef}) + \bar{\psi}_{cf}(\bar{\mathbf{C}}, D_{cf})$

(14) $\sigma = \frac{2}{J}\mathbf{F}\frac{\partial \psi}{\partial \mathbf{C}}\mathbf{F}^T$

(15) $\mathbb{C} = \mathbb{C}_{vol} + \mathbb{C}_{iso} + \mathbb{C}_{ef} + \mathbb{C}_{cf}$

(16) Return to step number (2)

3.2.6 Material Calibration

To verify the proposed constitutive model, the response of the digested and intact samples has been obtained at different stages, namely, (i) when no damage accumulates in the tissue, (ii) the stage at which damage starts to accumulate in the elastin fibres but no damage has accumulated in the collagen fibres and (iii) the stage at which damage is accumulating in both elastin and collagen fibres. Material parameters associated with capturing the damage accumulation in the elastin fibres only influence the stress calculation when the damage threshold for the elastin fibres has been passed (at this stage other material parameters such as c_{10}, k_{1ef}, k_{2ef}, remain constant) and damage parameters for the collagen fibres have only been incorporated in the response of the tissue when the damage threshold for collagen fibres has been exceeded (at this stage other material parameters such as c_{10}, k_{1ef}, k_{2ef}, k_{1cf}, k_{2cf}, α_{cf} remain constant). Collagen fibres and elastin fibres have also been constrained to only contribute in the load bearing of the tissue under tension. The damage thresholds in the collagen and elastin fibres are functions of stretch in the fibres which has been captured by calculating the deviatoric invariants associated with the direction of the elastin and collagen fibres, $I_{M_{ef}}$ and $I_{M_{cf}}$ respectively, see Equation (5). In order to set the damage threshold for damage accumulation in collagen fibres, the results of studies such as (Converse et al. 2018; Zitnay et al. 2017) were employed. In these studies collagen hybridizing peptide (CHP) was utilised to detect damage initiation in collagen fibres under stretch. In addition, the difference in stiffness between elastin and collagen fibres is highlighted in studies such as (Shadwick 1998; Shadwick 1999). However, to the best of the authors' knowledge, to-date no specific damage threshold for elastin fibres has been presented in the literature. In this research we assumed that damage accumulation in the elastin fibres starts as soon as their stretch is slightly greater than one (1.02). A sensitivity analysis has been performed to explore the influence of selecting different damage thresholds on damage accumulation and stress calculations for both collagen and elastin fibres. The results of this sensitivity analysis are included in Appendix B.

Stress-time curves from samples in the circumferential and axial directions of the vessel wall have been used simultaneously to account for the anisotropic behaviour of the non-collagenous and intact samples. Similar approaches have been used to adjust material models to experimental data in studies such as (Balzani and Schmidt 2015; Maher et al. 2012; Pena 2014). It should be mentioned that data obtained for the values of permanent set have not been incorporated into the curve fitting process and have enabled us to further assess the suitability of this damage model for arterial tissue.

An inverse FE algorithm was implemented to adjust the parameters of our damage model to the experimental data using Isight 5.9 (Dassault Systèmes Simulia corporations, Vèlizy-

Villacoublay, France). To simulate our cyclic mechanical tests, the stretch read from the video extensometer during the experimental tests was applied on one single element using displacement boundary conditions. A compressibility constraint was also imposed by using a hybrid element type (C3D8H). A schematic of this simulation and boundary conditions are presented in Figure 3.3.

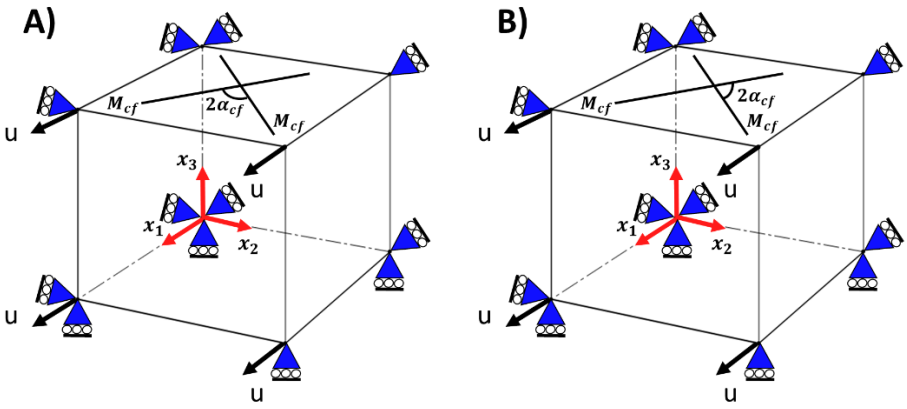

Figure 3.3. *A schematic of uniaxial mechanical tests simulated for specimens in (A) circumferential and (b) axial directions by applying the displacements boundary condition (u) in Abaqus.*

Two sets of experimental data, one in the axial and the other one in the circumferential direction, were used to determine the material parameters for both intact and digested samples simultaneously. A combination of global and local optimization methods were employed to minimize the sum of the square difference of the measured stress between the experiments and the model, and the error was calculated as follows (Balzani et al. 2012);

$$error = \sum_{e=1}^{n_e} \sqrt{\frac{1}{n_{mp}} \sum_{m=1}^{n_{mp}} \left(\frac{\sigma_{mp}^{exp} - \sigma_{mp}^{model}}{\max(\sigma^{exp})} \right)^2} \tag{3.25}$$

Where n_e is the number of experimental datasets (axial and circumferential), n_{mp} is the total number of experimental points in the loading and reloading paths , σ^{exp} is the measured stress in the experiments and σ^{model} is the calculated stress from the model. In this research, we have used two sets of experimental data ($n_e = 2$) simultaneously, with 100 points ($n_{mp} = 100$) on each loading and reloading path.

In the first step of the minimization, a multi-objective genetic algorithm based optimization method was used to characterize the material parameters of the media layer of the porcine common carotid arteries. One of the main benefits of using a genetic algorithm based optimization method at this stage is that it examines a large population of random material

parameter combinations in a certain domain to minimize the objective functions in each iteration. This technique can be particularly useful when no proper first estimation of the material parameters exists. This method also accelerates the process of finding the global minimum of the objective functions by adding penalty values to the local minimums. The general specifications of the genetic algorithm that we have used in this research are given in Table 3.3. For a more detailed description of the genetic algorithm and its application in identifying material parameters and inverse problems the reader is referred to (El Sayed et al. 2008). We have restricted all parameters to remain positive during the optimization process. The angle of collagen fibres is assumed to be between 10 and 80 degrees with respect to the circumferential direction of the vessel wall. The dispersion of collagen fibres was permitted to be between 0 and 0.33.

Table 3-3. *The genetic algorithm options that have been used in this study*.

Initial size	80
Population size	120
Selection	Myriad of different heuristics
Crossover probability	0.9
Mutation probability	0.5
Initialization mode	Random
Number of function evaluations	1000
Failed run penalty value	10^{30}

The material parameters obtained in the first step of the optimization were then used as the preliminary material parameters for the second step of minimization where the Downhill simplex method was employed as the local optimization method. The Downhill simplex method is a gradient free geometrically intuitive exploratory technique. For a detailed description of the Downhill simplex method and its implementation the reader is referred to, for example, (Press et al. 1987). The options that we have used for Downhill simplex method are given in Table 3.4. A schematic of the implemented optimization method is shown in Figure 3.4.

Table 3-4. *The options of the Downhill simplex method that have been used in this study.*

Initial simplex size	0.1
Max iterations	400
Failed run penalty value	10^{30}

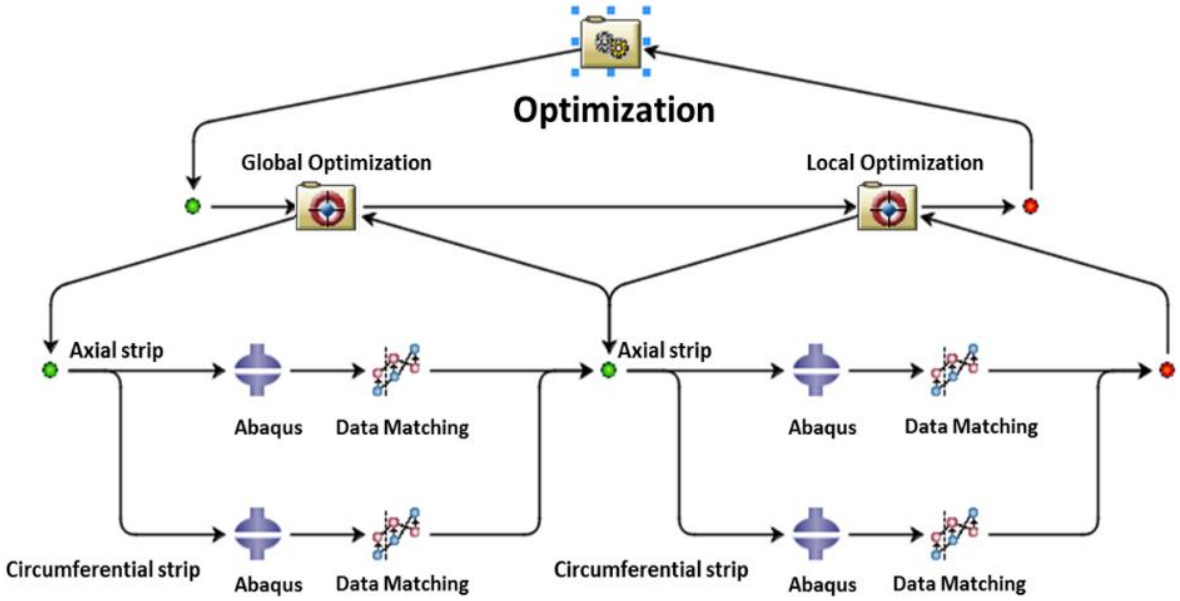

Figure 3.4. *A schematic presentation of the implemented inverse FE algorithm for material calibration of the media layer of porcine carotid arteries in Isight. Different parameterized Abaqus input files have been designated for the specimens in the axial and circumferential directions. The input files were imported into the Abaqus component of Isight and the material parameters selected as optimization variables. The results from the experiments and simulation have been imported into the data matching component where the sum of the stress difference for 100 points on each loading and reloading path have been defined as objective functions separately for samples in axial and circumferential directions. A hybrid optimization algorithm was then performed to characterize the material parameters of each specimen.*

3.3 Results

The permanent deformation of the three intact and three digested arteries in the circumferential and axial samples are compared in Figure 3.5. The summary of the samples which have been used for this study are shown in Table 3.1. The permanent set in each sample has been evaluated by reading the accumulated residual strain in each specimen at zero force in the reloading paths, similar to (Maher et al. 2012; Pena 2014). A linear relationship between the resulting permanent set and peak strain has been observed in the intact and digested samples in both the circumferential and axial directions. Our observations confirm that there is no statistically significant difference in the captured permanent set in either the circumferential and axial directions, or between the intact and digested samples. To perform this statistical analysis, a one-way analysis of variance (ANOVA) was performed with a significance level of 0.05, see Appendix C.

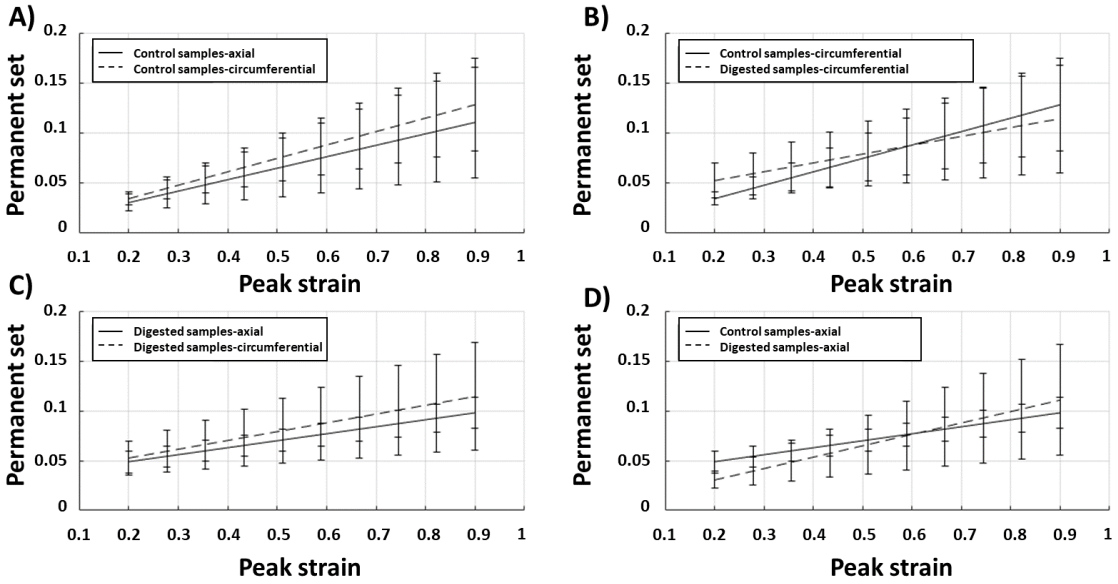

Figure 3.5. *The obtained permanent set in the cyclic mechanical tests at high strain levels in (A) axial and circumferential directions of intact samples, (B) circumferential samples of intact and digested arteries, (C) circumferential and axial directions of digested samples, (D) axial samples of intact and digested samples.*

The stress-stretch curves obtained from one intact and one digested artery in the axial and circumferential directions are compared in Figure 3.6 in the circumferential and axial directions. This figure shows larger levels of softening accumulate in the intact samples compared to the digested samples. This figure also shows that rupture of the collagen fibre digested samples occurs at much lower stress levels.

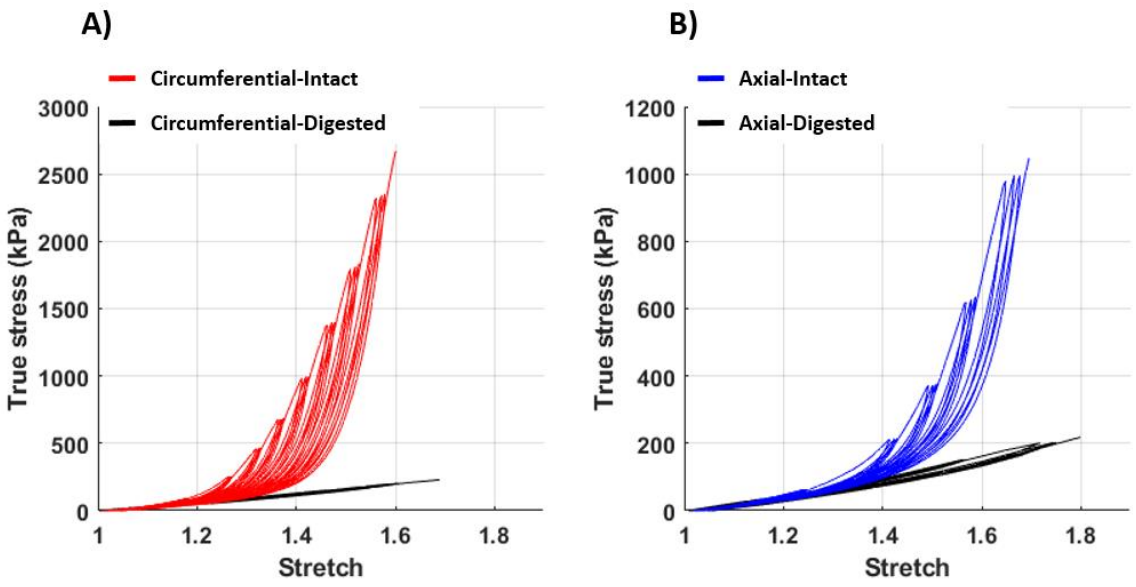

Figure 3.6. *The stress-stretch curves obtained from intact and collagen fibre digested samples in A) circumferential and B) axial directions.*

The stress-stretch curves obtained from cyclic mechanical loading of one collagen fibre digested sample in the circumferential and axial direction have been compared with the response of the damage model in Figure 3.7 (A) and (C). It should be mentioned that to calibrate this constitutive model only the stress computed by our damage model was compared with the stress obtained from experiments and the error was calculated using Equation (3.25). The values of the permanent set which was measured from the experiments and the predicted permanent set by the constitutive model are compared in Figure 3.7 (B) and (D). It is worth mentioning that the data obtained for permanent set from experiments has not been incorporated in the calibration process and Figure 3.7 (B) and (D) represent the prediction of the model.

The material parameters to describe the mechanical behaviour of digested samples to supra-physiological loadings are shown in Table 3.5. Although a low level of anisotropic behaviour has been observed from the experimental data, the results computed by our damage model show that a material model with two families of elastin fibres at 45 degrees with respect to the circumferential direction of the vessel wall can successfully capture the low levels of discontinuous and continuous softening that occur in the ECM along with the associated permanent set in the soft tissue.

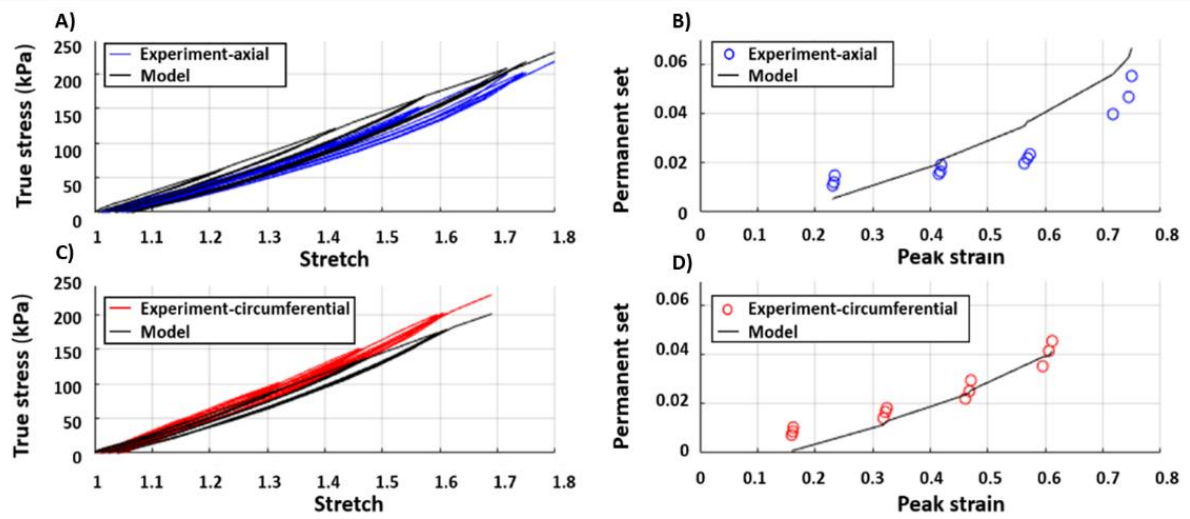

Figure 3.7. *Cyclic uniaxial tension tests of the collagen digested media layer of a porcine common carotid artery in axial (A, B) and circumferential (C, D) directions.*

Table 3-5. *The material parameters which have been used to capture the mechanical behaviour of digested samples shown in Figure (3.6).*

c_{10} (kPa)	k_{1ef} (kPa)	k_{2ef}	$\gamma_{\infty_{ef}}(kPa)$	$\beta_{s_{ef}}$	$error$
40.82	42.577	4.831	6.70	1.271	0.004

The stress-stretch curves obtained from cyclic mechanical loading of axial and circumferential samples from two intact arteries at high strain levels have been compared with the response of the implemented CDM model, see Figure 3.8. A summary of the samples which have been used in this study to explore the response of the intact samples to supra-physiological loads are shown in Table 3.1. The effect of continuous and discontinuous softening on the response of the arteries can be seen in Figure 3.8 (A) and (D). The permanent set obtained from mechanical tests has been compared with the permanent set calculated using our FE simulation in Figure 3.8 (B),(C), (E) and (F). It should be mentioned that, similar to collagen fibre digested samples, the data obtained for permanent set from experiments has not been incorporated in the curve fitting process. The material parameters to describe the mechanical behaviour of each artery are shown in Table 3.6.

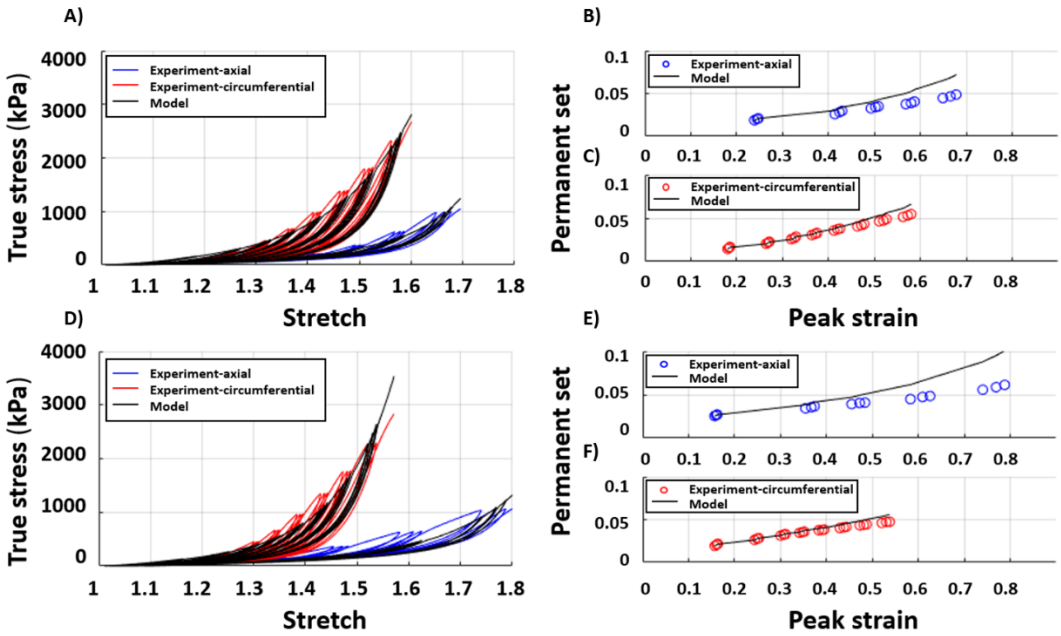

Figure 3.8. *Cyclic uniaxial tension tests of the intact media of two porcine common carotid arteries in the axial and circumferential directions.*

Table 3-6. *The material parameters which have been used to capture the mechanical behaviour of the two intact arteries in the axial and circumferential directions, shown in Figure 3.7.*

$c_{10}\,(kPa)$	$k_{1ef}\,(kPa)$	k_{2ef}	$\gamma_{\infty_{ef}}(kPa)$	$\beta_{s_{ef}}$	$k_{1cf}\,(kpa)$	k_{2cf}	$\alpha_{cf}(deg)$	κ	$\gamma_{\infty_{cf}}(kPa)$	$\beta_{s_{cf}}$	$error$
32.22	21.78	45.5	10.50	7.81	454.66	16.5	37.6	0.03	10.61	3.18	0.006
37.40	28.53	28.3	10.81	3.18	279.568	14.9	36.1	0.02	13.08	3.20	0.017

3.4 Discussion

The obtained experimental results show that there is no significant difference between the resulting permanent set in the intact and digested samples in the circumferential and axial directions. These observations confirm the role of matrix, as opposed to fibres, in the inelastic deformation of arterial tissue at supra-physiological loads. To-date, several constitutive models have assumed that damage in the arterial tissue occurs only within the collagen fibres (Balzani et al. 2012; Balzani and Schmidt 2015; Weisbecker et al. 2013), and as such, the model can adequately capture the damage accumulation in the collagen fibres, but not the overall inelastic behaviour of the tissue at supra-physiological loads.

Although constitutive models such as (Balzani et al. 2012; Maher et al. 2012; Pena 2014) can mathematically capture the inelastic deformation of different biological soft tissues at high loading conditions, no specific structural element has been designated in those models to attribute the inelastic deformation of the artery to the matrix. In this study, the constitutive model that was demonstrated in (Holzapfel 2000) was adapted to capture the behaviour of the

matrix at supra-physiological loading conditions by incorporating two symmetric families of elastin fibres at 45 degrees with respect to the circumferential direction of the vessel wall . A reduction factor has then been incorporated in the exponential term of this constitutive model which enables the permanent set phenomenon in the media layer of the porcine common carotid arteries to be captured. Although some levels of anisotropy have been observed in the mechanical behaviour of the matrix, the proposed transversely isotropic strain energy function for elastin fibres can adequately predict all of the damage relevant phenomena of the non-collagenase matrix. These findings are similar to the observations in (Weisbecker et al. 2013) whereby they show that an isotropic neo-Hookean material model can sufficiently describe the behaviour of the extracellular matrix (ECM) at physiological loads.

It was shown that softening in the arterial tissue is mainly due to the presence of collagen fibres see Figures 3.6. Collagen fibre digested samples also ruptured at much lower stress levels with ultimate tensile strength (UTS) of 216.4 kPa and 227.5 kPa for the axial and circumferential samples, respectively. True stress-stretch curves of these samples are shown in Figure 3.7. The UTS values obtained for intact samples are shown in Figure 3.8 (A) and are 627 kPa and 1670 kPa for the samples in the axial and circumferential directions, respectively, and 605 kPa and 1802 kPa for the samples shown in Figure 3.8 (D) in the axial and circumferential directions, respectively. These observations highlight the important role of collagen fibres in the load bearing capacity of the arterial tissue.

Balzani and Schmidt (2015) compared different damage functions to determine their influence on the numerical stability of the tangent modulus tensor at the transition point between the undamaged and damaged states. In this research, the material Jacobian has been obtained by incrementally perturbing the deformation gradient tensor and performing a forward difference of the associated Kirchhoff stresses, following the method demonstrated in (Miehe 1996; Sun et al. 2008) which produces a concise mathematical formulation of the tangent modulus. Using this technique, we did not encounter any convergence issues.

To-date, CDM has been extensively used to capture the mechanical behaviour of biological soft tissues, although one of the main limitations associated with this approach is calibrating the material parameters. In order to minimize the effect of the number of material parameters, in this research, only two material parameters for elastin fibres ($\gamma_{\infty_{ef}}, \beta_{s_{ef}}$) and two material parameters for collagen fibres ($\gamma_{\infty_{cf}}, \beta_{s_{cf}}$) have been employed in the constitutive model to control the damage accumulation in the arterial tissue. These material parameters are associated with two internal variables for both elastin and collagen fibres and evolve according to fictitious strain invariants as defined in Equation (7). In this study, stretch in elastin and collagen fibres was used as the main metric to define the pre- and post-damage states of the

fibres. The results of a sensitivity analysis, with regards to the threshold of stretch used for damage accumulation in collagen and elastin, show that selecting lower stretches as the damage thresholds for elastin and collagen fibres leads to increased accumulation of damage in the specimens and consequently a higher level of softening in the tissue. Further experimental studies are required to determine the values of these damage thresholds in elastin and collagen fibres.

A two-step optimization method has been employed to characterize the material parameters which have been used in the constitutive model for intact and digested samples. In the first step of the minimization a large number of random material parameters have been examined using a multi-objective genetic algorithm-based optimization method to simultaneously minimize the sum of the square difference in stresses in the axial and circumferential directions from experiments and simulations. The results of the first step of the optimization have then been used as the first estimation for the local optimization method. This approach can be particularly useful when there is no clear first estimation of the material properties in the constitutive model.

Although this proposed two-constituent damage model can successfully capture all the passive damage relevant phenomena in the arterial tissue, as shown in the preceding sections, some limitations still need to be addressed. Although the experimental tests in this study were performed on arterial samples of intima and media layers together, the contribution of the intima in supporting the loads have been neglected as the pigs were healthy and very young at the time they were slaughtered. For further information on the effect of age and disease on the stiffening of the intimal layer of arterial tissue and intimal thickening the reader is referred to, for example, (Holzapfel 2008). The proposed damage model does not relate the softening in the tissue with the viscoelastic response of the arterial tissue. The viscoelastic behaviour of soft tissue has been explored experimentally in studies such as (Alastrue et al. 2008; Armentano et al. 2006). Pena et al. (2010) also demonstrates a model to capture viscoelasticity and softening behaviour of biological soft tissue, although other damage relevant phenomena such as permanent set and hysteresis were not investigated in that research. Although this damage model has been simultaneously calibrated for strips in the axial and circumferential directions, multiaxial mechanical tests would more accurately describe the mechanical behaviour of soft tissues (Holzapfel and Ogden 2009; Sommer et al. 2010).

Despite these limitations the proposed model can accurately capture all of the passive damage relevant phenomena in arterial tissue, namely, Mullin's effect, hysteresis, permanent set up to the level of rupture in the tissue. The proposed constitutive model is the only damage model

that has been fit to cyclic mechanical tests at high strain levels on intact and collagenase digested samples that incorporates softening and permanent set. Such material models provide a means to better understand the mechanical response of arterial tissue under different loading conditions, such as the risk of atherosclerotic plaque rupture as a result of arterial tissue damage. Investigating the damage relevant phenomena in arterial tissue is also important since they can be linked to arterial growth and remodelling responses where supra-physiological loading conditions are imposed; including stiffening of arterial walls following interventional procedures such as stenting and balloon angioplasty.

Chapter 4 Re-orientation of collagen fibres in the healthy and diseased carotid arteries

4.1 Introduction

Atherosclerotic plaque rupture in carotid arteries can lead to stroke which is one of the leading causes of death worldwide (Benjamin et al. 2017). Development of atherosclerotic plaque alters the mechanical properties of the healthy tissue (Holzapfel et al. 2000). Healthy arterial tissue continuously adapts to mechanical loads by remodelling their internal structure (Driessen et al. 2008). Remodelling is a complex process which occurs in biological tissue in response to alterations in mechanical, chemical or biological environment (Aparício et al. 2016; Rouillard and Holmes 2012). Gibbons and Dzau (1994) described the remodelling process as the ability of the tissue to make the following alterations (i) cell growth, (ii) cell death, (iii) cell migration and (iv) production or degradation of extracellular matrix such as elastin and collagen fibres. Re-orientation of collagen fibres is the other important part of the remodelling process (Baaijens et al. 2010).

Collagen fibres are the main load bearing constituent in the arteries and many other soft biological tissues (Baaijens et al. 2010; Hariton et al. 2006), see also section 2.3 of this thesis. The important role of collagen fibres in bearing the physiological loads is emphasised in studies such as (Sommer et al. 2010). The influence of the collagen fibres in the response of arteries to supra-physiological loads is discussed in studies such as (Ghasemi et al. 2018; Schriefl et al. 2015b; Weisbecker et al. 2013). Collagen fibre directions evolve *in vivo* to maximize the load bearing capacity of the tissue. Principal stresses and strains are the most commonly used mechanical stimuli to determine the optimum fibre directions (Baaijens et al. 2010; Fausten et al. 2016). For further information on the role of collagen fibres in the mechanical properties of the arterial tissue the reader is referred to section 2.3 and 2.4 of this thesis. For further information on the re-orientation of collagen fibres and the constitutive models to capture the re-orientation of fibres in arteries the reader is referred to sections 2.4 and 2.6.4, respectively.

Recently, there has been investigations about the stiffness and strain levels of the vulnerable plaques in the atherosclerotic carotid arteries, using imaging techniques such as ultrasound elastography (Huang et al. 2016; Zhang et al. 2015) . The results of these studies show that

plaques with higher grades of vulnerability are softer and consequently experience higher strain levels. However, these studies do not provide any further insights into the influence of the remodelling of collagen fibres on the vulnerability of the atherosclerotic plaques in the arterial wall.

Creane et al. (2011b) proposed a remodelling metric which demonstrates the mean rotational effort required for one family of collagen fibres to re-orient into another distribution using the concept of adaptation of the earth mover's distance. It was shown that the proposed remodelling metric had higher values in the geometries obtained from symptomatic patients indicating that more effort was required for fibres in these arteries to reach their optimum configuration in comparison with arteries obtained from asymptomatic patients. Although the proposed remodelling metric was able to successfully distinguish the symptomatic and asymptomatic patients, it couldn't provide enough insights into alterations in the mechanical behaviour of the plaque tissue during the re-orientation process or how remodelling of fibres can reduce the risk of plaque rupture, given that fibres were limited to the healthy arterial tissue.

In this study a local stress modulated re-orientation algorithm is proposed to explain the mechanical response of the tissue to the re-orientation of collagen fibres. This stress driven re-orientation algorithm is then used to predict the optimum distribution of fibres in healthy and diseased human carotid bifurcations obtained using Magnetic Resonance Imaging (MRI) from healthy volunteers and symptomatic patients who were undergoing endarterectomy surgery, respectively. Healthy geometries were segmented into two layers: media and adventitia. Diseased geometries were composed of four components: adventitia, media, plaque atheroma and lipid pool (when observed in the MRI images). A novel meshing technique for hexahedral meshing of these geometries was also developed.

Having observed the influence of the presence of collagen fibres in the response of the arterial tissue to physiological and supra-physiological loads and considering the evolution of the internal variables in the proposed CDM model in Chapter 3 of this thesis, (Ghasemi et al. 2018), in the next step of this study, a CDM based novel remodelling metric (RM) is developed to characterise the lack of remodelling in the diseased arterial tissue in terms of lack of re-orientation to the optimum fibre distribution in the plaque atheroma. The motivation behind such an idea was to correlate the stiffness of arterial tissue to the distribution of collagen fibres within the arterial wall. Arterial tissue should have its optimum stiffness where collagen fibres are aligned with an optimum configuration measured according to the ratio of maximum and intermediate Cauchy stresses (Fausten et al. 2016; Hariton et al. 2006). However, the further away collagen fibres are from this optimum configuration, the more the

stiffness of the tissue is reduced and this could result in higher strain levels which increases the risk of atherosclerotic plaque rupture (Huang et al. 2016; Zhang et al. 2015). To assess the functionality of this metric three different scenarios were postulated where fibres in the plaque atheroma were assumed to be: (i) parallel to the maximum principal stresses, (ii) at 45 degrees with respect to the direction of the maximum principal stresses and **(iii)** parallel to the direction of the intermediate principal stresses. In each case fibres were re-orientated toward the optimum fibre distribution. Using CDM, the internal variables which were associated with the remodelling metric could evolve as re-orientation of fibres occurred towards the optimum fibre configuration.

The values obtained for this remodelling metric showed larger values for the cases when fibres were further away from their optimum configuration (parallel to the intermediate principal stresses) indicating that there is a greater lack of remodelling in these cases in the arterial wall and plaques. This lack of remodelling results in a weaker arterial wall that could increase the risk of atherosclerotic plaque rupture. This remodelling metric can be used to quantitatively link the vulnerability of atherosclerotic plaques to the spatial configuration of collagen fibres in the tissue. Such valuable information enhances the assessment of the risk of plaque rupture in the asymptomatic and symptomatic patients by investigating the distribution of collagen fibres in the arterial tissue.

4.2 Material and Methods

4.2.1 Imaging Protocol

In vivo MRI scans of the carotid arteries were obtained from five patients under evaluation for a carotid endarterectomy procedure. A 3T whole body MRI scan (Achieva, Phillips Medical Systems, Best, Netherlands) combined with an 8-channel dedicated bilateral carotid artery coil (Shanghai Chenguang Medical Technologies, Shanghai, China) were used. The imaging parameters used for the creation of the geometries are given in Table 4.1 with the field of view (FOV) cantered on the regions of bifurcation (Johnston et al. 2018b). The scanning of patients took place at the Advanced Center of Medical Imaging (CAMI) in St. James Hospital in Dublin while the scanning of volunteers took place in the Trinity Centre for Neuroscience (TCIN). Ethical approval was obtained for the scanning of volunteers and patients by the relevant regulatory bodies.

Table 4-1. *Scanning parameters used for the reconstruction of arteries*

Acquisition parameters	*T1W 2D*	*T2W 2D*	*T2W_TSE 2D*	*TOF 3D*
Resolution (mm)	0.5 x 0.5	0.5 x 0.5	0.5 x 0.5	0.5 x 0.5
Repetition Time (TR) (ms)	984	3000	2 R-R Intervals	25
Echo Time (TE) (ms)	11	38	38	3
Slice thickness	3	3	3	3
Number of slices	8	8	8	48
Number of echoes	0	0	12	0

4.2.2 Segmentation Protocol

In healthy geometries, arterial walls were manually segmented from T2 weighted images using Simpleware ScanIP (Synopsys, Inc., Mountain View, USA). The dataset was initially cropped to the region of interest and the vessel wall was delineated from T2 weighted Images (Johnston et al. 2018a). This incorporated the variability in the wall thickness seen throughout the vessel wall as emphasised in (Delfino et al. 1997).

To obtain the required information about the plaque components in the vessel wall, multiple image contrasts were used. Iso-intense to hyper-intense areas on T1W images with varying intensity on T2W and TOF images were considered to correspond to the lipid rich necrotic core (LRNC) similar to the methods used in (Cai et al. 2005; Saam et al. 2005; Smits et al. 2016) Furthermore, T2-TSE sequence was used to isolate the plaque components (Biasiolli et al. 2013; Chai et al. 2017). This was due to the different relaxation times attributed to each component. The register background tool in Simpleware was used to segment the regions that correspond to the lipid core, plaque and the vessel wall (Johnston et al. 2018a).

4.2.3 Geometry Preparation

4.2.3.1 Idealized geometry

To investigate the influence of the re-orientation of fibres toward their optimum distribution on the mechanical behaviour of the tissue, one FE simulation was initially performed where the arterial wall was modelled as a quarter of a full cylinder with one element thickness of 0.1 mm. The thickness of the media and adventitial layers were assumed to be 0.7 and 0.4 mm, respectively (Sommer et al. 2010). The vessel wall was subjected to 16 kPa to present the physiological blood pressure. The response of the arterial tissue to the re-orientation of collagen fibres was studied at three different levels of axial strains: 0,5 and 10 %.

4.2.3.2 Healthy and diseased carotid bifurcations

The segmented geometries needed to be smoothed further to avoid the sharp edges in the reconstructed artery. This was especially important at the location of bifurcations, where an un-smoothed geometry could result in sharp elements that cause numerical convergence issues. Using ANSYS Spaceclaim (ANSYS Inc, USA), curves extracted from the boundaries of different components of the vessel wall such as lumen, plaque components and outermost surface of the vessel walls by obtaining the cross section of the geometry sectioned using a series of parallel planes, see Figure 4.1 . These curves were then connected to construct the inner and outer surfaces of the arterial wall and plaque components. The geometry was stitched together to ensure there were no gaps between component interfaces in the next step. The blend function was then applied to connect the inner and outer vessel wall and ensures a water tight geometry. This process is illustrated in Figure 4.1. These smoothed surfaces were then saved as STL meshes to export to a FE pre-processor.

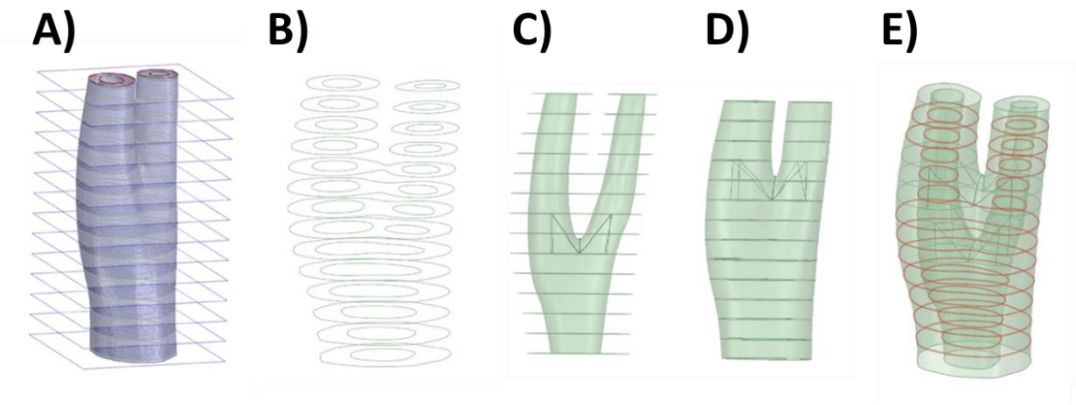

Figure 4.1. *Geometry preparation steps. Sectioning the geometry and extraction of the curves part (A) and (B), respectively. C) Skin the inner surface, D) Skin the outer surface, E) Stitching the geometry surfaces where required (red curve).*

4.2.4 Hexahedral meshing of bifurcations and plaques

To perform an accurate FEA, producing a high quality mesh is an essential primary step. However, producing such structured meshes are reported as a major limitation when it comes to analysing complex 3-D arterial geometries particularly at the location of bifurcations (Creane et al. 2010a; De Santis et al. 2011a). Development of a meshing protocol to accommodate the structured hexahedral meshes for 3-D real arterial geometries is a difficult task for most commercial FE packages (Creane et al. 2010a). There are a few studies dealing with producing high quality meshes from real arterial geometries in the literature as (Creane et al. 2010a; De Santis et al. 2011a; Ghaffari et al. 2015; Tarjuelo-Gutierrez et al. 2014; Zhang et al. 2007). However, most of these studies often considered luminal blood flow as the main 3D geometry and assigned uniform wall thickness for the vessel wall to capture the geometry of the vessel wall. In this study, we introduce a novel meshing technique by incorporating both

inner and out layers of the arterial wall. Figure 4.2, presents a schematic of different steps of our meshing protocol.

The STL meshes, constructed from smoothed geometries as describes in section 4.2.3, hex meshed using ANSA (v17.0, BETA CAE Systems, Thessaloniki, Greece). Appling the Hexa Block module, the volume of the artery was defined initially in form of a box. This box was then split into independent boxes defining the three sections of carotid artery: common carotid artery and internal and external branches of the carotid artery. These boxes converged at the apex of the bifurcation, See Figure 4.2 (A). The perimeters of each box were assigned to the outer wall of the geometry using the Project to Surfaces tool in the second step of meshing, See Figure 4.2 (B). To include the inner wall, the O-Grid function was used where the inner perimeters of the boxes were assigned to the interior wall, see Figure 4.2 (C). The Pure-Hexa function then was applied to generate hexahedral structure mesh in between the inner and outer geometries with the desired density. It is worth mentioning that a uniform thickness of the adventitial layer was considered in both healthy and diseased geometries which was incorporated in the meshing protocol by seeding the elements radially (The thickness of the outermost layer of elements in vessel wall). Figure 4.2 (D) present the final mesh generated from a carotid bifurcation of a healthy voluntee

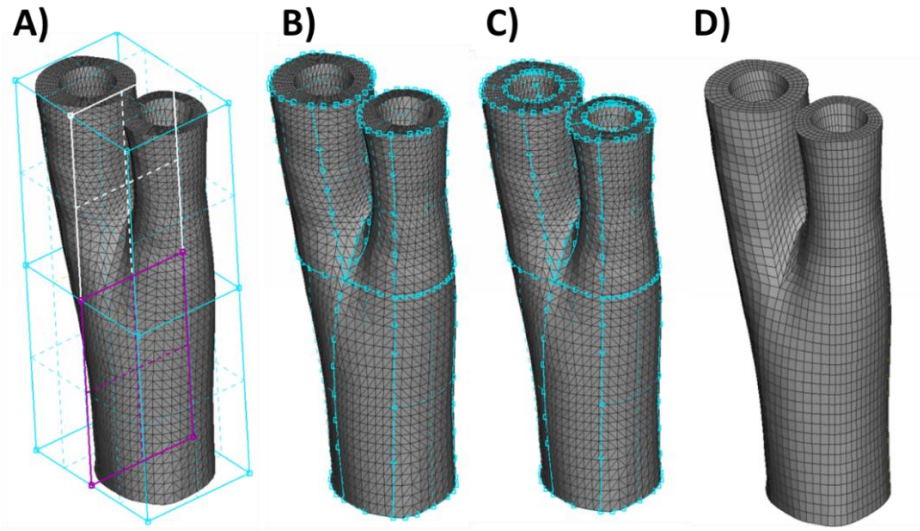

Figure 4.2. *The Sequence of generating structured hexahedral mesh from a human carotid bifurcation. A) The STL mesh and definition of the boxes indicating the common, internal and external carotid artery. B) Associating the boxes to outermost surface of the STL mesh. C) Using the O-Grid function to define the luminal surface. D) Final meshed geometry.*

Figure 4.3. depicts different stages of the meshing protocol applied on a geometry obtained from a patient who was under evaluation for an endarterectomy surgery.

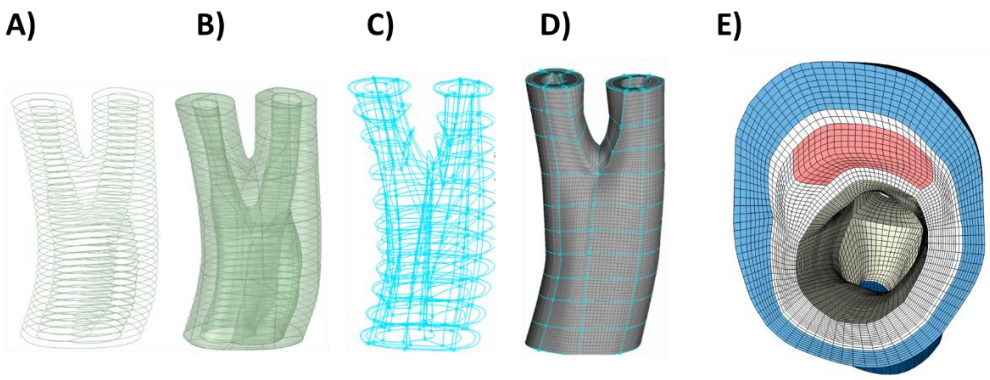

Figure 4.3. *Different stages for meshing a diseased carotid with plaque atheroma and lipid pool. A) Counters of different components of the arterial wall. B) Constructing and smoothing the inner and outer surfaces. C) The connectivity of the boxes associated with each component of the vessel wall. D) Hexahedral meshing the boxes. E) A cross section of the common carotid artery indicating the components the vessel wall and quality of the mesh at the apex of the bifurcation.*

4.2.5 Constitutive equations

In this study the anisotropic hyperelastic constitutive model, proposed in (Gasser et al. 2006) was used to capture the mechanical behaviour of the healthy and diseased arteria wall in the heathy and diseased arteries. This constitutive model captures the mechanical behaviour of the soft tissue by additively decomposing the response of the tissue into its components. The response of non-collagenous tissue was captured using the neo-Hookean material model (ψ_{vol}+ ψ_{iso}) using Equation (3.9) and (3.10). The response of the collagenous tissue was captured by postulating two symmetric families of collagen fibres, ψ_{cf} , see Equation 3.12. This SEF along with all the parameters are described in the section 3.4.2. The overall response of the tissue then was characterised as follows;

$$\psi = \psi_{vol} + \psi_{iso} + \psi_{cf} \tag{4.1}$$

The Cauchy stress tensor then can be defined as follows;

$$\boldsymbol{\sigma} = \frac{2}{J}\mathbf{F}\frac{\partial \psi}{\partial \mathbf{C}}\mathbf{F}^{T} \tag{4.2}$$

4.2.6 Re-orientation algorithm

Collagen fibre directions evolve *in vivo* to maximize the load bearing capacity of the tissue. Following Hariton et al. (2006) and Fausten et al. (2016), it was assumed that fibres are located in the plane made by the eigenvectors of two largest principal Cauchy stresses σ_1 and σ_2. The spectral decomposition of this stress tensor can be written as follows;

$$\sigma = \sigma_1 \vec{e}_1 \otimes \vec{e}_1 + \sigma_2 \vec{e}_2 \otimes \vec{e}_2 + \sigma_3 \vec{e}_3 \otimes \vec{e}_3 \tag{4.3}$$

where $\sigma_1 \geq \sigma_2 \geq \sigma_3$. In the first step of this re-orientation algorithm, the influence of collagen fibres on the response of the tissue was neglected. The stress values, in this step, were

calculated using a neo-Hookean material model. This assumption was also made in other re-orientation algorithms such as (Creane et al. 2011a; Driessen et al. 2008; Hariton et al. 2006)- just to name a few. One motivation behind such an assumption is that the anisotropic behaviour of soft tissue develops as a result of tissue remodelling and adaptation to mechanical loads and the mechanical behaviour of the tissue at neonatal stage is isotropic (Driessen et al. 2003a; Driessen et al. 2005b; Hariton 2006; Kuhl et al. 2005).

The ratio between the magnitude of the two largest principal stresses was used to define the angle of alignment of fibres with respect to the direction of the maximum principal stress, as follows;

$$tan(\alpha) = \sigma_2/\sigma_1 \tag{4.4}$$

Using this equation, two unit vectors defining the optimum directions of two families of collagen fibres in the spatial configuration were obtained as follows;

$$\overrightarrow{\boldsymbol{m_{4op}}} = \cos(\alpha)\,\vec{e}_1 + \sin(\alpha)\,\vec{e}_2 \tag{4.5}$$

$$\overrightarrow{\boldsymbol{m_{6op}}} = \cos(\alpha)\,\vec{e}_1 - \sin(\alpha)\,\vec{e}_2 \tag{4.6}$$

To calculate the stresses in the current configuration, the distribution of fibres in the undeformed configuration needed to be determined. For this purpose, the vectors $\overrightarrow{\boldsymbol{m_{4op}}}$ and $\overrightarrow{\boldsymbol{m_{6op}}}$ were pulled back to the reference configuration as follows;

$$\overrightarrow{\boldsymbol{M_{4op}}} = \frac{\mathbf{F}^{-1}\overrightarrow{\boldsymbol{m_{4op}}}}{\left|\mathbf{F}^{-1}\overrightarrow{\boldsymbol{m_{4op}}}\right|} \tag{4.7}$$

$$\overrightarrow{\boldsymbol{M_{6op}}} = \frac{\mathbf{F}^{-1}\overrightarrow{\boldsymbol{m_{6op}}}}{\left|\mathbf{F}^{-1}\overrightarrow{\boldsymbol{m_{6op}}}\right|} \tag{4.8}$$

In this study, dispersion of fibres was also subjected to remodelling rules. Following Driessen et al. (2008), the ratio of the maximum and intermediate principal stresses was used to define the optimum dispersion of the fibres in the spatial configuration, as follows,

$$b = \frac{\sigma_1}{\sigma_2} - 1 \tag{4.9}$$

where b is the concentration parameter. This parameter can be attributed to the von-Mises periodic distribution function as follows.

$$\rho(\alpha, b) = 4\sqrt{\frac{b}{2\pi}}\exp[bcos(2\alpha) + 1]\,/erfi(\sqrt{2b}) \tag{4.10}$$

The von-Mises distribution function has been widely used to define the distribution of collagen fibres in arterial tissue (Gasser et al. 2006; Holzapfel et al. 2015; Schriefl et al. 2012b). The concentration parameter b was correlated with the dispersion parameter κ, in Equation 3.12 as follows (Gasser et al. 2006);

$$\kappa = \frac{1}{4}\int_{-\pi}^{\pi} \rho(\alpha, b)\sin^3(\alpha) \tag{4.11}$$

Figure 4.4 presents the relationship between the concentration parameter b and the dispersion parameter κ. This relationship was obtained using Equation 4.9. For further information on the von Mises distribution function and the relationship between dispersion and the concentration parameter, the reader is referred to (Gasser et al. 2006).

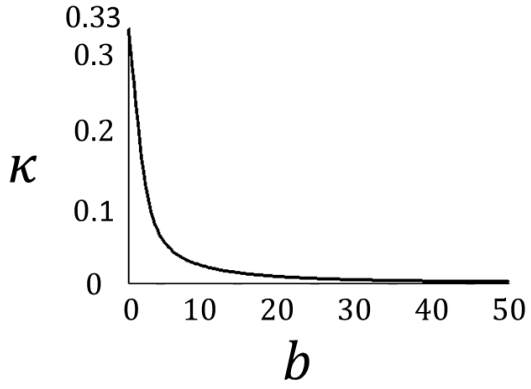

Figure 4.4. *Dispersion- concentration parameter curve obtained from Equation 4.11.*

Using Equations (4.9) to (4.11), the optimum dispersion parameter was calculated in the spatial configuration. Knowing the optimum vectors representing each family of the fibres (Equations 4.5 and 4.6) and the optimum dispersion of fibres, the preferred distribution of fibres in the deformed configuration can be presented using the concept of generalized structure tensors as follows (Gasser et al. 2006);

$$\mathbf{h} = c\mathbf{I} + (1 - 3c)\vec{\boldsymbol{a}}\otimes\vec{\boldsymbol{a}} \tag{4.12}$$

Were $\vec{\boldsymbol{a}}$ is an arbitrary vector presenting one family of fibre and c is the dispersion of fibres. The symmetric second-order tensor $\mathbf{h}$ can be visualised using an ellipsoid where eigenvalues ($v_{max}, v_{mid}, v_{min}$) and eigenvectors ($\vec{\mathbf{v}}_{\mathbf{max}}, \vec{\mathbf{v}}_{\mathbf{mid}}, \vec{\mathbf{v}}_{\mathbf{min}}$) of this tensor represent the direction and eccentricity of the ellipsoid (Curran et al. 2016), see Figure 4.5. In this study, we correlated the dispersion parameter c to the ratio of the two largest eigenvalues (v_{max}/v_{mid}) of the

structure tensor **h**. For this purpose, the dispersion parameter c was calculated at different ratios of ν_{max}/ν_{mid} using Equation 4.12. Then the relationship between the ratio of the two largest principal eigenvalues and dispersion parameter c was calculated by performing curve fitting, Equation 4.13, see Figure 4.5. Doing this, the eccentricity of this ellipsoid was correlated to the dispersion parameter c. It should be mentioned that once the ratio of ν_{max}/ν_{mid} exceeded the magnitude of 20 the distribution of fibres was assumed to be fully anisotropic and c was assumed to be equal to 0.01, this is also demonstrated in Figure 4.5.

$$c = 0.421 * \left(\frac{\nu_{max}}{\nu_{mid}}\right)^{-0.4154} - 0.0717 \tag{4.13}$$

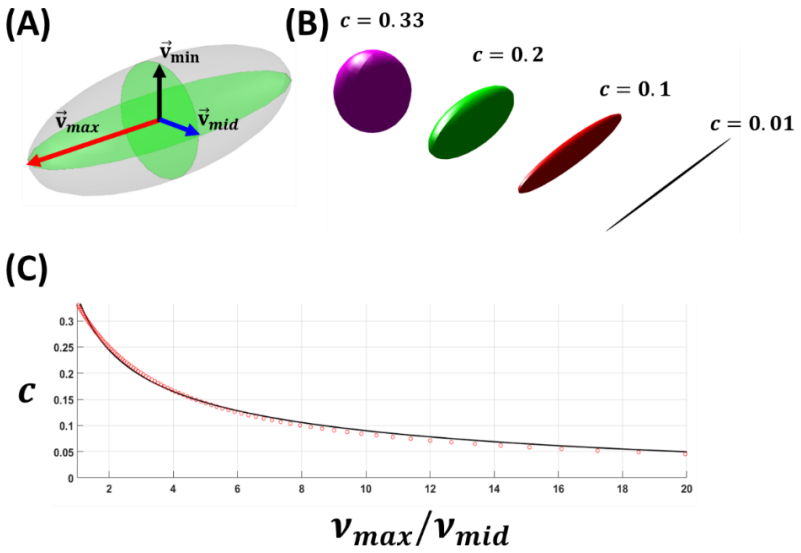

Figure 4.5. *A) A schematic presentation of each family of the collagen fibres in an ellipsoid form using the eigenvalues and eigenvectors of the generalized structure tensor* **h**. *B) A schematic presentation associating the dispersion of the fibres and eccentricity of the ellipsoid. C) The figure relating the ratio of the maximum and intermediate eigenvalues of the generalized structure tensor to dispersion of the fibres.*

To calculate the optimum dispersion of fibres in the undeformed configuration a generalized structure tensor was firstly made in the deformed configuration using both optimum direction and dispersion of fibres. This structure tensor **h** was then pulled back to the undeformed configuration as follows;

$$\mathbf{H} = \mathbf{F}^{-1}\mathbf{h}\mathbf{F}^{-T} \tag{4.14}$$

The spectral decomposition of the tensor **H** was calculated to determine the eigenvalues of the structure tensor **H** in the undeformed configuration. The ratio of the maximum and intermediate eigenvalues in the undeformed configuration was then used to calculate the dispersion of fibres in the undeformed configuration, using Equation 4.12.

Once the optimum direction and dispersion of fibres was calculated, both vectors and dispersion of fibres re-orientated toward this preferred configuration. The vector of fibres was re-orientated incrementally in the undeformed configuration toward its optimum direction by adding a fraction (τ) of the total difference between the optimum direction and initial direction of fibres. This process also established the next initial direction of the fibres for the next re-orientation step, see Figure 4.6. A similar approach was used in (Fausten et al. 2016).

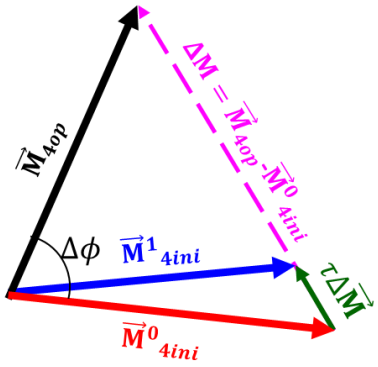

Figure 4.6. *A schematic presentation of the reorientation process. Once the vector presenting the optimum direction of the fibres was calculated ($\vec{M}_{4op}$) a fraction of the total difference between optimum fibre configuration and the initial configuration ($\tau\Delta\vec{M}$) was added to the initial configuration of the fibres ($\vec{M}^0{}_{4ini}$) resulting in the initial configuration for the next iteration of the re-orientation process ($\vec{M}^1{}_{4ini}$). In this figure, $\Delta\phi$ indicates the angle between the optimum fibre direction and initial direction of fibres.*

The dispersion of fibres was re-orientated toward its optimum value using a linear rate equations as follows;

$$\frac{d\kappa}{dt} = \frac{1}{\tau_\kappa}(\Delta\kappa) = \frac{1}{\tau_\kappa}\left(\kappa - \kappa^{ini}\right) \tag{4.15}$$

It is worth mentioning again that both angle and dispersion of collagen fibres were subjected to the remodelling rules in the undeformed configuration. The same approach was used in studies such as Fausten et al. (2016) or Hariton et al. (2007).

4.2.7 Remodelling metric

The stiffness of arterial tissue has been associated with the orientation of fibres in studies such as (Gasser et al. 2006; Holzapfel et al. 2000). In this study, the concept of CDM was employed to correspond the stiffness of the arterial tissue to the distribution of fibres. Arterial tissue is assumed to have its optimum stiffness where collagen fibres are aligned with the predicted optimum configuration of fibres, as mentioned previously, see sections 4.1 and 2.6.4. The lack of orientation from this optimum configuration results in softening and weakening of the tissue. Here, we used two internal variables (γ_{RM} and β_{RM}) to capture the softening that is associated with the lack of orientation of the fibres from their optimum configuration. This

remodelling metric can then be used as a metric for assessing the vulnerability of atherosclerotic plaque in the arterial tissue.

Evolution of the internal variable γ during the re-orientation process ([0,T]) can be written as follows;

$$\gamma_{RM} = \max_{t\in[0,T]} \langle \bar{I}_M^* - \bar{I}_M^{*ini} \rangle \tag{4.16}$$

Where $\bar{I}_M^*$ is a pseudo invariant associated with each family of fibres (**M**) and can be written as follows, as previously mentioned in Equation 3.7;

$$\bar{I}_M^* = \kappa \bar{I}_1 + (1 - 3\kappa)\bar{I}_M \tag{4.17}$$

In Equation (4.15), $\bar{I}_M^{*ini}$ is the value of $\bar{I}_M^*$ defined at the beginning of the re-orientation process. The internal variable β_{RM} can be defined as follows;

$$\beta_{RM} = \langle \tilde{\beta}_{RM} - \tilde{\beta}_{RM}^{ini} \rangle \tag{4.18}$$

Where $\tilde{\beta}_{RM}^{ini}$ is the value of the variable $\tilde{\beta}_{RM}$ at the initial increment of re-orientation step in the arterial tissue. The variable $\tilde{\beta}_{RM}$ can be written as follows;

$$\tilde{\beta}_{RM} = \int_0^T \langle \bar{I}_M^* \rangle ds \tag{4.19}$$

In equations 4.14, 4.16 and 4.18, $\langle(\bullet)\rangle$ are Macaulay brackets filter out the negative values. A similar form for evolution of internal variables was used in studies such as Miehe (1995) , Balzani et al. (2012) and Ghasemi et al. (2018).

These two internal variables were then attributed to a softening function as follows;

$$RM = RM_\infty[1 - \exp(-\frac{\gamma}{\gamma_\infty})]\left[1 - \exp\left(-\frac{\beta}{\beta_s}\right)\right], RM \in [0,1) \tag{4.20}$$

Where, γ_∞ and β_s are material properties. RM_∞ denotes a predefined maximum softening level for this function ($RM_\infty = 0.99$).

4.2.8 Finite Element implementation

This re-orientation algorithm was implemented into the commercial FE package Abaqus (Dassault Systèmes Simulia corporations, Vèlizy-Villacoublay, France). A user subroutine (UMAT) was used to define the behaviour of different components of healthy and diseased arteries where the definition of the Cauchy stress and tangent modulus was required.

The tangent modulus was calculated computationally using a technique introduced by (Miehe 1996) and used in (Ghasemi et al. 2018) and also discussed in sections 3.4.4 of this thesis.

The geometries were segmented into two parts; healthy arterial wall and plaque burden. Healthy vessel wall was composed of the media and adventitia layers and plaque burden was composed of plaque atheroma and lipid pool, where observed in the MRI images. Material properties of each component along with the references they were obtained from are shown in Table 4.2.

Table 4-2. *Material properties used to characterise the mechanical behaviour of the healthy arterial wall and plaque burden in carotid bbbifurcations.*

	C_{10}	k_1	k_2	γ_∞	β_s	
Media	67.28	20.6	18.8	-	-	(Sommer et al. 2010)
Adventitia	37.25	61.2	32.8	-	-	(Sommer et al. 2010)
Plaque atheroma	37.5	2029	25.2	6.52	0.37	(Chai et al. 2015) &(Balzani et al. 2012)
Lipid pool	50.537	-	-	-	-	(Teng et al. 2010b)

Three healthy and five diseased bifurcations were analysed in this study. The analysis was performed in three steps. In the first step, the artery was subjected to axial displacements. The healthy bifurcations were subjected to three different levels of axial strains of 0, 5 and 10%. However, the diseased bifurcations were subjected to 5% axial strain following (Balzani et al. 2012; Huang et al. 2014).

In the second step of this simulation both healthy and diseased bifurcations were subjected to systolic blood pressure of 16 kPa (Paritala et al. 2018). Optimum vector and dispersion of fibres were calculated in the end of this step.

In the third step of this simulation both vector and dispersion of fibres were subjected to remodelling rules. In the healthy arterial wall, in both healthy and diseased bifurcations, collagen fibres were assumed to be at 45^o with respect to the direction of the maximum principal stresses initially. Dispersion of fibres was also assumed to be 0.33 in the first increment of the re-orientation step. To analyse the diseased tissue, three different cases were postulated as the initial configuration of fibres in the plaque tissue, where fibres were located at: (i) parallel to the direction of maximum principal stresses, (ii) at 45 degrees with respect to the direction of maximum principal stresses and (iii) parallel to the direction of the intermediate principal stresses.

4.3 Results

4.3.1 Remodelling in idealised cylindrical artery

Figure 4.7 (A) and (B) present the values of α and κ through an idealized arterial wall thickness as a result of different axial strains and blood pressure of 16 kPa. $\Delta\phi$ and $\Delta\kappa$ during the re-orientation step are shown in Figure 4.7 (C) and (D), respectively. It can be seen that, the case with the lowest axial strain has the largest re-orientation gap from the optimum

distribution of fibres (Larger $\Delta\phi$ and $\Delta\kappa$). It should be noted again that the distribution of fibres in this simulation was assumed to be isotropic initially where fibres were postulated to be at 45^o with respect to the direction of maximum principal stresses and dispersion of fibres was assumed to be 0.33. Figure 4.7 (E) presents the decrease in the maximum principal strain in the healthy arterial wall as a response to the re-orientation of fibres toward the maximum principal stress. It can be seen in this section that the samples with the largest re-orientation gap experience the maximum decrease in the maximum principal strain. This section also indicates the contraction of the vessel wall as a result of the re-orientation of fibres. Figure 4.7 (F) shows the changes in the maximum principal stresses during the re-orientation of fibres toward their preferred distribution. This section indicates that although the maximum principal strain was decreased as a result of the re-orientation of fibres toward the optimum distribution, the principal stress increased as a result of the cooperation of the collagen fibres in bearing the loads. It can also be seen that the sample with the largest re-orientation difference from the optimum configuration experienced the largest increase in the maximum principal stress during the re-orientation process. However, in all of the three cases, the values of maximum principal stress converged to similar stress levels. Figure 4.7 (G) presents the stretch in the samples in the direction of the collagen fibres during the re-orientation process. This section shows that the largest increase in the stretch of fibres during the re-orientation process also occurred in the sample with the largest re-orientation gap. It can also be seen that in all of the three cases stretch in the fibres converged to similar levels, similar to the values obtained for maximum principal stress. Figure 4.7 (H) shows the evolution of pseudo invariant $\bar{I}_M^*$, Equation 4.15, during the re-orientation process. This section also shows that this invariant evolved to larger values in samples with larger $\Delta\Phi$ and $\Delta\kappa$. It should be mentioned that section C to H of Figure 4.7 present data obtained from the centroid of a luminal element while the medial and adventitial layers were meshed to have 8 and 4 elements respectively.

4.3.2 Remodelling in healthy carotid arteries

In the next stage of this study, the distribution of fibres in the healthy carotid bifurcations was investigated. The direction of the maximum principal stresses in 3 different sections of a healthy carotid bifurcation under 5 % axial strain are shown in Figure 4.8. The cross -section made by plan A shows the values obtained for angle and dispersion of fibres in the internal and external branches of this carotid bifurcation. Plane B and C correspond to the apex and common carotid artery. It is worth mentioning again that α represents the angle of fibres with respect to the direction of the maximum principal stress.

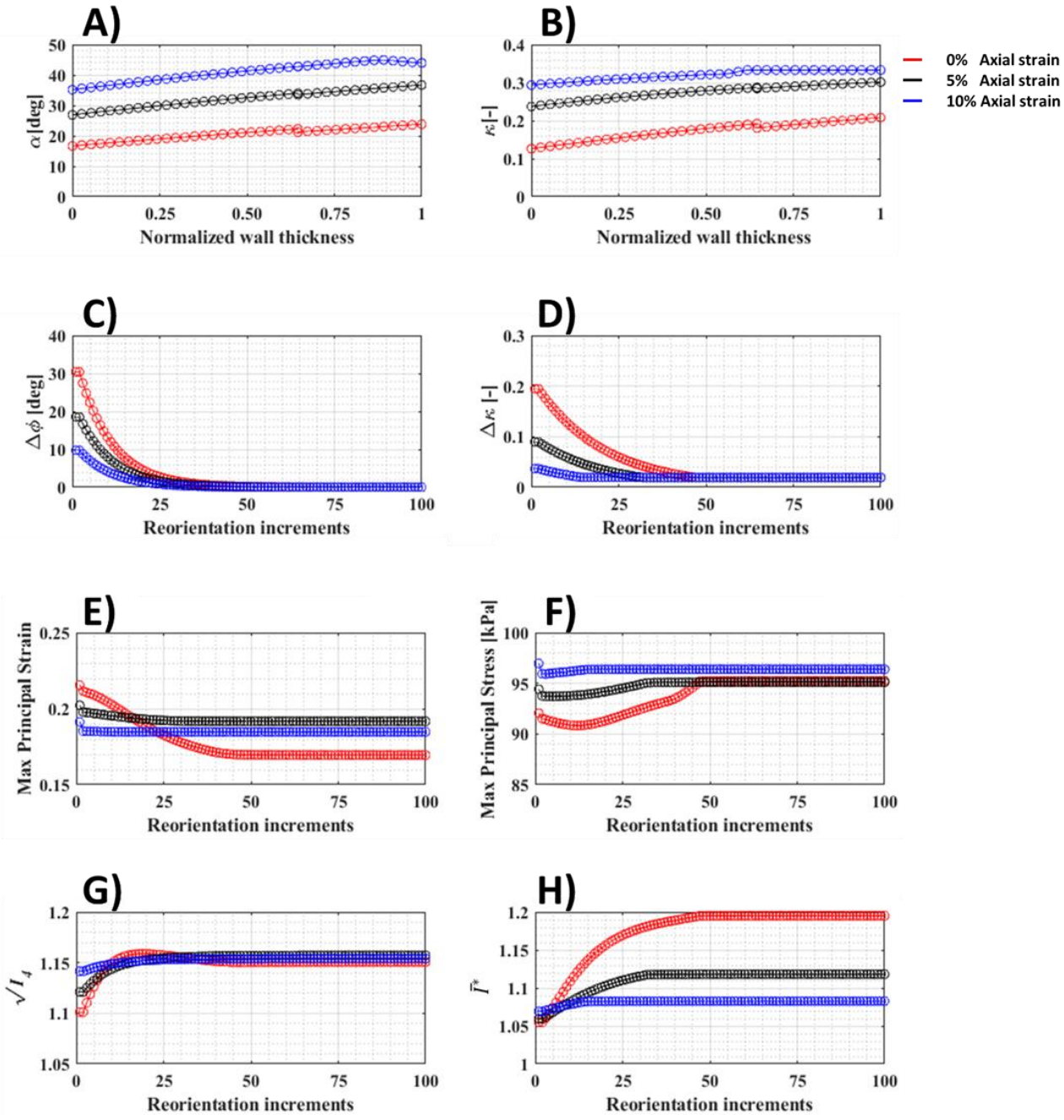

Figure 4.7. *The influence of the reorientation of fibres on the mechanical behaviour of the arterial wall A) Angle of fibres with respect to the direction of the maximum principal stress through the wall thickness. B) Dispersion of the fibres through the normalized arterial wall thickness. Sections D to H presents values obtained from the centroid of the luminal element. C) The difference between the angle of fibres from the optimum direction of collagen fibres in the centroid of the luminal element during the re-orientation step. D) The difference between the dispersion of fibres and the optimum distribution of fibres during the re-orientation step in the centroid of the luminal element. Changes in the maximum principal stress and maximum principal strain during the re-orientation step (E) and (F), respectively. G) Stretch in the sample in the direction of the collagen fibres. H) Evolution of the invariant I^* during the re-orientation step.*

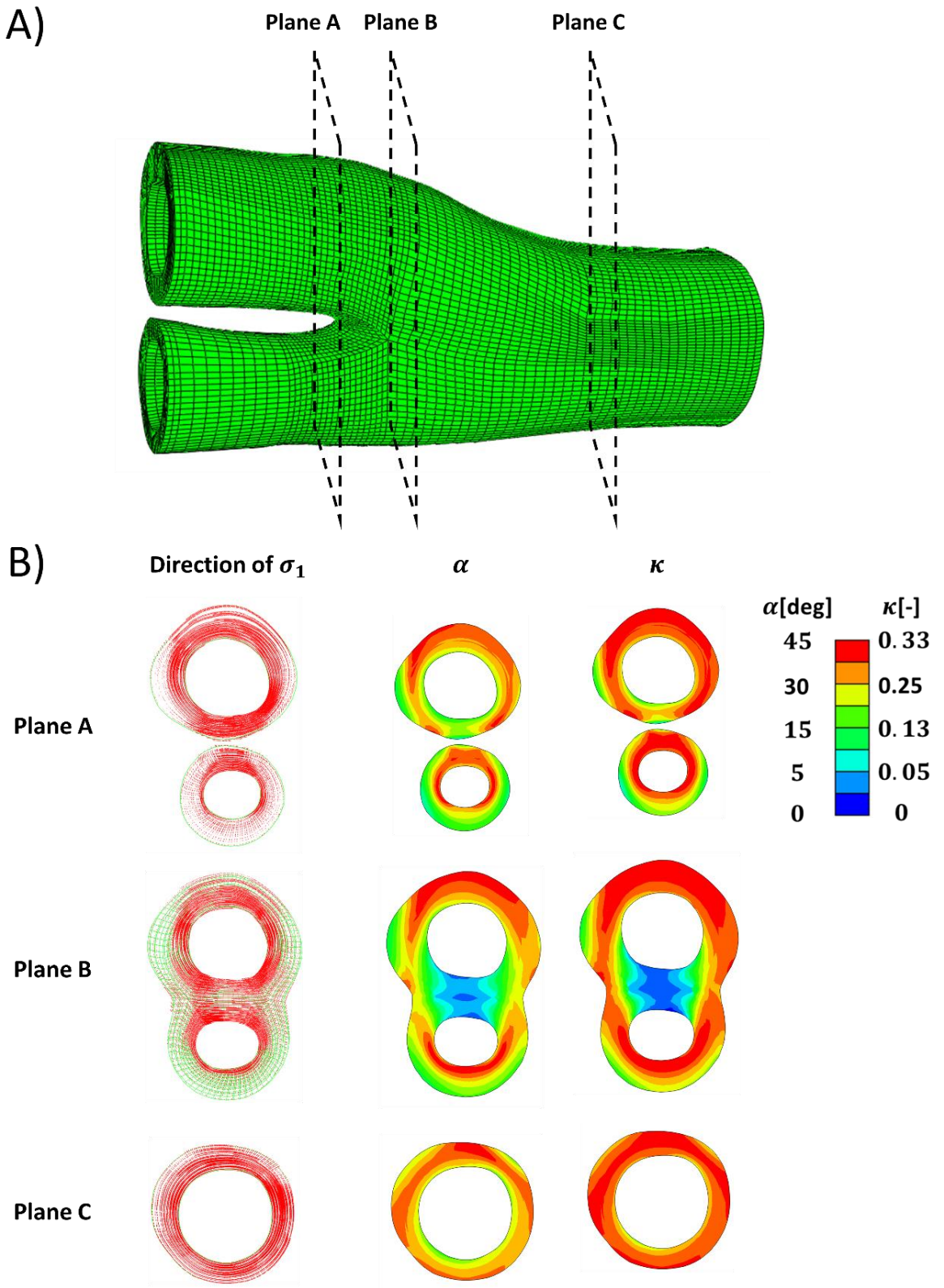

Figure 4.8. *A) A healthy carotid bifurcation cross sectioned using planes A, B and C. B) Presentation of the directions of the maximum and intermediate principal stresses in each cross section along with the angle and dispersion of fibres. The angle of fibres (α) is presented with respect to the direction of the maximum principal stress.*

Figure 4.9 presents geometries of three healthy carotid bifurcations. The predicted angle of fibres with respect to the direction of the maximum principal stress under three different levels of axial strain (ε_z) are shown in sections (I) to (III) for each geometry. The predicted dispersion of fibres in each family of collagen fibres is shown in the second row for each geometry, sections (IV) to (VI). This figure shows that in the absence of axial strain, collagen fibres are mainly predicted to be fully aligned with the direction of the maximum principal stress, with low angles and dispersion values. However, it can be seen that by increasing the axial strain, fibres re-orientate to maximize the load bearing capacity of the tissue in the plane made by directions of σ_1 and σ_2. It can also be observed that the distribution of the fibres remains constant in certain regions of healthy bifurcations although higher levels of axial strain were imposed on these arteries. The apex of the bifurcation in all three healthy geometries under different levels of axial strain exhibit highly aligned collagen fibre distribution. This concentrated distribution of fibres is the result of high values of maximum principal stress compared with the intermediate principal stresses in these regions. One main reason behind such large differences is the high curvature of the lumen at the apex which leads to high stress concentrations at these regions. It can also be observed that under the apex there are regions with highly isotropic distribution of the fibres, regions with $\alpha = 45^o$ and $\kappa = 0.333$. These observations agree with the results of studies such as (Creane et al. 2011a; Hariton et al. 2007).

The highly aligned orientation of the collagen fibres in the samples with no axial strain is shown in Figure 4.10 (A). The influence of the axial strain of 10% on the orientation of the fibres can be seen in Figure 4.10 (B). The highly aligned orientation of the fibres at the location of the apex is indicated in the top views using dashed rectangles.

4.3.3 Remodelling in patient specific diseased carotid arteries

Figure 4.11 presents five diseased bifurcations composed of healthy arterial wall and plaque burden. The healthy arterial wall is composed of the media and adventitia layers. The plaque burden is composed of plaque atheroma and lipid pool (where observed in the MRI images). The angle and dispersion of collagen is predicted in these geometries when the arteries are under 5% axial strain and the blood pressure was 16 kPa.

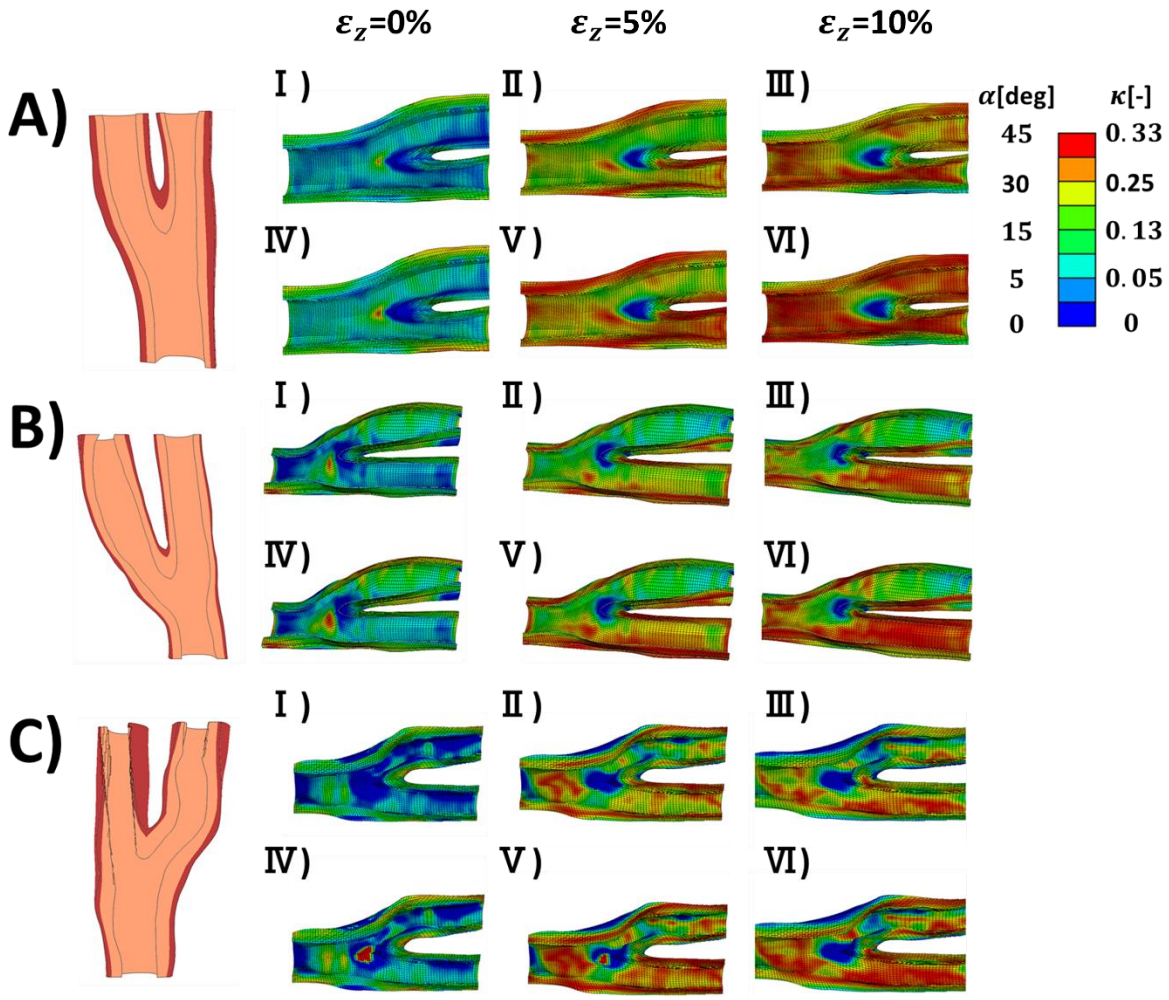

Figure 4.9. *Predicted angle and dispersion of collagen fibres in three healthy bifurcations. The first row for each geometry indicates the angle of fibres and the second row for each geometry indicates dispersion of the fibres.*

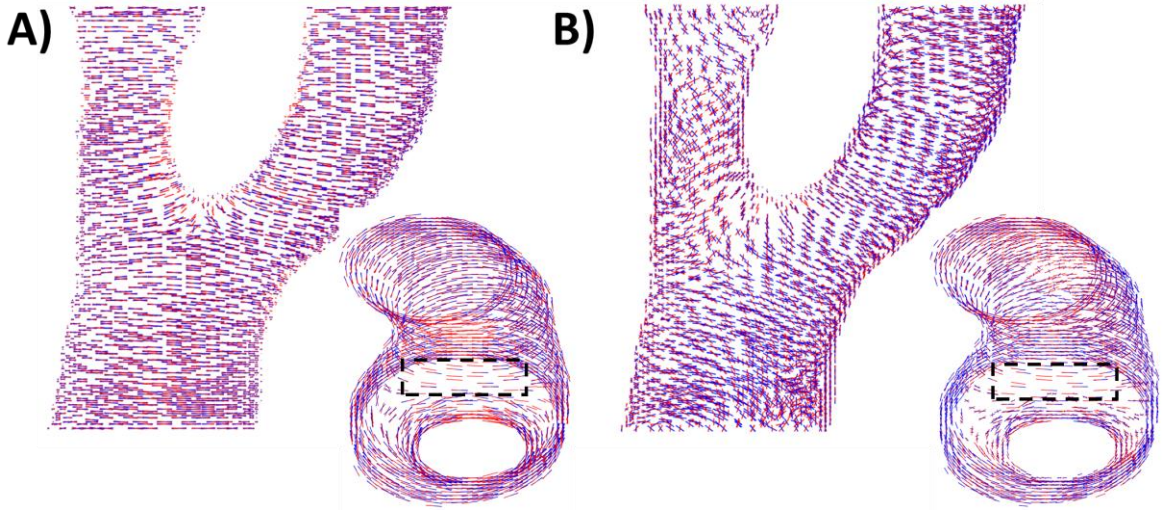

Figure 4.10. *The orientation of the fibres A) without applied axial strain and B) with applied axial strain of 10% under blood pressure of the 16 kPa .*

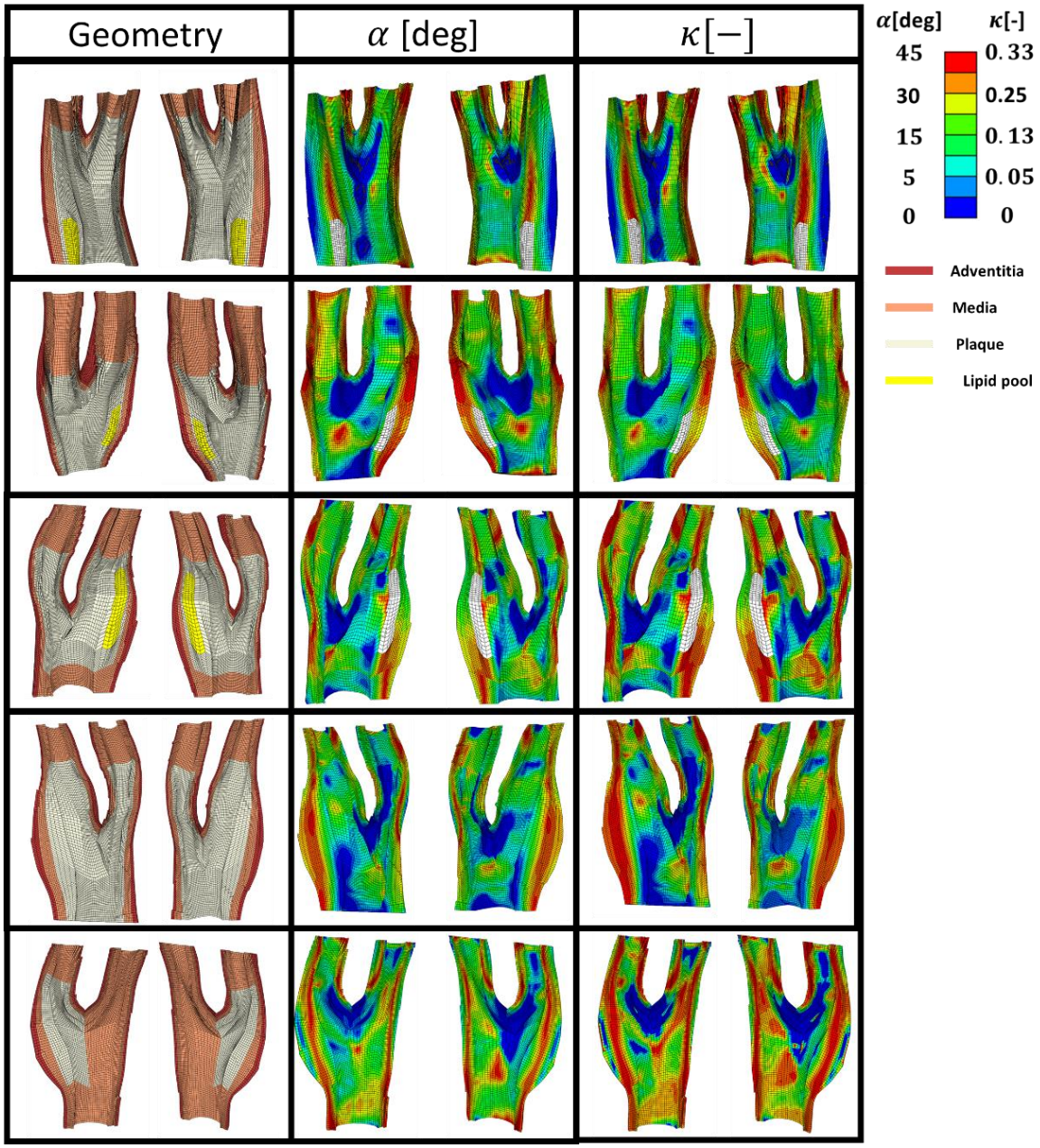

Figure 4.11. *The geometry of the five diseased carotid bifurcations obtained from symptomatic patients consisting of the adventitia and media layers (healthy arterial wall) and plaque burden made of plaque atheroma and lipid pool. The predicted angle of fibres with respect to the direction of the maximum principal stress is shown in the second column. The corresponding dispersion of the fibres in each family of collagen fibres is shown in the third column.*

Figure 4.12 presents the values of angle and dispersion of fibres shown in Figure 4.11 in the cross-sections of the arterial walls where lipid pool was observed in the geometry.

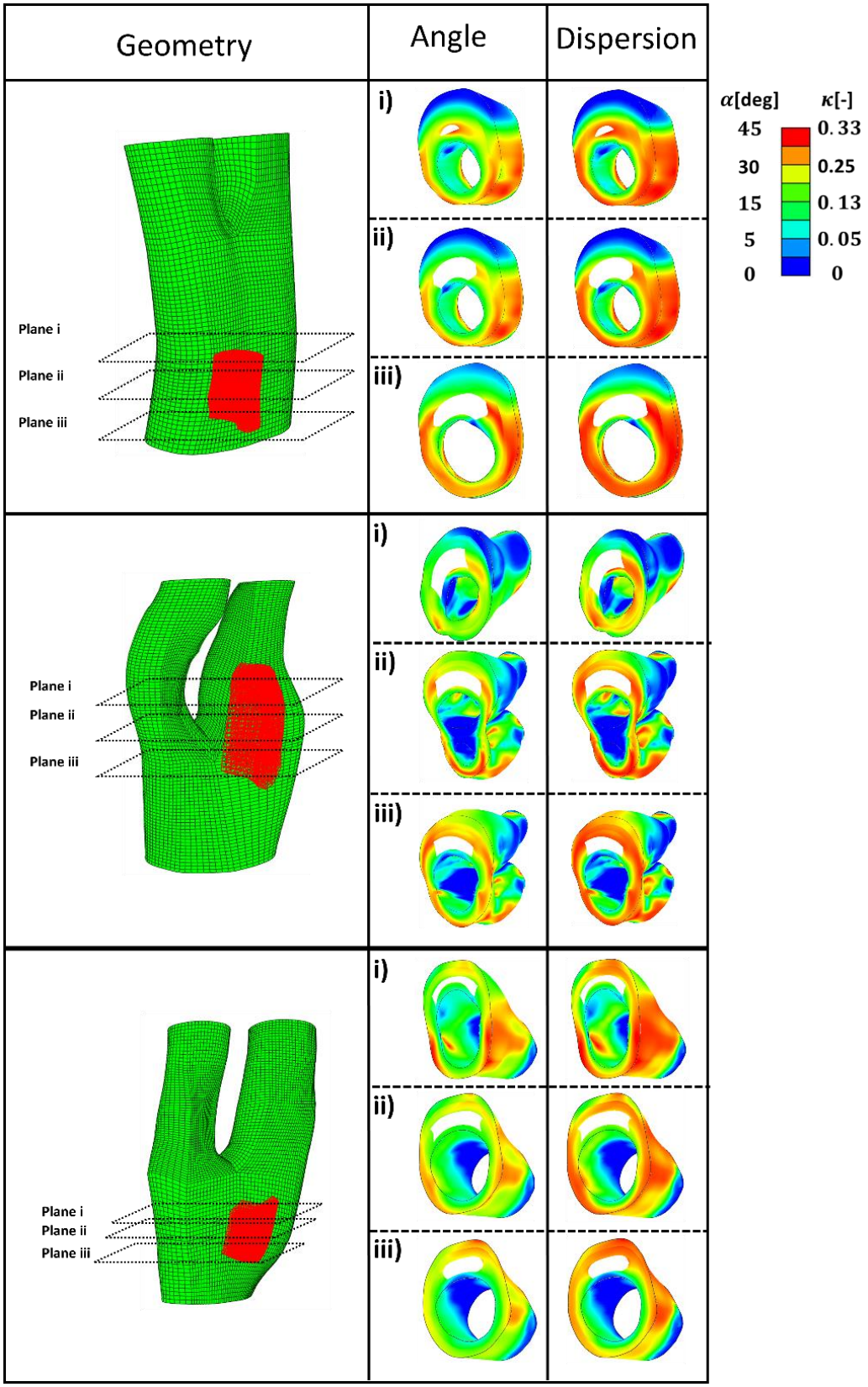

Figure 4.12. *The predicted angle and dispersion of fibres in three cross-sections of diseased bifurcations where lipid pool was observed in the geometry.*

Strain and stress counter plots of diseased geometries before and after re-orientation of collagen fibres toward the optimum fibre distribution are depicted in Figure 4.13, These geometries are ordered similar to Figure 4.11.

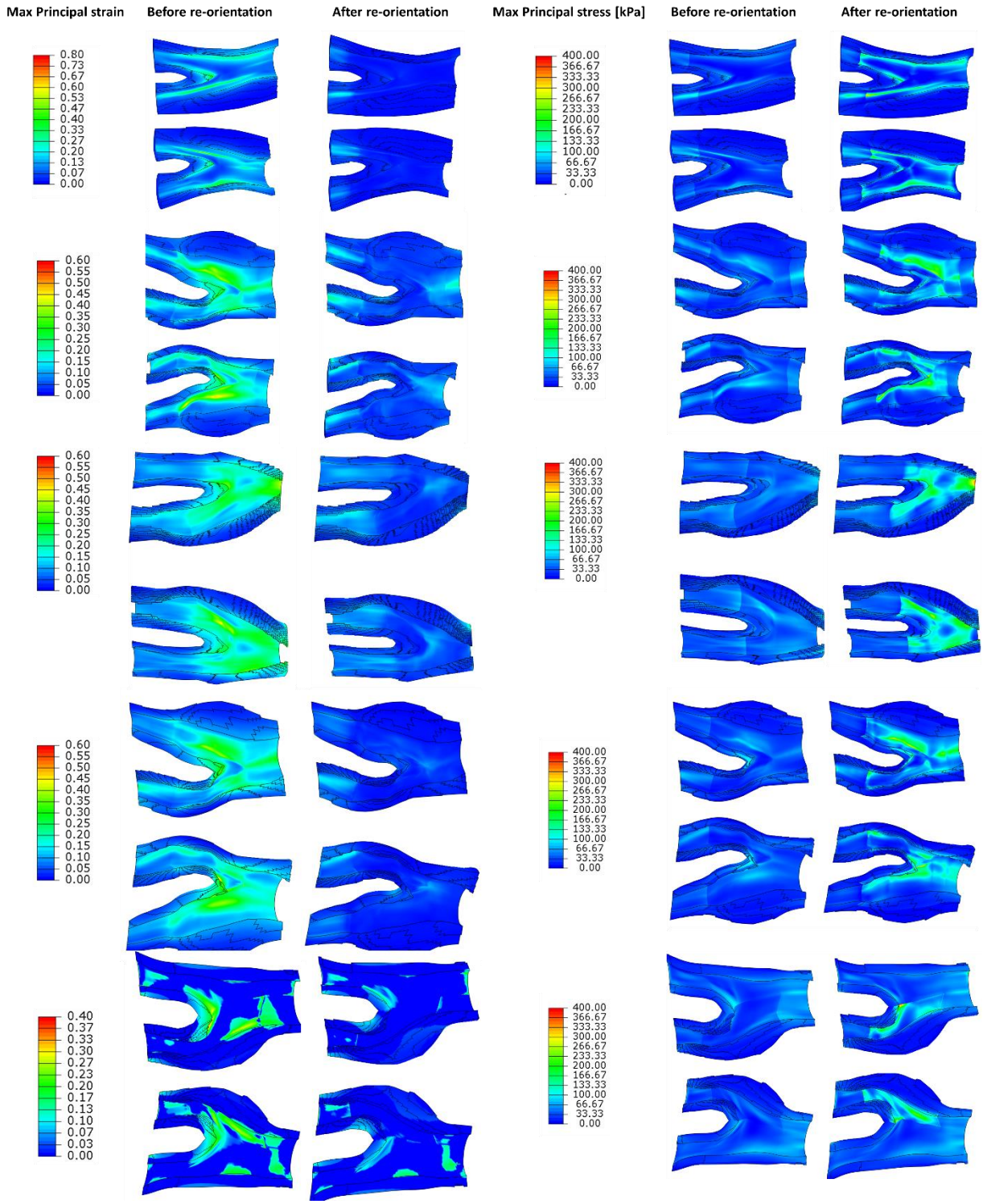

Figure 4.13. *The contour plots of maximum principal strain and stress values obtained before and after re-orientation of collagen fibres in the diseased geometries.*

Figure 4.14 presents the values of the remodelling metric captured during the re-orientation process in the diseased bifurcations by postulating the initial configuration of the fibres to be (i) parallel with the direction of intermediate principal stress (ii) at 45^o with respect to the direction of the maximum principal stress and (iii) parallel to the direction of the maximum principal stress. In each case collagen fibres re-orientated toward the optimum distribution calculated according to the ratio of maximum and intermediate principal stresses. Evolution of the internal variables during the re-orientation process was used as an indicator for the lack of remodelling. It is also assumed that there is no lack of remodelling in the healthy arterial walls. It can be seen from this figure that the remodelling metric has the highest values in case (i) where fibres had the largest re-orientation gap from the optimum distribution.

Figure 4.15, 4.16 and 4.17 present the values obtained for the remodelling metric at three different cross sections of the diseased bifurcations. Figure 4.15 presents the cross sections that corresponds to the bifurcation depicted in the first row of Figure 4.14. The cross-sections from arteries in the second and third rows of Figure 4.14 are shown in Figure 4.15 and 4.16, respectively. It can be seen from these Figures that arteries which correspond to the case (i), where fibres were parallel with the direction of the intermediate principal stress, show highest values for the remodelling metric. This indicates that in these areas there is a higher need for remodelling in term of re-orientation.

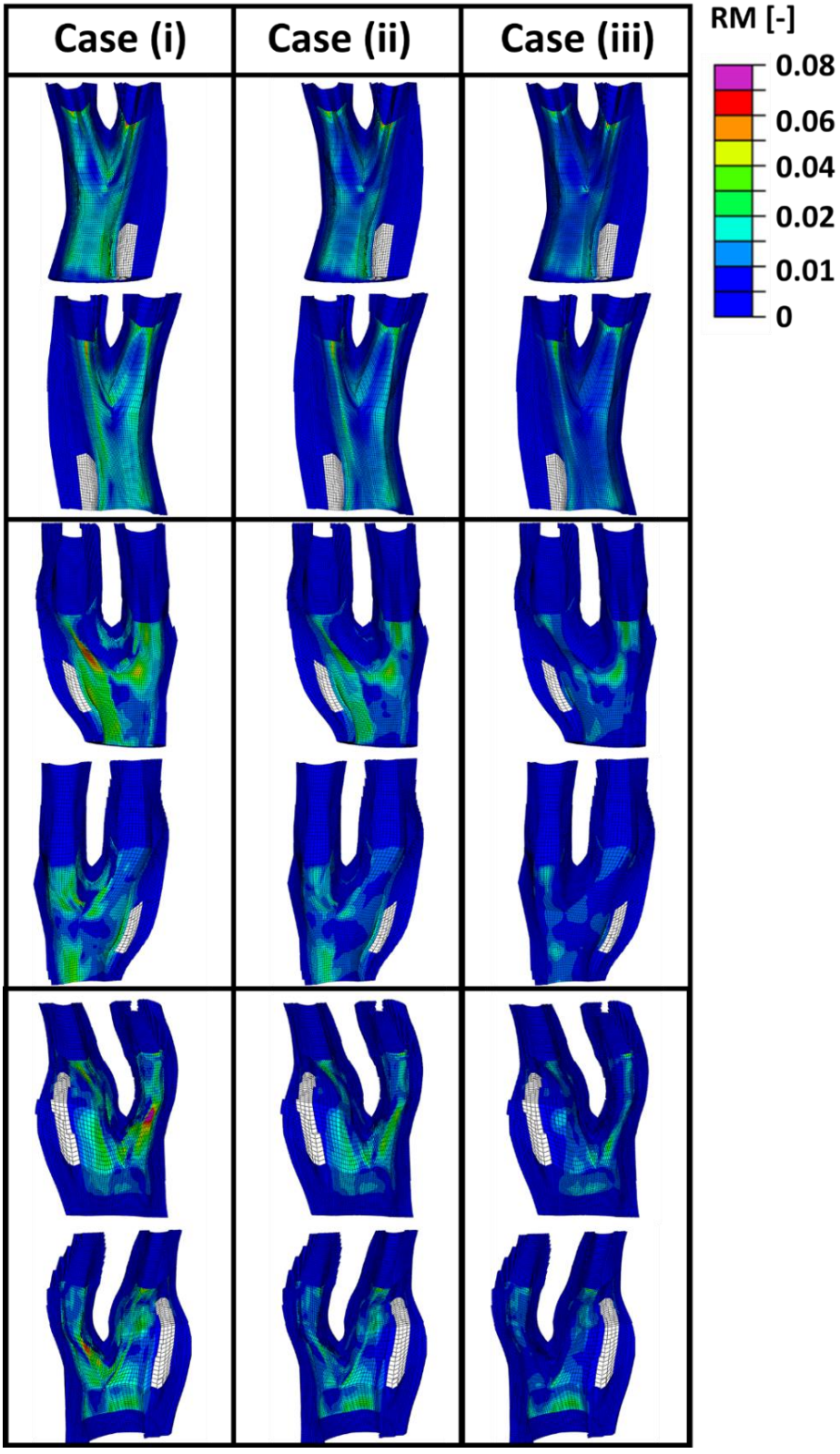

Continued next page

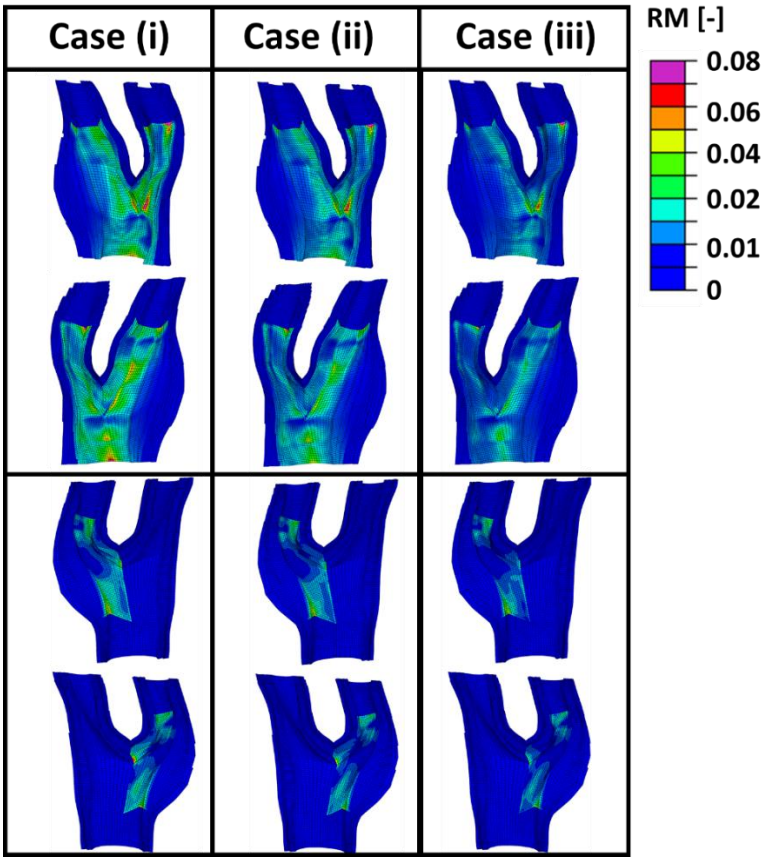

Figure 4.14. *The values obtained for the remodelling metric (RM) during the re-orientation step.*

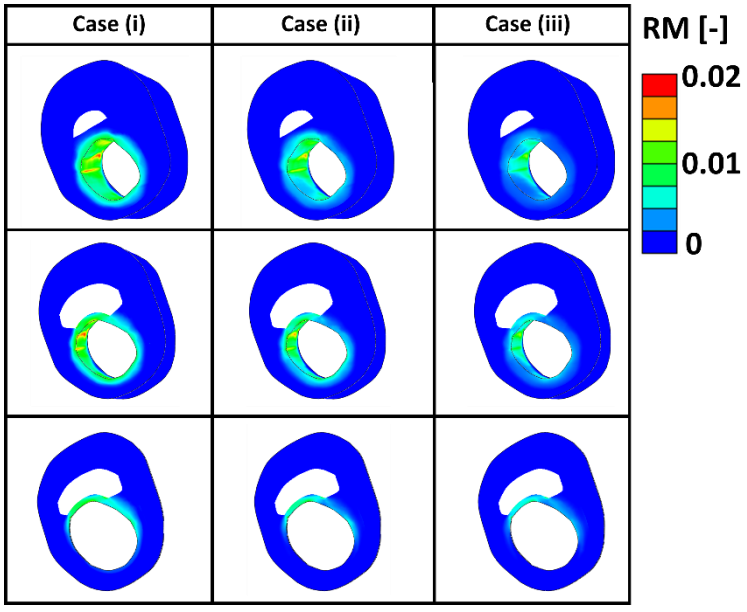

Figure 4.15. *The values of the remodelling metric for the three different cases at cross sections of the diseased bifurcation corresponds to the first row of Figure 4.14.*

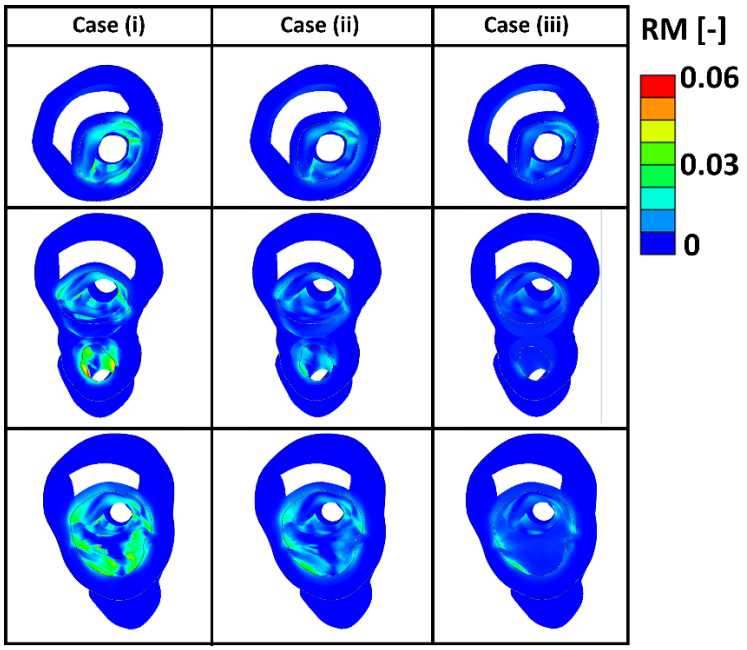

Figure 4.16 *The values of the remodelling metric for the three different cases at cross sections of the diseased bifurcation corresponds to the second row of Figure 4.14.*

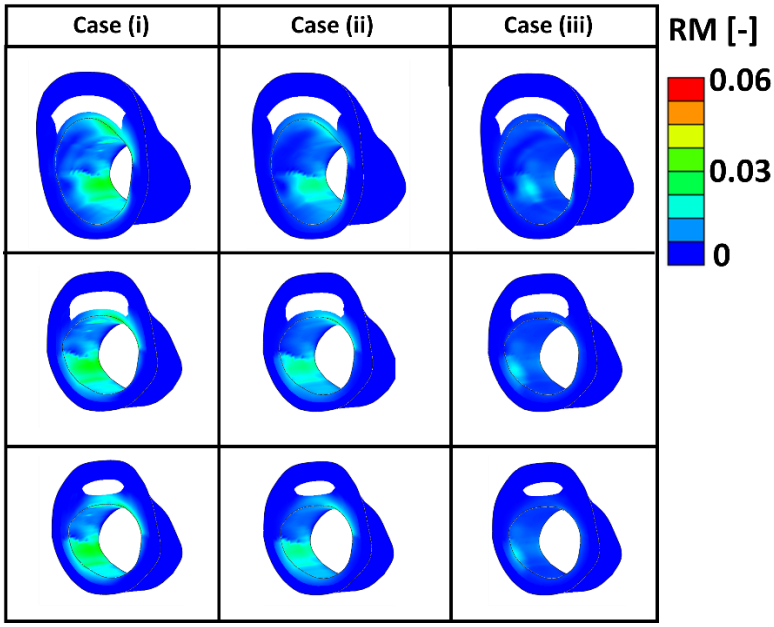

Figure ***4.17.*** *The values of the remodelling metric for the three different cases at cross sections of the diseased bifurcation corresponds to the third row of Figure 4.14.*

4.4 Discussion

Distribution of collagen fibres evolve *in vivo* to maximize the load bearing capacity of the arterial tissue. To-date, many studies suggest different forms of constitutive laws that incorporate the distribution of collagen fibres to capture the mechanical behaviour of the arterial tissue such as stress or strain in both axial and circumferential directions. It is shown in many studies that anisotropic behaviour of the tissue in the circumferential and axial directions is due to the orientation of the collagen fibres. Krasny et al. (2017) showed that in a healthy human carotid artery, circumferential samples are stiffer than diagonal and longitudinal samples by performing uniaxial mechanical tests. In that research, Krasny et al. (2017) demonstrated that collagen fibres in the media layers of carotid arteries are mainly in the circumferential direction in their unloaded configuration. However, collagen fibres in the adventitia layer had an isotropic distribution where they were slightly more aligned toward the axial direction of the artery. This difference in the orientation of the fibres in the media and adventitia layers can be explained by growth and remodelling of fibres during the process of aging. Arteries behave similar to isotropic material models at embryo stages. However, collagen fibres grow and remodel during the life to contribute to bearing the load imposed by blood pressure. As a result, fibres in the media layer grow more in the circumferential directions, the direction of the maximum principal stress, while the distribution of the fibres remains almost isotropic in the adventitial layer. Capturing the orientation of fibres during the uniaxial mechanical tests in the samples made in the circumferential, diagonal and axial directions of the vessel wall, Krasny et al. (2017) showed that collagen fibres in the adventitial layers can re-orient fully toward the direction of the loads in all the samples in the different directions. However, collagen fibres could only re-orient fully toward the direction of maximum load in the samples from the circumferential direction of the medial layer. In diagonal samples, collagen fibres had a reduced capacity to re-orient toward the dominant direction of load and this was further reduced in axial samples.

To capture the re-orientation of the collagen fibres in the arterial tissue, the influence of the re-orientation of the fibres was first demonstrated in a healthy idealized vessel wall, composed of the media and adventitial layers, see Figure 4.7. In this simulation, the fibres were allowed to re-orient toward the optimum configuration from a transversely isotropic distribution, $\alpha = 45$ and $\kappa = 0.33$, toward the optimum fibre distribution calculated from the ratio of the maximum and intermediate principal stresses. Three different scenarios were studied in this initial simulation where the arterial wall was considered to be under 16 kPa of blood pressure and axial stretches of 1,1.05 and 1.1. In all these three cases, the proposed re-orientation algorithm predicted a more aligned distribution of fibres in the inner most layer of the vessel wall, lower angle with respect to the direction of the maximum principal stress and lower

value for the dispersion. It is worth mentioning that in all the cases the maximum principal stresses were in the circumferential direction of the vessel wall except at the outermost layers of the artery when the axial stretch of 1.1 was applied. In this case the direction of the maximum principal stress was in the axial direction of the arterial wall. This variation in the direction of the maximum principal stress is the reason behind the decline in the slope of the curve in the outer layers of the artery at highest axial strain of 10%, see Figure 4.7 (A).

The results of this simulation also demonstrated the important role of the re-orientation of the collagen fibres in preserving the tissue integrity. This can be concluded by observing the contraction of the arterial wall and most notably the decrease in the maximum principal strains which were in the circumferential direction of the vessel wall, during the re-orientation of the collagen fibres toward their optimum distribution, see Figure 4.7 (E). Figure 4.7(E) also shows that the maximum contraction occurred in the case where no axial stretch was imposed in the vessel wall. In this case the maximum principal stresses were in the circumferential direction of the vessel wall and as the axial stress had its minimum values, fibres had to re-orient from an isotropic distribution toward a highly aligned distribution in the circumferential direction of the vessel wall. This large difference in the initial configuration of the fibres and the predicted optimum distribution of the fibres is the reason behind this large contraction. Interestingly, it can be seen from Figure 4.7 (F) that although the values of maximum principal strains in the arterial wall decreased by the re-orientation process, the values of maximum principal stress increased in all the cases. This increase in the maximum principal stress can be explained using Figure 4.7 (G). Figure 4.7 (G) shows that stretch of the fibres also increased during the re-orientation process as they went toward the maximum principal stress. The increase in the stretch of the collagen fibres is the reason behind the increase in the values obtained for maximum principal stresses, see Figure 4.7 (F). It is worth mentioning here that this increase in the maximum principal stress values does not indicate the failure in the arterial tissue. However, large strain values at the locations where there are no collagen fibres in the optimum direction to protect the tissue integrity and preserve the tissue from rupture could result in the tissue failure. It was also shown by Ghasemi et al. (2018) that paucity of collagen fibres in the arterial tissue results in the failure of the arterial samples at much lower stress values where fibres could not contribute in bearing the loads. Figure 4.7 (G) and (F) also showed that in all of the three cases, values of maximum principal stress and stretch in the fibres reached similar levels. This can be explained using Equation (3.5) where stretch in the direction of fibres is derived as a function of both direction and values of right Cauchy-Green tensor. The large decrease in the values of maximum principal strain in the sample with the largest lack of re-orientation from optimum fibre configuration influences the stress level in both non-collagenous tissue and collagen fibres. Whilst

contraction of arterial wall as a result of re-orientation of fibres decreased the level of maximum principal stress in the non-collagenous tissue, the values of stress in the collagen fibres increased as they were moving toward the direction of the maximum principal stress during the re-orientation process. As shown in Equation (3.8), here, the overall mechanical response of the arterial wall was captured by adding the response of the collagenous and non-collagenous tissue under loads. Interestingly, Figure 4.7 (G) and (F) show that in all of the three cases the increase in the stress of fibres and decrease in the stress values of non-collagenous tissue resulted in similar overall stress values in the arterial wall after the re-orientation process. Gyoneva et al. (2016) showed that remodelling in the collagenous and non-collagenous tissue result in a tensional homeostasis in the arterial tissue. In that study they explained that during the remodelling process the total stress in the tissue remain the same but the stress values of the constituents of the vessel wall can change as a result of collagen fibre removal or deposition. However, they did not study the influence of collagen fibre re-orientation in the process of remodelling in the arterial wall. Figure 4.7 (G) and (F) highlight the role that re-orientation of fibres can play during the remodelling process to maintain the tensional homeostasis in arterial wall. Finally, Figure 4.7 (H) showed the evolution of the pseudo invariant I^* during the re-orientation process which was correlated to the internal variables γ_{RM} and β_{RM} to define a remodelling metric in the next stages of this study.

In the next step of this study, distribution of collagen fibres in the healthy and diseased carotid bifurcations was predicted. The geometry of the healthy bifurcations were obtained from volunteers while the diseased geometries were obtained from symptomatic patients who were under evaluation for an endarterectomy surgery. Both healthy and diseased geometries were meshed using hexahedral elements. There are many reasons why structured hexahedral meshes should be preferred when it comes to FE analysis of arterial tissue. Arterial tissue acts as a nonlinear, nearly incompressible material. Tetrahedral elements are known to cause severe locking issues when it comes to dealing with such constitutive laws (Puso and Solberg 2006). Using a structured hexahedral mesh is particularly of importance when accurate stress measurement is required as using an unstructured tetrahedral mesh can result in obtaining higher values of stress due to their high stiffness (De Santis et al. 2011b). Structured hexahedral meshes are also computationally more efficient when it comes to large complex models such as human carotid arteries (Creane et al. 2010a). Here, a novel meshing technique was proposed that can be efficiently applied to produce high quality structured hexahedral meshes for carotid bifurcations considering both luminal and adventitial layers. It is worth mentioning that in former studies only the luminal surface of the arteries were used to generate hexahedral meshes for arterial walls (Creane et al. 2010a). These luminal surfaces then were expanded radially to estimate the outer layers of the arteries. Such approximation

of the outermost layers of the arteries can have considerable influence when it comes to FE analysis of the diseased carotid arteries where the presence of the plaque can result in outward remodelling of the arterial wall. It is also worth mentioning again that, here, the healthy arterial wall was segmented into the media and adventitia layers and plaque burden was segmented into plaque atheroma and lipid pool.

Having these geometries meshed, the angle and dispersion of the collagen fibres in the healthy carotid bifurcations was predicted in the first place, see Figure 4.8 and 4.9. Three healthy carotid bifurcations were analysed at three different axial strain levels: 0, 5 and 10%. It was observed that in the absence of the axial stretch the distribution of the fibres was predicted to be highly anisotropic and aligned in the circumferential direction of the vessel wall. However, increasing the axial stretch resulted in a more isotropic distribution. The reason behind such isotropic distribution at 10% axial strain is that this loading condition imposes high axial stresses on the vessel wall and increases the ratio of the ($\sigma_{mid}/\sigma_{max}$). The distribution predicted for collagen fibres in the healthy carotid bifurcation agrees with experimental studies such as Chai (2015) where MR-DTI technique was applied to characterize the distribution of the fibres and (Finlay et al. 1995a). These results were also compatible with the result of the re-orientation algorithm suggested by Creane et al. (2011a) where a strain based re-orientation algorithm was applied to capture both angle and dispersion of the fibres in the healthy vessel wall.

While many studies apply isotropic material models to characterise the mechanical behaviour of the atherosclerotic plaque in the carotid arteries such as (Creane et al. 2011a; Teng et al. 2015)- just to name a few, recently, experimental studies such as (Akyildiz et al. 2017; Chai et al. 2015) revealed the highly anisotropic response of the atherosclerotic plaque in the carotid arteries. Akyildiz et al. (2017) used DTI to investigate the distribution of the fibres in plaques. They observed varying distributions of the fibres in different regions of the carotid plaques. Their overall measurement of the fibre orientation in the plaque showed that on average 52% of the fibres were in the circumferential direction of the arterial wall, 34 % percent were in the longitudinal direction and 14% were orientated in the radial direction, as mentioned previously in section 2.6 of this thesis. Balzani and Schmidt (2015) also reported that collagen fibres are more aligned with the axial direction in the plaque cap while in the fibrotic media fibres are more aligned in the circumferential direction of the vessel wall. Douglas et al. (2017) used histological techniques to explore the alignment of the fibres in the coronary atherosclerotic plaque. In that study they observed that in the shoulder areas fibre alignment is reduced significantly compared to regions of the fibrous cap. However, they could not link the structure of the plaque to their observations from their FE simulation. One reason behind such incompatibility between histological measurement and FE simulation can be explained

by investigating the configuration at which fibres where studied. Using histological images to characterize the distribution of fibres can result in neglecting the role that loads such as blood pressure and axial stretch play to maintain the distribution of fibres in the arterial wall. In fact, histological techniques can only provide information about the distribution of the fibres in the unloaded configurations. This absence of loads can result in the re-orientation of the fibres. Thus the obtained distribution of fibres using histological techniques can be misinterpreted with the real spatial orientation of the fibres in the arterial tissue *in vivo* . The other limitation with histological techniques is that, using this technique only information from certain planes is obtained and out of plane distribution of the fibres can be missed.

These variations in the distribution of the collagen fibres in the atherosclerotic plaque may be explained by looking at remodelling phenomenon in the diseased tissue. Bennett (1999) demonstrated that apoptosis, or death of cells, during the remodelling process in the body, can change the architecture of the arterial wall and lead to positive or negative remodelling of the artery during the atherosclerotic plaque development. Bennett (1999) also explained that apoptosis of the vascular smooth muscle cells (VSMCs) can be one major reason behind vulnerable atherosclerotic plaque rupture where a paucity of VSMCs was observed particularly at plaque shoulders (Bennett 1999; Geng and Libby 1995). A paucity of VSMCs in the atherosclerotic atheroma can also result in lack of remodelling in terms of orientation of the fibres as new collagen fibres cannot be produced in the preferred direction to maximize the load bearing capacity of the tissue. Such lack of remodelling can lead to weakening of the arterial wall and result in the plaque rupture.

In this study, the optimum distribution of collagen fibres which gives the maximum strength to the atherosclerotic plaque was predicted, see Figure 4.11 and 4.12. The proposed re-orientation algorithm showed that a highly aligned distribution of the fibres is required to withstand the loads of the blood pressure at the regions of the plaque shoulder. Also it was observed that the proposed re-orientation algorithm predicted a more aligned distribution of fibres at regions of the fibrous cap (areas between the lumen and lipid pool) compared to other regions of that particular cross section, see Figure 4.12. However, collagen fibres were predicted to be less aligned in the regions of the plaque cap compared to the regions of the plaque shoulder. The reason behind such prediction is that the plaque cap has a smaller area compared to other areas of the atherosclerotic plaque. This smaller area results in larger stress values in the axial direction which results in larger ratios of the intermediate to maximum principal stresses.

The values obtained for maximum principal strain and stress before and after the re-orientation process in the diseased geometries are shown in Figure 4.13. This figure shows

that because of the re-orientation of fibres toward the optimum fibre configuration the values of the maximum principal strains decrease in the arterial wall. This contraction of the tissue improves the integrity of the vessel wall, makes the plaque more stable and minimizes the risk of plaque rupture. Also, this figure shows that the values of the stress in the arterial tissue increase which is due to the contribution of the fibres in bearing the loads. The other result of the contribution of fibres in bearing the load is the increase in the stiffness of the arterial walls. These observations explain the results achieved in studies such as (Huang et al. 2016; Zhang et al. 2015) where higher strain levels were found in plaques with higher levels of vulnerability.

In this study, a remodelling metric was also defined to characterise the lack of remodelling in the diseased carotid bifurcations in terms of lack of collagen fibre orientation. Motivated by the classification of alignment of fibres in carotid plaques performed in (Akyildiz et al. 2017), three different initial configuration of the collagen fibres were postulated, case (i) where fibres were assumed to be parallel to the direction of the intermediate principal stress, case (ii) where fibres were assumed to be at 45^o degrees with respect to the direction of the maximum principal stresses and case (iii) where fibres were assumed to be parallel to the direction of the intermediate principal stresses. In all cases the fibres were allowed to fully re-orient toward their optimum configuration. Evolution of the internal variables during the re-orientation process was then used as an indicator for the lack of re-orientation in the diseased atherosclerotic tissue, see Figures 4.14 to 4.17. The results indicated higher RM values at the areas of the plaque shoulders in case (i) where fibres were assumed to be parallel to the intermediate stress direction. This lack of orientation from the optimum distribution can occur in the diseased arteries due to a lack of cells to produce the sufficient fibres in the direction of the loads or due to the fibres being enveloped by the surrounding matrix such that the fibres cannot re-orient. This remodelling metric has the potential to be used as a pre-clinical indicator of the risk of atherosclerotic plaque rupture, particularly now that advancements in imaging modalities such as DTI show great promise in the *in vivo* characterisation of the structure of collagen fibres (Akyildiz et al. 2017; Shahid et al. 2017).

To the best of the author's knowledge, this is the first time that a computational algorithm has been employed to predict the optimum distribution of collagen fibres in complex real diseased carotid bifurcations obtained from symptomatic patients and used to characterise the lack of remodelling therein. However, there are limitations that can be associated with this study. Firstly, the geometries were obtained from the deformed configuration in the body and a blood pressure of 16 kPa was then applied on the arterial wall without pulling back the geometry to its unloaded configuration. The importance of calculating the unloaded state of the arterial wall is emphasised in studies such as (Chandra et al. 2016; Raghavan et al. 2006).

Such limitations also exist in many other studies such as (Creane et al. 2010a; Hariton 2006; Teng et al. 2010b)- just to name a few. The influence of the residual strains and stresses in the vessel walls was also not included. The importance of incorporating the residual stress in the mechanical behaviour of the arterial tissue is emphasised in studies such as (Alastrue et al. 2007; Delfino et al. 1997; Schröder and von Hoegen 2016)- just to name a few. Another important limitation of this study was the choice of the material properties. The material properties used in this study were obtained from uniaxial mechanical tests in the axial and circumferential directions of the vessel wall when a constant distribution of the fibres was postulated through the wall thickness. However, the re-orientation of the fibres may change the values reported for k_1 and k_2. Finally, the mechanical behaviour of the cells which play a very important role in the remodelling process, such as degradation of the fibres or in the healing process, was not incorporated in this study.

Inverse FE analysis in conjunction with imaging techniques such as MRI can be used to obtain the undeformed configuration of real vessel geometries and characterise the patient specific material properties (Johnston et al. 2018a). The proposed remodelling algorithm can then be used to determine the optimum configuration of the fibres in these vessels and to re-orient the fibres toward this preferred configuration. The values obtained for maximum principal strain at this optimum fibre configuration can then be compared with values for strain obtained using this imaging technique. The comparison between these strain values can be used to distinguish the areas at higher risk of atherosclerotic plaque rupture.

Chapter 5 Assessment of mechanical indicators of atherosclerotic plaque vulnerability; Geometrical curvature metric, plaque stresses and damage in tissue fibres

5.1 Introduction

Growth and development of atherosclerotic plaque can change both geometry and mechanical properties of the healthy arterial wall. Studies show that the geometry of arteries can undergo outward and inward remodelling due to the presence and growth of a plaque (Saam et al. 2016; Schoenhagen et al. 2001), as discussed previously in sections 2.5, 2.6 and 2.8.3 of this thesis.

Li et al. (2008) assessed the vulnerability of atherosclerotic plaques by constructing parameterized 2-D idealized models. Performing FE analysis and distinguishing the regions exposed to high von-Mises stress, Li et al. (2008) associated the highest risk of carotid plaque rupture with lumen shape, curvature and areas of thin fibrous cap. Teng et al. (2010b) also assessed the risk of carotid atherosclerotic plaque rupture using luminal curvature and fibrous cap thickness calculated from images obtained from MRI. Creane et al. (2010a) introduced the difference in the curvature of the inner and outer surface of the plaque as a new metric for assessing the risk of plaque rupture. In that study, this metric was applied on the arteries obtained from symptomatic and asymptomatic patients and compared with values obtained for von-Mises stress. To-date various methods have been applied for assessing the risk of atherosclerotic plaque rupture in the literature including the stenosis percentage, measuring the intimal medial thickness and angiography. A summary of these procedures is provided in section 2.7 of this thesis.

Continuum damage mechanics (CDM) has been widely used to assess the accumulated damage in different constituents of arterial tissue, such as matrix (Famaey et al. 2013; Pena 2011a), elastin fibres (Ghasemi et al. 2018) and collagen fibres (Balzani and Schmidt 2015; Ghasemi et al. 2018). Using CDM, different forms of internal variables can be defined which evolve according to the loading conditions in the tissue. Evolution of these internal variables enables us to capture damage relevant phenomena including: Mullins effect, permanent set,

hysteresis and ultimately rupture of fibres. For further information about the mechanical response of the arterial tissue under supra-physiological loads the reader is referred to section 2.4.2. A constituent specific study of the response of the collagenous and non-collagenous arterial tissue under high loads is provided in Chapter 3 (Ghasemi et al. 2018). The constitutive models used in the literature to characterize the response of the arterial tissue under high loads are reviewed in section 2.8.2.

Although the accuracy of constitutive models is verified in many studies such as (Ghasemi et al. 2018; Maher et al. 2012; Pena 2014), material calibration has been commonly mentioned to be one major limitation of these methods (Ghasemi et al. 2018; Pena 2014). Data from experiments such as pressure inflation, biaxial mechanical tests and uniaxial tests in the axial and circumferential directions are frequently used to calibrate anisotropic and isotropic material models under monotonic and cyclic loads (Macrae et al. 2016). Yet, when it comes to material parameters, patients specific data is needed given that material properties of the tissue alter according to the age, sex and health status (Ozolanta et al. 1998; Sommer and Holzapfel 2012). However, to perform these mechanical tests requires the patient tissue to be harvested, which is not feasible.

To minimize the aforementioned limitations, in this study a new geometrical metric for assessing the risk of plaque rupture is introduced. The functionality of this metric was systematically examined using idealized 2-D and 3-D geometries. In the second stage of this study the functionality of this geometrical metric was assessed on real vessel geometries. The areas distinguished as rupture-prone areas in these arteries by the novel geometrical metric, were compared with the areas at high risk of plaque rupture predicted by a CDM model. The results of our geometrical metric and CDM model were also compared with the results obtained from stress analysis performed using both isotropic and anisotropic material models for each component of the diseased arteries. Our diseased geometries were composed of: plaque cap, lipid pool, fibrotic media, media and adventitia. In the last part of this study, the aforementioned metrics were compared on a branch of a 3-D realastic diseased carotid artery, constructed from computerised tomographic angiography (CTA) images. Such comparisons can provide us with a potential clinical indicator that can be used to more efficiently distinguish the areas at high risk of rupture. Moreover, ultimately such metrics may also be used to determine the risk of stroke in asymptomatic patients.

5.2 Materials and methods

5.2.1 Constitutive models

Mechanical properties of arterial walls are most commonly defined using nearly incompressible isotropic or anisotropic hyperelastic material models where a Helmholtz free-energy function is assumed per unit reference volume of the tissue. Different forms of phenomenological and structural constitutive models have been used in the literature to define the mechanical behaviour of the soft tissue under physiological loads, A summary of these models is provided in section 2.8.1 and 2.8.2 of this thesis. Constitutive laws used to capture the response of the atherosclerotic plaques are summarised in section 2.8.3 of this thesis. In this study, an isotropic 2nd order Mooney-Rivlin material model, along with the CDM model introduced in chapter 3 (Ghasemi et al. 2018), were used to capture the mechanical response of the arterial tissue.

The SEF for the 2nd order Mooney-Rivlin material model can be defined as follows;

$$\psi_{iso}^{M}(\bar{\mathbf{C}}) = C_{10}(\bar{I}_1 - 3) + C_{01}(\bar{I}_2 - 3) + C_{20}(\bar{I}_1 - 3)^2 + C_{11}(\bar{I}_1 - 3)(\bar{I}_2 - 3) + C_{02}(\bar{I}_2 - 3)^2 \quad (5.1)$$

Where $\bar{I}_1$ and $\bar{I}_2$ are deviatoric invariants, see Equation (3.3), and C_{10}, C_{01}, C_{20}, C_{11} and C_{02} are material parameters.

In this study the CDM model demonstrated in chapter 3 was modified to capture the damage accumulation only in the collagen fibres of diseased atherosclerotic plaques. The SEF of this material model can be written as follows

$$\psi = \psi_{vol} + \psi_{iso} + \psi_{cf} \quad 5.2)$$

Where ψ_{vol}, ψ_{iso} and ψ_{cf} are explained in Equations (3.9), (3.10) and (3.15) in Chapter 3 of this thesis in the sections 3.4.2 and 3.4.3.

5.2.2 Geometries

5.2.2.1 Idealized 2-D Geometries

Two different idealized, parameterized geometries were created to model a vessel presenting with stenosis and outward remodelling, with a schematic of the geometries shown in Figure 5.1 (A) and (B), respectively along with the relevant dimensions.

In all stenotic geometries (Figure 5.1 (A)), the intimal-medial (IM) boundary was defined by a circle radius R_{IM} of 2.74 mm based on measurements provided in Krejza et al. (Krejza et al. 2006) and others (Acar et al. 2013; Limbu et al. 2006). The lumen was defined by an elliptical shape where the ratio of major to minor axes, $R_{\mathrm{maj}}/R_{\mathrm{min}}$, was parametrically altered whilst holding R_{min} constant. The centre of the ellipse was offset from the centre of the IM circle by

l_0. Four stenotic geometries were created based on this parameterization, the dimensions of which are presented in Table 5.1.

Conversely, the outward remodelled geometries were defined by a circular lumen radius R_L of 2.73 mm for all models, and the IM boundary by a parameterized ellipse with a ratio of major to minor axis $R_{\text{maj}}/R_{\text{min}}$. The lumen was offset from the IM boundary edge by l_0, and the thickness t was maintained constant for all models at 0.1 mm. Four outward remodelled geometries were created, the dimensions of which are given in Table 5.1.

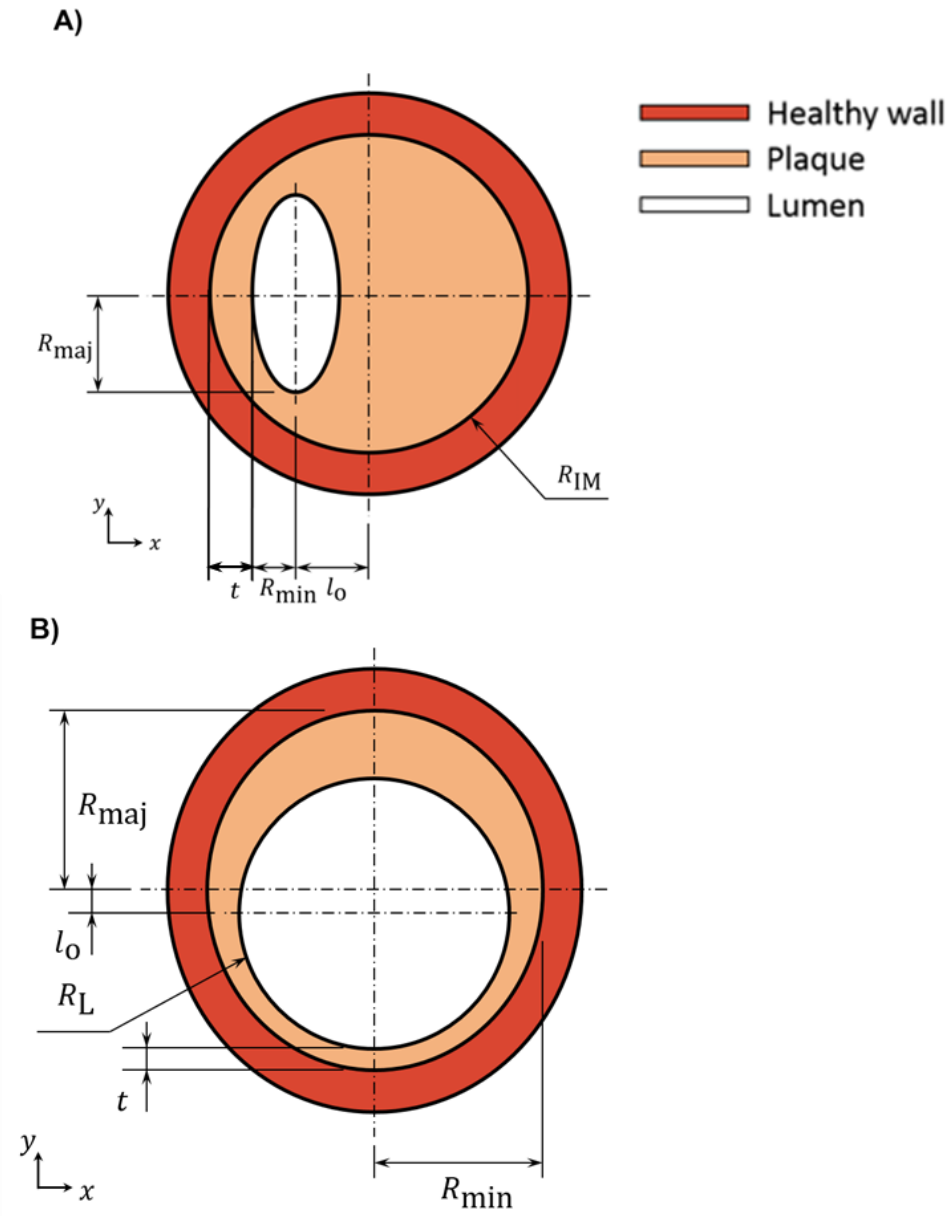

Figure 5.1. *Idealized 2-D geometries used to model diseased vessels. A) Stenotic geometry where the ratio R_{maj}/R_{min} is parametrically investigated, and R_{min} and l_0 are held constant for all models B) Outward remodelled geometry where the ratio R_{maj}/R_{min} is parametrically investigated.*

Table 5-1. *Geometric parameters used to examine the stenotic and outward remodelled, idealized 2-D geometries. four different geometries are examined for the two scenarios.*

	Stenotic Geometry				Outward Remodelled Geometry			
	R_{maj}/R_{min}	R_{min} (mm)	l_0 (mm)	t (mm)	R_{maj}/R_{min}	R_{min} (mm)	l_0 (mm)	t (mm)
Model 1	1	1.5	0.7	0.53	1.06	3.21	0.56	0.1
Model 2	1.2	1.5	0.7	0.53	1.06	3.45	0.84	0.1
Model 3	1.4	1.5	0.7	0.53	1.06	3.69	1.12	0.1
Model 4	1.6	1.5	0.7	0.53	1.06	3.93	1.4	0.1

5.2.2.2 Idealized 3-D Geometries

Two 3-D idealized geometries were created to simulate a vessel with stenosis and outward remodelling. To create these models, a series of the 2-D idealized geometries described in section 2.1.1 were stacked sequentially to form a 3-D geometry. The idealized 3-D stenotic geometry is shown in Figure 5.2.**Error! Reference source not found.** (A), the contour of the IM boundary remains circular while the lumen becomes more elliptical as it progresses in the longitudinal direction of the vessel, with the ratio R_{maj}/R_{min} ranging from 1.0 to 1.6 at the centre of the stenosis.

The idealized 3-D outward remodelled geometry is shown in Figure 5.2 (B). In this case each of the 2-D geometries given in were stacked sequentially together with an additional 2-D geometry of dimensions R_{maj}/R_{min} of 1.06, R_{min} of 4.17 mm and l_0 of 1.68 mm located at the centre. The 2-D geometries were positioned such that the lumen centreline in the 3-D geometry was straight.

The 3-D geometries were created in SolidWorks (v.2015, Dassault Systemes) using the loft function to connect each of the 2-D cross sections together.

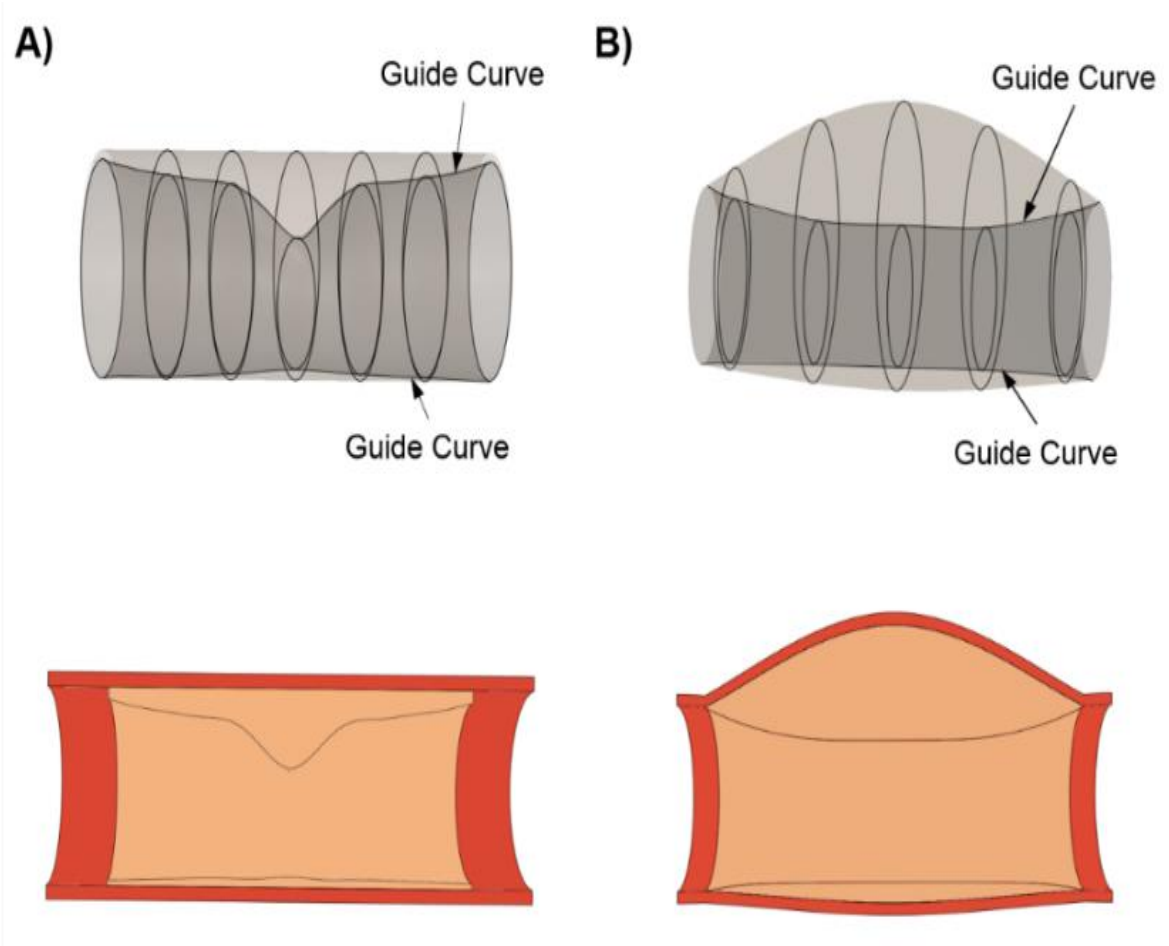

Figure 5.2. *The 3-D geometries examined: the A) idealized stenotic geometry, and B) outward remodelled geometry are created by lofting the parameterized 2-D geometries together, along the guide curves shown.*

5.2.2.3 3-D Plaque geometries

Plaque geometries of realistic, diseased vessels were obtained from a study conducted by Li et al. (2006). These geometries were from 5 symptomatic patients when all the individuals had either a retinal or cortical transient ischemic attack. Three out of these geometries had no sign of plaque rupture whilst two plaques were found to have ruptured. For further information on the high-resolution multi-sequence MR imaging and histological analysis used to construct these geometries the reader is referred to (Li et al. 2006). The plaques were segmented into regions of plaque cap, lipid pool and fibrotic media. The lumen and IM boundaries were contoured from the images for later use in curvature analysis. A uniform thickness of 0.7 mm for the media layer and 0.4mm for the adventitia layer was assumed following the measurement taken in (Sommer et al. 2010).

5.2.2.4 Branch of a carotid artery

The real 3-D geometry was created from CTA scans of a human carotid artery taken from patients under evaluation for a carotid endarterectomy procedure. This geometry was taken from a previous paper from our research group; Creane et al. (Creane et al. 2010b), where details on the image processing methodologies can also be found. Only one branch of the carotid artery was analysed in this study as that particular branch has regions of both stenosis and positive remodelling, as shown in Figure 5.3.

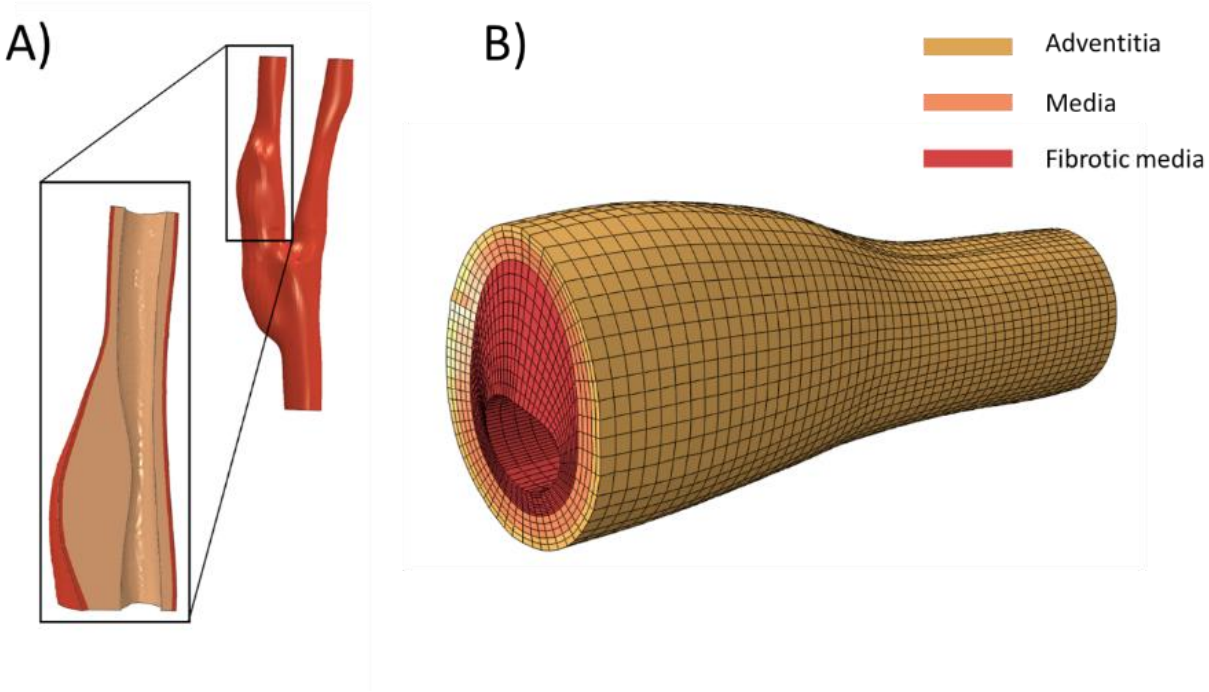

Figure 5.3. *A) A schematic of a geometry which was obtained from a patient who was undergoing endarterectomy showing the characteristics of both positive and negative remodelling. B) The generated hex mesh for this geometry.*

5.2.3 Finite Element Analysis

5.2.3.1 Material parameters

All vessel geometries were analysed using the FE method. The mechanical behaviour of the plaque cap, lipid pool, fibrotic media, media and adventitia are different, hence different material properties were used to simulate the mechanical behaviour of these constituents. Both isotropic and anisotropic material models were used to reproduce the mechanical behaviour of the arteries.

The 2nd order Moony-Rivlin constitutive model was used to perform stress analysis on the constituents of the atherosclerotic arteries. To analyse the 2-D and 3-D idealized models, arteries were decomposed into two components, namely: plaque and healthy vessel wall. The

material properties for these two models were obtained from (Creane et al. 2010a) and listed in Table 5.2.

The isotropic material properties used for 3-D plaque geometries and the references which were used to obtain them are listed in Table 5.3. It should be mentioned that, following (Creane et al. 2010a), similar isotropic material properties were used for both the media and adventitia layers. The anisotropic material properties for the CDM model for different constituents of the arterial wall and the references which were used to obtain them are listed in Table 5.3.

Table 5-2. *The isotropic material properties which were used for analysis of 2-D and 3-D idealized models.*

	$C_{10}[kPa]$	$C_{01}[kPa]$	$C_{20}[kPa]$	$C_{11}[kPa]$	$C_{02}[kPa]$
Healthy wall	50.45	30.49	400	120	10
Plaque	4.8	60	240	377	781

Table 5-3. *The isotropic material properties which were used for analysis of 3-D plaques.*

	$C_{10}[kPa]$	$C_{01}[kPa]$	$C_{20}[kPa]$	$C_{11}[kPa]$	$C_{02}[kPa]$	Reference
Fibrotic media	9.267	3.508	305.463	1183.01	504.507	(Teng et al. 2015)
Lipid pool	2.5	0	0	0	0	(Balzani et al. 2012)
Plaque cap	28.499	8.634	150.48	56.755	2721.01	(Teng et al. 2015)

Material properties which were used for the CDM model to capture the anisotropic stress in the atherosclerotic tissue and damage in collagen fibres are shown in Table 5.4 (Balzani et al. 2012).

Table 5-4. *The material properties which were used for different components of atherosclerotic tissue for the CDM model (Balzani et al. 2012).*

	C_{10}[kPa]	k_1[kPa]	k_2[-]	$\alpha[deg]$	κ	γ_∞[kPa]	β_s
Media	6.56	1482.38	564.81	37.03	0.16	6.52	0.37
Adventitia	4	1640.23	115.63	45.60	0.097	10.84	7.36
Fibrotic media	21.12	1951.48	925.37	25.55	0.0095	6.52	0.37
Fibrous cap	24.12	4778.44	1023.59	53.18	0.12	6.52	0.37
Lipid pool	2.5	0	0	0	0	0	0

5.2.3.2 Constitutive model development

The formulation of 2nd order Moony-Rivlin constitutive model was built in Abaqus 2017 (Dassault Systèmes Simulia corporations, Vèlizy-Villacoublay, France). The CDM model was implemented into Abaqus via a user-defined Fortran subroutine (UMAT) where the definitions of Cauchy stress tensor $\boldsymbol{\sigma}$ and the elasticity $\mathbb{C}$ was required. Cauchy stress can be defined using the SEF described in section 5.2.1 equation 5.2.

The elasticity tensor was calculated using the computational method explained in the section 3.4.4.This method for calculating the elasticity tensor was initially proposed by Miehe (1996) and used in studies such as (Creane et al. 2011b; Ghasemi et al. 2018; Sun et al. 2008). The algorithmic implementation of the CDM model is shown in Table 5.5.

Table 5-5. The summary of the quantities needed for FE implementation of the presented CDM model**.**

(1)	Material parameters for ground matrix μ
	Material parameters for collagen fibres $k_1, k_2, \alpha, \kappa, \gamma_\infty, \beta_s$
(2)	Deformation gradient $\mathbf{F}$
(3)	Deformation measures $\bar{\mathbf{F}} = J^{-\frac{1}{3}}\mathbf{F}$, $J = \det(\mathbf{F})$, $\bar{\mathbf{C}} = \bar{\mathbf{F}}^T\bar{\mathbf{F}}$, $\bar{I}_1$
(4)	Pseudo invariant measures $\bar{I}_M^* = \boldsymbol{\kappa}\bar{I}_\mathbf{1} + (\mathbf{1} - \mathbf{3}\boldsymbol{\kappa})\bar{I}_{\boldsymbol{M}}$
(5)	Check the initial damage threshold $\bar{I}_M^{*ini}$ for collagen fibres
	If $\bar{I}_M^* < \bar{I}_M^{*ini}$ then go to (6) otherwise go to (10)
(6)	$\psi = \psi_{vol} + \bar{\psi}_{vol}(\bar{\mathbf{C}}) + \bar{\psi}_{cf}(\bar{\mathbf{C}}, D), D = 0$
(7)	$\sigma = \frac{2}{J}\mathbf{F}\frac{\partial\psi}{\partial\mathbf{C}}\mathbf{F}^T$
(8)	$\mathbb{C} = \mathbb{C}_{vol} + \mathbb{C}_{iso} + \mathbb{C}_{cf}$
(9)	Return to step number (2)
(10)	$\beta = \langle\tilde{\beta} - \tilde{\beta}^{ini}\rangle$
(11)	$\gamma = \max_{S\in[0,S]}\langle\bar{I}_M^* - \bar{I}_M^{*ini}\rangle$
(12)	$D = D_\infty[1 - \exp(-\frac{\gamma}{\gamma_\infty})]\,[1 - \exp(-\frac{\beta}{\beta_s})], D_\infty \in [0,1[$
(13)	$\psi = \psi_{vol} + \bar{\psi}_{iso}(\bar{\mathbf{C}}, D_{ef}) + \bar{\psi}_{cf}(\bar{\mathbf{C}}, D_{cf})$
(14)	$\sigma = \frac{2}{J}\mathbf{F}\frac{\partial\psi}{\partial\mathbf{C}}\mathbf{F}^T$
(15)	$\mathbb{C} = \mathbb{C}_{vol} + \mathbb{C}_{iso} + \mathbb{C}_{cf}$
(16)	Return to step number (2)

5.2.3.3 Damage threshold

To identify the damage accumulation in the arteries, the values of the corresponding SEF function, Equation 5.2, in healthy arteries at the blood pressure of 180 mmHg was calculated. This blood pressure is associated with the third grade hypertension (Rysz et al. 2017) and was used as a damage threshold in other studies such as (Balzani et al. 2012). To accurately calculate the value of ψ_{cf} at this blood pressure a closing angle simulation was performed. The opening angle of the common carotid artery was chosen to be 130 degrees following (Delfino et al. 1997). The thickness of the media and adventitia layers were assumed to be 0.7 mm and 0.4 mm, respectively (Sommer et al. 2010). The radius of the stress free common carotid artery was assumed to be 4.42 mm (Delfino et al. 1997). The material properties for media and adventitia layers were shown in Table 5.4.

It is well known that due to the residual strain, the inner layers of the vessel walls are under compression and the outer layers of the vessel wall are under tension (Fung et al. 1992; Schröder and von Hoegen 2016). Greenwald et al. (1997) explored the distribution of residual strain in the artery wall by selectively digesting the elastin and collagen fibres and measuring the opening angles. In that study they showed that digesting the collagen fibres does not have a significant influence on the measured opening angles in different samples, as mentioned previously in the Chapter 2 of this thesis section 2.4.1.3. This observation suggested that collagen fibres do not play a major role at this configuration when no blood pressure is applied on the vessel wall (Schroder and Brinkhues 2014). This observation was also confirmed in the study conducted by (Gaul et al. 2018). In this study, to ensure that the deformation from closing-angle simulation will not influence the collagen fibres, a decomposition of the deformation gradient tensor before and after closing the angle was performed as follows, see Figure 5.4 (A).

$$\mathbf{F}_{12} = \mathbf{F}_2\mathbf{F}_1 \tag{5.3}$$

Where $\mathbf{F}_2 = \mathbf{F}_{12}\mathbf{F}_1^{-1}$ was used to obtain the maximum value of ψ_{cf} as the damage threshold. Such decomposition ensures that collagen fibres did not contribute in bearing the loads even under the tension of the circumferential residual strain in the outer layers of the arterial wall when no blood pressure was applied on the arterial wall. The values obtained for ψ_{cf} at a blood pressure of 180 mmHg is shown in Figure 5.4 (B) across the normalized wall thickness. The maximum value obtained for ψ_{cf} in this simulation (1.18 kPa) was used as the damage threshold for collagen fibres.

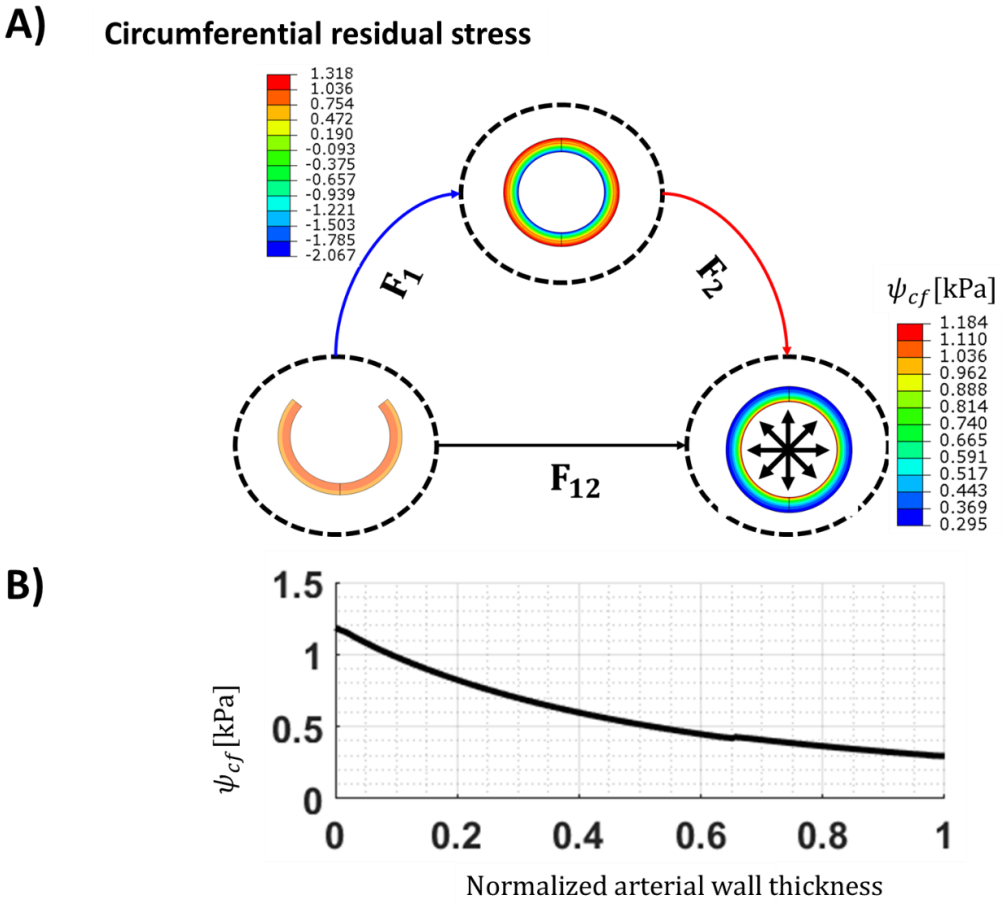

Figure 5.4. *A) A schematic explaining the decomposition of the deformation gradient tensor performed to calculate the damage threshold for collagen fibres. B) The values obtained for strain energy density function, Equation 3.12.*

5.2.3.4 Meshing and boundary conditions

The 2-D idealized geometries were meshed using between 22,960 and 82,974 triangular and quadrilateral plane strain elements. The 3-D idealized stenotic and outward remodelled geometries were meshed using 51,557 and 171,920 hexahedral elements respectively. A blood pressure of 15 kPa was imposed on the lumen of these vessels while 4 nodes on the outer most layers were constrained in the circumferential direction to restrict rigid body motion. An axial stretch of 1.05 was also imposed on the media and adventitia layers of the 3-D geometry.

The 3-D plaque geometries were meshed using between 14242 to 45634 elements. All the components were meshed using hexahedral elements except lipid pool which was meshed using tetrahedral elements. All these geometries were meshed using ANSA (v17.0, BETA CAE Systems, Thessaloniki, Greece). The thickness of each section was assumed to be 0.1 mm. Only one element was used through the axial thickness of these geometries. An axial stretch of 1.025 was imposed on all of these geometries. These geometries underwent a 100 cycles of

loading and unloading between 10 and 16 kPa. Nodes in the outermost layer of these geometries were also constrained in the circumferential direction to supress the rigid body motions. Similar to the 3-D idealized models, the branch of the carotid artery was meshed using 44250 hexahedral elements, see Figure 5.3 (B), using ANSA (v17.0, BETA CAE Systems, Thessaloniki, Greece), using the technique explained in section 4.2.4. A blood pressure of 15 kPa was imposed on the luminal surface of this geometry. The axial stretch of 1.05 was imposed on these geometries. Similar to 3-D plaque geometries, nodes on the outermost layer of this vessel was constrained in the circumferential direction to supress the rigid motion. Table 5-6 summarizes different geometries used in this study along with the boundary conditions applied.

Table 5-6. *A summary of the geometries used in this study along with the boundary conditions applied for FE analysis*

	Number	Systole blood pressure [kpa]	Axial stretch
2-D Idealized	8	15	-
3-D Idealized	2	15	1.05
3-D Plaques	6	16	1.025
3-D full branch of carotid artery	1	15	1.05

It is worth mentioning that different material properties and different boundary conditions were used in different sections of this study as mentioned in the preceding sections. The main reason behind such an inconsistency was lack of experimental information on the mechanical response of different components of human carotid arteries at physiological and supra-physiological load levels. To reduce the impact of selecting different material properties and boundary conditions, the results obtained for each group of geometries, see Table 5-6, were not compared with other groups of geometries.

Hybrid formulation elements were utilized for all the aforementioned geometries to enforce the incompressibility. The appropriate number of elements for each model was determined in a mesh convergence study; where the mesh was considered suitably dense if the computed maximum σ_{VM} in a simulation deviated by less than 5%.

5.2.4 Geometrical assessment of arteries

5.2.4.1 Two-Dimensional Curvature

Curvature κ is a quantitative scalar measure used to describe how much a given point on a curve deviates from being a straight line. Figure 5.5 (A) presents a schematic of how the curvature of a line is defined; for any point on a curve with unit tangent vector $\boldsymbol{T}$, curvature is the magnitude of infinitesimal tangent vector change $d\boldsymbol{T}$ per infinitesimal arc length ds,

$$\kappa \equiv \left|\frac{d\boldsymbol{T}}{ds}\right| \tag{5.4}$$

The curvature of a circle is an intuitive way to conceptualize this; it is calculated as the inverse of its radius, i.e. $\kappa = 1/r$, so the larger the circle the smaller the curvature and vice versa. In the special case of a straight line, $\kappa = 0$. Curvature has the desirable property of being invariant to translations and rotations. Consequently the calculation of curvature does not require any reorientation of the geometry, nor is it specific to a particular coordinate frame.

In the present study a geometric measure named the weighted curvature difference Ω was created to quantitatively assess a diseased vessel's risk of rupture. It was based on the difference in curvature between κ_l, curvature of the lumen, and κ_{IM}, curvature of the intima-media boundary, and was normalized by the plaque thickness at that location t. It is given as,

$$\Omega = \frac{\kappa_l - \kappa_{IM}}{t} \tag{5.5}$$

Figure 5.5 (B) is a schematic showing how the parameters comprising a single calculation of Ω were evaluated. A radial line is drawn outwards from the centroid of the lumen and the curvature is calculated at the intersection of this line with the lumen and IM boundaries. The plaque thickness is the distance between these two intersections. This calculation was repeated at 1° increments about the lumen centroid, encompassing the full circumference.

The curvature in the idealized 2-D geometries was determined using the closed form solutions for curvature of a circle and ellipse (Gray et al. 2006). For the real 2-D geometries, the x-y point data for the lumen and IM boundaries were mapped to a polar coordinate (r-θ) frame. A polar frame was used to avoid accuracy problems associated with joining two ends of a spline. A smoothing spline was fitted to $r(\theta)$ plots for the boundaries using MATLAB (R2015b, The Mathworks). This spline was subsequently used to evaluate the derivatives necessary for the calculation of curvature κ in a polar coordinate frame, given as,

$$\kappa(\theta) = \frac{r^2 + 2r'^2 - rr''}{(r^2 + r'^2)^{3/2}} \tag{5.6}$$

where $r = r(\theta)$, r' and r'' are the first and second derivatives of r with respect to θ (Larson and Edwards 2013).

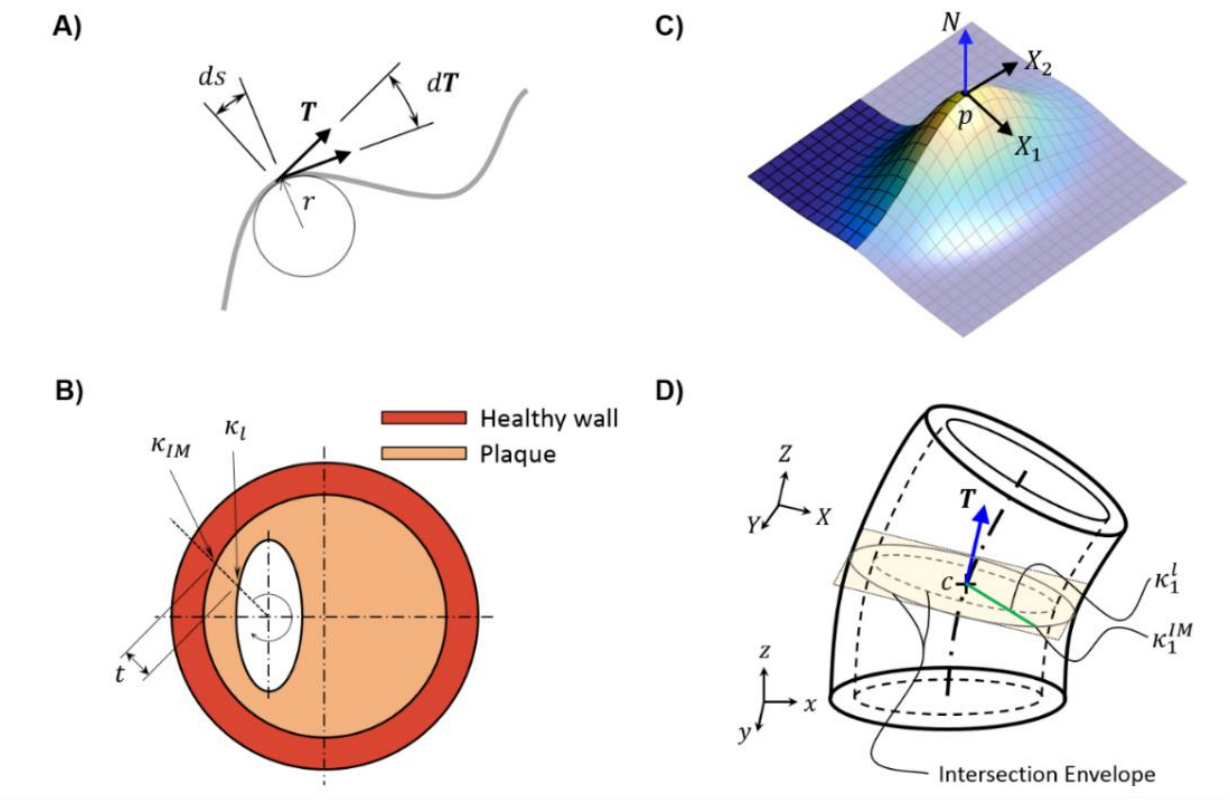

Figure 5.5*. A) Schematic outlining two definitions of 2-D curvature. The first and easiest to understand is that at every point on a curve a tangent circle may be constructed, the inverse of its radius is the curvature at that point. The second and more formal definition is that curvature is the magnitude of the infinitesimal change in tangent vector dT per change in arc length ds on a curve (note the magnitudes of dT and ds are exaggerated for diagrammatic purposes). B) Schematic presenting the 2-D boundaries used to calculate* κ_l *and* κ_{IM}*. These two curvature values were normalized by plaque thickness t to calculate Ω C) Schematic outlining curvature on a 3-D surface. At a point p on the surface the 2-D curvature may be calculated 360° about the normal to the surface N. The directions in which the maximum and minimum curvatures are found,* X_1 *and* X_2 *respectively, are the principal curvatures* κ_1 *and* κ_2 *respectively. Note that N,* X_1*, and* X_2 *form an orthogonal set. D) Schematic of curvature calculation in 3-D. A lumen centreline is computed and a plane is constructed normal to a tangent vector T of the centreline with a centrepoint c. This plane intersects the lumen and IM boundaries and the maximum principal curvature at these boundaries is calculated in a 360° arc in the plane and centred about c.*

5.2.4.2 Three-Dimensional Curvature

The concept of curvature can be extended into 3-D, where in this instance the curvature of surfaces is analysed, see Figure 5.5 (C). Any point p on a surface has a normal vector $\boldsymbol{N}$ and a tangent vector $\boldsymbol{X}$ which may point in any direction orthogonal to $\boldsymbol{N}$. The intersection of the plane defined by $\boldsymbol{N}$ and $\boldsymbol{X}$ with the surface produces a 2-D curve whose curvature at p can be calculated using the 2-D methods outlined above. At every point p there exists a tangent vector $\boldsymbol{X}_1$in which there is highest curvature, this is known as the maximum principal curvature κ_1. Likewise, $\boldsymbol{X}_2$ gives the direction of lowest curvature and defines the minimum principal curvature κ_2. Note that $\boldsymbol{N}$, $\boldsymbol{X}_1$ and $\boldsymbol{X}_2$ are an orthogonal set.

In the present study, the 3-D geometry of the lumen and IM boundaries were constructed using triangular surface meshes. To calculate curvature, a MATLAB function (Shabat 2014; Shabat and Fischer 2015) was used which has been specifically formulated for the numerical calculation of principal curvatures on triangular surface meshes (Rusinkiewicz 2004) . Briefly, the curvature was calculated at each vertex on a triangular face using a finite difference method. Importantly, weighted contributions from neighbouring triangular faces were included in the algorithm, resulting in the robust calculation of surface curvature.

The weighted curvature difference Ω was calculated in 3-D using the maximum principal curvature of the lumen and IM boundaries, κ_1^l and κ_1^{IM} respectively. Figure 5.5 (D) presents a schematic showing how Ω was calculated in 3-D vessels. A centreline was constructed through the centroid of the lumen. At any point c on the centreline, a plane can be constructed which is orthogonal to the tangent vector $\boldsymbol{T}$ at c. This plane intersects the lumen and IM boundaries forming a 2-D intersection envelope. The maximum principal curvatures, κ_1^l and κ_1^{IM}, used to calculate Ω were at the intersection of radial lines originating at c with the lumen and IM intersection envelope. The thickness t is the distance between these intersections.

The numerical algorithm to compute the intersection envelope of the plane orthogonal to $\boldsymbol{T}$ with the vessel boundaries is outlined in detail in Figure 5.6. The geometry was rigidly rotated and translated into a convenient configuration where the x-y plane and the plane orthogonal to $\boldsymbol{T}$ were coplanar (see Figure 3D). Next, the geometry was mapped to a polar coordinate system (R, θ, Z) and the lumen and IM boundary for equal values of θ in the plane $Z = 0$ were computed to construct the intersection envelope. This must then be mapped back to a Cartesian coordinate system, rotated, and translated back to the original configuration. The flowchart presented in Figure 5.6 explains the algorithmic implementation of this method.

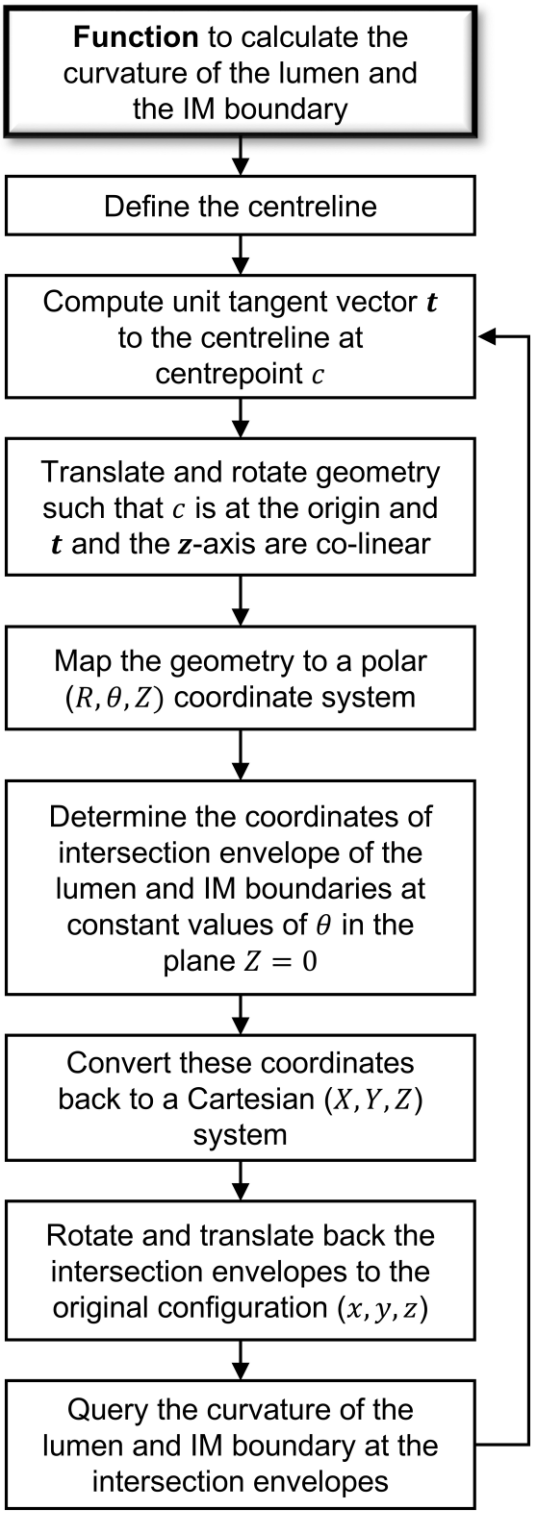

Figure 5.6. *Flowchart outlining the algorithmic procedure to calculate curvature in complex 3-D geometries*

5.3 Results

5.3.1 2-D Idealized modes

The results of the stress and curvature analysis of idealized 2-D stenosed vessels are presented in Figure 5.7. These results show that Ω and von-Mises stress both predict the same areas to be at high risk of plaque rupture.

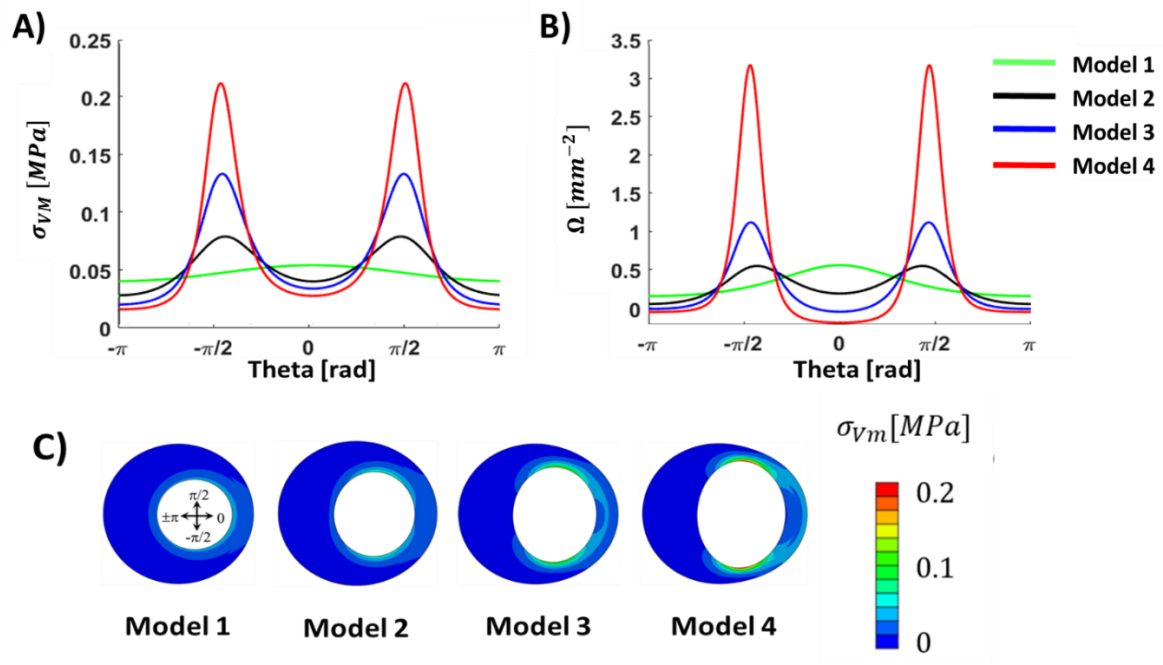

Figure 5.7. *Analysis of 2-D stenotic models. A) Stress distribution on the boundary of the lumen. B) The values obtained for Ω. C) The results of FE analysis of the geometries.*

The results of stress and curvature analysis of outward remodelled vessels are shown in Figure 5.8. Similar to stenosed models, it can be seen that the areas with higher values of Ω correspond to the areas with higher values of von-Mises stress.

In Figure 5.9, the values of lumen curvature (κ_l) are compared with the values of Ω in the idealized 2-D stenosed models (A and B) and outward remodelled geometries (C and D). These results demonstrate that lumen curvature alone cannot characterise the areas at higher risk of rupture in the outward remodelled vessels. However, it shows that Ω and von-Mises stress predict the same locations as areas at higher risk of plaque rupture.

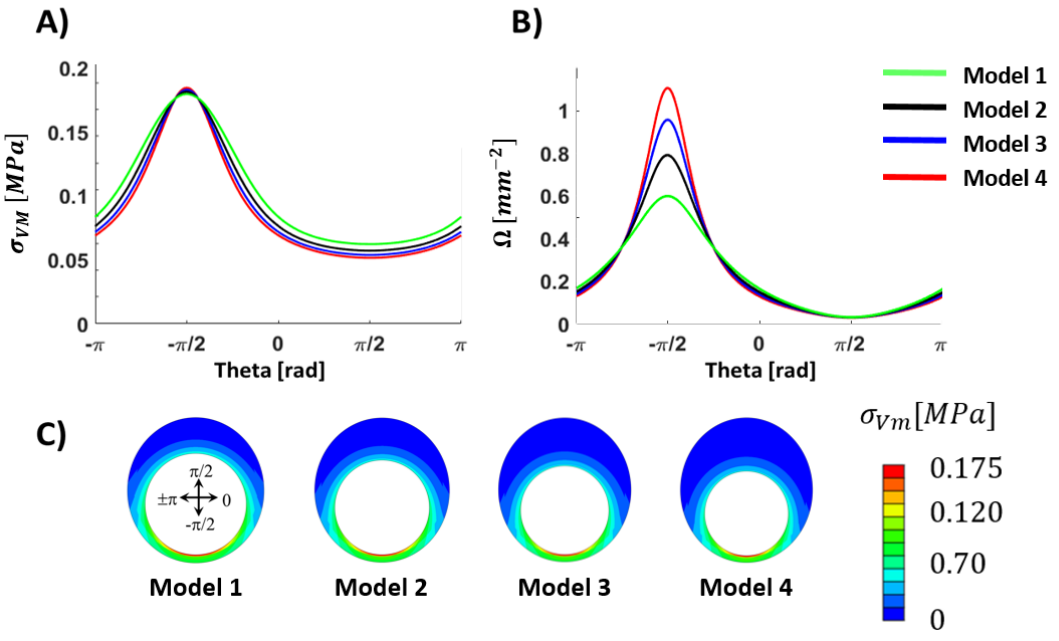

Figure 5.8. *Analysis of 2-D outward remodelled models. A) Stress distribution on the boundary of the lumen. B) The values obtained for Ω. C) The results of FE analysis of the geometries.*

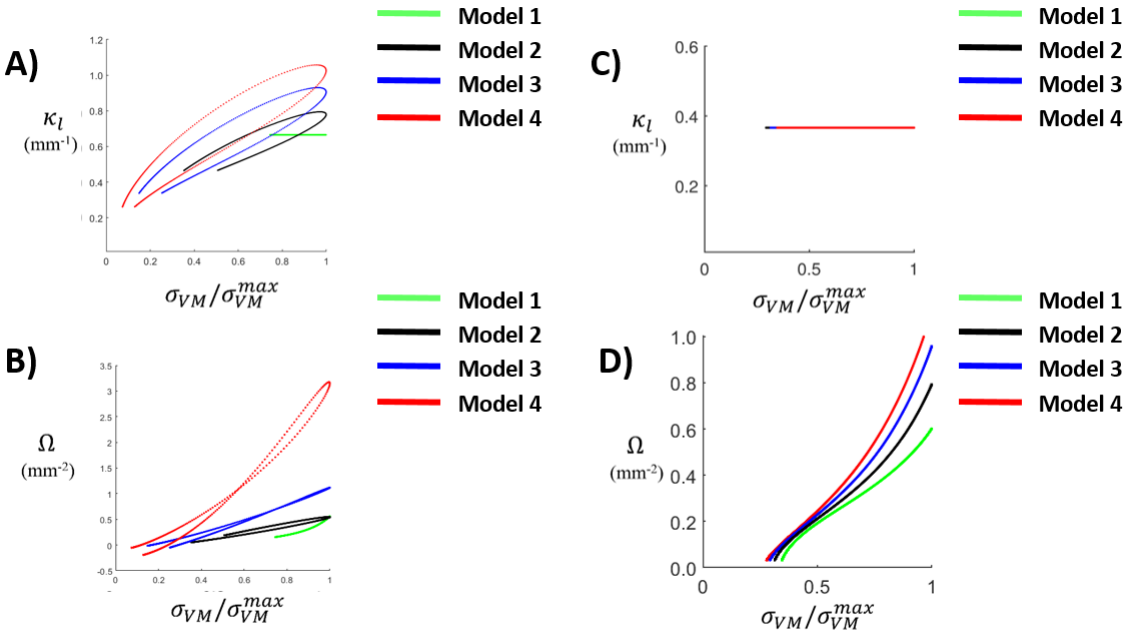

Figure 5.9. *The values calculated for lumen curvature (κ_l) and Ω in stenotic models (A) and (B), respectively. The values obtained for lumen curvature (κ_l) and Ω in outward remodelled vessels sections (C) and (D), respectively. The model numbers associate with the number of models in Figures 5.7 and 5.8.*

5.3.2 3-D Idealized modes

Figure 5.10 (A) shows the geometry of the lumen and IM boundaries of the idealized 3-D stenotic geometry. Figure 5.10 (B) and (C) are color-coded contour plots of Ω and σ_{VM} in the

stenotic geometry projected onto a 2-D plane. Note that there are 10 locations of notably high σ_{VM} in this geometry, each of which correspond to areas with high values of Ω.

The analysis results for the idealized 3-D outward remodelled geometry are also presented in Figure 5.10. Figure 5.10 (D), (E) and (F) are contour plots giving 2-D projections of κ_l, Ω, and σ_{VM}, respectively, in the 3-D outward remodelled geometry. Note that Ω is a good predictor of the two locations of high σ_{VM} in the geometry. However, κ_l is highest in the central regions which does not correspond to the regions of highest stress.

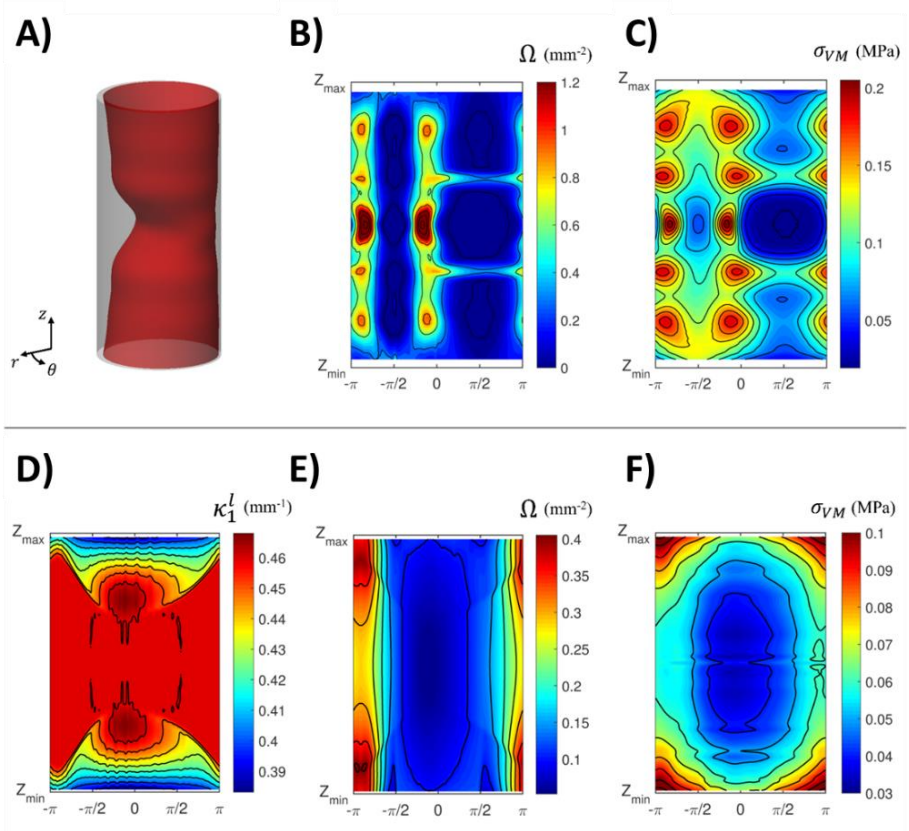

Figure 5.10. *A) Idealized 3-D stenotic geometry highlighting the lumen surface. B) Contour plot of the Ω at the lumen surface unwrapped onto a plane from −π to +π. C) Contour plot of the σ_{VM} at the lumen surface unwrapped onto a plane from −π to π. Analysis results of the idealized 3-D outward remodelled geometry. D) Contour plot of the lumen curvature at the lumen surface unwrapped onto a plane from +π to −π. E) Contour plot of the Ω at the lumen surface unwrapped onto a plane. F) Contour plot of the σ_{VM} at the lumen surface unwrapped onto a plane.*

5.3.3 3-D plaque geometry

The results of geometrical assessment of 3-D plaques along with stress and damage analysis are presented in Figure 5.11. Each geometry consists of five components, namely fibrous cap, lipid pool, fibrotic media, media and adventitia. The geometries of sections (A) to (C) of Figure 5.11 are associated with plaques which had not been ruptured. Sections (D) and (E) present

geometries of plaques which ruptured. To perform our geometrical assessment, these geometries were subjected to blood pressure firstly and then the boundary of the lumen and intimal-media layer were extracted. To capture the deformation of these boundaries after imposing the blood pressure, both isotropic and CDM models were used independently. The results obtained for Ω using the two different constitutive models are compared in the first part of each section (part (I)). The values obtained for Ω are also compared with the accumulated damage in the collagen fibres in the luminal side of these geometries in this section. In the second section for each artery (part (II)), the values of von-Mises stress on the luminal surface obtained from isotropic and CDM models are compared. It should be noted that since the luminal nodes were used for our geometrical assessment, the values of damage and von-Mises stress are also extracted from the nodes on the lumen. It can be seen from this figure that similar values have been obtained for Ω using both isotropic and CDM material models, confirming that calculation of Ω is independent of the choice of constitutive model, even though it is established on deformed geometries. This figure also shows that, similar areas were determined as areas at high risk of plaque rupture using the different metrics.

The contour plots of von-Mises stress, calculated from isotropic and CDM constitutive models, along with contour plots of the values obtained for damage accumulation in the collagen fibres are shown in Figure 5.12. It should be mentioned that all of the geometries are shown in the deformed configuration. The undeformed geometry of each plaque was shown in Figure 5.11.

Finally, the lumen and IM boundaries of a branch of a common carotid artery are shown in Figure 5.13 (A). Figure 5.13 (B) is a 2-D projection of Ω obtained for the lumen of the artery. Figure 5.13 (C) and (D) present the von-Mises stress calculated from isotropic and CDM constitutive models, respectively. Figure 5.13 (E) shows the distribution of accumulated damage in the collagen fibres in the lumen of the vessel wall. It should be mentioned that Ω was calculated using the geometry in the undeformed configuration as this artery was constructed while the lumen was subjected to blood pressure using CT images. The counter plots of von-Mises stress and damage in the collagen fibres are made in the deformed configuration after imposing the blood pressure

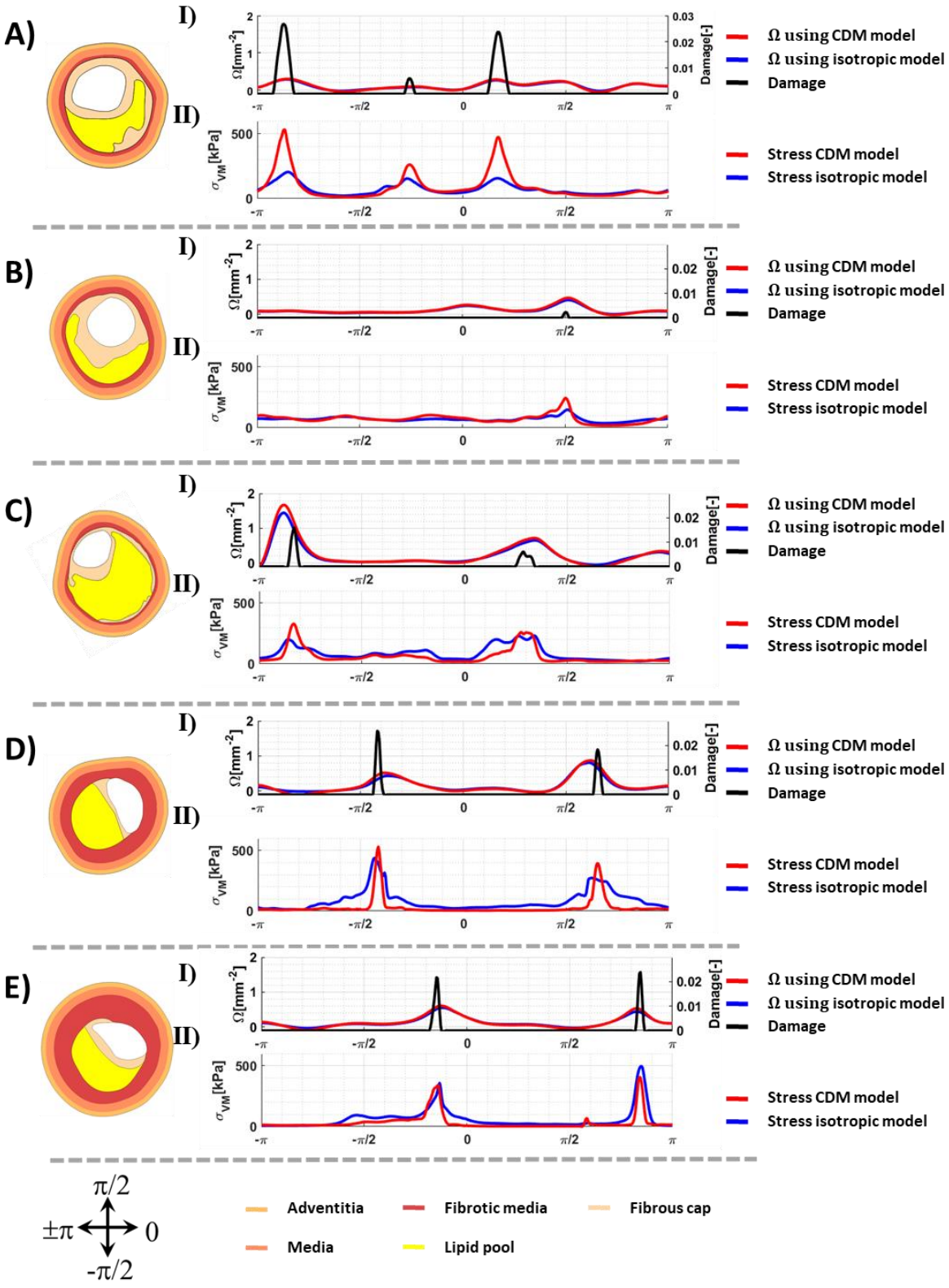

Figure 5.11. *Analysis results for the un-ruptured (A)-(C) and ruptured plaques (D)-(E)*

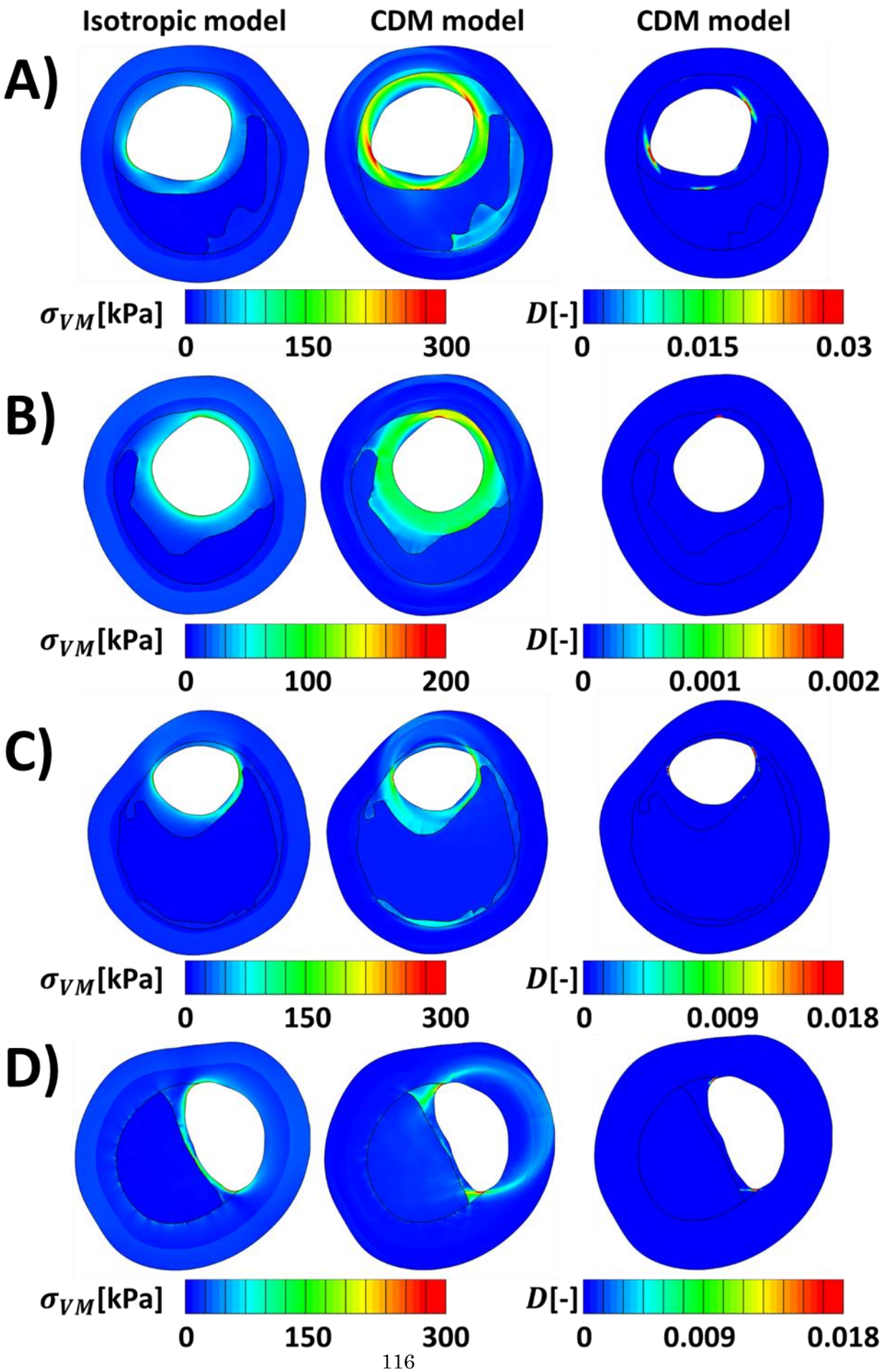
Isotropic model
CDM model
CDM model
A)
σ_{VM}[kPa]
0
150
300
D[-]
0
0.015
0.03
B)
σ_{VM}[kPa]
0
100
200
D[-]
0
0.001
0.002
C)
σ_{VM}[kPa]
0
150
300
D[-]
0
0.009
0.018
D)
σ_{VM}[kPa]
0
150
300
D[-]
0
0.009
0.018

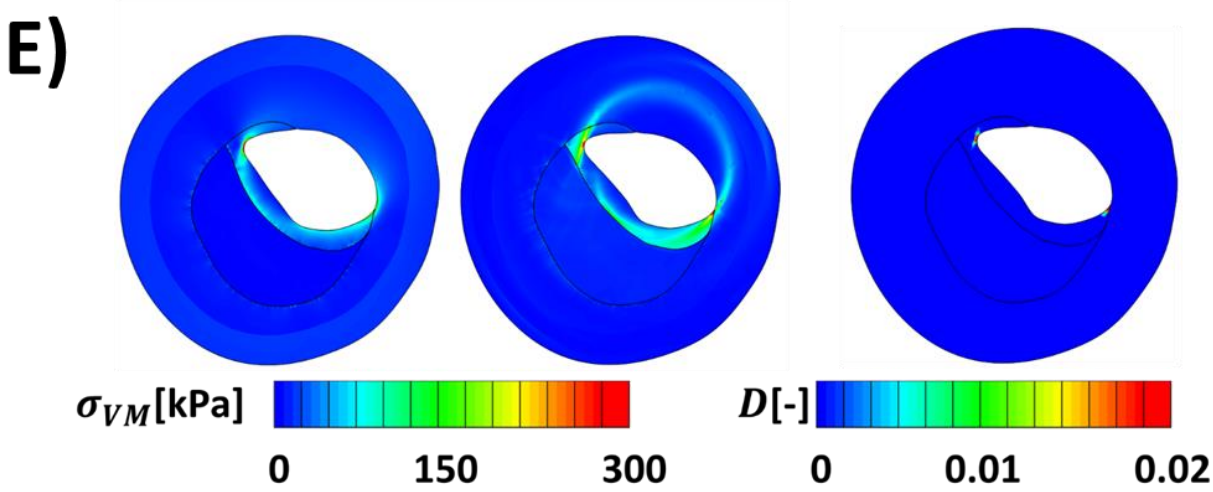

Figure 5.12. *The counterplots of von-Mises stress and damage accumulation in the collagen fibres in the geometries of Figure 5.11.*

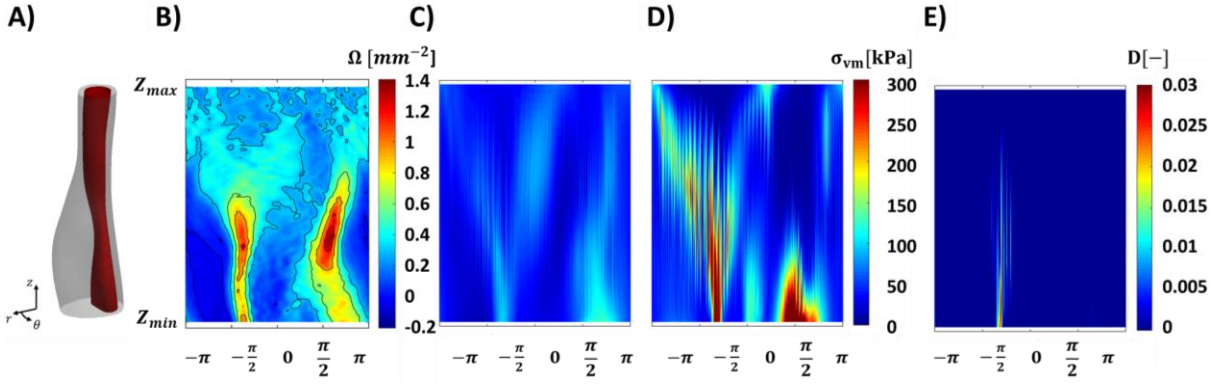

Figure 5.13. *A) Realistic 3-D stenotic geometry highlighting the lumen surface. B) Contour plot of Ω. C) Contour plot of the von-Mises stress calculated using the isotropic constitutive model. D) Contour plot of the von-Mises stress calculated using the CDM model. E) Contour plot of the damage accumulation in the collagen fibres calculated using the CDM model at the lumen surface.*

5.4 Discussion

In this study, different metrics were employed to distinguish the areas at high risk of atherosclerotic plaque rupture in carotid arteries. A new geometrical metric (Ω) is introduced and its performance was initially examined systematically using 2-D and 3-D idealized vessel geometries as showed in sections 5.3.1 and 5.3.2. Using idealized geometries it was also shown that lumen curvature by itself cannot be a sufficient indicator of vulnerability of plaques particularly in the case of positive remodelling. The results obtained from this part of the study showed that both the stress metric (von-Mises stress) and Ω predict similar areas to be at high risk plaque rupture.

In the next step of this study, we compared the rupture prone areas predicted using different metrics on real 3-D plaque geometries, see Figure 5.11. These geometries were obtained from a study conducted by (Li et al. 2006) using histological techniques. Availing of geometries obtained from histology we could find the un-loaded configuration of these diseased arteries. The boundaries of the luminal and IM surfaces were obtained after 100 cycles of loading and unloading between the blood pressure at systole and diastole to perform the geometrical assessment. A damage function was also incorporated in the constitutive model to investigate damage accumulation in collagen fibres in these geometries. 2nd order Mooney–Rivlin material model was also used to perform a stress analysis on these geometries using an isotropic material model. Doing this we were able to compare the predicted areas at high risk of plaque rupture using different metrics: Ω, damage, σ_{vms} (obtained using both isotropic and CDM material models). Interestingly, it was observed that the novel geometrical metric can successfully predict the areas with higher damage accumulation in collagen fibres and von-Mises stress in these diseased atherosclerotic arteries, see Figure 5.11 and 5.12.

In the final stage of this study, we examined the aforementioned indicators of the plaque rupture risk to assess the vulnerability of a plaque in a branch of human carotid artery obtained from CT image from a patient who was undergoing endarterectomy surgery, see Figure 5.13. The results of this simulation showed that von-Mises stress calculated using isotropic and CDM material models indicate similar areas at high risk of plaque rupture. Higher values of damage in collagen fibres was also accumulated at areas with higher von-Mises stress. Larger values of Ω were also obtained at these areas. Although all these techniques predict similar areas to be at high risk of plaque rupture, there are limitations associated with stress and damage calculations in this simulation. Firstly, in this simulation we did not calculate the unloaded state of the vessel wall. Also we assumed that no stress or damage was accumulated in the vessel wall at the configuration we obtained our geometry and prior to our simulation. These limitations are present in many studies performing FE analysis on real vessel geometries (Creane et al. 2010a; Hariton et al. 2007; Teng et al. 2010b), just to name a few. Many studies have emphasized the importance of obtaining the unloaded geometry of the arteries (Chandra et al. 2016; Raghavan et al. 2006; Riveros et al. 2013). Secondly, we did not incorporate the residual stress in the arterial wall. Studies such as (Alastrué et al. 2010; Schroder and Brinkhues 2014) have suggested numerical methods for estimating the residual stress in the vessel wall. Thirdly, in this study, we tried to calculate the damage threshold in collagen fibres by performing a closing angle simulation and measuring the values of strain energy function per reference volume. Although a decomposition of deformation gradient tensor before and after loading the vessel was performed to accurately measure the damage threshold for collagen fibres, assuming a

constant value for opening angle for an artery is over simplified. Ghasemi et al. (2018) explored the influence of this damage threshold on the capturing the overall mechanical behaviour of healthy arteries harvested from young swines undergoing supra-physiological loads. In that study, the damage threshold for collagen fibres was determined using the experimental data in (Converse et al. 2018; Zitnay et al. 2017) where collagen hybridizing peptide (CHP) was used to assess the damage accumulation in the collagen fibres in the tissue. Such experimental studies can further inform damage models to more accurately investigate damage accumulation in the arterial wall.

In this study, a CDM model was used to capture both discontinuous and continuous damage accumulation in the tissue by assigning two separate internal variables for these two phenomena. Similar approaches were used in studies such as (Balzani and Schmidt 2015; Ghasemi et al. 2018; Miehe 1995). Doing this, we observed that damage accumulated in the collagen fibres of the diseased vessels even at physiological blood pressure. This was due to the high stress concentrations at regions of plaque shoulders in the arterial walls.

Another important limitation which can be associated with the calculation of stress and damage in collagen fibres in this study is that a constant distribution of fibres was assumed through the arterial wall thickness. The important role of distribution of fibres through the wall thickness has been discussed in studies such as (Gasser et al. 2006; Holzapfel et al. 2015). Studies such as (Akyildiz et al. 2017) showed that orientation of collagen fibres vary in different regions of the atherosclerotic plaques. Advancements in imaging techniques such as DTI may reveal more information on the orientation of collagen fibres in healthy and diseased arteries, but these techniques are currently still limited to *ex vivo* observations (Akyildiz et al. 2017; Shahid et al. 2017). In future, this information could be used to more accurately predict the mechanical behaviour of healthy and diseased arterial tissue in constitutive models and FE simulations.

In this study, we also did not investigate the damage accumulation in the non-collagenous tissue. The importance of damage accumulation in the elastin fibre and extracellular matrix are emphasised in studies such as (Ghasemi et al. 2018; Weisbecker et al. 2013). The main reason that we did not incorporate damage accumulation in the non-collagenous tissue in this study was the lack of material properties for plaques.

Despite all of the aforementioned limitations associated with the stress and damage calculations in this study, and many other similar studies in the literature, the proposed novel geometrical metric could successfully distinguish the areas at high risk of atherosclerotic plaque rupture. It was shown that this new metric is insensitive to material property choice

by calculating the Ω metric from loaded geometries using both isotropic and anisotropic material models, see Figure 5.11.

Using vessel geometry as the basis for a clinical rupture risk metric has several benefits over a stress analysis. The necessary geometric information can be easily obtained from anatomical MRI or CT scans (Creane et al. 2010b), and curvature evaluations are computationally inexpensive; taking approximately 100 seconds. FE simulations require vessel material properties, and it is not currently possible to obtain such patient specific material properties in a non-invasive manner. Consequently, such analyses are somewhat limited in their value. In addition, FE models must be setup, and their results interpreted, by expert engineers who are typically not members of hospital staff. In contrast, geometric analyses may be easily performed and interpreted by radiographers and clinicians, without the need for patient specific vessel material properties. However, such a geometrical metric must be examined on a large number of asymptomatic and symptomatic patients. The result of this assessment can be used to define thresholds for the values of Ω at different stages of atherosclerotic plaque development. This valuable data could then be potentially used as a clinical tool for assessing the risk of stroke.

This study utilizes a robust methodology for the calculation of 2-D and 3-D curvatures. In particular, the authors found the 2-D curvature calculation method outlined in previous studies (Akyildiz et al. 2016; Teng et al. 2010a), where the circumcircle is created from three adjacent points on the lumen and the inverse of its radius is taken as the curvature, to be overly-sensitive to point spacing and precise point location. In contrast, the 3-D curvature calculation algorithm used here, and previously presented by Rusinkiewicz et al. (Rusinkiewicz 2004), produces consistent, accurate results when checked against shapes of known curvature.

In clinical studies, the curvature metric outlined here could be used alone or in conjunction with stress analyses as a means of identifying a rupture index in a similar manner to the study by Vande Geest et al. (2006) on abdominal aortic aneurysms. In that study, the estimated wall stresses were divided by tissue strength, where strength was measured based on intraluminal thickness (ILT), normalised vessel diameter (NORD), gender and genetics to establish a rupture index, i.e. a measure of potential risk of rupture. In this manner, the increased number of clinical measures provides a more powerful metric for identifying rupture risk.

The results presented in this study represent a proof-of-concept for the use of the weighted curvature difference, Ω, as a clinical metric for assessing the risk of rupture of an atherosclerotic vessel. To the best of the author's knowledge, full 3-D curvature analysis of

atherosclerotic vessels, both idealized and realistic vessels, has not previously been performed. A robust methodology for the calculation of κ_l and Ω in 3-D has been outlined in this study. Future work will aim to analyse large numbers of 2-D and 3-D patient geometries using this new metric.

Chapter 6 Final discussion, concluding remarks and future perspectives

6.1 Final discussion

Stroke is reported among the top 10 causes of death (Benjamin et al. 2017). Growth, development and rupture of atherosclerotic plaques in the carotid arteries is a major cause of stroke. Development of atherosclerotic plaques in arteries alters both mechanical behaviour and geometry of the vessel wall. A good understanding of the mechanical behaviour of the healthy and diseased arterial tissue can enhance the treatment and predictability of the risk of plaque rupture in asymptomatic and symptomatic patients.

Many studies in the literature have associated the risk of atherosclerotic plaque rupture with areas subjected to high stresses in the arterial wall (Li et al. 2006; Teng et al. 2010b). These observations suggest that development of the plaque in a healthy artery imposes high supra-physiological loads on the vessel wall even at physiological blood pressure. Treatment of the atherosclerotic plaque also requires surgical interventions such as endarterectomy or stenting that can impose large loads on the vessel. Thus, there is a need for further understanding the response of the arterial tissue under supra-physiological loading conditions. In the first study of this thesis, Chapter 3, the response of the arterial wall to such high loads was investigated. Collagen fibres are the main load bearing constituent of the vessel wall. To distinguish the role of the collagenous and non-collagenous tissue in response to high loads in the arterial tissue, cyclic mechanical tests on the intact and collagen fibre digested samples were performed. Four passive damage relevant phenomena were investigated in both collagenous and non-collagenous samples, namely (i) Mullins effect, (ii) hysteresis, (iii)permanent set and (iv) rupture of the tissue. The result of that study suggested that continuous and discontinuous softening phenomenon in the arterial tissue are mainly due to the presence of the collagen fibres. However, similar values were obtained for the permanent set phenomenon in the intact and collagen fibre digested samples in the axial and circumferential directions of the vessel wall. These observations emphasised the important role of the non-collagenous tissue in the permanent deformation of the arterial tissue. In the next step of this study we proposed a constitutive model to capture all these damage relevant phenomena in the non-collagenous and collagenous arterial tissue. To the best of the author's knowledge, it was the first time

that a structural constitutive model was developed and verified to capture the previously mentioned damage relevant phenomena in intact and non-collagenous tissue.

Having observed the important role of the collagen fibres in the response of the arteries to loads and damage accumulation in the arterial tissue, the distribution of the collagen fibres in healthy and diseased carotid bifurcations was investigated in Chapter 4 of this thesis. To-date many constitutive laws are proposed in the literature that incorporate the distribution of collagen fibres to more accurately capture the behaviour of the arterial tissue in the both axial and circumferential directions simultaneously (Gasser et al. 2006; Holzapfel et al. 2000; Zulliger et al. 2004). However, most of these studies consider a constant orientation of the fibres through the arterial wall thickness. Experimental observations confirm the variations in the distribution of collagen fibres in different layers of the arterial wall (Gaul et al. 2017; Krasny et al. 2017). There has been an increase in the interest in exploring the orientation of fibres in the atherosclerotic plaque over the last few years. However, inconclusive observations are reported in different studies regarding the distribution of the collagen fibres in different regions of the plaque (Pagiatakis et al. 2015). Re-orientation of collagen fibres is part of the remodelling process in the arteries that occurs both instantaneously and over time to maximize the load bearing capacity of the vessel wall (Baaijens et al. 2010). It is well-known that in the healthy arterial wall, collagen fibres grow and re-orient in their optimum configuration to maximize the load bearing capacity of the tissue (Driessen et al. 2008; Hariton et al. 2006). Growth and production of the collagen fibres in healthy arterial tissue is due to the presence of the cells. However, there is a paucity of the VSMCs in diseased arterial tissue such as atherosclerotic plaques (Bennett 1999). The paucity of the cells in the arterial tissue is correlated to both alterations in the geometry and lack of remodelling in the diseased vessel wall (Bennett 1999). This lack of remodelling can manifest itself as a lack of re-orientation of fibres toward the favourable collagen fibre distribution which weakens the vessel wall and increases the risk of plaque rupture. In Chapter 4, the influence of the re-orientation of the collagen fibres on the mechanical behaviour of the arterial wall was firstly demonstrated. It was shown that due to the re-orientation of fibres toward the fibre distribution, the maximum principal strains in the arterial tissue decrease. This contraction of the arterial tissue during the re-orientation process increases the integrity of the vessel wall. In the next stage of that study, the distributions of collagen fibres in healthy and diseased carotid bifurcations were predicted. It was shown that values of the maximum principal strains decreased as a result of collagen fibre re-orientation in the diseased arteries. These observations were in agreement with the results of studies such as (Huang et al. 2016; Zhang et al. 2015) where higher strain levels were correlated to higher levels of vulnerability of plaques in carotid arteries. A novel remodelling metric (RM) was also introduced to characterize the lack of remodelling in the

diseased arterial tissue in terms of lack of re-orientation. Such a remodelling metric can be used as an indicator of the lack of remodelling in arterial tissue which could increase the risk of atherosclerotic plaque rupture.

Both stress and RM values can successfully characterise the areas at higher risk of plaque rupture in arterial tissue, however the application of these metrics as a preclinical tool for assessing the vulnerability of atherosclerotic plaque requires accurate stress measurement. Material properties play an important role in accurate prediction of stresses in arterial tissue in the deformed configuration. Performing uniaxial mechanical tests in the axial and circumferential directions of the vessel wall and pressure inflation tests are among the most commonly used mechanical tests to calibrate different constitutive laws and obtain the mechanical properties. However, mechanical properties of arterial samples vary according to gender, age and even location of the specimens. Moreover, performing mechanical tests on patient specific specimens requires harvesting the tissue from a patient which isn't feasible. Performing accurate stress analysis also can be very time consuming particularly when it comes to large models such as diseased bifurcations. So, there is a need for a metric that more effectively characterises the risk of atherosclerotic plaque rupture. Such a metric can be used along with other indicators of risk of plaque rupture to more efficiently assess the vulnerability of the plaques in the vessel wall. In chapter 5 of this thesis a novel geometrical metric was introduced to distinguish the areas at higher risk of plaque rupture. The accuracy of this new geometrical metric was assessed systematically using parameterized 2-D idealized models, 3-D idealized models, and real vessel geometries. The high-risk areas detected using this geometrical metric were then compared with high risk areas obtained from stress analyses on isotropic and anisotropic material models and areas with highest damage accumulation in the collagen fibres within the arterial wall. The result of this study confirmed that such a geometrical metric can successfully determine rupture prone areas in the vessel wall independent of any material properties. This geometrical metric can also be used in parallel with the remodelling metric, RM, to indicate the areas with the poorest remodelling in the arterial wall, see Appendix D.

The studies conducted in this thesis improve the assessment of the vulnerability of atherosclerotic plaques by providing further insights into the mechanical properties of healthy and diseased arterial tissue. The presented computational models in this thesis enhance our understanding of mechanically induced collagen fibre remodelling in healthy and diseased arterial tissue. Such information can not only be used to assess the vulnerability of the atherosclerotic plaque rupture in the arterial wall but also aids the design and development of improved biomedical devices. The computational models presented in this thesis can be adjusted to optimize various aspects of biomedical devices according to the response of

different constituents of the healthy and diseased arteries. The application of these computational models is not limited to arterial tissues. It is expected that with relatively minor modifications of these algorithms, the mechanical response and damage accumulation of other types of soft biological tissues such as aortic valve, pericardium, myocardium and cornea could be studied.

6.2 Concluding Remarks

The main objective of this thesis was to improve the risk assessment of atherosclerotic plaque rupture in the arterial tissue which was achieved by experimental and computational analysis of the heathy and diseased arterial tissue. The key findings of the studies conducted in this thesis can be summarised as follows;

- A constituent specific study was performed to investigate the role of the intact and non-collagenous arterial tissue in response to the supra-physiological loads. This study showed that continuous and discontinuous softening in the arterial tissue is mainly due to the presence of collagen fibres. However, permanent set phenomenon was found to be associated with non-collagenous tissue.

- A structural constitutive model was implemented and verified to capture all the passive damage relevant phenomena in the non-collagenous and collagenous arterial tissue, namely (i) Mullins's effect, (ii) hysteresis, (iii) permanent set and (iv) collagen fibre rupture and tissue failure.

- A novel meshing technique was proposed to generate high quality structured hexahedral meshes for healthy and diseased carotid bifurcations and segmenting the arterial wall.

- A stress modulated re-orientation algorithm was implemented where both angle and dispersion of the collagen fibres were subjected to remodelling rules. Using this model, the important role of the re-orientation of collagen fibres in maintaining the integrity

of the arterial tissue and preserving the non-collagenous tissue was explained.

- The optimum distribution of collagen fibres was characterized in both healthy and diseased bifurcations. Such distribution of fibres maximizes the load bearing capacity of healthy and diseased arterial tissue and would minimize the risk of plaque rupture.

- The influence of re-orientation of collagen fibres toward an optimum configuration on the mechanical behaviour of the arterial wall was elucidated. It was shown that re-orientation of fibres increases the stability of the atherosclerotic plaque which would result in decreasing the risk of plaque rupture.

- Lack of remodelling in terms of re-orientation of fibres in the diseased carotid bifurcations was characterized by introducing a novel remodelling metric which evolved during the re-orientation process using internal variables.

- A novel geometrical metric was introduced for non-destructive detection of areas at higher risk of atherosclerotic plaque rupture. The accuracy and functionality of this new metric was systematically examined using idealized and realistic 2-D and 3-D geometries.

6.3 Future perspectives

Whilst this thesis makes considerable advancements in terms of assessment of risk of atherosclerotic plaque rupture in carotid arteries, the following recommendations are proposed for future investigations:

- In this thesis, the functionality of the proposed remodelling metric (RM) was assessed using five geometries obtained from symptomatic patients who were under evaluation for an endarterectomy surgery. Further assessment of this metric on larger cohorts of symptomatic and asymptomatic patients can provide more insights into the performance of this metric in assessing the risk of atherosclerotic plaque rupture.

Moreover, such studies are required to characterize an appropriate threshold between the lack of remodelling in terms of re-orientation between symptomatic and asymptomatic patients.

- The geometrical metric (Ω) proposed in this thesis was systematically assessed using idealized 2D, idealized 3D and realistic 3D geometries. Similar to the remodelling metric (RM), this metric is also recommended to be assessed on a larger number of geometries from symptomatic and asymptomatic patients. The result of such a study can be used to define Ω as a clinical tool for characterizing the risk of rupture particularly in asymptomatic patients.

- The constitutive model proposed in chapter 3 of this thesis can be used in conjunction with the re-orientation algorithm proposed in chapter 4 to determine the quality and orientation of collagen fibres in the arterial wall under high supra-physiological loads such as stenting or angioplasty. Such information can provide further insight into the role of the remodelling process in the response of the arterial tissue under high loads. The results of such a study can also be used to optimize biomedical devices to reduce damage to the arterial wall over time.

- In this thesis, the influence of the cells on the mechanical behaviour of the arterial tissue was neglected. A brief review of the constitutive models employed to characterise the behaviour of cells in arterial tissue is provided in chapter 2 of this thesis. These constitutive models can be employed in parallel to the computational models proposed in this thesis to gain more insights into the mechanical behaviour of the arterial wall *in vivo*.

- The influence of collagen fibre content in the response of the arterial tissue can also be added to the constitutive models proposed in Chapters 3 and 4. Such models can be

used to further investigate the growth and remodelling process and their influence on the response of the arteries to physiological and supra-physiological loads.

- The geometrical metric proposed in Chapter 5 of this thesis can also be used in conjunction with the constitutive models, suggested above, to more efficiently assess the risk of atherosclerotic plaque rupture in carotid arteries. This can be particularly useful as diseased carotid bifurcations are multi-component complex geometries and performing computational studies on them can be very resource intensive.

- Advancements in imaging techniques such as DTI also show great promise for gaining further insight into the underlying structure of healthy and diseased arteries. Such experimental observations can be used to further validate and improve the proposed constitutive models in this thesis.

- Finally there is a lack of information about the mechanical response of the carotid atherosclerotic plaques in human carotid arteries. A robust experimental study to investigate the mechanical behaviour and structure of the constituents of this tissue in different directions and loading conditions, for both physiological and supra-physiological levels, can provide further insights into developing clinical and pre-clinical metrics for assessing the vulnerability of atherosclerotic plaques in human carotid arteries. Such information can be used to inform different forms of constitutive laws which can be employed to predict the mechanical behaviour of the arterial tissue and predict the risk of plaque rupture.

References

Acar M, Salbacak A, Sakarya ME, Zararsiz I, Ulusoy M (2013) The morphometrical analysis of the external carotid artery and its branches with multidetector computerized tomography angiography technique International Journal of Morphology 31:1407-1414

Agewall S, Henareh L, Kublickiene KJA (2006) Endothelial function in conduit and resistance arteries in men with coronary disease 184:130-136

Akyildiz AC, Chai CK, Oomens CWJ, van der Lugt A, Baaijens FPT, Strijkers GJ, Gijsen FJH (2017) 3D Fiber Orientation in Atherosclerotic Carotid Plaques J Struct Biol 200:28-35 doi:10.1016/j.jsb.2017.08.003

Akyildiz AC et al. (2016) The effects of plaque morphology and material properties on peak cap stress in human coronary arteries Computer Methods in Biomechanics and Biomedical Engineering 19:771-779 doi:10.1080/10255842.2015.1062091

Alastrué V, Garía A, Peña E, Rodríguez J, Martínez M, Doblaré M (2010) Numerical framework for patient-specific computational modelling of vascular tissue International Journal for Numerical Methods in Biomedical Engineering 26:35-51

Alastrue V, Pena E, Martinez MA, Doblare M (2007) Assessing the use of the "Opening angle method" to enforce residual stresses in patient-specific arteries Annals of Biomedical Engineering 35:1821-1837 doi:10.1007/s10439-007-9352-4

Alastrue V, Pena E, Martinez MA, Doblare M (2008) Experimental study and constitutive modelling of the passive mechanical properties of the ovine infrarenal vena cava tissue J Biomech 41:3038-3045 doi:10.1016/j.jbiomech.2008.07.008

Amponsah WA, Tabi MM, Gibbison GAJOJoRN, Care H (2015) Health disparities in cardiovascular disease and high blood pressure among adults in rural underserved communities 15:185-208

Aparício P, Thompson MS, Watton PNJJob (2016) A novel chemo-mechano-biological model of arterial tissue growth and remodelling 49:2321-2330

Armentano RL et al. (2006) An in vitro study of cryopreserved and fresh human arteries: a comparison with ePTFE prostheses and human arteries studied non-invasively in vivo Cryobiology 52:17-26

Auerbach O, Garfinkel LJC (1980) Atherosclerosis and aneurysm of aorta in relation to smoking habits and age 78:805-809

Baaijens F, Bouten C, Driessen N (2010) Modeling collagen remodeling J Biomech 43:166-175 doi:10.1016/j.jbiomech.2009.09.022

Balzani D, Brinkhues S, Holzapfel GA (2012) Constitutive framework for the modeling of damage in collagenous soft tissues with application to arterial walls Computer Methods in Applied Mechanics and Engineering 213:139-151 doi:10.1016/j.cma.2011.11.015

Balzani D, Schmidt T (2015) Comparative analysis of damage functions for soft tissues: Properties at damage initialization Math Mech Solids 20:480-492 doi:10.1177/1081286513504945

Balzani D, Schroder J, Gross D (2006) Simulation of discontinuous damage incorporating residual stresses in circumferentially overstretched atherosclerotic arteries Acta Biomater 2:609-618 doi:10.1016/j.actbio.2006.06.005

Benjamin EJ et al. (2017) Heart disease and stroke statistics—2017 update: a report from the American Heart Association Circulation 135:e146-e603

Bennett MR (1999) Apoptosis of vascular smooth muscle cells in vascular remodelling and atherosclerotic plaque rupture Cardiovascular research 41:361-368

Bentzon JF, Otsuka F, Virmani R, Falk E (2014) Mechanisms of plaque formation and rupture Circ Res 114:1852-1866 doi:10.1161/CIRCRESAHA.114.302721

Biasiolli L, Lindsay AC, Chai JT, Choudhury RP, Robson MDJJoCMR (2013) In-vivo quantitative T 2 mapping of carotid arteries in atherosclerotic patients: segmentation and T 2 measurement of plaque components 15:69

Bots ML, Hoes AW, Koudstaal PJ, Hofman A, Grobbee DE (1997) Common carotid intima-media thickness and risk of stroke and myocardial infarction Circulation 96:1432-1437

Brodland GW How computational models can help unlock biological systems. In: Seminars in cell & developmental biology, 2015. Elsevier, pp 62-73

Brown LC, Powell JT (1999) Risk factors for aneurysm rupture in patients kept under ultrasound surveillance. UK Small Aneurysm Trial Participants Ann Surg 230:289-296; discussion 296-287

Burton AC (1962) Physical principles of circulatory phenomena: the physical equilibria of the heart and blood vessels Handbook of physiology 1:85-106

Cai J et al. (2005) In vivo quantitative measurement of intact fibrous cap and lipid-rich necrotic core size in atherosclerotic carotid plaque: comparison of high-resolution, contrast-enhanced magnetic resonance imaging and histology 112:3437-3444

Calvo B, Pena E, Martinez MA, Doblare M (2007) An uncoupled directional damage model for fibred biological soft tissues. Formulation and computational aspects International Journal for Numerical Methods in Engineering 69:2036-2057 doi:10.1002/nme.1825

Calvo B, Pena E, Martins P, Mascarenhas T, Doblare M, Jorge RN, Ferreira A (2009) On modelling damage process in vaginal tissue Journal of biomechanics 42:642-651

Cardamone L, Valentin A, Eberth JF, Humphrey JD (2009) Origin of axial prestretch and residual stress in arteries Biomech Model Mechanobiol 8:431-446 doi:10.1007/s10237-008-0146-x

Chaboche J-L (1981) Continuous damage mechanics — A tool to describe phenomena before crack initiation Nuclear Engineering and Design 64:233-247 doi:http://dx.doi.org/10.1016/0029-5493(81)90007-8

Chaboche J (1974) Une loi différentielle d'endommagement de fatigue avec cumulation non linéaire Revue française de mécanique 50:71-82

Chai C.K et al. (2015) Local anisotropic mechanical properties of human carotid atherosclerotic plaques–Characterisation by micro-indentation and inverse finite element analysis 43:59-68

Chai, C. K. (2015). Biomechanical properties of atherosclerotic plaques (Doctoral dissertation). Technische Universiteit Eindhoven. Retrieved from: https://research.tue.nl/en/publications/biomechanical-properties-of-atherosclerotic-plaques

Chai JT et al. (2017) Quantification of lipid-rich core in carotid atherosclerosis using magnetic resonance T2 mapping: relation to clinical presentation 10:747-756

Cham BE, Chase TR (2013) Intravascular infusion of autologous delipidated plasma induces antiatherogenic lipoproteins and causes regression of atherosclerosis—Studies in non-primates, monkeys and humans

Chandra S, Gnanaruban V, Riveros F, Rodriguez JF, Finol EAJJobe (2016) A Methodology for the Derivation of Unloaded Abdominal Aortic Aneurysm Geometry With Experimental Validation 138:101005

Chuong C, Fung Y (1986) Residual stress in arteries. In: Frontiers in biomechanics. Springer, pp 117-129

Converse MI, Walther RG, Ingram JT, Li Y, Yu SM, Monson KL (2018) Detection and characterization of molecular-level collagen damage in overstretched cerebral arteries Acta Biomater 67:307-318 doi:10.1016/j.actbio.2017.11.052

Creane A, Maher E, Sultan S, Hynes N, Kelly DJ, Lally C (2010a) Finite element modelling of diseased carotid bifurcations generated from in vivo computerised tomographic angiography Computers in Biology and Medicine 40:419-429

Creane A, Maher E, Sultan S, Hynes N, Kelly DJ, Lally C (2010b) Finite element modelling of diseased carotid bifurcations generated from in vivo computerised tomographic angiography Comput Biol Med 40:419-429 doi:10.1016/j.compbiomed.2010.02.006

Creane A, Maher E, Sultan S, Hynes N, Kelly DJ, Lally C (2011a) Prediction of fibre architecture and adaptation in diseased carotid bifurcations Biomechanics and modeling in mechanobiology 10:831-843

Creane A, Maher E, Sultan S, Hynes N, Kelly DJ, Lally C (2011b) A remodelling metric for angular fibre distributions and its application to diseased carotid bifurcations Biomechanics and Modeling in Mechanobiology 11:869-882 doi:10.1007/s10237-011-0358-3

Curran KM, Emsell L, Leemans A (2016) Quantitative DTI measures. In: Diffusion Tensor Imaging. Springer, pp 65-87

Davies PF (2009) Hemodynamic shear stress and the endothelium in cardiovascular pathophysiology Nat Clin Pract Cardiovasc Med 6:16-26 doi:10.1038/ncpcardio1397

Davis JR (2004) Tensile testing. ASM international,

De Luca L, Tomai FJBiCD (2015) Biomarkers of Coronary Plaque Composition and Vulnerability:1-17

De Santis G, De Beule M, Segers P, Verdonck P, Verhegghe BJCmib, engineering b (2011a) Patient-specific computational haemodynamics: generation of structured and conformal hexahedral meshes from triangulated surfaces of vascular bifurcations 14:797-802

De Santis G, De Beule M, Van Canneyt K, Segers P, Verdonck P, Verhegghe BJMe, physics (2011b) Full-hexahedral structured meshing for image-based computational vascular modeling 33:1318-1325

Delfino A, Stergiopulos N, Moore JE, Jr., Meister JJ (1997) Residual strain effects on the stress field in a thick wall finite element model of the human carotid bifurcation J Biomech 30:777-786

Demiray H (1972) A note on the elasticity of soft biological tissues Journal of biomechanics 5:309-311

Diani J, Brieu M, Vacherand JM (2006) A damage directional constitutive model for Mullins effect with permanent set and induced anisotropy European Journal of Mechanics - A/Solids 25:483-496 doi:http://dx.doi.org/10.1016/j.euromechsol.2005.09.011

Dorfmann A, Ogden RW (2004) A constitutive model for the Mullins effect with permanent set in particle-reinforced rubber International Journal of Solids and Structures 41:1855-1878 doi:10.1016/j.ijsolstr.2003.11.014

Douglas GR, Brown AJ, Gillard JH, Bennett MR, Sutcliffe MP, Teng ZJAobe (2017) Impact of fiber structure on the material stability and rupture mechanisms of coronary atherosclerotic plaques 45:1462-1474

Driessen NJ, Boerboom RA, Huyghe JM, Bouten CV, Baaijens FP (2003a) Computational analyses of mechanically induced collagen fiber remodeling in the aortic heart valve J Biomech Eng 125:549-557

Driessen NJ, Bouten CV, Baaijens FP (2005a) Improved prediction of the collagen fiber architecture in the aortic heart valve J Biomech Eng 127:329-336

Driessen NJ, Bouten CV, Baaijens FP (2005b) A structural constitutive model for collagenous cardiovascular tissues incorporating the angular fiber distribution J Biomech Eng 127:494-503

Driessen NJ, Cox MA, Bouten CV, Baaijens FP (2008) Remodelling of the angular collagen fiber distribution in cardiovascular tissues Biomech Model Mechanobiol 7:93-103 doi:10.1007/s10237-007-0078-x

Driessen NJ, Peters GW, Huyghe JM, Bouten CV, Baaijens FP (2003b) Remodelling of continuously distributed collagen fibres in soft connective tissues J Biomech 36:1151-1158

Driessen NJ, Wilson W, Bouten CV, Baaijens FP (2004) A computational model for collagen fibre remodelling in the arterial wall J Theor Biol 226:53-64

Duprez DA, Cohn JNJCar (2007) Arterial stiffness as a risk factor for coronary atherosclerosis 9:139-144

El Sayed T, Mota A, Fraternali F, Ortiz M (2008) A variational constitutive model for soft biological tissues Journal of biomechanics 41:1458-1466

Famaey N, Vander Sloten J, Kuhl E (2013) A three-constituent damage model for arterial clamping in computer-assisted surgery Biomechanics and modeling in mechanobiology 12:123-136

Famaey N, Verbeken E, Vinckier S, Willaert B, Herijgers P, Vander Sloten J (2010) In vivo soft tissue damage assessment for applications in surgery Medical engineering & physics 32:437-443

Fausten S, Balzani D, Schröder J (2016) An algorithmic scheme for the automated calculation of fiber orientations in arterial walls Computational Mechanics:1-18

Finlay H, McCullough L, Canham P (1995a) Three-dimensional collagen organization of human brain arteries at different transmural pressures Journal of vascular research 32:301-312

Finlay HM, McCullough L, Canham PBJJovr (1995b) Three-dimensional collagen organization of human brain arteries at different transmural pressures 32:301-312

Flory PJ (1961) Thermodynamic Relations for High Elastic Materials T Faraday Soc 57:829-& doi:Doi 10.1039/Tf9615700829

Franceschini G, Bigoni D, Regitnig P, Holzapfel GA (2006) Brain tissue deforms similarly to filled elastomers and follows consolidation theory J Mech Phys Solids 54:2592-2620 doi:10.1016/j.jmps.2006.05.004

Fukuda K, Iihara K, Maruyama D, Yamada N, Ishibashi-Ueda H (2014) Relationship between carotid artery remodeling and plaque vulnerability with T1-weighted magnetic resonance imaging Journal of Stroke and Cerebrovascular Diseases 23:1462-1470

Fung Y, Liu SJAJoP-H, Physiology C (1992) Strain distribution in small blood vessels with zero-stress state taken into consideration 262:H544-H552

Fung YC (1970) Mathematical representation of the mechanical properties of the heart muscle J Biomech 3:381-404

Fung YC, Fronek K, Patitucci P (1979) Pseudoelasticity of arteries and the choice of its mathematical expression The American journal of physiology 237:H620-631 doi:10.1152/ajpheart.1979.237.5.H620

Fung YJAobe (1991) What are the residual stresses doing in our blood vessels? 19:237-249

García A, Martínez MA, Peña EJJobe (2013) Determination and modeling of the inelasticity over the length of the porcine carotid artery 135:031004

Gasser TC (2011) An irreversible constitutive model for fibrous soft biological tissue: A 3-D microfiber approach with demonstrative application to abdominal aortic aneurysms Acta Biomaterialia 7:2457-2466 doi:10.1016/j.actbio.2011.02.015

Gasser TC, Holzapfel GA (2002) A rate-independent elastoplastic constitutive model for biological fiber-reinforced composites at finite strains: continuum basis, algorithmic formulation and finite element implementation Computational Mechanics 29:340-360 doi:10.1007/s00466-002-0347-6

Gasser TC, Ogden RW, Holzapfel GA (2006) Hyperelastic modelling of arterial layers with distributed collagen fibre orientations Journal of the royal society interface 3:15-35

Gasser TC, Schulze-Bauer CA, Holzapfel GA (2002) A three-dimensional finite element model for arterial clamping J Biomech Eng 124:355-363

Gaul R, Nolan D, Ristori T, Bouten C, Loerakker S, Lally CJAb (2018) Strain mediated enzymatic degradation of arterial tissue: Insights into the role of the non-collagenous tissue matrix and collagen crimp 77:301-310

Gaul RT, Nolan DR, Lally C (2017) Collagen fibre characterisation in arterial tissue under load using SALS Journal of the Mechanical Behavior of Biomedical Materials 75:359-368 doi:10.1016/j.jmbbm.2017.07.036

Geng Y-J, Libby PJTAjop (1995) Evidence for apoptosis in advanced human atheroma. Colocalization with interleukin-1 beta-converting enzyme 147:251

Gestrelius S, Borgstrom P (1986) A dynamic model of smooth muscle contraction Biophysical journal 50:157-169 doi:10.1016/S0006-3495(86)83448-8

Ghaffari M, Hsu C-Y, Linninger AA (2015) Automatic reconstruction and generation of structured hexahedral mesh for non-planar bifurcations in vascular networks. In: Computer Aided Chemical Engineering, vol 37. Elsevier, pp 635-640

Ghasemi M, Nolan DR, Lally C (2018) An investigation into the role of different constituents in damage accumulation in arterial tissue and constitutive model development Biomech Model Mechanobiol doi:10.1007/s10237-018-1054-3

Ghazanfari S, Driessen-Mol A, Strijkers G, Kanters F, Baaijens F, Bouten CJB, communications br (2012) A comparative analysis of the collagen architecture in the carotid artery: second harmonic generation versus diffusion tensor imaging 426:54-58

Gibbons GH, Dzau VJJNEJoM (1994) The emerging concept of vascular remodeling 330:1431-1438

Golledge J, Greenhalgh RM, Davies AH (2000) The symptomatic carotid plaque Stroke 31:774-781

Govindjee S, Simo J (1991) A Micro-Mechanically Based Continuum Damage Model for Carbon Black-Filled Rubbers Incorporating Mullins Effect J Mech Phys Solids 39:87-112 doi:Doi 10.1016/0022-5096(91)90032-J

Gow BS, Taylor MGJCR (1968) Measurement of viscoelastic properties of arteries in the living dog 23:111-122

Gray A, Abbena E, Salamon S (2006) Modern differential geometry of curves and surfaces with Mathematica. Studies in advanced mathematics, 3rd edn. Chapman & Hall CRC, Boca Raton, FL

Gray H (2001) Anatomy of the human body. Philadelphia: Lea & Febiger, 1918; Bartleby. com, 2000.

Greenwald S, Moore J, Rachev A, Kane T, Meister J-JJJobe (1997) Experimental investigation of the distribution of residual strains in the artery wall 119:438-444

Grobbee D, Bots M (1994) Carotid artery intima-media thickness as an indicator of generalized atherosclerosis Journal of internal medicine 236:567-573

Grytz R, Meschke G (2010) A computational remodeling approach to predict the physiological architecture of the collagen fibril network in corneo-scleral shells Biomech Model Mechanobiol 9:225-235 doi:10.1007/s10237-009-0173-2

Guo Z, Sluys L (2008) Constitutive modelling of hyperelastic rubber-like materials HERON, 53 (3)

Gyoneva L, Hovell CB, Pewowaruk RJ, Dorfman KD, Segal Y, Barocas VH (2016) Cell-matrix interaction during strain-dependent remodelling of simulated collagen networks Interface Focus 6:20150069 doi:10.1098/rsfs.2015.0069

Hariton I (2006) Out-of-plane shear deformation of a neo-Hookean fiber composite Physics Letters A 354:156-160

Hariton I, deBotton G, Gasser TC, Holzapfel GA (2006) Stress-driven collagen fiber remodeling in arterial walls Biomechanics and Modeling in Mechanobiology 6:163-175 doi:10.1007/s10237-006-0049-7

Hariton I, deBotton G, Gasser TC, Holzapfel GA (2007) Stress-modulated collagen fiber remodeling in a human carotid bifurcation J Theor Biol 248:460-470 doi:10.1016/j.jtbi.2007.05.037

Harwood J, Mullins L, Payne A (1965) Stress softening in natural rubber vulcanizates. Part II. Stress softening effects in pure gum and filler loaded rubbers Journal of Applied Polymer Science 9:3011-3021

Henry M, Henry I (2017) CAROTID ANGIOPLASTY STENTING WITH THE MICROMESCH STENT Journal of Indian College of Cardiology

Hilbert S, Sword L, Batchelder K, Barrick M, Ferrans VJJoBMRAOJoTSfB, Biomaterials TJSf (1996) Simultaneous assessment of bioprosthetic heart valve biomechanical properties and collagen crimp length 31:503-509

Hill A (1938) The heat of shortening and the dynamic constants of muscle Proceedings of the Royal Society of London B: Biological Sciences 126:136-195

Holzapfel G, Stadler M, Ogden R Aspects of stress softening in filled rubbers incorporating residual strains. In: Proceedings of the First European Conference on Constitutive Models for Rubber, 1999. Balkema, pp 189-193

Holzapfel GA (2000) Nonlinear solid mechanics vol 24. Wiley Chichester,

Holzapfel GA (2008) Collagen in arterial walls: biomechanical aspects. In: Collagen. Springer, pp 285-324

Holzapfel GA, Gasser TC (2001) A viscoelastic model for fiber-reinforced composites at finite strains: Continuum basis, computational aspects and applications Computer Methods in Applied Mechanics and Engineering 190:4379-4403 doi:Doi 10.1016/S0045-7825(00)00323-6

Holzapfel GA, Gasser TC, Ogden RW (2000) A new constitutive framework for arterial wall mechanics and a comparative study of material models J Elasticity 61:1-48 doi:Doi 10.1023/A:1010835316564

Holzapfel GA, Mulvihill JJ, Cunnane EM, Walsh MT (2014) Computational approaches for analyzing the mechanics of atherosclerotic plaques: A review Journal of Biomechanics 47:859-869 doi:10.1016/j.jbiomech.2014.01.011

Holzapfel GA, Niestrawska JA, Ogden RW, Reinisch AJ, Schriefl AJ (2015) Modelling non-symmetric collagen fibre dispersion in arterial walls J R Soc Interface 12:20150188 doi:10.1098/rsif.2015.0188

Holzapfel GA, Ogden RW (2009) On planar biaxial tests for anisotropic nonlinearly elastic solids. A continuum mechanical framework Math Mech Solids 14:474-489

Holzapfel GA, Ogden RW Constitutive modelling of arteries. In: Proceedings of the Royal Society of London A: Mathematical, Physical and Engineering Sciences, 2010. vol 2118. The Royal Society, pp 1551-1597

Holzapfel GA, Sommer G, Auer M, Regitnig P, Ogden RW (2007) Layer-Specific 3D Residual Deformations of Human Aortas with Non-Atherosclerotic Intimal Thickening Annals of Biomedical Engineering 35:530-545 doi:10.1007/s10439-006-9252-z

Holzapfel GA, Sommer G, Gasser CT, Regitnig P (2005) Determination of layer-specific mechanical properties of human coronary arteries with nonatherosclerotic intimal thickening and related constitutive modeling Am J Physiol Heart Circ Physiol 289:H2048-2058 doi:10.1152/ajpheart.00934.2004

Huang C et al. (2016) Ultrasound-based carotid elastography for detection of vulnerable atherosclerotic plaques validated by magnetic resonance imaging 42:365-377

Huang Y, Teng Z, Sadat U, Graves MJ, Bennett MR, Gillard JHJJob (2014) The influence of computational strategy on prediction of mechanical stress in carotid atherosclerotic plaques: comparison of 2D structure-only, 3D structure-only, one-way and fully coupled fluid-structure interaction analyses 47:1465-1471

Hult J (1974) Creep in continua and structures, Topics in Applied Continuum Mechanics Vienna: Springer

Humphrey J (1999a) An evaluation of pseudoelastic descriptors used in arterial mechanics TRANSACTIONS-AMERICAN SOCIETY OF MECHANICAL ENGINEERS JOURNAL OF BIOMECHANICAL ENGINEERING 121:259-262

Humphrey J Review Paper: Continuum biomechanics of soft biological tissues. In: Proceedings of the Royal Society of London A: Mathematical, Physical and Engineering Sciences, 2003. vol 2029. The Royal Society, pp 3-46

Humphrey JD (1994) Mechanics of the arterial wall: review and directions Critical reviews in biomedical engineering 23:1-162

Humphrey JD (1999b) Remodeling of a collagenous tissue at fixed lengths J Biomech Eng-T Asme 121:591-597 doi:Doi 10.1115/1.2800858

Humphrey JD (2013) Cardiovascular solid mechanics: cells, tissues, and organs. Springer Science & Business Media,

Humphrey JD, Rajagopal KR (2002) A constrained mixture model for growth and remodeling of soft tissues Math Mod Meth Appl S 12:407-430 doi:Doi 10.1142/S0218202502001714

Humphrey JJJobe (1999c) An evaluation of pseudoelastic descriptors used in arterial mechanics 121:259-262

Huxley AF, Simmons RM (1971) Proposed mechanism of force generation in striated muscle Nature 233:533-538

Johnston R, Nolad D, Ghasemi M, Kerskens C, Lally C Optimizated patient specific finite element models at the carotid bifurcation. In: World Congress of Biomechanics, Ireland, Dublin, 2018a.

Johnston R, Nolan D, Botella-Barillot D, Ghasemi M, Kerskens C, Lally C Optimization of Magnetic Resonance Imaging (MRI) based Patient Specific Models with mechanical property estimation from inverse finite element analysis. In: 16th European Mechanics of Materials Conference, Nantes, France, 2018b.

Kaliske M, Nasdala L, Rothert H (2001) On damage modelling for elastic and viscoelastic materials at large strain Computers & Structures 79:2133-2141 doi:http://dx.doi.org/10.1016/S0045-7949(01)00061-X

Khedr H, Eweda A, Hamza M, Salem A, Elshemy W, Tawfik AM (2016) Carotid endarterectomy versus carotid artery stenting without protection devices for the management of carotid artery stenosis The Egyptian Journal of Surgery 35:225

Krasny W, Morin C, Magoariec H, Avril S (2017) A comprehensive study of layer-specific morphological changes in the microstructure of carotid arteries under uniaxial load Acta Biomater 57:342-351 doi:10.1016/j.actbio.2017.04.033

Krejza J et al. (2006) Carotid artery diameter in men and women and the relation to body and neck size Stroke 37:1103-1105

Kuhl E, Garikipati K, Arruda EM, Grosh KJJotM, Solids Po (2005) Remodeling of biological tissue: mechanically induced reorientation of a transversely isotropic chain network 53:1552-1573

LaDisa JF, Olson LE, Hettrick DA, Warltier DC, Kersten JR, Pagel PS (2005) Axial stent strut angle influences wall shear stress after stent implantation: analysis using 3D computational fluid dynamics models of stent foreshortening Biomedical engineering online 4:59

Lally C, Dolan F, Prendergast PJ (2005) Cardiovascular stent design and vessel stresses: a finite element analysis J Biomech 38:1574-1581 doi:10.1016/j.jbiomech.2004.07.022

Laraba-Abbes F, Ienny P, Piques R (2003) A new 'Tailor-made' methodology for the mechanical behaviour analysis of rubber-like materials: II. Application to the hyperelastic

behaviour characterization of a carbon-black filled natural rubber vulcanizate Polymer 44:821-840 doi:http://dx.doi.org/10.1016/S0032-3861(02)00719-X

Larson R, Edwards BH (2013) Multivariable calculus. Cengage Learning,

Laurent S et al. (2006) Expert consensus document on arterial stiffness: methodological issues and clinical applications 27:2588-2605

Lemaitre J (1972) Evaluation of dissipation and damage in metals submitted to dynamic loading Mechanical behavior of materials:540-549

Lemaitre J, Chaboche J (1975) A non-linear model of creep-fatigue damage cumulation and interaction(for hot metallic structures) Mechanics of visco-elastic media and bodies:1975

Li W (2016) Damage Models for Soft Tissues: A Survey J Med Biol Eng 36:285-307 doi:10.1007/s40846-016-0132-1

Li ZY et al. (2006) Stress analysis of carotid plaque rupture based on in vivo high resolution MRI J Biomech 39:2611-2622 doi:10.1016/j.jbiomech.2005.08.022

Li ZY, Tang T, U-King-Im J, Graves M, Sutcliffe M, Gillard JH (2008) Assessment of carotid plaque vulnerability using structural and geometrical determinants Circ J 72:1092-1099 doi:DOI 10.1253/circj.72.1092

Limbu YR, Gurung G, Malla R, Rajbhandari R, Regmi SR (2006) Assessment of carotid artery dimensions by ultrasound in non-smoker healthy adults of both sexes Nepal Medical College journal: NMCJ 8:200-203

Liu M, Liang L, Sun WJJotmbobm (2017) A new inverse method for estimation of in vivo mechanical properties of the aortic wall 72:148-158

Macrae RA, Miller K, Doyle BJ (2016) Methods in Mechanical Testing of Arterial Tissue: A Review Strain 52:380-399 doi:10.1111/str.12183

Madu CN (2003) Statistics as easy as 1, 2, 3 with Microsoft Excel for Windows. Chi Publishers Inc,

Maher E, Creane A, Lally C, Kelly DJ (2012) An anisotropic inelastic constitutive model to describe stress softening and permanent deformation in arterial tissue Journal of the mechanical behavior of biomedical materials 12:9-19

Malek AM, Alper SL, Izumo S (1999) Hemodynamic shear stress and its role in atherosclerosis JAMA 282:2035-2042

Martins P, Pena E, Calvo B, Doblare M, Mascarenhas T, Natal Jorge R, Ferreira A (2010) Prediction of nonlinear elastic behaviour of vaginal tissue: experimental results and model formulation Comput Methods Biomech Biomed Engin 13:327-337 doi:10.1080/10255840903208197

Mateo I et al. (2011) What Measure of Carotid Wall Thickening Is the Best Atherosclerotic Loading Score in the Hypertensive Patient: Maximum or Mean Value? Rev Esp Cardiol 64:417-420 doi:10.1016/j.rec.2010.06.012

Miehe C (1995) Discontinuous and Continuous Damage Evolution in Ogden-Type Large-Strain Elastic-Materials Eur J Mech a-Solid 14:697-720

Miehe C (1996) Numerical computation of algorithmic (consistent) tangent moduli in large-strain computational inelasticity Computer Methods in Applied Mechanics and Engineering 134:223-240 doi:Doi 10.1016/0045-7825(96)01019-5

Miura T et al. (2011) Plaque vulnerability in internal carotid arteries with positive remodeling Cerebrovascular diseases extra 1:54-65

Moore WS et al. (2016) Carotid angiographic characteristics in the CREST trial were major contributors to periprocedural stroke and death differences between carotid artery stenting and carotid endarterectomy J Vasc Surg 63:851-858. e851

Moresoli P, Habib B, Reynier P, Secrest MH, Eisenberg MJ, Filion KB (2017) Carotid stenting versus endarterectomy for asymptomatic carotid artery stenosis: a systematic review and meta-analysis Stroke 48:2150-2157

Mullins L (1948) Effect of stretching on the properties of rubber Rubber Chemistry and Technology 21:281-300

Mullins L (1969) Softening of rubber by deformation Rubber chemistry and technology 42:339-362

Mullins L, Tobin N (1957) Theoretical model for the elastic behavior of filler-reinforced vulcanized rubbers Rubber chemistry and technology 30:555-571

Mullins L, Tobin N (1965) Stress softening in rubber vulcanizates. Part I. Use of a strain amplification factor to describe the elastic behavior of filler-reinforced vulcanized rubber Journal of Applied Polymer Science 9:2993-3009

Munoz MJ et al. (2008) An experimental study of the mouse skin behaviour: damage and inelastic aspects J Biomech 41:93-99 doi:10.1016/j.jbiomech.2007.07.013

Murtada S-I, Kroon M, Holzapfel GA (2010) A calcium-driven mechanochemical model for prediction of force generation in smooth muscle Biomechanics and modeling in mechanobiology 9:749-762

Nishioka T, Luo H, Eigler NL, Berglund H, Kim C-J, Siegel RJ (1996) Contribution of inadequate compensatory enlargement to development of human coronary artery stenosis: an in vivo intravascular ultrasound study Journal of the American College of Cardiology 27:1571-1576

Nolan D, Gower A, Destrade M, Ogden R, McGarry J (2014) A robust anisotropic hyperelastic formulation for the modelling of soft tissue Journal of the mechanical behavior of biomedical materials 39:48-60

Ogden R, Roxburgh D A pseudo–elastic model for the Mullins effect in filled rubber. In: Proceedings of the Royal Society of London A: Mathematical, Physical and Engineering Sciences, 1999. vol 1988. The Royal Society, pp 2861-2877

Ohayon J et al. (2008) Necrotic core thickness and positive arterial remodeling index: emergent biomechanical factors for evaluating the risk of plaque rupture Am J Physiol Heart Circ Physiol 295:H717-727 doi:10.1152/ajpheart.00005.2008

Ozolanta I, Tetere G, Purinya B, Kasyanov VJMe, physics (1998) Changes in the mechanical properties, biochemical contents and wall structure of the human coronary arteries with age and sex 20:523-533

Pagiatakis C, Galaz R, Tardif JC, Mongrain R (2015) A comparison between the principal stress direction and collagen fiber orientation in coronary atherosclerotic plaque fibrous caps Medical & Biological Engineering & Computing 53:545-555 doi:10.1007/s11517-015-1257-z

Palombo C, Kozakova MJVp (2016) Arterial stiffness, atherosclerosis and cardiovascular risk: pathophysiologic mechanisms and emerging clinical indications 77:1-7

Paritala PK, Yarlagadda PK, Wang J, Gu Y, Li ZJEFM (2018) Numerical Investigation of Atherosclerotic Plaque Rupture using Optical Coherence Tomography Imaging and XFEM

Patel DJ, Fry DL, Janicki JSJCr (1969) The elastic symmetry of arterial segments in dogs 24:1-8

Pena E (2011a) Prediction of the softening and damage effects with permanent set in fibrous biological materials J Mech Phys Solids 59:1808-1822 doi:10.1016/j.jmps.2011.05.013

Pena E (2011b) A rate dependent directional damage model for fibred materials: application to soft biological tissues Computational Mechanics 48:407-420 doi:10.1007/s00466-011-0594-5

Pena E (2014) Computational aspects of the numerical modelling of softening, damage and permanent set in soft biological tissues Computers & Structures 130:57-72 doi:10.1016/j.compstruc.2013.10.002

Pena E, Alastrue V, Laborda A, Martinez MA, Doblare M (2010) A constitutive formulation of vascular tissue mechanics including viscoelasticity and softening behaviour J Biomech 43:984-989 doi:10.1016/j.jbiomech.2009.10.046

Peña E, Calvo B, Martínez M, Doblaré M (2008) On finite-strain damage of viscoelastic-fibred materials. Application to soft biological tissues International Journal for Numerical Methods in Engineering 74:1198-1218

Pena E, Doblare M (2009) An anisotropic pseudo-elastic approach for modelling Mullins effect in fibrous biological materials Mechanics Research Communications 36:784-790 doi:10.1016/j.mechrescom.2009.05.006

Pena E, Martins P, Mascarenhas T, Natal Jorge RM, Ferreira A, Doblare M, Calvo B (2011) Mechanical characterization of the softening behavior of human vaginal tissue J Mech Behav Biomed Mater 4:275-283 doi:10.1016/j.jmbbm.2010.10.006

Pena E, Pena JA, Doblare M (2009) On the Mullins effect and hysteresis of fibered biological materials: A comparison between continuous and discontinuous damage models International Journal of Solids and Structures 46:1727-1735 doi:10.1016/j.ijsolstr.2008.12.015

Pignoli P (1984) Ultrasound B-mode imaging for arterial wall thickness measurement Atherosclerosis reviews 12:177-184

Press WH, Flannery BP, Teukolsky SA, Vetterling WT, Chipperfield J (1987) Numerical recipes: the art of scientific computing: Cambridge University Press, Cambridge, 1986 (ISBN 0-521-30811-9). xx+ 818 pp. Price£ 25.00. Elsevier,

Puso M, Solberg JJIJfNMiE (2006) A stabilized nodally integrated tetrahedral 67:841-867

Qi N, Gao H, Ogden RW, Hill NA, Holzapfel GA, Han H-C, Luo X (2015) Investigation of the optimal collagen fibre orientation in human iliac arteries Journal of the mechanical behavior of biomedical materials 52:108-119

Rabotnov Y (1963) On the equations of state for creep. Progress in applied mechanics. Prager Anniversary vol. New York: Macmillan,

Rachev A, Greenwald SJJob (2003) Residual strains in conduit arteries 36:661-670

Raghavan M, Ma B, Fillinger MFJAobe (2006) Non-invasive determination of zero-pressure geometry of arterial aneurysms 34:1414-1419

Rekhter MD, Zhang K, Narayanan AS, Phan S, Schork MA, Gordon D (1993) Type I collagen gene expression in human atherosclerosis. Localization to specific plaque regions Am J Pathol 143:1634-1648

Rhodin J (1980) Handbook of physiology: The cardiovascular system Architecture of the vessel wall:1-31

Riveros F, Chandra S, Finol EA, Gasser TC, Rodriguez JFJAobe (2013) A pull-back algorithm to determine the unloaded vascular geometry in anisotropic hyperelastic AAA passive mechanics 41:694-708

Roach MR, Burton ACJCjob, physiology (1957) The reason for the shape of the distensibility curves of arteries 35:681-690

Rodriguez JF, Cacho F, Bea JA, Doblare M (2006) A stochastic-structurally based three dimensional finite-strain damage model for fibrous soft tissue J Mech Phys Solids 54:864-886 doi:10.1016/j.jmps.2005.10.005

Roger VL et al. (2011) Heart disease and stroke statistics—2012 update: a report from the American Heart Association:CIR. 0b013e31823ac31046

Rouillard AD, Holmes JWJTJop (2012) Mechanical regulation of fibroblast migration and collagen remodelling in healing myocardial infarcts 590:4585-4602

Rusinkiewicz S Estimating curvatures and their derivatives on triangle meshes. In: 3D Data Processing, Visualization and Transmission, 2004. 3DPVT 2004. Proceedings. 2nd International Symposium on, 2004. IEEE, pp 486-493

Rysz J, Franczyk B, Banach M, Gluba-Brzozka A (2017) Hypertension - Current Natural Strategies to Lower Blood Pressure Curr Pharm Des 23:2453-2461 doi:10.2174/1381612823666170215144649

Saam T et al. (2005) Quantitative evaluation of carotid plaque composition by in vivo MRI 25:234-239

Saam T et al. (2016) Expansive arterial remodeling of the carotid arteries and its effect on atherosclerotic plaque composition and vulnerability: an in-vivo black-blood 3T CMR study in symptomatic stroke patients 18:11

Schoenhagen P, Ziada KM, Vince DG, Nissen SE, Tuzcu EM (2001) Arterial remodeling and coronary artery disease: the concept of "dilated" versus "obstructive" coronary atherosclerosis J Am Coll Cardiol 38:297-306

Schriefl AJ, Schmidt T, Balzani D, Sommer G, Holzapfel GA (2015a) Selective enzymatic removal of elastin and collagen from human abdominal aortas: uniaxial mechanical response and constitutive modeling Acta Biomater 17:125-136 doi:10.1016/j.actbio.2015.01.003

Schriefl AJ, Schmidt T, Balzani D, Sommer G, Holzapfel GA (2015b) Selective enzymatic removal of elastin and collagen from human abdominal aortas: Uniaxial mechanical response and constitutive modeling Acta biomaterialia 17:125-136

Schriefl AJ, Schmidt T, Balzani D, Sommer G, Holzapfel GAJAb (2015c) Selective enzymatic removal of elastin and collagen from human abdominal aortas: Uniaxial mechanical response and constitutive modeling 17:125-136

Schriefl AJ, Zeindlinger G, Pierce DM, Regitnig P, Holzapfel GA (2012a) Determination of the layer-specific distributed collagen fibre orientations in human thoracic and abdominal aortas and common iliac arteries J R Soc Interface 9:1275-1286 doi:10.1098/rsif.2011.0727

Schriefl AJ, Zeindlinger G, Pierce DM, Regitnig P, Holzapfel GAJJotRSI (2012b) Determination of the layer-specific distributed collagen fibre orientations in human thoracic and abdominal aortas and common iliac arteries 9:1275-1286

Schroder J, Brinkhues S (2014) A novel scheme for the approximation of residual stresses in arterial walls Arch Appl Mech 84:881-898 doi:10.1007/s00419-014-0838-x

Schröder J, von Hoegen M (2016) An engineering tool to estimate eigenstresses in three-dimensional patient-specific arteries Computer Methods in Applied Mechanics and Engineering 306:364-381

Shabat YB (2014) Curvature Estimationl On triangle mesh (http://uk.mathworks.com/matlabcentral/fileexchange/47134-curvature-estimationl-on-triangle-mesh). The Mathworks, MATLAB Central File Exchange

Shabat YB, Fischer A (2015) Design of Porous Micro-Structures Using Curvature Analysis for Additive-Manufacturing Procedia CIRP 36:279-284

Shadwick RE (1998) Elasticity in Arteries: A similar combination of rubbery and stiff materials creates common mechanical properties in blood vessels of vertebrates and some invertebrates American Scientist 86:535-541

Shadwick RE (1999) Mechanical design in arteries Journal of Experimental Biology 202:3305-3313

Shahid SS, Gaul RT, Kerskens C, Flamini V, Lally C (2017) Quantifying the ultrastructure of carotid arteries using high-resolution micro-diffusion tensor imaging—comparison of intact versus open cut tissue Physics in Medicine & Biology 62:8850

Sherwood L (2011) Fundamentals of human physiology. Cengage Learning,

Sicard GA, Zwolak RM, Sidawy AN, White RA, Siami FS (2006) Endovascular abdominal aortic aneurysm repair: Long-term outcome measures in patients at high-risk for open surgery J Vasc Surg 44:229-236 doi:10.1016/j.jvs.2006.04.034

Simo J, Ju J (1987) Strain-and stress-based continuum damage models—I. Formulation International journal of solids and structures 23:821-840

Singh C, Wong C, Wang XJJofb (2015) Medical textiles as vascular implants and their success to mimic natural arteries 6:500-525

Smits LP, van Wijk DF, Duivenvoorden R, Xu D, Yuan C, Stroes ES, Nederveen AJJPo (2016) Manual versus Automated Carotid Artery Plaque Component Segmentation in High and Lower Quality 3.0 Tesla MRI Scans 11:e0164267

Sommer G, Holzapfel GA (2012) 3D constitutive modeling of the biaxial mechanical response of intact and layer-dissected human carotid arteries J Mech Behav Biomed Mater 5:116-128 doi:10.1016/j.jmbbm.2011.08.013

Sommer G, Regitnig P, Koltringer L, Holzapfel GA (2010) Biaxial mechanical properties of intact and layer-dissected human carotid arteries at physiological and supraphysiological loadings Am J Physiol-Heart C 298:H898-H912 doi:10.1152/ajpheart.00378.2009

Stålhand J, Klarbring A, Holzapfel GA (2008) Smooth muscle contraction: mechanochemical formulation for homogeneous finite strains Progress in biophysics and molecular biology 96:465-481

Steinman DA, Vorp DA, Ethier CR (2003) Computational modeling of arterial biomechanics: Insights into pathogenesis and treatment of vascular disease J Vasc Surg 37:1118-1128 doi:10.1067/mva.2003.122

Sun W, Chaikof EL, Levenston ME (2008) Numerical approximation of tangent moduli for finite element implementations of nonlinear hyperelastic material models J Biomech Eng 130:061003 doi:10.1115/1.2979872

Taber LA, Humphrey JD (2001) Stress-modulated growth, residual stress, and vascular heterogeneity J Biomech Eng 123:528-535

Takamizawa K, Hayashi K (1987a) Strain energy density function and uniform strain hypothesis for arterial mechanics Journal of biomechanics 20:7-17

Takamizawa K, Hayashi KJJob (1987b) Strain energy density function and uniform strain hypothesis for arterial mechanics 20:7-17

Tarjuelo-Gutierrez J et al. (2014) High-quality conforming hexahedral meshes of patient-specific abdominal aortic aneurysms including their intraluminal thrombi 52:159-168

Teng Z et al. (2010a) Arterial luminal curvature and fibrous-cap thickness affect critical stress conditions within atherosclerotic plaque: an in vivo MRI-based 2D finite-element study Annals of biomedical engineering 38:3096-3101

Teng ZZ et al. (2010b) Arterial Luminal Curvature and Fibrous-Cap Thickness Affect Critical Stress Conditions Within Atherosclerotic Plaque: An In Vivo MRI-Based 2D Finite-Element Study Annals of Biomedical Engineering 38:3096-3101 doi:10.1007/s10439-010-0078-3

Teng ZZ et al. (2015) The influence of constitutive law choice used to characterise atherosclerotic tissue material properties on computing stress values in human carotid plaques Journal of Biomechanics 48:3912-3921 doi:10.1016/j.jbiomech.2015.09.023

Thondapu V, Bourantas CV, Foin N, Jang IK, Serruys PW, Barlis P (2016) Biomechanical stress in coronary atherosclerosis: emerging insights from computational modelling Eur Heart J:ehv689 doi:10.1093/eurheartj/ehv689

Timmins LH, Moreno MR, Meyer CA, Criscione JC, Rachev A, Moore JE, Jr. (2007) Stented artery biomechanics and device design optimization Med Biol Eng Comput 45:505-513 doi:10.1007/s11517-007-0180-3

Trivedi RA, U-King-Im J, Graves MJ, Horsley J, Goddard M, Kirkpatrick PJ, Gillard JH (2004) Multi-sequence in vivo MRI can quantify fibrous cap and lipid core components in human carotid atherosclerotic plaques Eur J Vasc Endovasc 28:207-213 doi:Doi 10.1016/S1078-5884(04)00219-9

Vaishnav RN, Vossoughi J (1983) Estimation of residual strains in aortic segments. In: Biomedical Engineering II. Elsevier, pp 330-333

Vaishnav RN, Vossoughi J (1987) Residual stress and strain in aortic segments Journal of biomechanics 20:235-239

Vande Geest JP, Di Martino ES, Bohra A, Makaroun MS, Vorp DA (2006) A biomechanics-based rupture potential index for abdominal aortic aneurysm risk assessment: demonstrative application Ann N Y Acad Sci 1085:11-21 doi:10.1196/annals.1383.046

Varnava AM, Mills PG, Davies MJ (2002) Relationship between coronary artery remodeling and plaque vulnerability Circulation 105:939-943 doi:10.1161/hc0802.104327

von Maltzahn WW, Warriyar RG, Keitzer WFJJob (1984) Experimental measurements of elastic properties of media and adventitia of bovine carotid arteries 17:839-847

Waffenschmidt T, Menzel A (2014) Extremal states of energy of a double-layered thick-walled tube - application to residually stressed arteries J Mech Behav Biomed Mater 29:635-654 doi:10.1016/j.jmbbm.2013.05.023

Weisbecker H, Pierce D, Holzapfel G Modeling of damage-induced softening for arterial tissue. In: Proceedings of the 2011 SCATh joint workshop on new tecnologies for computer/robot assisted surgery, Graz, 2011. pp 1-4

Weisbecker H, Pierce DM, Regitnig P, Holzapfel GA (2012) Layer-specific damage experiments and modeling of human thoracic and abdominal aortas with non-atherosclerotic intimal thickening Journal of the mechanical behavior of biomedical materials 12:93-106

Weisbecker H, Viertler C, Pierce DM, Holzapfel GA (2013) The role of elastin and collagen in the softening behavior of the human thoracic aortic media J Biomech 46:1859-1865 doi:10.1016/j.jbiomech.2013.04.025

Weiss JA, Maker BN, Govindjee S (1996) Finite element implementation of incompressible, transversely isotropic hyperelasticity Computer Methods in Applied Mechanics and Engineering 135:107-128 doi:10.1016/0045-7825(96)01035-3

Weizsacker HW, Pinto JGJJob (1988) Isotropy and anisotropy of the arterial wall 21:477-487

Wittek A, Derwich W, Karatolios K, Fritzen CP, Vogt S, Schmitz-Rixen T, Blase CJJotmbobm (2016) A finite element updating approach for identification of the anisotropic hyperelastic properties of normal and diseased aortic walls from 4D ultrasound strain imaging 58:122-138

Wuyts F, Vanhuyse V, Langewouters G, Decraemer W, Raman E, Buyle S (1995) Elastic properties of human aortas in relation to age and atherosclerosis: a structural model Physics in medicine and biology 40:1577

Yadav JS et al. (2004) Protected carotid-artery stenting versus endarterectomy in high-risk patients New England Journal of Medicine 351:1493-1501

Yan XX et al. (2009) Increased serum HMGB1 level is associated with coronary artery disease in nondiabetic and type 2 diabetic patients 205:544-548

Yang J, Clark JW, Jr., Bryan RM, Robertson C (2003) The myogenic response in isolated rat cerebrovascular arteries: smooth muscle cell model Med Eng Phys 25:691-709

Yu X, Turcotte R, Seta F, Zhang YJJoTRSI (2018) Micromechanics of elastic lamellae: unravelling the role of structural inhomogeneity in multi-scale arterial mechanics 15:20180492

Zhang Q et al. (2015) Quantification of carotid plaque elasticity and intraplaque neovascularization using contrast-enhanced ultrasound and image registration-based elastography 62:253-262

Zhang Y, Bazilevs Y, Goswami S, Bajaj CL, Hughes TJJCmiam, engineering (2007) Patient-specific vascular NURBS modeling for isogeometric analysis of blood flow 196:2943-2959

Zitnay JL et al. (2017) Molecular level detection and localization of mechanical damage in collagen enabled by collagen hybridizing peptides Nat Commun 8:14913 doi:10.1038/ncomms14913

Zohdi TI, Holzapfel GA, Berger SA (2004) A phenomenological model for atherosclerotic plaque growth and rupture J Theor Biol 227:437-443 doi:10.1016/j.jtbi.2003.11.025

Zulliger MA, Fridez P, Hayashi K, Stergiopulos N (2004) A strain energy function for arteries accounting for wall composition and structure Journal of biomechanics 37:989-1000

Appendices

A Calculating Cauchy stress equations from SEFs

Calculation of Cauchy stress from SEFs is explained in this section. Equation A.1 shows the relationship between Cauchy stress and an arbitrary SEF ψ.

$$\sigma = \frac{2}{J}\mathbf{F}\frac{\partial \psi}{\partial C}\mathbf{F}^T \tag{A.1}$$

The SEF function that corresponds to volumetric Cauchy stress can be expressed as follows, see Equation 3.9;

$$\psi_{vol} = \frac{1}{2}k_0(J-1)^2 \tag{A.2}$$

Equations A.3 to A.9 demonstrate how volumetric Cauchy stress can be derived using Equations A.1 and A.2.

$$\frac{\partial \psi_{vol}}{\partial C} = \frac{\partial \psi_{vol}}{\partial J}\frac{\partial J}{\partial \mathbf{C}} \tag{A.3}$$

$$\frac{\partial \psi_{vol}}{\partial J} = k_0(J-1) \tag{A.4}$$

$$\frac{\partial J}{\partial \mathbf{C}} = \frac{1}{2}J\mathbf{C}^{-1} \tag{A.5}$$

$$\boldsymbol{\sigma} = \frac{2}{J}Fk_0(J-1)\frac{J}{2}\mathbf{C}^{-1}F^T \tag{A.6}$$

$$\begin{gathered}\mathbf{C} = \mathbf{F}^T\mathbf{F} \\ \mathbf{C}^{-1} = \mathbf{F}^{-1}\mathbf{F}^{-\mathrm{T}}\end{gathered} \tag{A.7}$$

$$\boldsymbol{\sigma} = \mathbf{F}k_0(J-1)\mathbf{F}^{-1}\mathbf{F}^{-\mathrm{T}}\mathbf{F}^T \tag{A.8}$$

$$\boldsymbol{\sigma}_{\mathbf{vol}} = k_0(J-1)I \tag{A.9}$$

Equation A.10 correspond to the SEF used in this theses for the ground matrix, see also Equation 3.10 .

$$\bar{\psi}_{iso}(\bar{\mathbf{C}}) = \frac{1}{2}\mu_0(\bar{I}_1 - 3) \tag{A.10}$$

Equations A.11 to A.21 show how $\boldsymbol{\sigma}_{\mathbf{iso}}$ can be derived from Equation A.10 using equation A.1.

$$\bar{I}_1 = J^{-\frac{2}{3}}I_1 \tag{A.11}$$

$$\psi_{iso}(\mathbf{C}) = \frac{1}{2}\mu_0(J^{-\frac{2}{3}}I_1 - 3) \tag{A.12}$$

$$\frac{\partial \psi_{iso}}{\partial \mathbf{C}} = \frac{1}{2}\mu_0\left[\frac{\partial}{\partial \mathbf{C}}(J^{-\frac{2}{3}})I_1 + \frac{\partial}{\partial \mathbf{C}}(I_1)J^{-\frac{2}{3}}\right] \tag{A.13}$$

$$\frac{\partial}{\partial \mathbf{C}}(J^{-\frac{2}{3}}) = -\frac{1}{3}J^{-\frac{2}{3}}\mathbf{C^{-1}} \tag{A.14}$$

$$\frac{\partial}{\partial C}(I_1) = I \tag{A.15}$$

$$\frac{\partial \psi_{iso}}{\partial \mathbf{C}} = \frac{1}{2}\mu_0[-\frac{1}{3}J^{-\frac{2}{3}}\mathbf{C}^{-1}I_1 + J^{-\frac{2}{3}}I] \tag{A.16}$$

$$\frac{2}{J}\frac{\partial \psi_{iso}}{\partial \mathbf{C}} = J^{-1}\mu_o[-\frac{1}{3}J^{-\frac{2}{3}}\mathbf{C}^{-1}I_1 + J^{-\frac{2}{3}}I] \tag{A.17}$$

$$\mathbf{B} = \mathbf{F}\mathbf{F}^{\boldsymbol{T}} \tag{A.18}$$

$$\frac{2}{J}\mathbf{F}\frac{\partial \Psi_{iso}}{\partial \mathbf{C}}\mathbf{F}^T = J^{-1}\mu_0[-\frac{1}{3}J^{-\frac{2}{3}}\mathbf{F}\mathbf{F^{-1}}\mathbf{F^{-T}}\mathbf{F^T}I_1 + J^{-\frac{2}{3}}\mathbf{B}] \tag{A.19}$$

$$\overline{\mathrm{B}} = J^{-\frac{2}{3}}\mathbf{B} \tag{A.20}$$

$$\boldsymbol{\sigma}_{\mathbf{iso}} = J^{-1}\mu_0[-\frac{1}{3}\bar{I}_1 I + \overline{\mathbf{B}}] \tag{A.21}$$

Equation A.22 depicts the isochoric anisotropic SEF used for capturing the behaviour of the elastin fibres under physiological load levels, Equation 3.11.

$$\bar{\psi}_{ef}(\bar{\mathbf{C}}) = \frac{k_1}{2k_2}(e^{(k_2(\bar{I}_4-1)^2)} - 1) \tag{A.22}$$

Equation A.23 to A.35 show the Cauchy stress ψ_{ef} was derived using Equations A.22 and A.1

$$\bar{I}_4 = J^{-\frac{2}{3}}I_4 \tag{A.23}$$

$$\psi_{ef}(\mathbf{C}) = \frac{k_1}{2k_2}(e^{(k_2(J^{-\frac{2}{3}}I_4-1)^2)} - 1) \tag{A.24}$$

$$\frac{\partial \psi_{ef}}{\partial \mathbf{C}} = \frac{\partial}{\partial \mathbf{C}}(\frac{k_1}{2k_2}e^{(k_2(J^{-\frac{2}{3}}I_4-1)^2)}) \tag{A.25}$$

$$\frac{\partial \psi_{ef}}{\partial \mathbf{C}} = \frac{k_1}{2k_2}\frac{\partial}{\partial \mathbf{C}}(e^{(k_2(J^{-\frac{2}{3}}I_4-1)^2)}) \tag{A.26}$$

$$\frac{\partial \psi_{ef}}{\partial \mathbf{C}} = \frac{k_1}{2k_2}(e^{(k_2(J^{-\frac{2}{3}}I_4-1)^2)})\frac{\partial}{\partial \mathbf{C}}(k_2(J^{-\frac{2}{3}}I_4 - 1)^2) \tag{A.27}$$

$$\frac{\partial \psi_{ef}}{\partial \mathbf{C}} = \frac{k_1}{2k_2}(e^{(k_2(J^{-\frac{2}{3}}I_4-1)^2)})((2k_2)(J^{-\frac{2}{3}}I_4 - 1)(\frac{\partial}{\partial \mathbf{C}}(J^{-\frac{2}{3}})I_4 + \frac{\partial}{\partial \mathbf{C}}(I_4)J^{-\frac{2}{3}})) \tag{A.28}$$

$$\frac{\partial I_4}{\partial \mathbf{C}} = \boldsymbol{a_4} \otimes \boldsymbol{a_4} = \boldsymbol{a_4}\boldsymbol{a_4^T} \tag{A.29}$$

where $\boldsymbol{a_4}$ indicate a unit vector presenting one family of collagen fibres.

$$\frac{\partial \psi_{ef}}{\partial \mathbf{C}} = \frac{k_1}{2k_2}(e^{(k_2(J^{-\frac{2}{3}}I_4-1)^2)})((2k_2)(J^{-\frac{2}{3}}I_4 - 1)(-\frac{1}{3}J^{-\frac{2}{3}}\mathbf{C}^{-1}I_4 + (\boldsymbol{a_4} \otimes \boldsymbol{a_4})J^{-\frac{2}{3}})) \tag{A.30}$$

$$F((\boldsymbol{a_4}\otimes\boldsymbol{a_4})J^{-\frac{2}{3}})F^T=\mathbf{F}(J^{-\frac{2}{3}}\boldsymbol{a_4}\boldsymbol{a_4^T})\mathbf{F^T}=((J^{-\frac{1}{3}}\mathbf{F})(\boldsymbol{a_4}))((J^{-\frac{1}{3}}F)(\boldsymbol{a_4}))^T \tag{A.31}$$

$$\bar{\mathbf{F}}=J^{-\frac{1}{3}}\mathbf{F} \tag{A.32}$$

$$\bar{\boldsymbol{a}}_{\boldsymbol{4}}=\bar{\mathbf{F}}\boldsymbol{a_4} \tag{A.33}$$

$$\frac{2}{J}\mathbf{F}\frac{\partial\psi_{ef}}{\partial C}\mathbf{F^T}=\frac{2}{J}k_1(J^{-\frac{2}{3}}I_4-1)(e^{(k_2(J^{-\frac{2}{3}}I_4-1)^2)})(-\frac{1}{3}\bar{I}_4I+(\bar{\boldsymbol{a}}_{\boldsymbol{4}}\otimes\bar{\boldsymbol{a}}_{\boldsymbol{4}})) \tag{A.34}$$

$$\boldsymbol{\sigma_{ef}}=\frac{2}{J}k_1(\bar{I}_4-1)(e^{(k_2(\bar{I}_4-1)^2)})(-\frac{1}{3}\bar{I}_4I+(\bar{\boldsymbol{a}}_{\boldsymbol{4}}\otimes\bar{\boldsymbol{a}}_{\boldsymbol{4}})) \tag{A.35}$$

The isochoric anisotropic SEF used to capture the mechanical behaviour of collagen fibres under physiological loads is as follow, Equation 3.15;

$$\bar{\psi}_{cf}(\bar{\mathbf{C}})=\frac{k_1}{2k_2}(e^{(k_2(\kappa\bar{I}_1+(1-3\kappa)\bar{I}_4-1)^2)}-1) \tag{A.36}$$

Equations A.37 to A.44 show how Cauchy stress $\boldsymbol{\sigma}_{cf}$ can be derived using equations A.1 and A.36.

$$\frac{\partial\bar{\psi}_{cf}}{\partial\mathbf{C}}=\frac{k_1}{2k_2}(e^{(k_2(\kappa\bar{I}_1+(1-3\kappa)\bar{I}_4-1)^2)})\frac{\partial}{\partial\mathbf{C}}(k_2(\kappa\bar{I}_1+(1-3\kappa)\bar{I}_4-1)^2) \tag{A.37}$$

$$\frac{\partial}{\partial\mathbf{C}}(k_2(\kappa\bar{I}_1+(1-3\kappa)\bar{I}_4-1)^2)=2k_2(\kappa\bar{I}_1+(1-3\kappa)\bar{I}_4-1)\frac{\partial}{\partial\mathbf{C}}(\kappa\bar{I}_1+(1-3\kappa)\bar{I}_4-1) \tag{A.1}$$

$$\frac{\partial}{\partial\mathbf{C}}(\kappa\bar{I}_1+(1-3\kappa)\bar{I}_4-1)=\kappa\frac{\partial}{\partial\mathbf{C}}(J^{-\frac{2}{3}}I_1)+(1-3\kappa)\frac{\partial}{\partial\mathbf{C}}(J^{-\frac{2}{3}}I_4) \tag{A.38}$$

$$\frac{\partial}{\partial\mathbf{C}}(J^{-\frac{2}{3}}I_1)=-\frac{1}{3}J^{-\frac{2}{3}}C^{-1}I_1+J^{-\frac{2}{3}}I \tag{A.39}$$

$$\frac{\partial}{\partial\mathbf{C}}(J^{-\frac{2}{3}}I_4)=-\frac{1}{3}J^{-\frac{2}{3}}C^{-1}I_4+(a_4\otimes a_4)J^{-\frac{2}{3}} \tag{A.40}$$

$$\begin{gathered}\frac{\partial\psi_{cf}}{\partial\mathbf{C}}=\frac{k_1}{2k_2}(e^{(k_2(\kappa\bar{I}_1+(1-3\kappa)\bar{I}_4-1)^2)})(2k_2(\kappa\bar{I}_1+(1-3\kappa)\bar{I}_4-1)).\\ [\kappa(-\frac{1}{3}J^{-\frac{2}{3}}\bar{\mathbf{C}}I_1+J^{-\frac{2}{3}}I)+(1-3\kappa)(-\frac{1}{3}J^{-\frac{2}{3}}\mathbf{C}^{-1}I_4+(\boldsymbol{a_4}\otimes\boldsymbol{a_4})J^{-\frac{2}{3}})]\end{gathered} \tag{A.41}$$

$$\begin{gathered}\mathbf{F}\frac{\partial\psi_{cf}}{\partial C}\mathbf{F}^T=k_1(e^{(k_2(\kappa\bar{I}_1+(1-3\kappa)\bar{I}_4-1)^2)})(\kappa\bar{I}_1+(1-3\kappa)\bar{I}_4-1).\\ [\kappa(-\frac{1}{3}J^{-\frac{2}{3}}I_1+J^{-\frac{2}{3}}\mathbf{F}\mathbf{I}\mathbf{F}^{\mathbf{T}})+(1-3\kappa)(-\frac{1}{3}J^{-\frac{2}{3}}I_4+\left(\left(J^{-\frac{1}{3}}\mathbf{F}\right)(\boldsymbol{a_4})\right)^{\mathrm{T}})]\end{gathered} \tag{A.42}$$

$$\begin{gathered}\frac{2}{J}\mathbf{F}\frac{\partial\psi_{cf}}{\partial C}\mathbf{F}^T=\frac{2}{J}k_1(e^{(k_2(\kappa\bar{I}_1+(1-3\kappa)\bar{I}_4-1)^2)})(\kappa\bar{I}_1+(1-3\kappa)\bar{I}_4-1)\\ [\kappa(-\frac{1}{3}\bar{I}_1+\bar{\mathbf{B}})+(1-3\kappa)(-\frac{1}{3}\bar{I}_4I+(\bar{\boldsymbol{a}}_{\boldsymbol{4}}\otimes\bar{\boldsymbol{a}}_{\boldsymbol{4}})]\end{gathered} \tag{A.43}$$

$$\begin{gathered}\boldsymbol{\sigma_{cf}}=\frac{2}{J}k_1(e^{(k_2(\kappa\bar{I}_1+(1-3\kappa)\bar{I}_4-1)^2)})(\kappa\bar{I}_1+(1-3\kappa)\bar{I}_4-1)\\ [\kappa(-\frac{1}{3}\bar{I}_1+\bar{\boldsymbol{B}})+(1-3\kappa)(-\frac{1}{3}\bar{I}_4I+(\bar{\boldsymbol{a}}_{\boldsymbol{4}}\otimes\bar{\boldsymbol{a}}_{\boldsymbol{4}})]\end{gathered} \tag{A.44}$$

The SEF to calculate Cauchy stress when damage is accumulating in the tissue is shown in Equation 3.15. This Equation can also be written as follows.

$$\psi^{ti} = m(p(\mathbf{C}, D)) \tag{A.45}$$

$$p = (1 - D)\psi^{ti,0} - c \tag{A.46}$$

Where $\psi^{ti,0}$ indicates the intact strain energy function, when no damage has been accumulated in the tissue. Equation A.47, shows the components of Equation 3.15 when they are written in the form of Equation A.45 and A.46.

$$\begin{aligned} m(p(\mathbf{C}, D)) &= \tfrac{k_1}{2k_2}(e^{k2\langle p\rangle^2} - 1) \\ \psi^{ti,0} &= \kappa\bar{I}_1 + (1 - 3\kappa)\bar{I}_4\,, c = 1 \end{aligned} \tag{A.47}$$

Equations A.48 to A.57 presents how Cauchy stress can be calculated from these equations using Equation A.1.

Calculation of $\frac{\partial m}{\partial p}$

$$\frac{\partial m}{\partial p} = \frac{\partial}{\partial p}\left(\frac{k_1}{2k_2}(e^{k2\langle p\rangle^2} - 1)\right) \tag{A.48}$$

$$\frac{\partial m}{\partial p} = \frac{k_1}{2k_2}(e^{k2\langle p\rangle^2})\left(\frac{\partial}{\partial p}\right)(k2\langle p\rangle^2) \tag{A.49}$$

$$\frac{\partial m}{\partial p} = \frac{k_1}{2k_2}(e^{k2\langle p\rangle^2})\left(\frac{\partial}{\partial p}\right)(k2\langle p\rangle^2) \tag{A.50}$$

$$\frac{\partial m}{\partial p} = \frac{2k_2k_1}{2k_2}(e^{k2\langle p\rangle^2})(\langle p\rangle)\left(\frac{\partial}{\partial p}\langle p\rangle\right) \tag{A.51}$$

$$\frac{\partial}{\partial X}\langle X\rangle = \frac{1}{2}(sign(X) + 1) \tag{A.52}$$

$$\frac{\partial m}{\partial p} = \frac{1}{2}k_1(e^{k2\langle p\rangle^2})(\langle p\rangle)(sign(p) + 1) \tag{A.53}$$

Calculation of $S^{ti,0}$

$$S^{ti,0} = 2\frac{\partial \Psi^{ti,0}}{\partial C} = 2\frac{\partial}{\partial C}(k\bar{I}_1 + (1 - 3k)\bar{I}_4) \tag{A.54}$$

$$\frac{\partial}{\partial C}(k\bar{I}_1 + (1 - 3k)\bar{I}_4) = k\frac{\partial}{\partial C}(\bar{I}_1) + (1 - 3k)\frac{\partial}{\partial C}(\bar{I}_4) \tag{A.55}$$

$$\frac{\partial}{\partial C}(\bar{I}_1) = -\frac{1}{3}J^{-\frac{2}{3}}C^{-1}I_1 + J^{-\frac{2}{3}}I \tag{A.56}$$

$$\frac{\partial}{\partial C}(\bar{I}_4) = \frac{\partial}{\partial C}(J^{-\frac{2}{3}})I_4 + \frac{\partial}{\partial C}(I_4)J^{-\frac{2}{3}} = (-\frac{1}{3}J^{-\frac{2}{3}}C^{-1}I_4 + (a_4 \otimes a_4)J^{-\frac{2}{3}})) \tag{A.57}$$

$$\frac{\partial \Psi^{ti,0}}{\partial C} = \kappa(-\frac{1}{3}J^{-\frac{2}{3}}C^{-1}I_1 + J^{-\frac{2}{3}}I) + (1 - 3\kappa)(-\frac{1}{3}J^{-\frac{2}{3}}C^{-1}I_4 + (a_4 \otimes a_4)J^{-\frac{2}{3}}) \tag{A.58}$$

To calculate the Cauchy Stress using Equation A.1;

$$F\frac{\partial \Psi^{ti,0}}{\partial C}F^T = \kappa(-\frac{1}{3}\bar{I}_1 I + \bar{B}) + (1-3\kappa)(-\frac{1}{3}\bar{I}_4 I + (\bar{\boldsymbol{a}}_{\boldsymbol{4}} \otimes \bar{\boldsymbol{a}}_{\boldsymbol{4}})) \quad \text{(A.54)}$$

$$\frac{2}{J}F\frac{\partial \Psi^{ti,0}}{\partial C}F^T = \frac{2}{J}(\kappa(-\frac{1}{3}\bar{I}_1 I + \bar{B}) + (1-3\kappa)(-\frac{1}{3}\bar{I}_4 I + (\bar{\boldsymbol{a}}_{\boldsymbol{4}} \otimes \bar{\boldsymbol{a}}_{\boldsymbol{4}}))) \quad \text{(A.55)}$$

Using Equation A.47 Cauchy stress can then be written as follows;

$$\boldsymbol{\sigma}(\bar{\mathbf{C}}, D_{cf}) = \frac{1}{2}k_1(e^{k2\langle p\rangle^2})(\langle p\rangle)(sign(p)+1)(1-D_{cf})(\frac{2}{J}(k(-\frac{1}{3}\bar{I}_1 I + \bar{\mathbf{B}}) + (1-3k)(-\frac{1}{3}\bar{I}_4 I + (\bar{\boldsymbol{a}}_{\boldsymbol{4}} \otimes \bar{a}_4)))) \quad \text{(A.56)}$$

$$p = (1-D_{cf})(k\bar{I}_1 + (1-3k)\bar{I}_4) - 1 \quad \text{(A.57)}$$

$$\boldsymbol{\sigma}(\bar{\mathbf{C}}, D_{cf}) = \frac{1}{2}k_1(e^{k2\langle p\rangle^2})(sign(p)+1)(1-D_{cf})(\frac{2}{J}(k(-\frac{1}{3}\bar{I}_1 I + \bar{\mathbf{B}}) + (1-3k)(-\frac{1}{3}\bar{I}_4 I + (\bar{\boldsymbol{a}}_{\boldsymbol{4}} \otimes \bar{\boldsymbol{a}}_{\boldsymbol{4}}))))$$
$$p = (1-D_{cf})(k\bar{I}_1 + (1-3k)\bar{I}_4) - 1$$
(A.58)

The final form of this equation can be written as follows;

$$\boldsymbol{\sigma}(\bar{\mathbf{C}}, D_{cf}) = \frac{1}{2}k_1(1-D_{cf})(\langle p\rangle)(\frac{2}{J}(k(-\frac{1}{3}\bar{I}_1 I + \bar{B}) + (1-3k)(-\frac{1}{3}\bar{I}_4 I + (\bar{\boldsymbol{a}}_{\boldsymbol{4}} \otimes \bar{\boldsymbol{a}}_{\boldsymbol{4}}))))(e^{k2\langle(1-D)(k\bar{I}_1+(1-3k)\bar{I}_4)-1\rangle^2})(sign(p)+1)$$

(A.59)

B Sensitivity analysis of the CDM model to the damage threshold

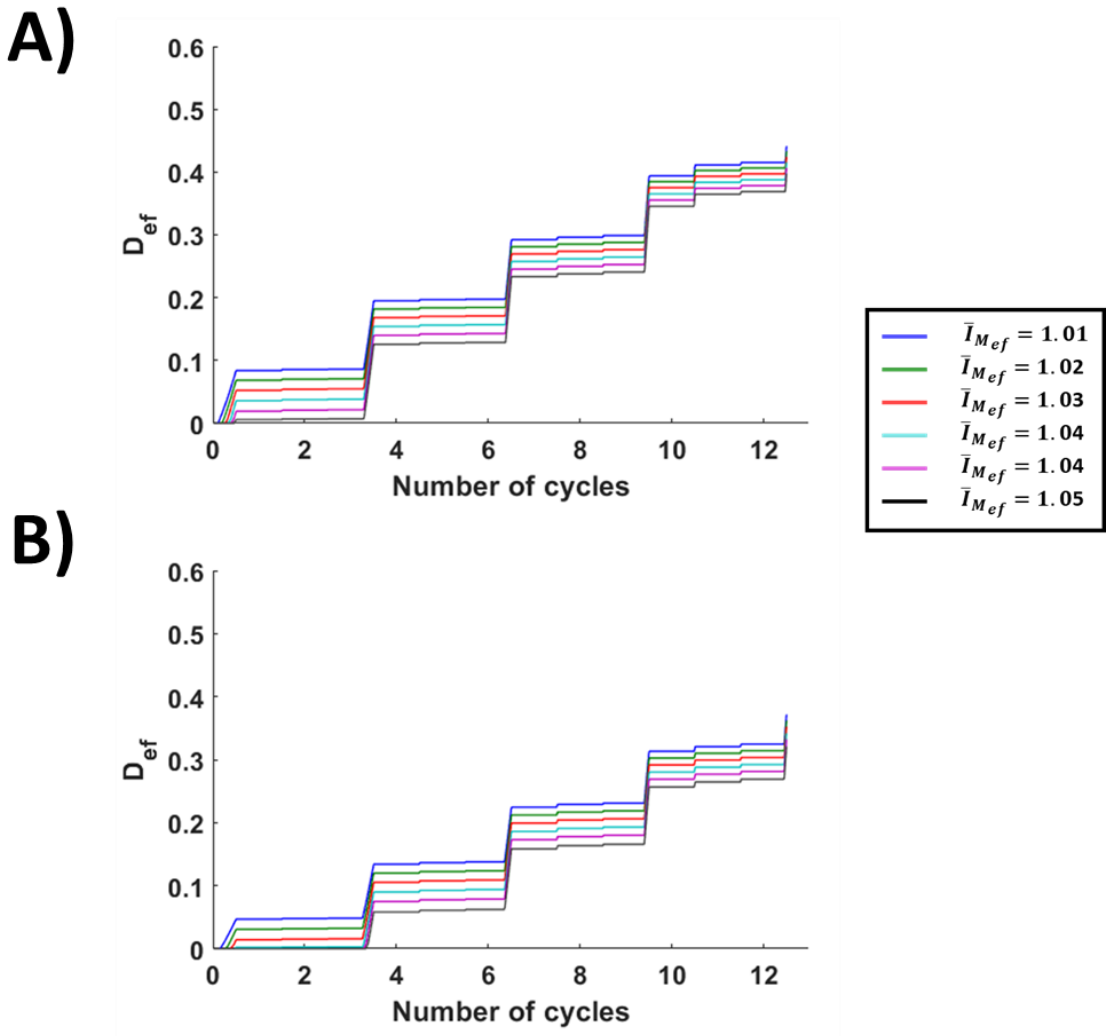

Figure B1. *The influence of selecting different damage thresholds on the damage accumulation in the elastin fibres in (A) axial and (B) circumferential directions of collagen fibre digested samples. The associated stress-strain curves are presented in Figure 3.6.*

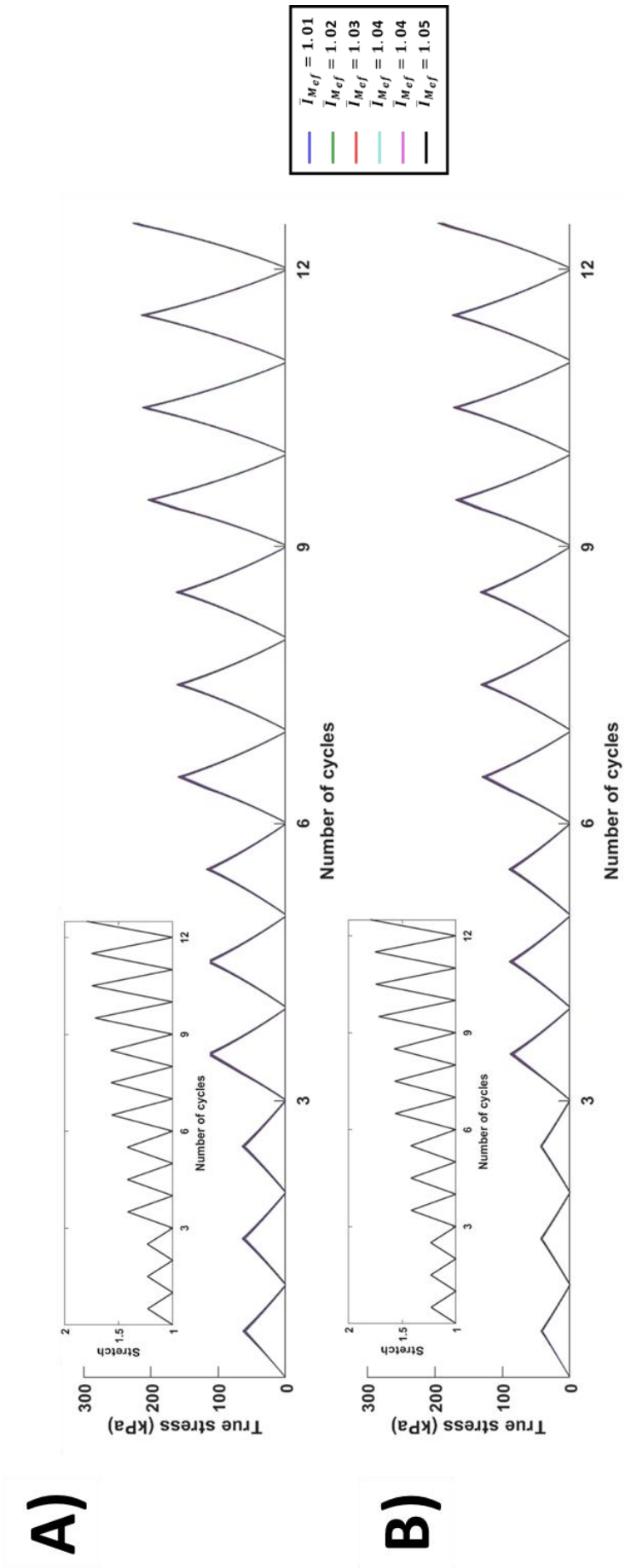

Figure B2. *The influence of selecting different damage thresholds on the stress calculation in the collagen fibre digested samples in (a) axial and (b) circumferential directions. The associated stress-strain curves are presented in Figure 3.6.*

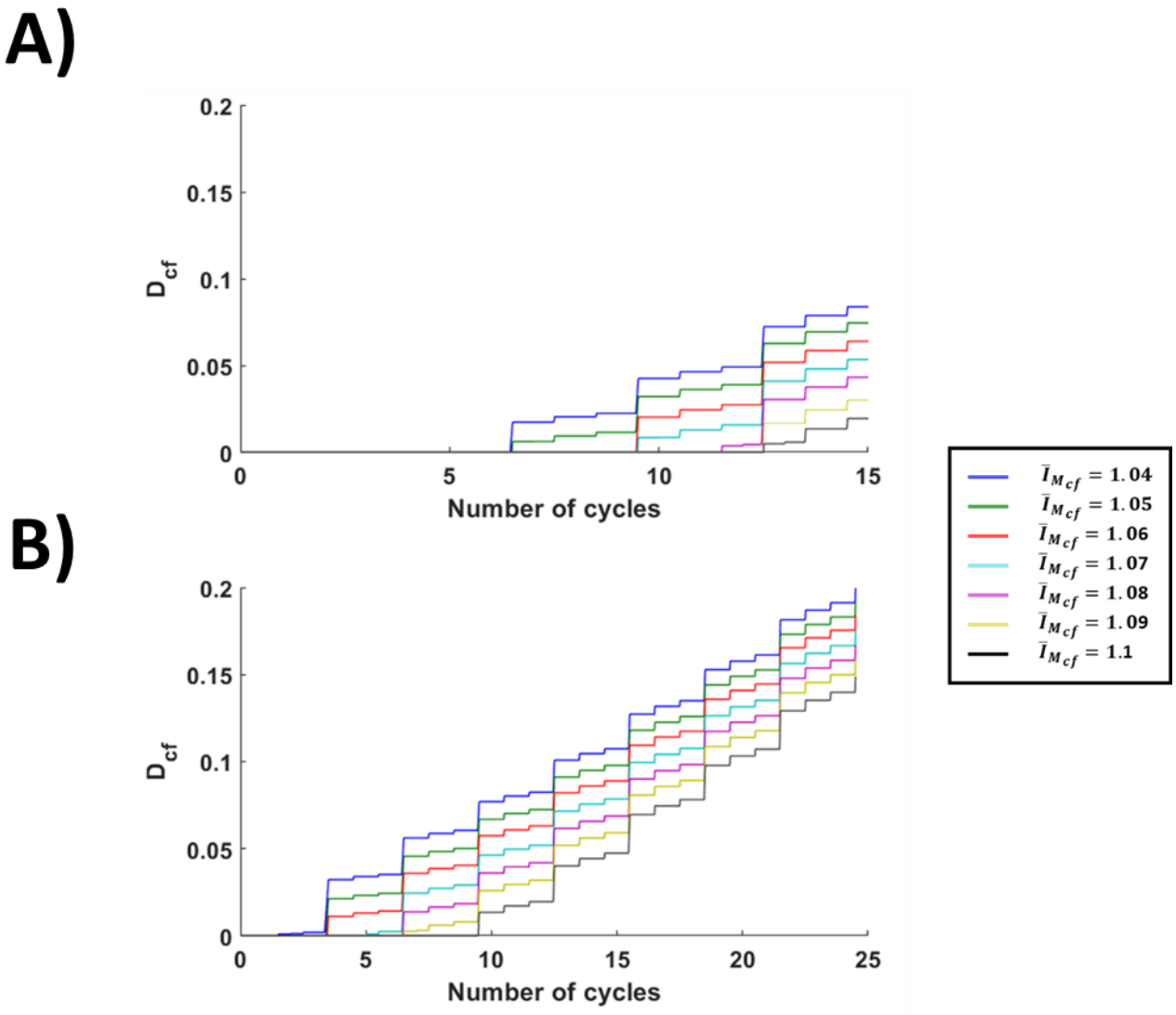

Figure B.3. *The influence of selecting different damage thresholds on the damage accumulation in the collagen fibres in (A) axial and (B) circumferential intact samples. The associated stress-strain curves are presented in Figure 7(A).*

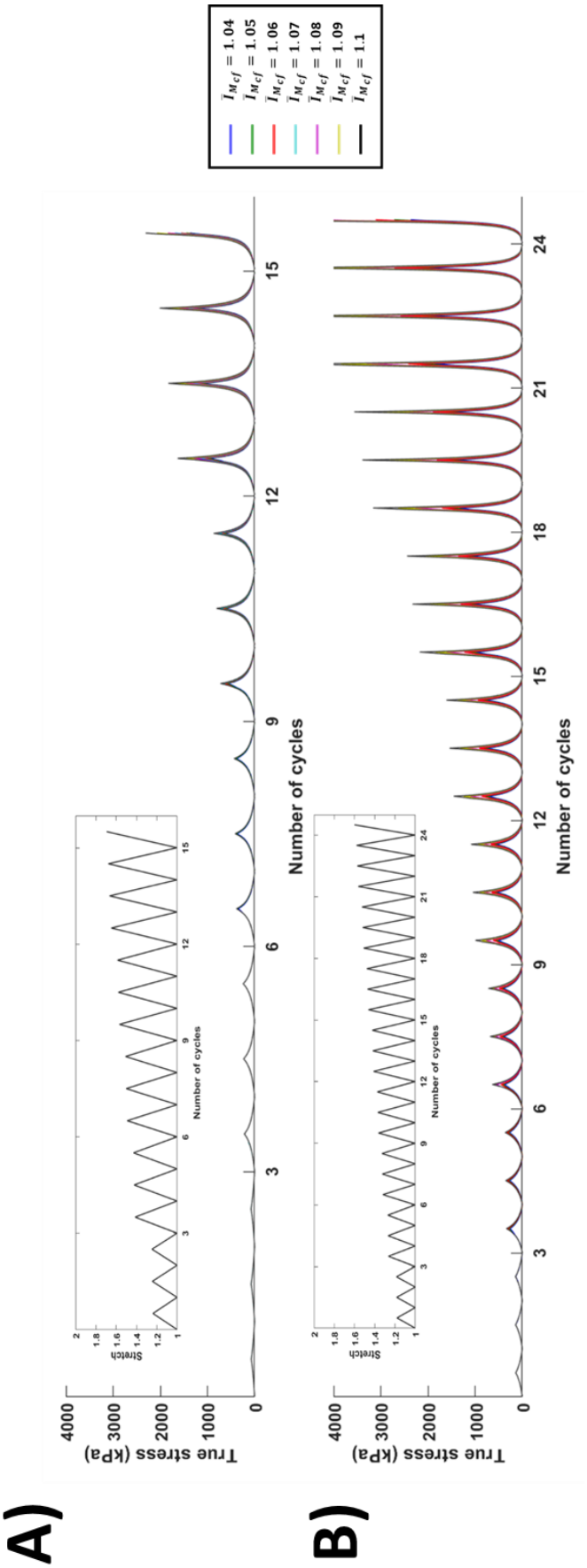

Figure B.4. *The influence of selecting different damage thresholds on the stress calculation in (a) axial and (b) circumferential intact samples. The associated stress-strain curves are presented in Figure 7(a).*

C Statistical analysis of permanent set values in the intact and digested samples

The values obtained for permanent set in the intact and collagen fibre digested samples in axial and circumferential directions were compared using a one-way analysis of variance (ANOVA). The mean values of permanent set for these samples are shown in Figure 3.5. Here, the values of permanent set at each peak strain level were grouped. These groups are shown in Table C-1 at each peak strain level. There are three values for permanent set in each group. A summary of the samples used for this analysis is shown in Table 3-1.

Table C-1 presents the results of the statistical analyses performed on the values of permanent set in each group. The null hypothesis was that the four group means are not significantly different from each other at peak strain levels. In this table, SS shows the values of sum of squares between and within each group. df is the values of degrees of freedom and MS presents the values of mean squares. For further information about the interpretation of these values the reader is referred to, for example, Madu (2003). All the analyses were performed with a significance level of 0.05. The same level of significance was used in many studies such as (Agewall et al. 2006; Yan et al. 2009) –just to name a few. The results show that at all the cases the obtained P-values are larger than 0.05. These P-values show that the null hypothesis cannot be rejected and there is no statistically significant difference between the values obtained for permanent set in the intact and collagen fibre digested samples in axial and circumferential directions.

Table 0-1. *A summary of the statistical analysis performed on the values of permanent set obtained from intact and digested samples in the axial and circumferential directions at different peak strain levels.*

SUMMARY							ANOVA				
Peak strain	0.2	*Groups*	*Count*	*Sum*	*Average*	*Variance*	***Source of Variation***	*SS*	*df*	*MS*	***P-value***
		$Intact_{circ}$	3	0.103325	0.034442	4.14E-05	**Between Groups**	0.001037	3	0.000346	**0.124606**
		$Intact_{axial}$	3	0.091579	0.030526	7.25E-05	**Within Groups**	0.001064	8	0.000133	
		$Digested_{circ}$	3	0.157522	0.052507	0.000299					
		$Digested_{axial}$	3	0.146616	0.048872	0.000119	**Total**	0.002102	11		
Peak strain	0.275	*Groups*	*Count*	*Sum*	*Average*	*Variance*	***Source of Variation***	*SS*	*df*	*MS*	***P-value***
		$Intact_{circ}$	3	0.1346	0.044867	0.000118	**Between Groups**	0.000731	3	0.000244	**0.385569**
		$Intact_{axial}$	3	0.118286	0.039429	0.000188	**Within Groups**	0.001691	8	0.000211	
		$Digested_{circ}$	3	0.178125	0.059375	0.000427					
		$Digested_{axial}$	3	0.162978	0.054326	0.000113	**Total**	0.002423	11		
Peak strain	0.355	*Groups*	*Count*	*Sum*	*Average*	*Variance*	***Source of Variation***	*SS*	*df*	*MS*	***P-value***
		$Intact_{circ}$	3	0.165874	0.055291	0.000234	**Between Groups**	0.000512	3	0.000171	**0.676747**
		$Intact_{axial}$	3	0.144993	0.048331	0.000358	**Within Groups**	0.002595	8	0.000324	
		$Digested_{circ}$	3	0.198729	0.066243	0.000594					
		$Digested_{axial}$	3	0.17934	0.05978	0.000111	**Total**	0.003107	11		
Peak strain	0.433	*Groups*	*Count*	*Sum*	*Average*	*Variance*	***Source of Variation***	*SS*	*df*	*MS*	***P-value***
		$Intact_{circ}$	3	0.197149	0.065716	0.000388	**Between Groups**	0.000379	3	0.000126	**0.84707**
		$Intact_{axial}$	3	0.1717	0.057233	0.000583	**Within Groups**	0.003775	8	0.000472	
		$Digested_{circ}$	3	0.219332	0.073111	0.000802					
		$Digested_{axial}$	3	0.195703	0.065234	0.000115	**Total**	0.004154	11		
Peak strain	0.51	*Groups*	*Count*	*Sum*	*Average*	*Variance*	***Source of Variation***	*SS*	*df*	*MS*	***P-value***
		$Intact_{circ}$	3	0.228424	0.076141	0.000582	**Between Groups**	0.000332	3	0.000111	**0.914034**
		$Intact_{axial}$	3	0.198407	0.066136	0.000862	**Within Groups**	0.005232	8	0.000654	
		$Digested_{circ}$	3	0.239936	0.079979	0.001049					
		$Digested_{axial}$	3	0.212065	0.070688	0.000123	**Total**	0.005564	11		
Peak strain	0.59	*Groups*	*Count*	*Sum*	*Average*	*Variance*	***Source of Variation***	*SS*	*df*	*MS*	***P-value***
		$Intact_{circ}$	3	0.259699	0.086566	0.000815	**Between Groups**	0.000399	3	0.000133	**0.938159**
		$Intact_{axial}$	3	0.225114	0.075038	0.001195	**Within Groups**	0.008041	8	0.001005	
		$Digested_{circ}$	3	0.259699	0.086566	0.000815					
		$Digested_{axial}$	3	0.225114	0.075038	0.001195	**Total**	0.00844	11		
Peak strain	0.66	*Groups*	*Count*	*Sum*	*Average*	*Variance*	***Source of Variation***	*SS*	*df*	*MS*	***P-value***
		$Intact_{circ}$	3	0.281143	0.093714	0.001665	**Between Groups**	0.000499	3	0.000166	**0.927819**
		$Intact_{axial}$	3	0.244789	0.081596	0.000152	**Within Groups**	0.008974	8	0.001122	
		$Digested_{circ}$	3	0.290974	0.096991	0.001088					
		$Digested_{axial}$	3	0.251821	0.08394	0.001582	**Total**	0.009474	11		
Peak strain	0.75	*Groups*	*Count*	*Sum*	*Average*	*Variance*	***Source of Variation***	*SS*	*df*	*MS*	***P-value***
		$Intact_{circ}$	3	0.301746	0.100582	0.002032	**Between Groups**	0.000713	3	0.000238	**0.914459**
		$Intact_{axial}$	3	0.261151	0.08705	0.000174	**Within Groups**	0.01126	8	0.001408	
		$Digested_{circ}$	3	0.322248	0.107416	0.001399					
		$Digested_{axial}$	3	0.278528	0.092843	0.002024	**Total**	0.011973	11		
Peak strain	0.82	*Groups*	*Count*	*Sum*	*Average*	*Variance*	***Source of Variation***	*SS*	*df*	*MS*	***P-value***
		$Intact_{circ}$	3	0.322349	0.10745	0.00244	**Between Groups**	0.001013	3	0.000338	**0.896647**
		$Intact_{axial}$	3	0.277514	0.092505	0.000201	**Within Groups**	0.013823	8	0.001728	
		$Digested_{circ}$	3	0.353523	0.117841	0.00175					
		$Digested_{axial}$	3	0.305235	0.101745	0.002521	**Total**	0.014835	11		
Peak strain	0.9	*Groups*	*Count*	*Sum*	*Average*	*Variance*	***Source of Variation***	*SS*	*df*	*MS*	***P-value***
		$Intact_{circ}$	3	0.342953	0.114318	0.002888	**Between Groups**	0.001399	3	0.000466	**0.877155**
		$Intact_{axial}$	3	0.293876	0.097959	0.000232	**Within Groups**	0.016662	8	0.002083	
		$Digested_{circ}$	3	0.384798	0.128266	0.002139					
		$Digested_{axial}$	3	0.331942	0.110647	0.003071	**Total**	0.018061	11		

D Remodelling metric compared with geometrical metric Ω

In this part, the results obtained for the novel geometrical metric (Ω) is compared with results obtained for the remodelling metric (RM) on a branch of an atherosclerotic carotid artery obtained from a patient under evaluation for an endarterectomy procedure. This artery is subjected to blood pressure of 16 kPa and axial strain of 5 %. The geometry of this artery is depicted in Figure C.1 . The results obtained for Ω on the luminal surface of this artery is depicted in Figure C.2. Figure C.3 to C.4 present the values obtained for RM during the re-orientation of the fibres from three different initial configurations toward an optimum fibre distribution. Figure C.3 presents the values of RM obtained in a situation where fibres were postulated to be parallel with the direction of the intermediate principal stress. Fibres were postulated to be at 45^o and parallel with respect to the direction of maximum principal stress in Figure C.3 and 4 respectively. This figure shows that higher values of RM are obtained at the areas with higher values of Ω indicating that there is a higher lack of remodelling at plaque shoulders. Also, higher values of RM were obtained in the case where fibres were assumed to be parallel with the direction of the intermediate principal stress indicating that more remodelling is required in terms of re-orientation in this case.

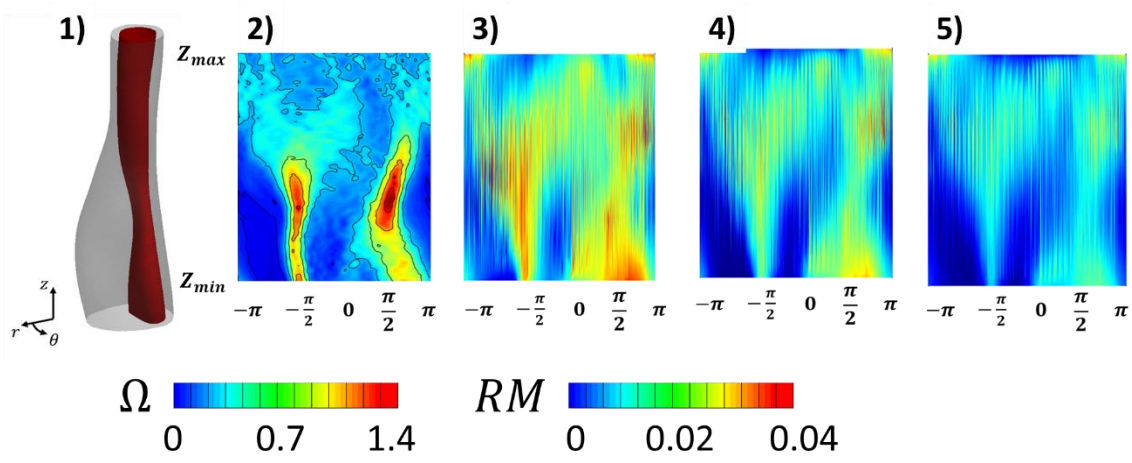

Figure D.1*. Geometry of a branch of an atherosclerotic carotid artery. 2. Values of Ω obtained for the luminal surface of this artery. Values of RM obtained for three different initial configurations of fibres: 3) Parallel with the direction of the intermediate principal stress, 4) at* 45^o *with respect to the direction of the intermediate principal stress and 5) parallel with direction of the maximum principal stress.*